JUPITER: A STUDY OF ATMOSPHERIC COMPOSITION, STRUCTURE, AND DYNAMICS USING MICROWAVE TECHNIQUES.

A Dissertation
Presented to
The Academic Faculty

By

Amadeo Bellotti

In Partial Fulfillment
of the Requirements for the Degree
Doctor of Philosophy in the
School of Electrical and Computer Engineering

Georgia Institute of Technology

May 2018

JUPITER: A STUDY OF ATMOSPHERIC COMPOSITION, STRUCTURE, AND DYNAMICS USING MICROWAVE TECHNIQUES.

Approved by:

Dr. Paul G. Steffes, Advisor
School of Electrical and Computer Engineering
Georgia Institute of Technology

Dr. Morris B. Cohen
School of Electrical and Computer Engineering
Georgia Institute of Technology

Dr. Andrew F. Peterson
School of Electrical and Computer Engineering
Georgia Institute of Technology

Dr. Gregory D. Durgin
School of Electrical and Computer Engineering
Georgia Institute of Technology

Dr. Carol Paty
School of Earth and Atmospheric Sciences
Georgia Institute of Technology

Date Approved: February 12, 2018

The normal person classifies an object, and then forgets about it. The creative person, by contrast, is always open to new possibilities.

Jordan B. Peterson

To my parents,

Who are always putting education first.

ACKNOWLEDGEMENTS

I would like to express my deepest gratitude to my adviser Professor Paul Steffes for his support and guidance throughout the course of this research. His constant wealth of knowledge, support, and patience helped me in completing this work. Although electromagnetism, planetary remote sensing, and planetary science are not fields I would have seen myself working with during my undergraduate years, Dr. Steffes, eased me into it in a way I feel allowed me to grow and enjoy it. I would also like to thank my committee members Dr. Morris B. Cohen, Dr. Andrew F. Peterson, Dr. Gregory D. Durgin, and Dr. Carol Paty for providing me with the time and effort in carefully reviewing my thesis work.

I acknowledge the NASA Juno Program for the financial support of this work. This work was supported by NASA Contract NNM06AA75C from the Marshall Space Flight Center supporting the Juno Mission Science Team, under Subcontract 699054X from the Southwest Research Institute.

The success of the laboratory experiments was made possible as a result of many contributions. I wish to thank Dr. Bryan Karpowicz for developing the high-pressure centimeter-wavelength measurement system, Dr. Kirtuthika Devaraj for the development of her ammonia absorption model, and Dr. Thomas Hanley for providing the data processing code. All of these were utilized in this research work.

The success of the retrieval method was made possible by suggestions from the entire Juno MWR team. Their support and guidance in these new fields was invaluable. I would particularly like to thank Prof. Andrew Ingersol and Dr. Cheng Li of California Insitute of Technology for explaining and reexplaining the physics behind why some of my crazy ideas wouldn't work.

My graduate student experience would not have been complete had it not been for the friends I made over the years. I thank my friends for making my stay at Georgia Tech and Atlanta a blast: Dalton Brown, Morgan Lilly, Grayson Lilly, Alex Tam, Jackson

McCormick, Nick Gross, Marc Higginson-rollins, Alex Atkins, and Parker Singletary.

I would also like to thank my girlfriend Eva Chamberlain for putting up with me finishing this thesis for the past two years. The past two years have been amazing and I look forward to our new adventure in Dallas.

The constant support and encouragement from my family has allowed me to pursue my goals throughout these years. I cannot thank them enough for pushing me to go to graduate school.

TABLE OF CONTENTS

LIST OF TABLES

LIST OF FIGURES

SUMMARY

The objective of this research has been to advance the understanding of Jupiter's atmospheric composition, structure and dynamics using microwave techniques. Jupiter is not only the largest planet in our solar system, but one of the most interesting and complex. Although constraints have been inferred on the amounts of certain gases present, the global abundances and distributions of water vapor and ammonia were relatively unknown. Measurements of water vapor and ammonia in Jupiter's deep atmosphere (to pressures exceeding 100 bars) are best accomplished via passive microwave emission measurements taken by the Juno Microwave Radiometer (MWR).

Accurate retrievals of atmospheric parameters in Jupiter's atmosphere requires accurate models. This work includes laboratory measurements which have been used to refine previously-existing models for the microwave opacity of gaseous ammonia and water vapor. Additionally, this work involves integration of these new models, plus four additional models (derived as part of this work), into an existing forward model for emission from the jovian atmosphere. The four models derived in this work are: (1) The effects of virga on the microwave emission spectrum of Jupiter, (2) The effects of a potential radiative zone deep in Jupiter's atmosphere, (3) The effect of possible ionized alkali metals in the deep atmosphere on the jovian microwave emission, and (4) auroral effects on the jovian microwave emission.

These models were then used to perform retrievals of atmospheric parameters using measurements taken by the Juno MWR. The retrieval utilizes a neural network as a surrogate to the forward model. This surrogate is able to quickly and accurately predict results from the forward model. The surrogate is then paired with the L-BFGS-B minimization algorithm and results in a two part retrieval. The first part retrieves the deep abundance of ammonia and water vapor at a place most resembling an ideal adiabat. The second uses these retrieved values to produce an ammonia distribution map.

CHAPTER 1
INTRODUCTION

1.1 Motivation and Background

The solar system is comprised of the sun, eight planets, their moons and smaller solar orbiting bodies. The planets are further divided into two groups: terrestrial planets and gas giants. Mercury, Venus, Earth, and Mars, the four planets closest to the sun, are known as the terrestrial planets; Jupiter, Saturn, Uranus, and Neptune are known as the gas giants. Unlike the terrestrial planets, the gas giants do not have a surface. Rather, the gas giants are composed of gases held together by gravity that become denser towards the center of the planet. Like the sun and the majority of the universe, the gas giants are mostly composed of hydrogen and helium. Heavier elements, such as carbon and oxygen, are formed throughout the universe by fusion of helium nuclei in the cores of giant stars. Further fusion creates massive atoms (sulfur, silicon, iron, etc.) that account for the majority of the terrestrial planets' mass.

Jupiter, the largest planetary body in our solar system, is 2.5 times larger than all other planets in our solar system combined. Due to strong gravity fields and relatively low temperatures, Jupiter, and other jovian planets, retained a large portion of the composition from the primordial solar nebula which formed our solar system. Consequently, studying and understanding the molecular composition can reveal much information about the formation of our solar system and lead to vital hints about the formation of similar planetary systems.

Jupiter's microwave emission spectrum (centimeter- and millimeter-wavelengths) consists of both thermal and non-thermal components. The thermal emission originates from the neutral atmosphere while the non-thermal emission is from electrons and ions trapped above the neutral atmosphere in Jupiter's inner radiation belts. While ground-based radio

observations at frequencies greater then 3 GHz (10 cm) are dominated by thermal emissions, the non-thermal (synchrotron) emissions dominate at frequencies less than 3 GHz (Berge and Gulkis, 1976; de Pater et al., 2003). Even at 10 GHz (3 cm), there is approximately a 10% contribution from the synchrotron component to the total emission from Jupiter (Berge and Gulkis, 1976; de Pater et al., 2003).

The NASA Juno Mission is a solar-powered, spin-stabilized robotic spacecraft that launched on August 5, 2011 from Cape Canaveral Air Force Station. After an Earth flyby and gravity assist in October 2013, Juno arrived at Jupiter and entered its orbit on July 4, 2016. Over the course of its residency at Jupiter, it will complete 36 highly elliptical, 53-day polar orbits around the planet while collecting data on the dynamics of its atmosphere, radiation belts, magnetosphere, and gravity field. The orbital path (a minimum altitude of 3000 km above the cloud tops) was selected to allow the spacecraft to pass between the planet's strong radiation belts and the top of the atmosphere, allowing atmospheric observations from low altitudes while avoiding synchrotron radiation (See Figure 1.1) (Matousek, 2005). From this vantage point, the microwave radiometer (MWR) onboard Juno measures thermal emissions from Jupiter's atmosphere in the 0.6–22 GHz (50–1.36 cm) range using six separate channels (Pingree et al., 2008). All atmospheric data is obtained during a period of approximately three hours centered on the Juno spacecraft's closest approach to Jupiter, known as perijove (PJ).

As the spacecraft moves through perijove, each 30-second spin sweeps the MWR beams through a great circle on the sky, and scans Jupiter generally along the subspacecraft track, depending on the orientation of the spacecraft spin vector. Each latitude along the subspacecraft track is observed numerous times over a range of emission angles. There are three orbit spin plane orientations used thus far by the Juno spacecraft: Gravity, MWR, and MWR Tilt. The Gravity orientation is when the spacecraft's communication antenna is pointed toward Earth and used primarily for gravity science. Due to the geometry, this orbit does not guarantee the radiometer will be pointing nadir. The second orientation, MWR,

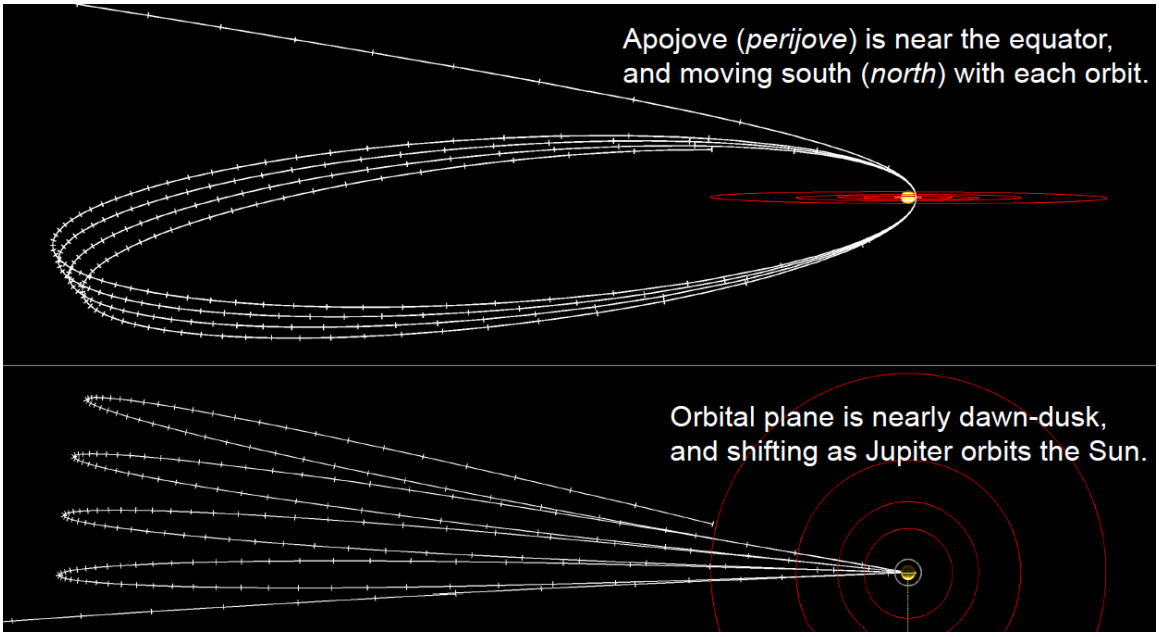

Figure 1.1: Juno orbital trajectory through Perijove 4. The top figure is the view of Jupiter from the Sun while the bottom is a north-pole view of Jupiter. Each tick mark on the figure represents the distance traveled by Juno in 1 day.

is when the spacecraft's spin plane is oriented to contain Jupiter's center, ensuring that the MWR instrument will measure nadir across all latitudes. The third orientation, MWR Tilt, compensates for the longitudinal drift of the MWR footprint due to Jupiter's rotation. In this orbit the spacecraft spin vector is oriented approximately 14° out of the equatorial plane of Jupiter, allowing measurements of the same parcel of atmosphere at multiple emission angles (Janssen et al., 2017a). The perijoves considered in this work, along with their dates, altitude, orientation, and minimum emission angle at perijove are listed in Table 1.1

It is well known that the microwave emission spectrum of Jupiter's atmosphere reflects the abundance and distribution of constituents like ammonia and water vapor (Janssen et al., 2005), but there are a number of factors that can limit the accuracy of using microwave remote sensing to measure these constituents (de Pater et al., 2005). The most important of these factors is the knowledge of microwave absorption properties of these constituents under jovian conditions. These properties are dependent on the observation frequency and the temperature, pressure, and composition (fTPC space) of the atmosphere (Janssen, 1993).

Table 1.1: List of Perijoves, dates, altitude, and orbit orientation used in this work.

Perijove	Date	Altitude at Perijove (km)	Orbit Orientation	Minimum Emission Angle at Perijove
1	August 27, 2016	4147	Gravity	2.8°
3	December 11, 2016	4154	Gravity	19.2°
4	February 2, 2017	4304	MWR	0.0°
5	March 27, 2017	3409	MWR Tilt	0.0°
6	May 19, 2017	3503	Gravity	15.1°
7	July 11, 2017	3501	MWR	0.0°
8	September 1, 2017	3501	Gravity	22.8°
9	October 24, 2017	3500	MWR Tilt	0.0°

To interpret the observed emission spectra of the jovian atmosphere, the emission spectra are compared with accurate jovian atmospheric models. Consistent physical profiles of various constituents are then obtained from the comparisons. While a lack of laboratory measurements of the centimeter- and millimeter-wavelength properties of various gases has been cited as a major hindrance for modeling the atmosphere (de Pater and Mitchell, 1993; de Pater et al., 2005), recent measurement campaigns in our laboratory (Devaraj et al., 2014; Karpowicz and Steffes, 2011a; Karpowicz and Steffes, 2011b; Hanley et al., 2009; Bellotti et al., 2016) have made great strides in better understanding these properties.

The atmospheres of Jupiter and other jovian planets (Saturn, Uranus, and Neptune) are primarily composed of hydrogen (H_2) and helium (He), with various trace constituents such as ammonia (NH_3), water vapor (H_2O), methane (CH_4), hydrogen sulfide (H_2S), and phosphine (PH_3) (de Pater and Lissauer, 2001; Atreya et al., 2003). In Jupiter's atmosphere, gaseous ammonia is the strongest contributor to the centimeter-wavelength absorption spectra. Hence, accurate laboratory measurements of the microwave opacity of ammonia facilitate accurate retrievals of the concentration and distribution of ammonia, as well as that of water vapor by the Juno MWR.

The primary goal of the Juno MWR experiments is to measure the abundance of water and ammonia in the deep atmosphere of Jupiter. Studying the composition of Jupiter will aid in the studies of our planetary system's creation and evolution. By utilizing JPL's

Jupiter Atmospheric Microwave Radiative Transfer code (JAMRT, described in Janssen et al. (2013) and Janssen et al. (2017a)), a retrieval technique utilizing artificial neural networks has been developed to retrieve such abundance profiles from the data collected by the Juno MWR.

1.2 Science Objectives and Applications

The objective of this research is to advance the understanding of Jupiter's atmospheric composition, structure, and dynamics through microwave radiometry. This work includes laboratory measurements that have been used to refine previously-existing models for the microwave opacity of gaseous ammonia and water vapor. Additionally, this work involves integration of these new opacity models, plus additional models derived as part of this work, into an existing forward model for emission from the jovian atmosphere. These additional models include the microwave effects of virga (precipitation on that evaporates before hitting the planets surface), a deep radiative zone, and deep ionization of alkali metals. Finally, the forward model has been used to train retrieval algorithms to analyze data currently being collected from the Mission Juno Microwave Radiometer (MWR). The aim of these analyses is to detect the abundance and distribution of ammonia and water vapor and to investigate the possible presence of virga, and other deep atmospheric effects.

Studies of the jovian microwave emission using JAMRT indicate a significant contribution of the emission at 24– and 50–cm wavelengths from the ammonia and water vapor in Jupiter's atmosphere. The emissions at these wavelengths have been shown to originate from deep within the jovian atmosphere (at temperatures at or exceeding 600 K). Since the absorption models created for ammonia and water vapor have been based on laboratory measurements reaching only 500 K, it is an important goal of this work to carefully evaluate any extrapolation of these two absorption models to higher temperatures.

One motivation behind this work is the difference in the calculated microwave emission from the jovian atmosphere when the absorption model for ammonia is changed between

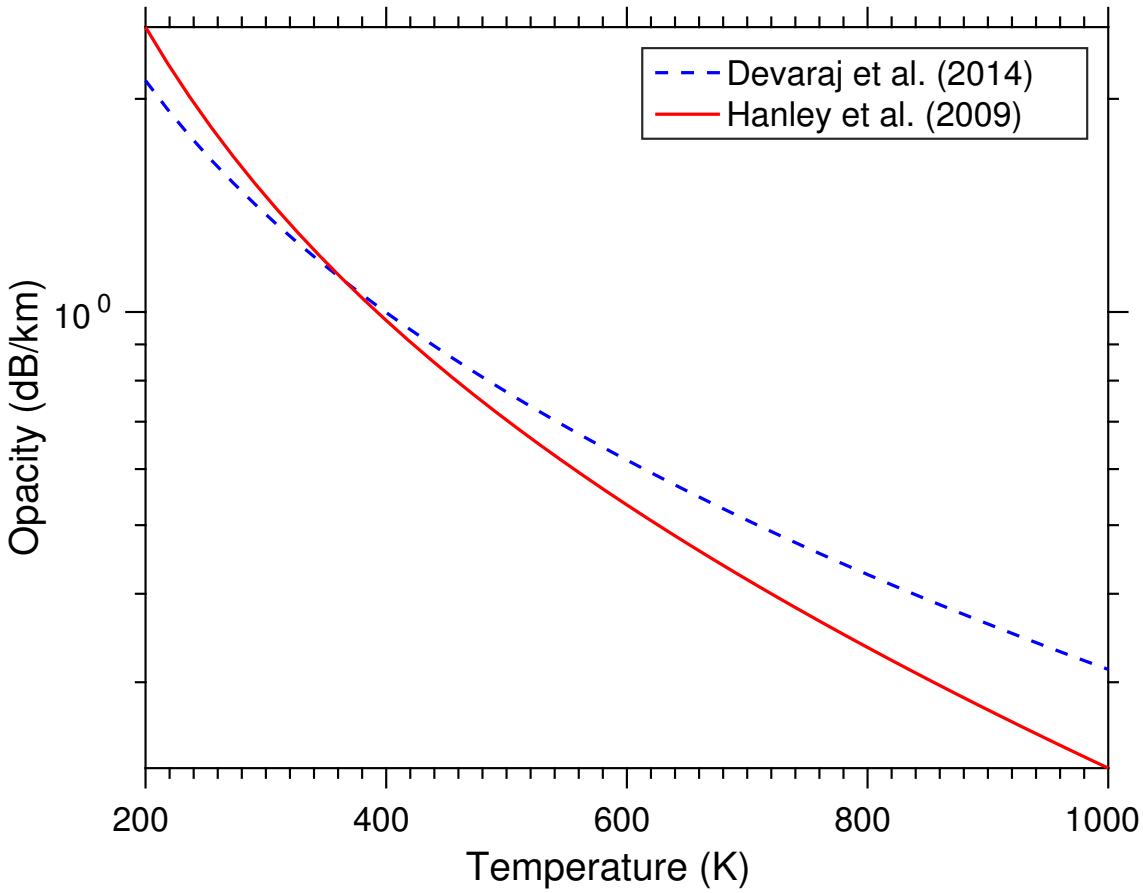

Figure 1.2: The temperature dependences of the Devaraj et al. (2014) model and the Hanley et al. (2009) model. Here the mixture is NH_3 = 0.15%, H_2 = 86.65%, He = 13.2% at a pressure of 82.432 bars and frequency of 1.5 GHz.

the Devaraj et al. (2014) model and the Hanley et al. (2009) model (both developed at Georgia Tech). These two models perform equally well when compared to laboratory data relevant to Juno (frequencies under 27 GHz) (Devaraj et al., 2014). While the models are similar in the measured fTPC space, they differ significantly when extrapolated to higher temperatures. The differences between the two models significantly change the modeled emission at 600 MHz as modeled using JAMRT. After examination of the models it was concluded that the temperature dependencies of both differ significantly. This is shown in Figure 1.2 where the temperature dependencies of the two models are shown under high-pressure conditions. As part of this work, additional laboratory measurement data has been obtained at 600K, to better resolve this inconsistency.

A successful measurement campaign of water vapor's centimeter-wavelength microwave absorption under a jovian atmosphere was conducted by Karpowicz and Steffes (2011a) and Karpowicz and Steffes (2011b). While nearly 2000 laboratory measurements were conducted at pressures from 30 mbars to 101 bars and temperatures up to 525 K, the model developed by Karpowicz and Steffes (2011a) and Karpowicz and Steffes (2011b) produces non-physical results at temperatures greater than 550 K. That is, the opacity model shows no temperature dependence for temperatures greater than 550 K. As a result, a set of laboratory measurements of the centimeter-wavelength opacity of water vapor were conducted at 597 K. These measurements were used to verify a correction to the Karpowicz model.

While initial modeling studies have shown it is possible to retrieve deep water vapor abundances in Jupiter's atmosphere using a multi-channel radiometer (Janssen et al., 2005), there are a number of factors which will limit the accuracy of this approach. The most significant limitation is the underdetermined nature of the problem. The weighting functions of each six channels are broad, with the longest channel probing to pressures greater than 300 bars. While using measurements from multiple emission angles and the limb darkening does constrain the problem, initial results show that ammonia is depleted down to at least 50–60 bars except near the equator. This added complexity forces the use of regularization and other physical constraints in the retrieval of deep water vapor abundance. Unlike infrared spectroscopy, inversion of the microwave spectra is difficult because the spectral features are nearly absent in the microwave regime. The prevailing method of fitting the microwave spectra is by forward modeling and by using trial-and-error methods to find models that reproduce the data. Multiple methods of retrievals have been developed using machine learning techniques, which both automates this trial-and-error method and invert the data.

1.3 Organization

This dissertation covers multiple topics:

- the microwave absorption of gaseous constituents
- the design and measurement procedures for measuring microwave absorption properties of gaseous ammonia and water vapor under jovian conditions
- an empirically-derived model for NH_3 opacity under jovian conditions
- the Juno Microwave Radiometer data analysis pipeline
- virga on jovian planets
- deep jovian atmospheric effects
- the jovian aurora
- a formal description of machine learning algorithms
- results from applying the machine learning algorithms to the Juno MWR data.

The work is split into three parts: the first explains laboratory measurements made in support of the Juno MWR, the second describes the modeling and theory needed to analyze the data from the Juno MWR, and the third is an analysis of the data from the Juno MWR. Figure 1.3 is a flowchart showing the different parts of this thesis and how they are interconnected.

Part I is divided into two chapters. In Chapter 2, the theory of microwave absorption and forward modeling is discussed, with a brief presentation of the various absorption lineshapes. Chapter 3 discusses the approach for measuring absorption of gasses in the centimeter-wavelength region, highlighting the measurement procedure, data processing, and measurement uncertainties. Additional discussion of and modeling done for NH_3, H_2O, and CH_4 are included.

Part II is divided into two chapters. Chapter 4 discusses modeling the jovian atmosphere, deconvolution of the Juno MWR data, and modeling potential atmospheric phenomena. The first of these phenomena modeled is the effects of virga on the microwave

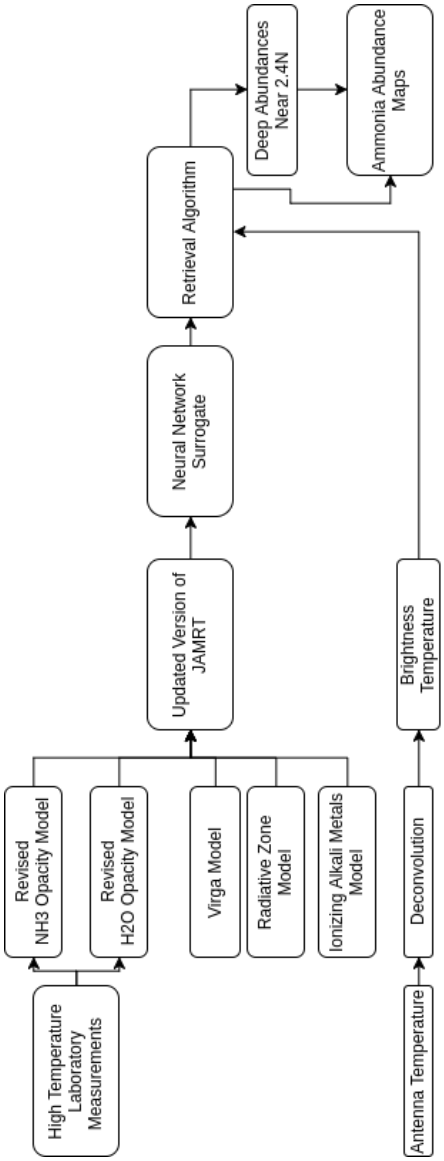

Figure 1.3: Flowchart showing how the different parts of this thesis are interconnected

emission spectra, followed by a description of the radiative zone model and its effects on data from the Juno MWR. This chapter ends with a discussion of the effects of ionization of alkali metals in the deep jovian atmosphere and auroral effects on measurements taken by the Juno MWR. Chapter 5 includes a formal discussion machine learning theory and the Neural Network algorithms used to analyze the Juno MWR data.

Part III is divided into two chapters. Chapter 6 shows the data taken by the Juno MWR during the nine perijoves. Chapter 7 discusses the application of the machine learning based retrievals models on the MWR data and the produced ammonia abundance profiles.

Finally, Chapter 8 concludes this dissertation with a summary of the major contributions and the direction of future research.

Part I

Laboratory Measurements

CHAPTER 2

MICROWAVE REMOTE SENSING TECHNIQUES AND THEORY

Juno's Microwave Radiometer instrument (MWR) measures the atmospheric composition beneath the cloud layers, deeper than 300 bars of pressure. The Juno MWR uses six separate radiometers with wavelengths ranging from 1.3–50 cm to measure the planet's thermal emission (Janssen et al., 2005). The antennas for each channel are located on the sides of the spacecraft so that, as the spacecraft rotates, the antennas will scan the planet along the track of the spacecraft. Brightness temperature measurements of each location, at different emission angles, are taken as the spacecraft moves. These brightness temperatures, with the aid of a radiative transfer model, make possible the determination of the concentrations of water vapor and ammonia at various depths and locations covering the planet. This assumes that the radiative transfer model uses accurate microwave absorption coefficients for H_2O and NH_3, and accurate models for deep atmospheric structure. This chapter discusses the theory of microwave spectroscopy and radiative transfer modeling.

2.1 Microwave Spectroscopy and the Ammonia Spectrum

Electromagnetic radiation incident on a gaseous molecule can produce an absorption or emission of energy at a particular wavelength. Radiation incident on a molecule is absorbed when the molecule transitions from a low energy state to a higher energy state. The frequency associated with this energy change is given by

$$f = \frac{\Delta E}{h} \tag{2.1}$$

where ΔE is the change in energy between the upper and lower states, $h = 6.624 \times 10^{-34}$ Jsec (Planck's constant), and f is the frequency. An isolated molecule's internal energies

are composed primarily of electronic, vibrational, and rotational energies. These are typically associated with absorption or emission in the visible, infrared, and microwave regions, respectively. Vibrational transitions occur when the atoms are in periodic motion while the molecule has a constant rotational motion. A linear molecule with N atoms has 3N-5 normal modes of vibration since the rotation of the molecular axis cannot be observed. A non-linear molecule with N atoms has 5N-6 normal modes of vibration. The terms linear and non-linear refer to the bond angle between bonded atoms, either 180° (linear) or any other bond angle (non-linear). While these frequencies are typically in the infrared region, it's possible for the energy to be in the microwave domain if the molecule is polar. Rotational transitions occur when a molecule that has a magnetic or electric dipole rotates about its center of mass. Polar molecules interacting with electromagnetic radiation are active absorbers of the microwave energy. While non-polar molecules do not possess a permanent dipole moment, they can exhibit pressure-induced absorption resulting from collisionally-induced dipole moments in the molecules. Since the bulk of the jovian atmosphere consists of hydrogen, helium, and methane, it is important to consider the collisionally-induced dipoles from H_2-H_2, H_2-He, and H_2-CH_4 collisions.

2.1.1 Absorption Spectra of Ammonia

Ammonia is a symmetric top molecule with a trigonal pyramidal shape and a bond angle of 107.8° (Figure 2.1). The central nitrogen atom has eight electrons total which are arranged tetrahedrally. Three of these pairs are used to bond with hydrogen which leaves one lone pair. The lone pair repels the bonds more strongly, therefore the bond angle is 107.8° and not 109.5°. This shape gives the ammonia molecule an electric dipole moment and makes it polar.

The central nitrogen atom cannot be allowed in the plane of the hydrogen atoms because of the large potential-energy hump at this position. However, the nitrogen atom can "tunnel" through the plane of the hydrogen atoms and vibrate from one side to the other.

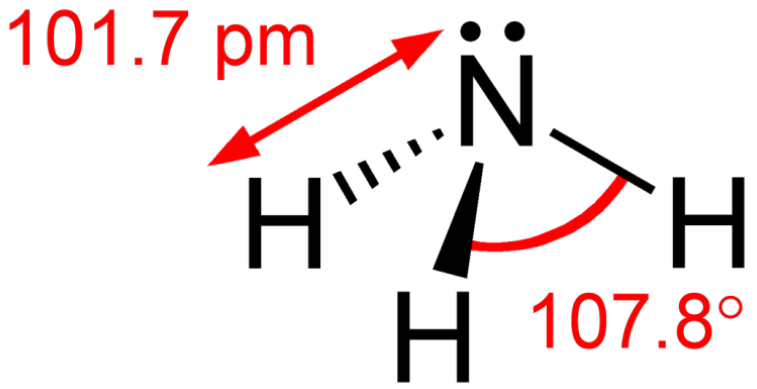

Figure 2.1: Ammonia molecules. Distance is in picometers, pm.

These hindered motions are, in principal, vibrational transitions, but are referred to as inversion transitions. Although the vibrational transitions absorb or emit infrared frequencies, the inversion transitions occur in the microwave region because they are slowed down by the hindering potential of the hydrogen plane (Townes and Schawlow, 1975).

The interaction between the rotational and vibrational motion of ammonia results in a series of closely spaced lines in the rotational spectrum, each corresponding to different vibrational states. The interaction between inversion and rotational transitions of ammonia results in a series of lines in the inversion spectrum, each corresponding to a different rotational state (Townes and Schawlow, 1975).

2.1.2 Line Intensity

The absorption from a collisionally broadened gas is a function of the absorption at the line center, the linewidth, and the lineshape function. The absorption coefficient for a particular molecule at a given frequency, ν, is given by,

$$\alpha = \sum DA_j \pi \Delta\nu_j F_j(\nu, \nu_{0,j,\ldots}) \tag{2.2}$$

where $\nu_{0,j}$ is the line frequency for line j, D is a correction term which unless otherwise stated is unity, A_j is the line center absorption, $\Delta\nu_j$ is the line-width, and F_j is the line-

shape function. Note that the lineshape function seldom varies from line-to-line, but may vary among classes of lines.

An important note is that an absorption coefficient of 1 Nepers/km = 2 optical depths per km (or km^{-1}) = 8.686 dB/km. The first notation is used in electrical engineering, the second is the usual form in physics and astronomy, and the third is the common (logarithmic) form. The third form is often used in order to avoid a possible factor-of-two ambiguity.

The absorption at each line center is calculated using the line intensity information from the online JPL catalog as per Pickett et al. (1998)

$$A_j = \frac{nI_{j(T)}}{\pi \Delta \nu_j} \tag{2.3}$$

where n is the number density of the gas, $I_j(T)$ is the intensity of the line at temperature T, and $\Delta\nu_j$ is the linewidth. The line intensity at the measurement temperature (T) is calculated as per Pickett et al. (1998),

$$I_j(T) \approx I_j(T_0) \left(\frac{T_0}{T}\right)^{\eta+1} \exp\left(\left(\frac{1}{T_0} - \frac{1}{T}\right) E_{(l,j)} \left(hc/k_B\right)\right) \tag{2.4}$$

where $I_j(T_0)$ is the intensity of the line at the reference temperature T_0, $E_{(l,j)}$ is the lower state energy of transition in cm^{-1}, c is the speed of light in cm/s, k_B is Boltzmann's constant, h is the Planck's constant in Jsec, and η is the temperature dependence. The temperature dependence parameter for a diatomic or linear molecule is 1 and for a symmetric rotor is 3/2.

2.1.3 Linewidths

Transitions of an isolated, stationary molecule occur at specific energies and frequencies, however various types of disturbances can modify these energies and frequencies. Broadening of a spectral line is caused when these disturbances give the spectra line a "width" and change the line's center frequency. The full width at half maximum (FWHM) is defined

as the spectral width that accounts for at least half of the molecules in transition.

There are multiple sources of line-broadening including, pressure broadening, molecular collisions against walls, saturation broadening, and Doppler broadening. Doppler broadening is due to the molecules moving relative to the direction of the electromagnetic radiation's propagation. This results in a frequency shift due to the Doppler effect, and is quantified by

$$\Delta\nu_{Doppler} = 3.581 \times 10^{-7}\nu\sqrt{\frac{T}{M}} \tag{2.5}$$

were ν is the center frequency, T is the temperature of the gas, and M is the molecular weight. While the Doppler broadening is significant for low density gas mixtures, under jovian conditions the Doppler effect is negligible. The same is true for saturation broadening.

Under jovian conditions, the greatest source of broadening is pressure broadening due to molecular collisions. The collisions result in a transfer of kinetic energy between the molecules. Each molecular species has a broadening cross-section that depends on its size and dipole moment. When a molecule collides with another molecule of the same species, the resulting broadening is called self-broadening.

Foreign gas broadening is caused when a collision between two molecules of different species occurs. The foreign gas broadening occurs even if the colliding molecules do not have any microwave absorption lines themselves (as with hydrogen and helium).

2.1.4 Lineshapes

The "lineshape" of molecular collisions is used to describe the spectral dependence of the microwave opacity. The first lineshape model of the pressure broadening of gasses was developed by Lorentz (1906). Debye (1929) developed a theory that described the refraction and absorption in the polar molecules using a theory that was different from Lorentz at the zero resonant frequency. Vleck and Weisskopf (1945) then combined the

two theories to produce the Van Vleck-Weisskopf lineshape, given by

$$F_{VVW}(\nu, \nu_{(0,j)}\Delta\nu_j) = \frac{1}{\pi}\left(\frac{\nu}{\nu_{(0,j)}}\right)^2\left[\frac{\Delta\nu_j}{(\nu_{(0,j)}-\nu)^2+\Delta\nu_j^2}+\frac{\Delta\nu_j}{(\nu_{(0,j)}+\nu)^2+\Delta\nu_j^2}\right] \quad (2.6)$$

where for the line j, $\Delta\nu_j$ is the half width at half-maximum, $\nu_{(0,j)}$ is the center frequency of the line transition, and ν is the frequency of the incident electromagnetic wave. Gross (1955) assumed a different distribution of molecular velocities (Maxwellian over Boltzmann) and derived the Gross lineshape:

$$F_G(\nu, \nu_{(0,j)}) = \frac{1}{\pi}\left(\frac{\nu}{\nu_{(0,j)}}\right)\left[\frac{4\nu\nu_{(0,j)}\Delta\nu_j}{(\nu_{(0,j)}^2-\nu^2)^2+4\nu^2\Delta\nu_j^2}\right] \quad (2.7)$$

While the Van Vleck-Weisskopf and Gross lineshapes converge at the line centers, the Gross lineshape has higher skirts away from the line center. Ben-Reuven (1966) derived a lineshape with two additional parameters, a line shift (δ) proportional to the gas density, and a line-to-line coupling element (ζ). The Ben-Reuven lineshape is given by

$$F_{BR}(\nu, \nu_{(0,j)}, \gamma_j, \zeta_j, \delta_j) = \frac{2}{\pi}\left(\frac{\nu}{\nu_{(0,j)}}\right)^2\left[\frac{(\gamma_j-\zeta_j)\nu^2+(\gamma_j+\zeta_j)[(\nu_{(0,j)}+\delta_j)^2+\gamma_j^2+\zeta_j^2]}{[\nu^2-(\nu_{(0,j)}+\delta_j)^2-\gamma_j^2+\zeta_j^2]^2+4\nu^2\gamma_j^2}\right] \quad (2.8)$$

where for the line j, $\gamma_j = \Delta\nu_j$ is the linewidth. The Gross lineshape is a special case of the Ben–Reuven lineshape under the assumption that only sense-reversing collisions take place, in which case $\gamma_j = \zeta_j$ and $\delta = 0$ (Waters, 1976).

2.2 Radiative Transfer Modeling

The Jupiter Atmospheric Microwave Radiative Transfer Code (JAMRT) (Janssen et al., 2013; Janssen et al., 2017a) was developed by the NASA Jet Propulsion Laboratory using the microwave absorption coefficients developed in this dissertation. A pencilbeam forward model is employed, which computes brightness temperatures corresponding to a set of atmospheric parameters. This section discusses the general theory of Radiative Transfer

Modeling. Section 4.1 describes the JAMRT model more in-depth.

2.2.1 Theoretical Background

The emission from the jovian atmosphere can be computed using a Radiative Transfer Model (RTM). Radiative transfer is a method used to solve for the emission of electromagnetic energy from a medium. In a most basic RTM, the solution for intensity (or brightness temperature) is computed from emissions along an infinitely thin beam (pencil beam). A second assumption is that the atmosphere is in local thermodynamic equilibrium (LTE). LTE implies that, for a given moment or snapshot in time, the atmosphere is static; the model does not consider atmospheric dynamics when solving the radiative transfer equation. The differential form of the radiative transfer equation is

$$dI_\nu = -\alpha I_\nu ds + \alpha J ds \tag{2.9}$$

where dI_ν is the change in intensity, in W sr^{-1}m^{-2}Hz^{-1}, at a given frequency ν over a path length ds, α is the absorption coefficient or attenuation over a path length ds, and J is the source function, in W sr^{-1}m^{-2}Hz^{-1} (Liou, 2002).

In the microwave and millimeter wave regime, effects from scattering approach the Rayleigh-Jeans limit, and may be neglected without introducing significant error. Therefore the source function J becomes the Plank function.

$$J_\nu = B_\nu(T) = \frac{h\nu^3}{c^2}\frac{1}{\exp(\frac{h\nu}{kT}) - 1} \approx \frac{2kT\nu^2}{c^2} \tag{2.10}$$

where T is the temperature in Kelvin, h is Planck's constant, k is Boltzman's constant, and c is the speed of light (Karpowicz, 2010). The approximation in equation 2.10 is for cases where $h\nu \ll kT$ (characteristic of centimeter and millimeter-wavelengths) and is known as the Rayleigh-Jeans approximation.

If equation 2.9 is integrated over the path s it becomes

$$I_\nu(s) = I_{\nu,o}(s_0)e^{-\tau_\nu(s_0)} + \int_0^{s_0} \alpha_\nu(s)B_\nu(T)e^{-\tau_\nu(s)}ds \tag{2.11}$$

where the first term is the intensity at the boundary of the integration and represents contributions to emissions from sources other than those over the path of integration, such as background or surface emission, and τ is the optical depth defined by

$$\tau_\nu(s) = \int_0^{s} \alpha_\nu(s')ds' \tag{2.12}$$

For gas giants like Jupiter, the surface term can be dropped simplifying equation 2.11 to

$$I_\nu(s) = \int_0^{s_0} \alpha_\nu(s)B_\nu(T)e^{-\tau_\nu(s)}ds \tag{2.13}$$

While intensity is a quantity often used in solar and ultra-violet remote sensing, it is far more common to use brightness temperature for longer wavelengths such as infrared and microwave. This quantity is found by taking the approximation in equation 2.10 and solving for T. Brightness temperature, in K, is defined as,

$$T_b = \frac{Tc^2}{2\nu k} \tag{2.14}$$

Substituting equations 2.10 and 2.14 into 2.13, and solving for brightness temperature, the equation for radiative transfer becomes,

$$T_b(\nu) = \int_0^{s_0} \alpha_\nu(s)T(s)e^{-\tau_\nu(s)}ds \tag{2.15}$$

where T is the physical temperature along the integration path.

The discrete form of 2.15 can be expressed as,

$$T_b = \sum_{i=1}^{N} T_i(1 - \exp(-\tau_{\nu,i})) \exp(-\tau_{\nu,i}) \tag{2.16}$$

where $\tau_{\nu,i}$ is the optical depth in layer i, and T_i is the physical temperature in layer i. The optical depth of layer i is given by

$$\tau_i = \int_{s(z=z_i)}^{s(z=z_{i+1})} \alpha(s) ds \tag{2.17}$$

where z_i is the height of the i^{th} layer (Jenkins et al., 2002).

It is also useful to know how each layer of the atmosphere affects the brightness temperature; this can be found through calculation of the weighting function,

$$W_i = (1 - e^{\tau_i}) e^{-\tau_{i+1 \to N}} \tag{2.18}$$

where $\tau_{i+1 \to N}$ is the optical depth from layer $i + 1$ to layer N.

$$\tau_{j \to k} = \sum_{i=j}^{k} \tau_i \tag{2.19}$$

2.2.2 Parameters of the Radiative Transfer Model

The input parameters of the radiative transfer model (RTM) are the opacity formalisms for the various atmospheric constituents, the index of refraction for each atmospheric layer, the temperature-pressure profiles, and the vertical abundance profiles for the absorbing constituents. Together, the last two parameters make up the Thermo-Chemical model of the atmosphere.

The temperature-pressure profiles and the vertical abundance profiles for the jovian atmosphere are calculated using the Thermo-chemical model described in Karpowicz and Steffes (2013). The atmospheric lapse rate is assumed to be a dry adiabat where there are

no clouds, and a moist adiabat where clouds are present.

There are several absorbing constituents in the jovian atmosphere. The major microwave absorbing constituents are ammonia (NH_3), and water vapor (H_2O). Laboratory work was done to improve the understanding of these two species and is presented in Chapter 3.

The refractive index is important in calculating the path that a ray takes through the atmosphere. Given the known concentration of H_2 and He, as well as the density-normalized refractivity values, the refractivity profile $N(z)$ is computed via

$$N(z) = \frac{NP(z)}{RT(z)} \tag{2.20}$$

where $P(z)$ is the pressure, in bars, $T(z)$ is the temperature, in K, R is the ideal gas constant, and N is the normalized refractivity of the jovian atmosphere. The refractive index profile $n(z)$ is defined in terms of refractivity via

$$n(z) = N(z) \times 10^{-6} + 1 \tag{2.21}$$

2.2.3 Ray-tracing

While a basic radiative transfer equation can be used to solve for brightness temperatures measured by an orbiting spacecraft, the basic formalism assumes an infinitely narrow beamwidth and neglects the effects of refraction between atmospheric layers. Here we present a more advanced ray tracing approach used in the developed RTM employing the technique described by Hoffman (2001).

Ray-tracing Described

Most radio observations of planets are done by measuring emitted rays that originate deep in the atmosphere. However, for modeling purposes it is easier to model ray-paths orig-

inating from the observer and entering the planet's atmosphere. These are equivalent by reciprocity.

The origin of the ray is the location of the radiometer (either on the spacecraft or on earth) in a Cartesian space with the origin defined as the center of the planet. Reference Figure 2.2 for the following discussion. The initial ray direction is set as the pointing direction of the antenna. First, the boresight ray-path is calculated. Once the ray intersects the first layer, the vector location of this intersection is recorded and, from this, the local normal (ray pointing from the origin to the location of intersection) and the zenith angle can be calculated. The incidence angle is then found and Snell's law is applied to find the vector direction of the transmitted ray. Once the vector direction is determined, the vector origin of the ray-segment is set as the initial intersection. A new sphere is defined by the next layer and the ray-sphere intersection algorithm is applied with the new inputs. The algorithm calculates the distance and this is recorded. Using this distance, the new intersection is calculated, which can be either at the next deeper layer or the previous layer (the latter occurs only when observing the limb of the planet). This continues until the ray hits the planetary surface, exits from the back of the planet, or the layer medium becomes so opaque that no significant transmission occurs. It is important to note that ray tracing is only valid for slowly varying media.

Ray-tracing Algorithm Mathematics

The mathematical foundation for the ray-tracing component of the RTM is developed in this section. The ray-sphere intersection algorithm begins with definition of the parametric equation for a ray. A ray is defined as,

$$\begin{aligned} R_{origin} = R_o &= \begin{bmatrix} X_o & Y_o & Z_o \end{bmatrix} \\ R_{direction} = R_d &= \begin{bmatrix} X_d & Y_d & Z_d \end{bmatrix} \end{aligned} \tag{2.22}$$

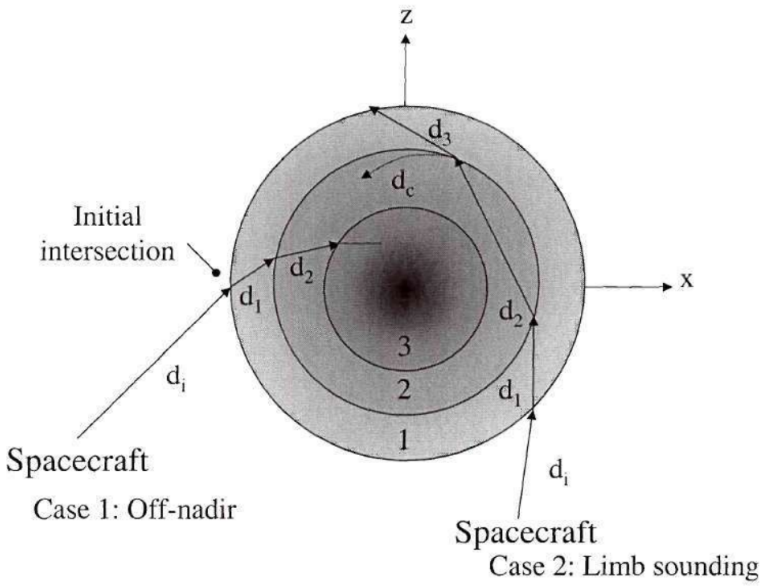

Figure 2.2: A two dimensional graphic example of the ray-tracing process taken from Hoffman (2001). An off-nadir (left) and a limb sounding case (right) are shown. Two possible outcomes for the limb-sounding case are shown. d_3 shows the ray exiting the atmosphere, while d_c shows critical refraction.

where

$$\|R_d\|_2^2 = 1 \tag{2.23}$$

where $\|R_d\|_2^2$ is the L-2 norm squared of the direction vector. This defines a ray as a set of points described by the equation for a line,

$$R = R_o + R_d \times t \tag{2.24}$$

where time, t is greater then zero. The sphere is defined by,

$$\begin{aligned} S_{center} = S_c &= \begin{bmatrix} X_c & Y_c & Z_c \end{bmatrix} \\ S_{radius} &= S_r \\ S_{surface} = S_s &= \begin{bmatrix} X_s & Y_s & Z_s \end{bmatrix} \end{aligned} \tag{2.25}$$

where

$$\|S_s - S_c\|_2^2 = S_r^2 \tag{2.26}$$

Using equation 2.24 as the intersection equation for the ray we can substitute that into equation 2.26, resulting in,

$$\|(R_o + R_d \times t) - S_c\|_2^2 = S_r^2 \tag{2.27}$$

which can be expanded to,

$$(X_o + X_d t - X_c)^2 + (Y_o + Y_d t - Y_c)^2 + (Z_o + Z_d t - Z_c)^2 = S_r^2 \tag{2.28}$$

This can be simplified into a quadratic equation

$$At^2 + Bt + C = 0 \tag{2.29}$$

where,

$$A = \|R_d\|_2^2 = 1 \tag{2.30}$$

$$B = 2\left((R_o - S_c) \bullet R_d\right) \tag{2.31}$$

$$C = \|R_o - S_c\|_2^2 - S_r^2 \tag{2.32}$$

The solutions to this equation are the standard quadratic solutions

$$t_{0,1} = \frac{-B \pm \sqrt{B^2 - 4AC}}{2A} \tag{2.33}$$

where the t's (solutions) are the distance to the intersection point from the ray origin. If the discriminant of these equations is negative, the ray misses the sphere. For the purpose of the RTM, these are the cases where the ray misses the planet or it exits out of the planet's atmosphere. The smallest positive t value is the correct solution. Once the t is found the vector location of the intersection is

$$r_{int} = r_i = \begin{bmatrix} x_i & y_i & z_i \end{bmatrix} = \begin{bmatrix} X_o + X_d t & Y_o + Y_d t & Z_o + Z_d t \end{bmatrix} \tag{2.34}$$

and the unit vector normal at the surface is then

$$r_{normal} = r_n = \frac{(r_i - S_c)}{S_r} = \begin{bmatrix} \frac{(x_i - X_c)}{S_r} & \frac{(y_i - Y_c)}{S_r} & \frac{(z_i - Z_c)}{S_r} \end{bmatrix} \tag{2.35}$$

In terms of the RTM, the solution to the quadratic equation (t) is the distance the ray travels through a given layer. The origin of the transmitted ray is set at the intersection location r_{int} and the direction of the transmitted ray is calculated from the intersection r_{int} and the surface normal r_{normal} using Snell's law.

The vector form of Snell's law requires two vectors: the incident ray vector ($\boldsymbol{I}$) and the local surface normal ($\boldsymbol{N}$). Refer to Figure 2.3 for a graphical demonstration. The incident

angle is calculated using

$$\cos(\theta_1) = -\boldsymbol{I} \cdot \boldsymbol{N} \tag{2.36}$$

From Snell's law, the relative index of refraction (η) is,

$$\eta = \frac{\sin(\theta_2)}{\sin(\theta_1)} = \frac{\eta_1}{\eta_2} \tag{2.37}$$

The angle of the transmitted ray (θ_2) can be computed from known quantities,

$$\cos(\theta_2) = \sqrt{\left(1 - \sin^2(\theta_2\right)} = \sqrt{\left(1 - \eta^2 \sin^2(\theta_1)\right)} = \sqrt{(1 - \eta^2(1 - \cos^2(\theta_1)))} \tag{2.38}$$

The vector direction of the transmitted ray is computed as,

$$\boldsymbol{T} = \eta \boldsymbol{I} + (\eta \cos(\theta_1) - \cos(\theta_2))\boldsymbol{N} \tag{2.39}$$

where the values of $\boldsymbol{I}$ and $\boldsymbol{N}$ are the vectors R_d and r_n respectively. The output of this formula ($\boldsymbol{T}$) is the new value for R_d. Using this algorithm and techniques described in the previous sections we can trace a path through each layer of the atmosphere.

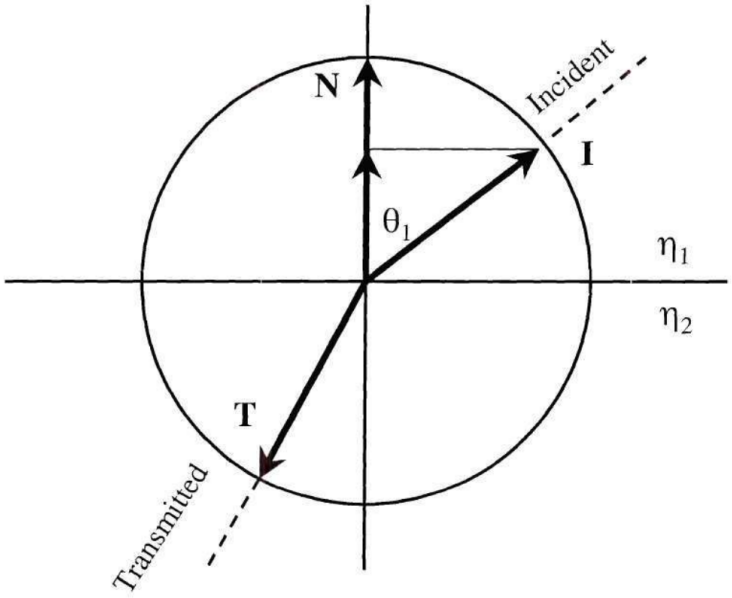

Figure 2.3: Vector implementation of Snell's Law. Image courtesy of Hoffman (2001)

Planetary Oblateness

Jupiter's equatorial and polar radii, at the 1 bar level, are 71,492 km and 66,854 km respectively (Seidelmann et al., 2007). If we assume the sphere size of Jupiter is the mean radius, the spherical ray-tracing described previously would be accurate when the antenna boresight is close to nadir. However, if the antenna boresight was pointed near the limb of Jupiter, the model may return the erroneous result that the boresight missed the planet. Hoffman (2001) describes how to account for oblateness in the ray tracing procedure, and that technique is employed in this work.

CHAPTER 3

LABORATORY MEASUREMENTS AND RESULTS

Over the past decade, several extensive laboratory studies were conducted of the microwave opacity of ammonia and water vapor in preparation for interpretation of the precise measurements of Jovian microwave emission to be made with the Microwave Radiometer (MWR) instrument aboard the NASA Juno Mission (See, e.g., Hanley et al. (2009), Karpowicz and Steffes (2011a), Karpowicz and Steffes (2011b), and Devaraj et al. (2014)). These works included models for the opacity of these constituents valid over the pressure and temperature ranges measured in the laboratory experiments (temperatures up to 500 K and pressures up to 100 bars). However, measurements of the microwave emission made using the Juno MWR indicate that significant contributions to the emission at the 24-cm and 50-cm wavelengths Juno MWR are from layers of the atmosphere with temperatures at or exceeding 600 K (Bolton et al., 2017). While the ammonia opacity models described by Hanley et al. (2009) and Devaraj et al. (2014) give consistent results at temperatures up to 500 K (within 6 %), they diverge significantly at temperatures and pressures exceeding 550 K and 50 bars, respectively. Similarly, at temperatures above 500 K, the model for water vapor opacity developed by Karpowicz and Steffes (2011a) and Karpowicz and Steffes (2011b) exhibits non-physical attributes. To resolve these ambiguities, we have conducted laboratory measurements of the microwave opacity of ammonia at temperatures up to 600 K and that for water vapor at temperatures up to 600 K. These measurements have resulted in updated models for the opacities of ammonia and water vapor under conditions of the deep Jovian atmosphere. Additionally, since the microwave opacity of ammonia is influenced by pressure-broadening from methane (a significant constituent in jovian atmospheres), measurements of the effects of methane on the ammonia absorption spectrum previously conducted by Chinsomboon (2012) have been used to reflect the effects of methane on the

ammonia absorption spectrum in the new model.

3.1 Measurement Theory

Verifying the centimeter-wavelength absorption spectrum of microwave absorbing constituents is important for accurate retrievals of their abundances in the jovian atmosphere. Conducting measurements under simulated jovian conditions assures the accuracy and usefulness of any model derived from such measurements.

In this experimental program, measurements of the quality factor (Q) of a resonant mode of a resonator are used to determine the absorption of a gas or gas mixture at that resonant frequency (Hanley and Steffes, 2007). The relationship between quality factor and absorption is given by

$$\alpha = 8.686\frac{\pi}{\lambda}\left(\frac{1-\sqrt{t_{loaded}}}{Q^m_{loaded}} - \frac{1-\sqrt{t_{matched}}}{Q^m_{matched}}\right) dB/km \tag{3.1}$$

where α is the absorptivity of the gas (dB/km), λ is the wavelength of the resonance (in km), t is the transmissivity of the resonance, and Q is the quality factor of the resonance. The subscripts $loaded$ and $matched$ refer to the measurements made with the test gas and pure argon respectively. The full derivation of this equation is described below.

The quality factor (Q) of a resonant mode of a resonator is used to measure the absorption of a gas or gas mixture where the quality factor of a resonance is given by Mattaei and Jones (1980) as

$$Q = \frac{2\pi f_0 \text{ x Energy Stored}}{\text{Average Power Loss}} \tag{3.2}$$

where f_0 is the resonant frequency. The Q of a resonance can be measured directly from f_0 by dividing it by its half-power bandwidth (HPBW).

$$Q = \frac{f_0}{HPBW} \tag{3.3}$$

The Q of a lossy gas (ϵ'/ϵ'') and its opacity are related by

$$\alpha \approx \frac{\epsilon'' \pi}{\epsilon' \lambda} = \frac{1}{Q_{gas}} \frac{\pi}{\lambda} \tag{3.4}$$

where ϵ' and ϵ'' are the real and imaginary permittivity of the gas, λ is the wavelength in km, and α is the absoptivity of the gas in Nepers/km (1 Neper = 8.686 dB). Since Q can be affected by more than just the gas added, the Q of the gas-filled resonator is given by

$$\frac{1}{Q^m_{loaded}} = \frac{1}{Q_{gas}} + \frac{1}{Q_r} + \frac{1}{Q_{ext1}} + \frac{1}{Q_{ext2}} \tag{3.5}$$

where Q^m_{loaded} is the measured quality factor of a resonance in the presence of a test gas, Q_{gas} is the quality factor of the gas under test, Q_r is the quality factor of the resonator in the absense of coupling losses, and Q_{ext1} and Q_{ext2} are the effects on Q due to external coupling losses. Since the resonator used is symmetric, it is safe to assume $Q_{ext1} = Q_{ext2}$. Coupling losses can be derived from the transmissivity $t = 10^{-S/10}$, where S is the measured insertion loss of the resonator in decibels (dB) at the frequency of a particular resonance using the following relationship (Mattaei and Jones, 1980)

$$t = \left[2 \frac{Q^m}{Q_{ext}} \right]^2, \tag{3.6}$$

$$Q_{ext} = \frac{2Q^m}{\sqrt{t}} \tag{3.7}$$

Q_r is related to the measured Q at a vacuum by

$$\frac{1}{Q^m_{vac}} = \frac{1}{Q_r} + \frac{1}{Q_{ext1}} + \frac{1}{Q_{ext2}} \tag{3.8}$$

where Q^m_{vac} is the measured Q under vacuum conditions. Substituting equation 3.7 into

equations 3.5 and 3.8 gives

$$\frac{1}{Q_{gas}} = \frac{1-\sqrt{t_{loaded}}}{Q^m_{loaded}} - \frac{1-\sqrt{t_{vac}}}{Q^m_{vac}} \tag{3.9}$$

where t_{loaded} and t_{vac} are the transmissivity of the resonance taken under loaded and vacuum conditions respectively. When gas is added to the resonator, there is a shift in the center frequency corresponding to the refractive index of the test gas. Since the quality factor is reliant on the center frequency, this will affect the comparison between the two measurements, even if the gas being tested is lossless. This effect is called dielectric loading (DeBoer and Steffes, 1994) and can be corrected by performing additional measurements of the quality factor with a lossless gas present. Adding the lossless gas shifts the center frequency of the resonances and, by adding more or less gas, the center frequency can be adjusted to be exactly the same as that with the lossy gas present. These measurements are used in place of the vacuum measurements in equation 3.9 and, by converting Nepers/km to dB/km equation 3.4 becomes

$$\alpha = 8.686\frac{\pi}{\lambda}\left(\frac{1-\sqrt{t_{loaded}}}{Q^m_{loaded}} - \frac{1-\sqrt{t_{matched}}}{Q^m_{matched}}\right) dB/km \tag{3.10}$$

Described below is the laboratory equipment and measurement procedure used in the measurements of gaseous NH_3, H_2O, and CH_4 under simulated deep jovian atmospheric conditions.

3.2 High-Temperature and High-Pressure Centimeter-Wavelength Measurement System

A high-pressure measurement system was used to conduct measurements of the 5–20 cm-wavelength absorptivity of ammonia and water vapor under deep jovian conditions at temperatures up to 600 K. The high-pressure measurement system consists of a planetary atmospheric simulator, centimeter-wavelength subsystem, and a data handling system.

3.2.1 The Planetary Atmospheric Simulator

The planetary atmospheric simulator was based on one used by Karpowicz and Steffes (2011a) and Karpowicz and Steffes (2011b). The simulator consists of a high-pressure vessel, temperature chamber, temperature and pressure gauges, vacuum pump, various gas bottles, and gas handling valves and pipes. The main component of the planetary atmospheric simulator is a high-pressure vessel that operates at pressures up to 100 bars and temperatures up to 525 K. The pressure vessel's maximum pressure can be de-rated to 80 bars at 600 K. This is placed in a Grieve industrial oven (model AB-650 rated up to 615 K). The oven acts as a stable temperature chamber and maintains the temperature within ± 0.5°C. The oven is placed on an outdoor concrete pad and enclosed by a metallic shed for protection.

Ultra-high-purity UHP300 grade Airgas bottles (pre-mixed hydrogen/helium, ammonia, methane and argon) required for the measurements are placed on a gas cylinder rack adjacent to the shed. Pressure regulators control the gas delivery to the system through Manifold Swagelok fittings and seamless stainless steel tubing. An exhaust valve is used to vent the gases to ambient pressure, and a Welch DuoSeal vacuum pump model 1376B-01 is used to evacuate the pressure vessel from ambient pressure down to vacuum (better than 0.1 mbar).

A GE Druck DPI 10430A Digital Test Gauge is used for pressure sensing in the 0 to 2 bar range, and a GE Druck DPI 1043000A Digital Test Gauge is used for pressure sensing in the 2 to 200 bar range. An Omega resistance temperature detector RTD (PR-11-2-100-1/4-9-E) is used for sensing gas temperature in the pressure vessel. A block diagram of the various components of the simulator is shown in Figure 3.1.

3.2.2 Centimeter-Wavelength Subsystem

A type 304 stainless steel cylindrical cavity resonator with gold-plated interior is placed inside the ultra-high pressure vessel. The interior of the cavity resonator measures approx-

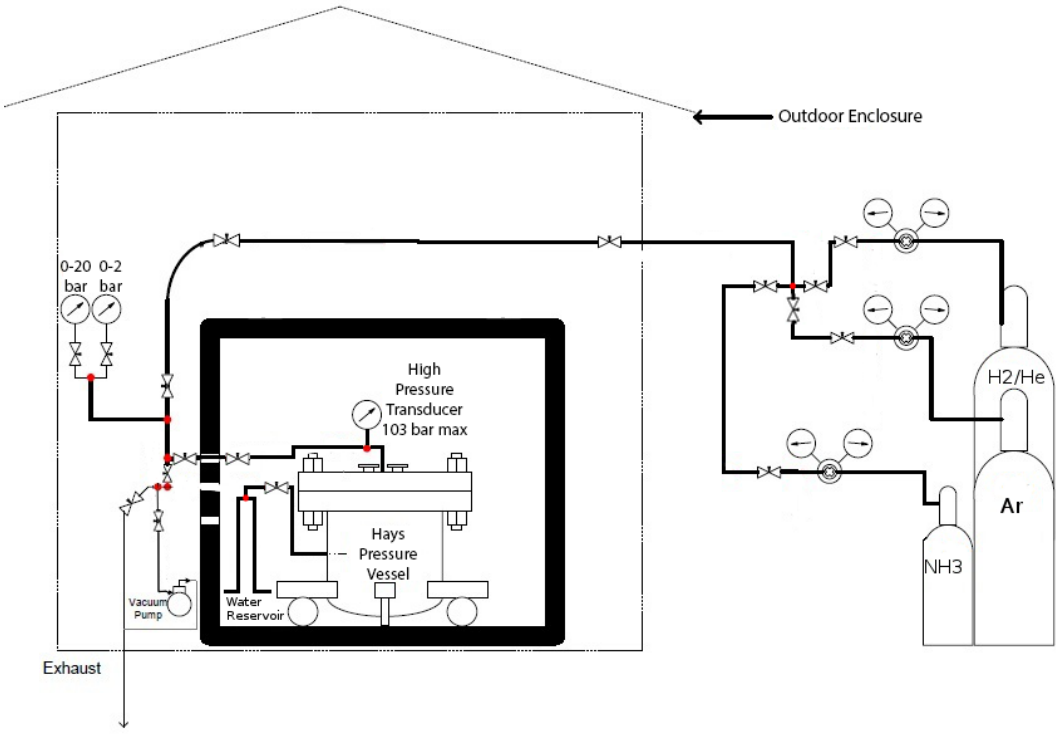

Figure 3.1: The Georgia Tech high-pressure system used for studying the centimeter-wavelength properties of ammonia under simulated jovian conditions.

imately 13.1 cm in diameter and 25.5 cm in height. One dozen high-Q, low-asymmetry resonances in the 5–20 cm wavelength range were selected and used as "standard resonances" for all the measurements. A detailed description of the selection criteria for the resonances is provided by Hanley et al. (2009).

As shown in Figure 3.2, Ceramtec microwave feedthroughs, model 16545-01-CF, are used for coupling microwave energy through the top-plate of the pressure vessel to the resonator via Times Microwave high-temperature (SiO_2) cables. The cables are rated up to 875 K and the feedthroughs are rated to 103 bars and 625 K. Exterior to the pressure vessel, two 1 m long sections of the same cable are connected to two sections of 25 m length Andrews CNT 600 microwave cable outside the oven. These are connected to an Agilent E5071C vector network analyzer that is placed inside the laboratory environment to ensure temperature stability. The network analyzer S-parameter measurements are recorded by the data acquisition system via General Purpose Interface Bus (GPIB).

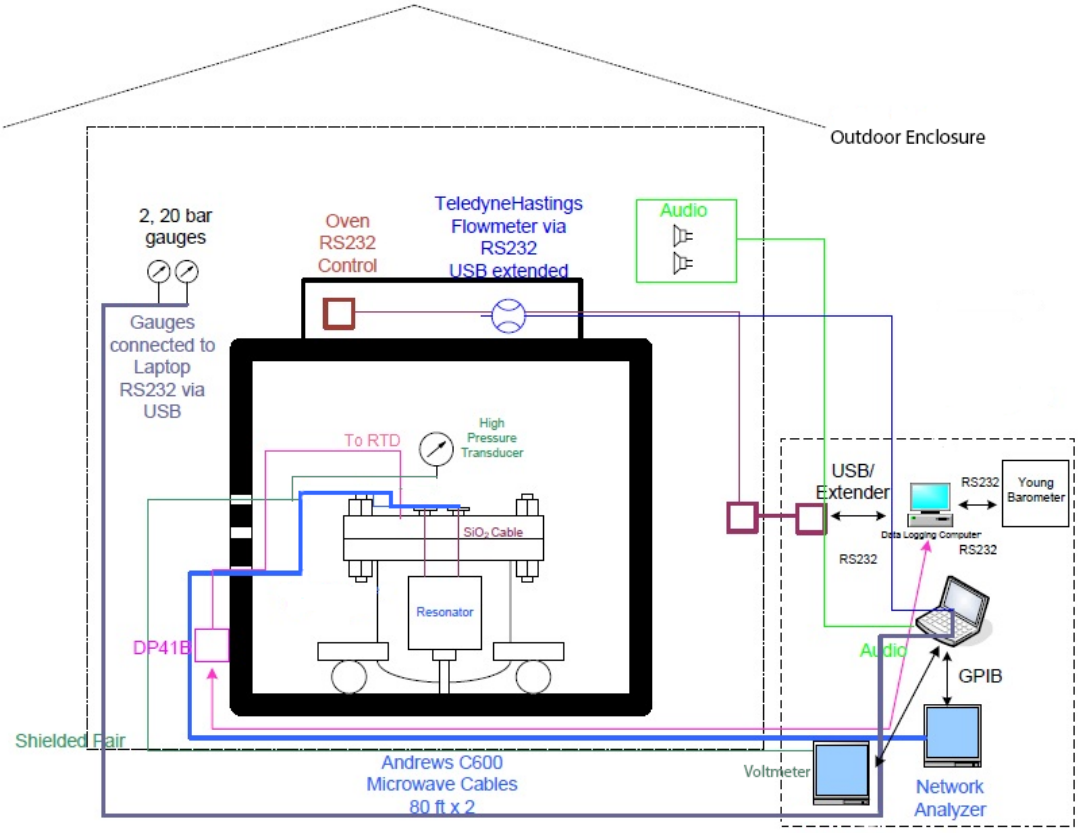

Figure 3.2: The centimeter-wavelength subsystem and the data-acquisition components of the high-pressure system.

3.2.3 Data Acquisition Subsystem

The data acquisition subsystem consists of a laptop computer connected to the network analyzer and a digital multimeter via GPIB. The extended USB buses allow the computer to remain inside the laboratory. The network analyzer is controlled via MATLAB® software. The software used is similar to that used by Hanley and Steffes (2007) and a detailed description of the data acquisition system is provided by Karpowicz and Steffes (2011a). A block diagram of the various components of the simulator is shown in Figure 3.2.

3.3 Measurement Procedure

The most important prerequisite for performing measurement of gas properties is ensuring a leak-proof system. Pressure integrity was verified using two methods: the first, by drawing a vacuum inside the pressure vessel and verifying the integrity of the vacuum over time. The second method is adding a positive pressure of Argon to the system and ensuring there are no leaks in any of the connectors and valves. Ensuring a leak-proof system allows for not only precise measurements but also that no toxic gases are released into the testing environment.

After the system is established to be leak-proof and at a stable temperature, a vacuum is drawn and measurement is taken. This allows for a baseline measurement of the cavity resonator's resonances and their quality factors. Once this baseline is established, the gas under test is added to the system.

Once the gas temperature has stabilized, another set of tests measuring the resonant frequencies and quality factors is taken. More gas is added and the procedure is repeated until measurements at all suitable pressures are taken. A vacuum is then drawn for an extended period (12 hours) to minimize the possibility of adsorption (or "sticking") of the gas (NH_3) to metal surfaces inside the vessel. This second vacuum measurement is taken to measure any possible system drift.

Once the second vacuum measurement is taken, a microwave transparent gas (Argon) is then added to the vessel until the center frequencies of the resonances are matched to the same frequency as with the test gas. Again, measurements are taken and this is repeated for every pressure of the test gas. Once completed, a vacuum is drawn and another test is taken.

Lastly, it is important to account for loss in the long microwave cables and the connectors between the network analyzer and the resonator. Three sets of straight-through measurements of signal levels are made (without the resonator present) under the same temperature conditions at each frequency point of the test gases. This calculated loss is used to correct the measurements of the transmissivities (equation 3.7) of the test gases and the dielectric matching gas.

The measurements include disconnecting the Andrews CNT 600 microwave cables from the Times Microwave high-temperature cables and connecting them via a SMA jumper cable. The loss of the SMA jumper cable, Times Microwave high-temperature cable, and Ceramtec microwave feedthroughs are well characterized and used to adjust the signal level measured. The connections are disconnected and reconnected between each set of transmissivity measurements in order to better statistically characterize the reproducibility of the electrical connections (Devaraj et al., 2011).

3.4 Data Processing

Data processing is performed after each measurement cycle using software written in MATLAB®. The software used is similar to that described in Hanley and Steffes (2007) and Karpowicz and Steffes (2011a), but with some modifications to account for the new configuration of the system. The software reads, processes, and calculates the absorptivity of the test gas. The cable losses at each measurement point are calculated by taking the mean of 30 sweeps of the signal level, then averaging the three sets of the measurement. The test gas insertion loss and dielectrically matched insertion loss are obtained by subtracting the cable loss

from the peak power measurements of both the test gas and the dielectrically matched gas.

3.4.1 Measurement Uncertainties

There are five types of errors that create uncertainty for absorptivity measurements using this system (Hanley and Steffes, 2007): instrumentation errors and electrical noise (Err_{inst}), errors in dielectric matching (Err_{diel}), errors in transmissivity measurement (Err_{trans}), errors due to resonance asymmetry (Err_{asym}), and errors in measurement conditions (Err_{cond}) resulting from uncertainties in temperature, pressure, and mixing ratio. The term Err represents 2σ uncertainties.

Instrumental errors and electrical noise result from to the limited sensitivity of the electrical devices and their ability to accurately measure bandwidth ($BW_{measured}$) and the center frequency (f_o). Electrical noise arises from the limited-stability frequency references and noise from internal electronics. Electrical noise is uncorrelated, so best estimate of instrumental uncertainty is the statistical variance of multiple measurements. The contribution of electrical noise is outlined in Hanley et al. (2009),

$$Err_n = B \times \frac{S_n}{\sqrt{n_{samples}}} \tag{3.11}$$

where S_n is the sample standard deviation, B is the confidence coefficient and $n_{samples}$ is the number of independent measurements. For the centimeter-wavelength system, 30 sets of independent measurements of each resonance are taken (this includes measurements of the resonance center frequency, bandwidth, and transmissivity). A confidence coefficient (B) of 2.045 is used (for each 30-sample data point). This corresponds to the 95% confidence interval (approximately 2σ) (Student, 1908). The center frequency standard deviation is very small and its effect on the uncertainty in Q is negligible. Therefore, S_n is the standard deviation of the bandwidth of the measurements.

The instrumentation errors considered in Err_{inst} are limited to instrumentation errors

associated with the microwave test equipment and electrical noise. Two parameters of interest in calculating Err_{inst} are the error in measuring the center frequency of a resonance (Err_0) and the error in measuring the bandwidth of a resonator (Err_{BW}). The instrument used in this experiment is the same Agilent E5071C-ENA Vector Network Analyzer used in Hanley et al. (2009).

The 3σ stability of the center frequency measurement or bandwidth measurement is 0.05 ppm plus 0.5 ppm/year within the temperature range of 18°C to 28°C, and after a 90-minute warm-up period. Since the relative uncertainty in frequency is of greater concern than the absolute uncertainty, Err_0 is calculated as

$$Err_0 = f_{measured} \times \left(5 \times 10^{-8} + 5 \times 10^{-7} \times years\_since\_calibrated\right)(Hz) \quad (3.12)$$

with the measured frequency given in Hz. The error for uncertainty in measured bandwidth for the network analyzer is calculated as

$$Err_{BW} = BW_{measured} \times \sqrt{2} \times \left(5 \times 10^{-8} + 5 \times 10^{-7} \times years\_since\_calibrated\right)(Hz) \quad (3.13)$$

with the measured bandwidth given in Hz.

The worst-case scenario is used to transform the uncertainty in center frequency and bandwidth for both loaded and dielectrically matched measurements into an uncertainty in absorptivity as described in DeBoer and Steffes (1994).

$$Err_{\Psi}^2 = \langle F_l^2 \rangle + \langle F_m^2 \rangle - \langle F_l F_m \rangle \quad (3.14)$$

where

$$\langle F_i^2 \rangle = \frac{\Upsilon_i^2}{f_{oi}^2} \left[\frac{Err_o^2}{Q_l^2} + Err_{BW}^2 + Err_{n,i}^2 + \frac{2 Err_o Err_{BW}}{Q_i} \right], i = l, m \quad (3.15)$$

$$\langle F_l F_m \rangle = -\frac{\Upsilon_l \Upsilon_m}{f_{ol} f_{om}} \left[\frac{Err_o^2}{Q_i Q_m} + Err_{BW}^2 + \frac{Err_o Err_{BW}}{Q_l} + \frac{Err_o Err_{BW}}{Q_m} \right] \tag{3.16}$$

$$Q_i = \frac{f_{oi}}{f_{BWi}}, i = l, m \tag{3.17}$$

$$\Upsilon_i = 1 - \sqrt{t}, i = l, m \tag{3.18}$$

where l, m denote loaded and dielectrically matched cases respectively and $f_{ol,om}$ and $f_{BWl,BWm}$ represent center frequency and bandwidth of loaded and dielectrically matched cases respectively. The 2σ uncertainty of the measured gas absorption due to instrumental errors and electrical noise is given by

$$Err_{inst} = \pm \frac{8.686\pi}{\lambda} Err_\Psi \ (dB/km) \tag{3.19}$$

where λ is the wavelength in km.

Errors in dielectric matching occur when the center frequency of the matched measurement are not precisely aligned with the center frequency of the loaded measurement. Since the Q of the resonator can vary with center frequency, this creates an uncertainty in the Q of the matched measurement at the nominal center frequency of the loaded measurement. The method used to calculate the magnitude of this effect is similar to Hanley and Steffes (2007). While this error is small due to the high precision of the software-controlled matching, it is important to include. The magnitude of this effect is calculated by comparing the Q of the three vacuum measurements to that of the dielectric matched measurements:

$$\left(\frac{dQ}{df} \right)_i = \left| \frac{Q_{vac,i} - Q_{matched,i}}{f_{vac,i} - f_{matched,i}} \right| \text{ for } i = 1, 2, 3 \tag{3.20}$$

The maximum of the three values is used to calculate a dQ value

$$dQ = \left(\frac{dQ}{df} \right)_{max} \times |f_{loaded} - f_{matched}| \tag{3.21}$$

where f_{loaded} and $f_{matched}$ are the center frequencies of the resonances under loaded and matched conditions, respectively. The error in absorptivity due to imperfect dielectric matching is then computed by comparing the computed absortivity (equation 3.10) by adding dQ to the matched measurement with that calculated with dQ subtracted from the matched measurement.

$$Err_{diel} = \frac{8.686\pi}{\lambda} \times \left| \left(\frac{1-\sqrt{t_{loaded}}}{Q^m_{loaded}} - \frac{1-\sqrt{t_{matched}}}{Q^m_{matched}+dQ} \right) - \left(\frac{1-\sqrt{t_{loaded}}}{Q^m_{loaded}} - \frac{1-\sqrt{t_{matched}}}{Q^m_{matched}-dQ} \right) \right| \ (dB/km) \tag{3.22}$$

Transmissivity errors result from the uncertainties in the measurement amplitude. This is caused by variations in gains or losses of the centimeter-wavelength instruments, cables, adapters, and feedthroughs used in this system. This is done by taking multiple test measurements of signal loss through the system without the resonator, finding the standard deviation (S_N) of the signal loss, and weighing it by its confidence coefficient

$$Err_{msl} = \frac{4.303}{\sqrt{3}} S_N \tag{3.23}$$

The total uncertainty in insertion loss for the centimeter-wavelength system is calculated by

$$Err_{ins\ loss} = \sqrt{Err^2_{msl} + 0.50^2 + 0.25^2}\ (dB) \tag{3.24}$$

where the factor of 0.25 dB is added to account for uncertainty in the modeled loss of the cables and feedthroughs. The additional 0.5 dB uncertainty is added to account for the uncertainty related to variations in the cable losses due to temperature variations in the outdoor cables.

The error in insertion loss is used to compute the transmissivity error

$$Err_{t,i} = \frac{1}{2}(10^{-S_i + Err_{ins\ loss}} - 10^{-S_i - Err_{ins\ loss}}), i = l, m \tag{3.25}$$

where l, m are the loaded and matched cases, respectively, and S is the insertion loss of the resonator. This is used to compute the 2σ uncertainties in opacity, expressed as

$$Err_{trans} = \frac{8.686\pi}{2\lambda} \times \left| \left(\frac{\sqrt{t_l + Err_{t,l}} - \sqrt{t_l - Err_{t,l}}}{Q^m_{loaded}} - \frac{\sqrt{t_m - Err_{t,m}} - \sqrt{t_m + Err_{t,m}}}{Q^m_{matched}} \right) \right| (dB/km) \tag{3.26}$$

Errors from asymmetry result from the asymmetric nature of the resonances. These are more prominent at low temperatures and short wavelengths. Errors due to the asymmetry result from the disproportionate asymmetric broadening of the loaded measurements compared to the matched measurements. Equivalent full bandwidths based on assuming symmetry of the high and low sides of the resonances are calculated as

$$BW_{high} = 2 \times (f_{high} - f_{center}) \tag{3.27}$$

$$BW_{low} = 2 \times (f_{center} - f_{low}) \tag{3.28}$$

where BW_{high}, BW_{low}, are the high and low bandwidth, respectively, f_{high}, f_{center}, and f_{low} are the higher frequency half power point, center frequency, and lower frequency half power point, respectively. For a perfectly symmetric resonance, $BW_{high} = BW_{low}$. The difference between the opacities calculated using BW_{high} and BW_{low} is defined as Err_{asym}

and is calculated by

$$Err_{asym} = \frac{8.686\pi}{\lambda} \times \left| \left(\frac{1-\sqrt{t_{loaded}}}{Q^m_{loaded,high}} - \frac{1-\sqrt{t_{matched}}}{Q^m_{matched,high}} \right) - \left(\frac{1-\sqrt{t_{loaded}}}{Q^m_{loaded,low}} - \frac{1-\sqrt{t_{matched}}}{Q^m_{matched,low}} \right) \right| (dB/km) \tag{3.29}$$

where $Q^m_{matched,high/low}$ and $Q^m_{loaded,high/low}$ are the measured Q's evaluated using the high and low bandwidths for loaded and matched cases. Thus, the resulting 95% confidence for the total measurement uncertainty is expressed in dB/km as per Hanley and Steffes (2007)

$$Err_{tot} = \sqrt{Err_n^2 + Err_{diel}^2 + Err_{trans}^2 + Err_{asym}^2}\ (dB/km) \tag{3.30}$$

The uncertainties in measured temperature, pressure, and concentration in the centimeter-wavelength system contribute to the total uncertainty due to the measurement conditions (Err_{cond}). While uncertainties in measurement conditions do not directly affect the measurements of centimeter-wavelength absorptivity, they still need to be accounted for when evaluating the opacity formalisms. It is computed by

$$Err_{cond} = \sqrt{Err_{temp}^2 + Err_p^2 + Err_c^2}\ (dB/km) \tag{3.31}$$

with Err_{temp}, Err_p, and Err_c representing the 2σ uncertainties of the measured opacity resulting from variations in temperature, pressure, and concentration (or mole fraction) respectively. Each of these are calculated by taking the maximum modeled opacity with each uncertainty, subtracting the minimum modeled opacity, and halving the difference. Since Err_{cond} is dependent on the opacity model, this uncertainty is maintained separately from Err_{tot}.

3.5 Ammonia

Previous measurement campaigns involved laboratory measurements of the opacity of ammonia under simulated deep jovian conditions at pressures up to 100 bars and temperatures up to 500 K (Devaraj et al., 2014). This work extends the temperature range to nearly 600 K. Since the pressure seals of the system had limited performance at such high temperatures, only measurements of the absorptivity of pure ammonia (0.5 bar pressure) were completed. The UHP (Ultra-High Purity) grade ammonia used in the measurements of absorptivity and the UHP grade argon used for the dielectric matching process were provided by Airgas, Inc.

The process of measuring ammonia's absorption began by adding 500 mbar of ammonia to an evacuated pressure chamber heated to 595 K. The gas was allowed to heat up, and measurements of its absorptivity and refractivity were taken. The chamber was then evacuated and the dielectric matching process with argon gas was conducted.

3.5.1 Revisions to Existing Models

The primary goal of the work described in this chapter has been to develop an ammonia model that adheres to strict physical principals. While previous models (Devaraj et al., 2014; Hanley et al., 2009) of ammonia's centimeter- and millimeter-wave absorption fit the available laboratory measurements, anomalous behavior of these models when extrapolated to higher temperatures shows that it is necessary to examine them from a physical viewpoint.

The model created by Hanley et al. (2009) has three distinct weaknesses: (i) No high pressure and/or high temperature data was used in the model development, (ii) Only one H_2/He mixing ratio was used, and (iii) the model employ a now-outdated line catalog. When the Hanley model was developed, the only data used to fit the model was measured at or less than 12 bars, and at temperatures at or less than 450K. While the H_2/He mixing ratio

(86.3%/13.7%) used was characteristic of Jupiter, it does not apply to all outer planets. By not varying the H_2/He, mixing ratio, the model was required to assume Helium parameters from Berge and Gulkis (1976), which were not directly measured. The line catalog used by Hanley et al. (2009) only has 190 lines while the current one has 5914 lines (Yu et al., 2010a; Yu et al., 2010b; Yu et al., 2010c).

Similarly, the Devaraj et al. (2014) model has a number of physical weaknesses: (i) the temperature dependence of the coupling parameters (Z_i) were unnecessarily limited during model creation, (ii) the rotational line parameters are unnecessarily coupled to the inversion line parameters, (iii) in the high pressure model, the shift parameter (δ_j) of the inversion lines is positive, and (iv) a significant discontinuity occurs in the model at the pressure where the parameters are "switched". Limiting the temperature dependence of the coupling parameter (i) directly limits the search space of the fitting function for the model parameters. While the temperature dependence of the coupling parameter can be as large as is needed, it must be positive. The positive shift parameter (iii) is nonphysical because inversion lines must be shifted lower in frequency with increasing pressure (Townes and Schawlow, 1975).

When fitting the coefficients for the new model, special steps have been taken to address these issues. The new model uses all the data available (Hanley et al., 2009; Devaraj et al., 2014, and the high temperature data presented in this work). This addresses the limited pressure, temperature, and mixing ratio issues present in the development of the Hanley et al. (2009) model. When fitting the model, the temperature dependence of the coupling parameters are forced to be positive (Rosenkranz, personal communication, August 2015) and the rotational line parameters are not coupled to those from the inversion lines. The pressure switch present in the Devaraj et al. (2014) model (iv) has been converted to a frequency switch with a much smaller discontinuity.

The data fitting process employed is similar to the one used by Hanley et al. (2009). Ammonia opacity measurements in the 75–150 GHz range at pressures up to 3 bars and

temperatures up to 300 K made by Devaraj et al. (2011), the high-pressure measurements in the 1.5-6 GHz range at pressure up to 100 bars and temperatures up to 500 K made by Devaraj et al. (2014), the 1.5–27 GHz measurements a pressures up to 12 bars and temperatures from 184 K to 450 K made by Hanley et al. (2009), and the high-temperature measurements in the 1.5–6 GHz range made as part of this work were utilized for the data fitting process. Similar to Hanley et al. (2009) and Devaraj et al. (2014), a data set consisting of 250 data points in the 22–40 GHz range using a Fabry-Perot resonator (FPR) at room temperature and pressures up to 3 bars was used as an independent test set to verify the validity of the model. The Limited-memory BFGS (Broyden–Fletcher–Goldfarb–Shanno) with simple box constraints (L-BFGS-B) optimization technique (Byrd et al., 1995) is used in this work, and has a minimization function

$$\chi = \frac{DW \times (\alpha_{measured} - \alpha_{model})^2}{Err^2_{measured}} \tag{3.32}$$

where DW is the data weight assigned to the data point, $\alpha_{measured}$ is the measured opacity, α_{model} is the modeled opacity, and $Err_{measured}$ is the 2σ uncertainty in opacity conservatively calculated as

$$Err_{measured} = Err_{tot} + Err_{cond} \tag{3.33}$$

where Err_{tot} is the total 2σ measurement uncertainty and Err_{cond} is the 2σ uncertainty due to measurement conditions. Multiple iterations of the minimization function with random initial inputs were run to ensure a global minimum was reached. The data weight is given as (Hanley et al., 2009)

$$DW = \frac{1}{n_f} + \frac{1}{n_T} + \frac{1}{n_P} + \frac{1}{n_C} \tag{3.34}$$

where n_f, n_T, n_P, and n_C represent the number of measurements conducted at each frequency, temperature, pressure, and gas concentration range. The data points are divided into roughly equally spaced fTPC bins and scaled to prevent the model from being skewed toward the most frequently measured conditions.

The data was then split into two groups: Group I, data where frequency is less than 24 GHz, and Group II, data where frequency is greater than 24 GHz. The inversion lines are fit to a Ben-Reuven lineshape using data only from Group I. Exactly, 2618 data points are used to fit the 14 free inversion parameters. The data in Group II was best fit with the low pressure model already presented in Devaraj et al. (2014).

3.5.2 New ammonia absorption formalism

The NH_3 inversion, rotational, and roto-vibrational lines were obtained from the JPL Spectral line catalog (Pickett et al., 1998). A modified Ben-Reuven lineshape (Ben-Reuven, 1966) was used for the inversion transitions and a modified Gross lineshape (Gross, 1955) was used for the rotational and robo-vibrational transitions. Line transitions where no broadening parameters were available were made free parameters and were derived for this work.

The cumulative ammonia opacity from the inversion, rotational, and roto-vibrational transitions is calculated by

$$\alpha = (\alpha_{inv} + \alpha_{rot} + \alpha_{\nu_2}) \times 434294.5 \text{ (dB/km)} \tag{3.35}$$

where α_{inv}, α_{rot}, and α_{ν_2} are the opacities from the inversion, rotational, and roto-vibrational lines in cm^{-1}. The factor 434294.5 converts the total opacity from cm^{-1} to dB/km.

A detailed description of the opacity calculations for the rotational and roto-vibrational lines is given by Devaraj et al. (2011). Since the roto-vibrational and rotational transitions of ammonia occur in the millimeter-wavelength range, and the jovian atmospheric layers that contribute to emissions at these frequencies have pressures less than a few bars (Joiner and Steffes, 1991), using this model (low pressure Devaraj et al. (2014)) as a high frequency model follows physical principals. A new set of inversion model parameters have been found to better fit the data at centimeter-wavelengths. The opacity from the ensemble of

inversion lines is given by

$$\begin{aligned}\alpha_{inv} &= \frac{0.1 D_{inv} P_{NH_3}}{k_b T}\left(\frac{2}{\pi}\right)\left(\frac{T_0}{T}\right)^{\eta+1} \\ &\quad \times \sum_j \left(I_j\left(T_0\right) \exp\left(\left(\frac{1}{T_0}-\frac{1}{T}\right) E_{(I,j)}\left(\frac{hc}{k_B}\right)\right)\left(\frac{\nu}{\nu_{(0,j)}}\right)^2 \right. \\ &\quad \left. \left[\frac{(\gamma_j-\zeta_j)\nu^2 + (\gamma_j+\zeta_j)\left[(\nu_{(0,j)}+\delta_j)^2+\gamma_j^2-\zeta_j^2\right]}{\left[\nu^2-(\nu_{(0,j)}+\delta_j)^2-\gamma_j^2+\zeta_j^2\right]^2+4\nu^2\gamma_j^2}\right]\right) \end{aligned} \tag{3.36}$$

Where for inversion line j, $\nu_{(0,j)}$, γ_j, ζ_j, and δ_j are the center frequency, linewidth, coupling parameter, and shift parameter, respectively, in cm^{-1}, and D_{inv} is a unitless scale factor. The frequency, linewidth, coupling, and shift parameters are converted from GHz to cm^{-1} before they are used. The linewidth and coupling parameters are calculated by summing the contributions from ammonia, hydrogen, and helium. The linewidth and coupling parameters are given by

$$\begin{aligned}\gamma_j &= \gamma_{H_2} P_{H_2}\left(\frac{300}{T}\right)^{\Gamma_{H_2}} + \gamma_{He} P_{He}\left(\frac{300}{T}\right)^{\Gamma_{He}} \\ &\quad + \gamma_{NH_3}\gamma_{(0,j)} P_{NH_3}\left(\frac{295}{T}\right)^{\Gamma_{NH_3}} \text{ (GHz)} \end{aligned} \tag{3.37}$$

$$\begin{aligned}\zeta_j &= \zeta_{H_2} P_{H_2}\left(\frac{300}{T}\right)^{Z_{H_2}} + \zeta_{He} P_{He}\left(\frac{300}{T}\right)^{Z_{He}} \\ &\quad + \zeta_{NH_3}\gamma_{(0,j)} P_{NH_3}\left(\frac{295}{T}\right)^{Z_{NH_3}} \text{ (GHz)} \end{aligned} \tag{3.38}$$

where for inversion line j and constituent $i = \mathrm{H_2}$, He, $\mathrm{NH_3}$, γ_i and ζ_i are constant scale terms (in GHz/bar), and Γ_i and Z_i represents the constant temperature dependences of the broadening of each of the gases, P_i are the ideal partial pressures in bar, and $\gamma_{(0,j)}$ are the self-broadening linewidths of the inversion transitions of ammonia in MHz/Torr. The conversion to GHz/bar is incorporated in the scale terms γ_{NH_3} and ζ_{NH3}. The values for

$\gamma_{(0,j)}$ are from the calculations of Poynter and Kakar (1975) assuming a T_0 of 295 K. For the lines with a center frequency below 7.2 GHz and $J > 16$, where J represents the total angular momentum vector for the ammonia molecule, γ_0 is expressed as

$$\gamma_0(J,K) = 25.923\frac{K}{\sqrt{J(J+1)}} \text{ (MHz/Torr)} \tag{3.39}$$

where K is the projection of J onto the molecular axis. The pressure shift parameter is calculated by

$$\delta_j = d \times \gamma_i \tag{3.40}$$

where d is an empirically derived constant. All the inversion lines are assigned the same set of model constants (either low-frequency or high-frequency) even though each line behaves differently (Hanley et al., 2009). The equation for computing the opacity from the inversion transitions has 14 free parameters.

A new set of free-parameters for the centimeter-wavelength inversion transitions has been empirically derived by data fitting as shown in Table 3.1. Table 3.2 shows the millimeter-wavelength effects of the inversion transitions to be identical to the values calculated by Devaraj et al. (2011). The rotational and roto-vibrational transitions from Devaraj et al. (2011) are shown in Table 3.3 and 3.4 respectively.

Table 3.1: Values of the low-frequency inversion model constants used for computing the H_2/He-broadened NH_3 absorptivity when f $\leq$ 30 GHz.

	i=H_2	i=He	i=NH_3	Units
γ_i	1.6937	0.6997	0.7523	(GHz/bar)
Γ_i	0.8085	1.0	1.0	
ζ_i	1.3263	0.1607	0.6162	(GHz/bar)
Z_i	0.8199	0.0	1.3832	
d		-0.0139		
D_{inv}		0.9619		

Due to the asymmetry of the Ben-Reuven lineshape, it was decided that the frequency switch should be in the range between 25–70 GHz. Using the weighting functions for the

Table 3.2: Values of the high-frequency inversion model constants used for computing the H_2/He-broadened NH_3 absorptivity when f $>$ 30 GHz.

	i=H_2	i=He	i=NH_3	Units
γ_i	1.7465	0.9979	0.7298	(GHz/bar)
Γ_i	0.8202	1.0	1.0	
ζ_i	1.2163	0.0291	0.5152	(GHz/bar)
Z_i	0.8873	0.8994	2/3	
d		-0.0627		
D_{inv}		0.9862		

Table 3.3: Values of the model constants of the new model used for computing the H_2 /He-broadened NH_3 absorptivity from the rotational transitions (Devaraj et al., 2011).

	i=H_2	i=He	i=NH_3
c_i	1.7761	0.6175	3.1518
ξ_i	0.5	0.5663	1.0
D_{rot}		2.7252	

Table 3.4: Values of the model constants of the new model used for computing the H_2 /He-broadened NH_3 absorptivity from the roto-vibrational transitions (Devaraj et al., 2011).

	i=H_2	i=He	i=NH_3	Units
$\Delta\nu_i$	0.5982	0.6175	5.0894	(GHz/bar)
ξ_i	0.5	0.5505	0.9996	
D_{ν_2}		0.7286		

jovian planets at frequencies from 25–70 GHz, the appropriate search space for pressure, temperature, ammonia concentration, and helium concentration have been identified and are shown in Table 3.5. A Monte-Carlo method was used to explore this search space to minimize the difference between the two inversion models. Multiple simulations indicate that a frequency switch located at 30 GHz had the smallest average model discontinuity.

Table 3.5: Values of the parameter search space used in the Monte-Carlo switch minimization algorithm.

Pressure:	0–7 bars
Temperature:	100-250 K
Ammonia Concentration:	0–0.2%
Helium Concentration:	10–20%

3.5.3 Model Performance

Model performance is evaluated based on the fit to the data over the parameter space where the model is effective. (Note: The model uses the low-frequency inversion line parameters at f $\leq$ 30 GHz and a high-frequency inversion line parameters at f $>$ 30 GHz). The model was compared with the 11 data points of the 1.5–6 GHz high temperature data measured in this work, the 1431 data points of the 1.5–27 GHz opacity of ammonia, and the 250 data points of the 22–40 GHz opacity of ammonia measured by Hanley et al. (2009), 1013 data points of the 75–150 GHz opacity of ammonia measured by Devaraj et al. (2011), and the 1176 data points of the 1.5–6 GHz opacity of ammonia measured by Devaraj et al. (2014).

This new ammonia opacity model fits 100% of the high-temperature cavity resonator measurements, 96.09% of the 1.5–27 GHz cavity resonator measurements, 90.0% of the 22–40 GHz FPR measurements, 89.53% of the 75–150 GHz FPR measurements, and 67.34% of the 1.5–6 GHz high-pressure measurements. Comparison of the new model performance with models of Hanley et al. (2009) and Devaraj et al. (2014) is listed in Table 3.6. Figure 3.3 shows the high temperature data compared to various models.

Similar to the model developed by Devaraj et al. (2014), the model presented in this

Table 3.6: The percentage of the ammonia opacity measurement data points within 2σ uncertainty of the new model in comparison with the existing models.

Model	Cavity (1.–27 GHz)	FPR (22–40 GHz)	FPR (75–150 GHz)	High Pressure (1.5–6 GHz)	High Temperature (1.5–6 GHz)	Total
Hanley et al. (2009)	96.09	88.0	14.61	65.14	100.00	61.65
Devaraj et al. (2014)	93.92	91.86	89.53	70.92	36.36	76.59
This work	**96.09**	**90.0**	**89.53**	**67.34**	**100.00**	**82.80**

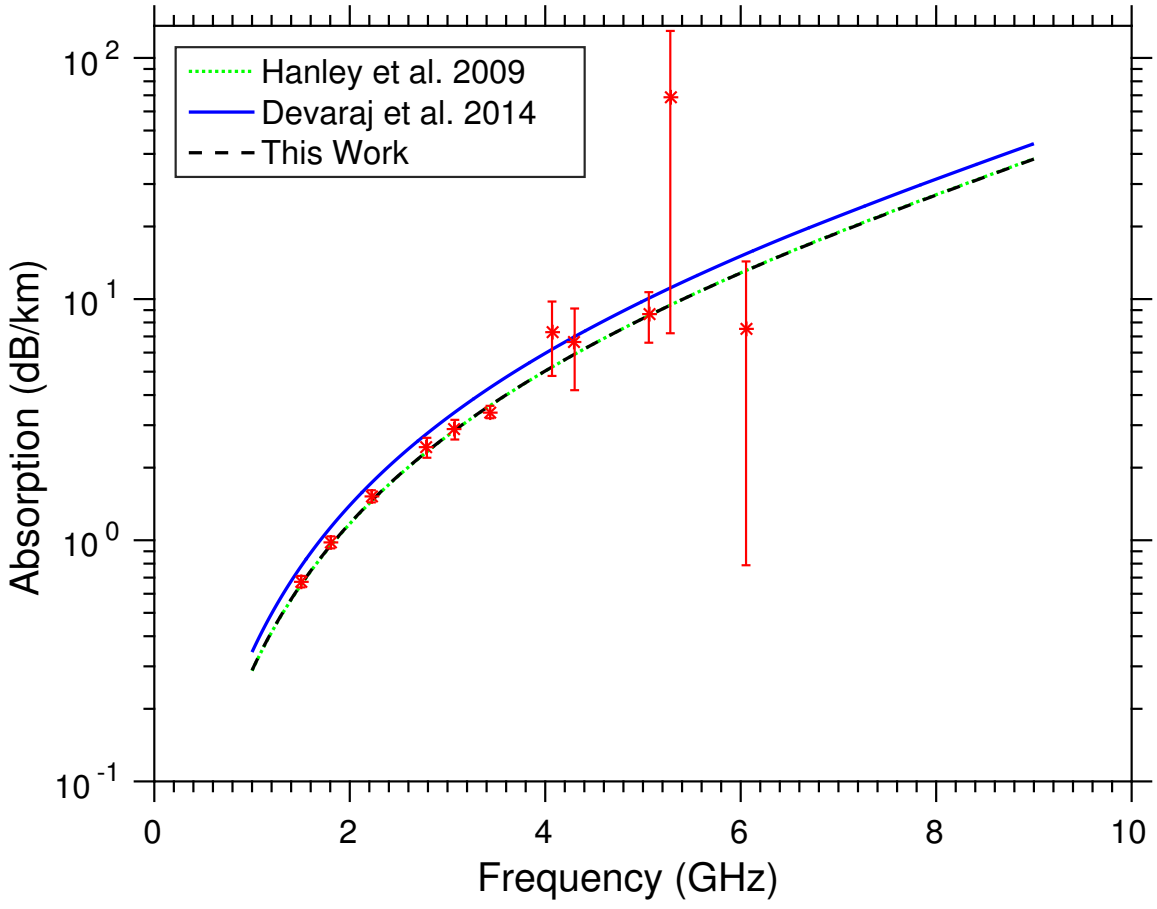

Figure 3.3: Opacity data measured using the high-temperature centimeter-wavelength system for pure NH_3 at a pressure of 0.5 bar and temperature of 595 K compared to various models. It is important to note that This work and the Hanley et al. (2009) models are overlapping.

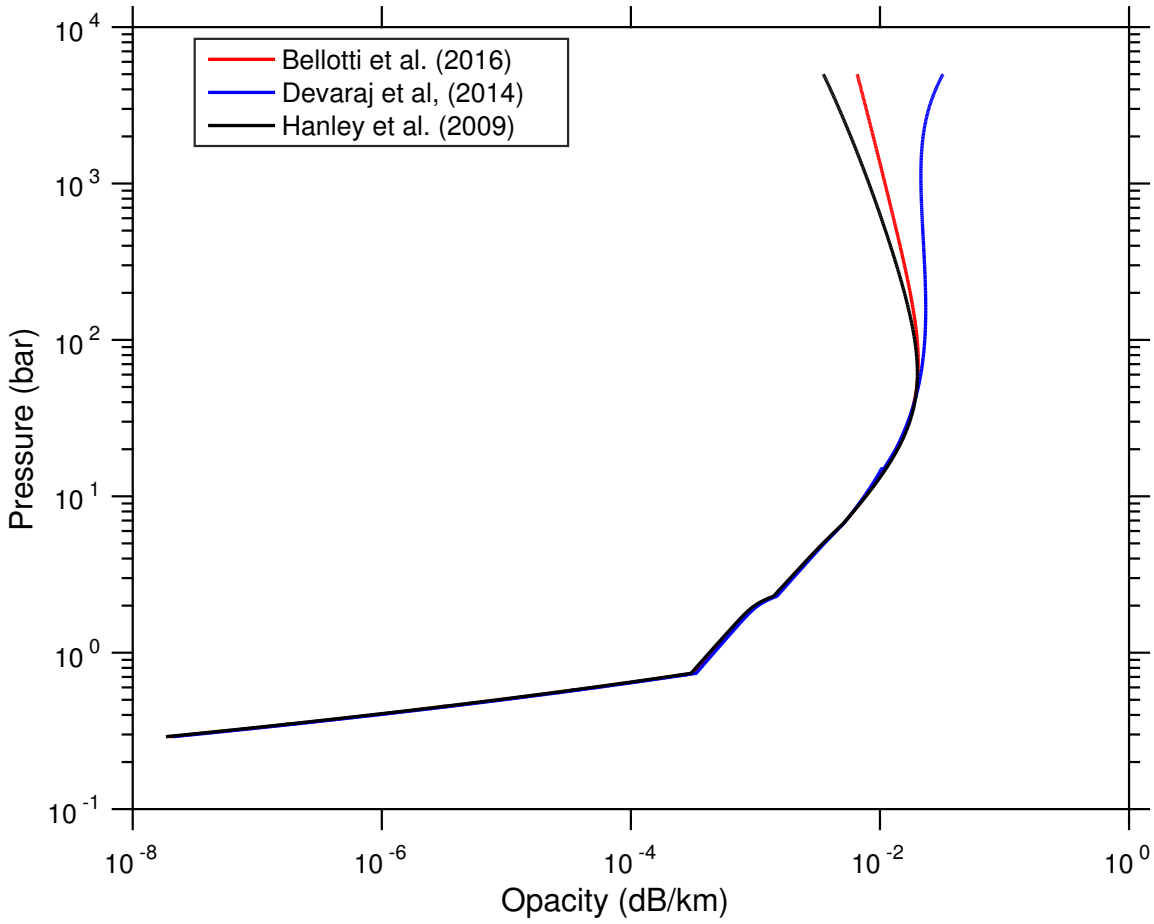

Figure 3.4: Comparison of different ammonia absorption models as a function of altitude represented by pressure. The atmosphere assumes a deep abundance of NH_3 and H_2O of 2.7 and 4.0x solar, respectively.

work diverges from the Hanley et al. (2009) model when extrapolated to extreme temperatures. However, the new model does not exhibit the singularity found in the Devaraj et al. (2014) model under deep Jovian conditions (See Figure 3.4). Other differences between this model and the Devaraj et al. (2014) model occur at 15 bars (the "switching" pressure of the Devaraj et al. (2014) model) and at high temperatures when there are no broadening gases present (as shown in Figure 3.3).

3.5.4 Water vapor's influence on ammonia's absorption spectrum

Devaraj et al. (2014) conducted the first laboratory measurement campaign to measure water vapor's broadening of the 5–20 cm-wavelength opacity of ammonia over a range of jovian conditions. While the model described previously in this section only accounts for broadening due to hydrogen and helium, a simple modification to this model can account for water vapor's broadening of ammonia's absorption spectrum.

Pure ammonia's opacity due to inversion transitions is modeled with a modified Ben-Reuven line shape described previously. The relationship for the opacity due to inversion lines is shown in equation 3.36. The linewidth and coupling parameters are modified by adding the contribution of water vapor to equations 3.37 and 3.38 as follows

$$\begin{aligned}\gamma_j &= \gamma_{H_2O} P_{H_2O} \left(\frac{300}{T}\right)^{\Gamma_{H_2O}} + \gamma_{H_2} P_{H_2} \left(\frac{300}{T}\right)^{\Gamma_{H_2}} + \gamma_{He} P_{He} \left(\frac{300}{T}\right)^{\Gamma_{He}} \\ &\quad + \gamma_{NH_3} \gamma_{(0,j)} P_{NH_3} \left(\frac{295}{T}\right)^{\Gamma_{NH_3}} \text{ (GHz)} \end{aligned} \tag{3.41}$$

$$\begin{aligned}\zeta_j &= \zeta_{H_2O} P_{H_2O} \left(\frac{300}{T}\right)^{Z_{H_2O}} + \zeta_{H_2} P_{H_2} \left(\frac{300}{T}\right)^{Z_{H_2}} + \zeta_{He} P_{He} \left(\frac{300}{T}\right)^{Z_{He}} \\ &\quad + \zeta_{NH_3} \gamma_{(0,j)} P_{NH_3} \left(\frac{295}{T}\right)^{Z_{NH_3}} \text{ (GHz)} \end{aligned} \tag{3.42}$$

where for the inversion line j and constituent i = H_2O, H_2, He, NH_3, γ_i and ζ_i are constant scale terms, and Γ_i and Z_i represent the constant temperature dependences of the

broadening of each of the gases, P_i are the ideal partial pressures in bar, and $\gamma_{(0,j)}$ are the self-broadening linewidths of the inversion transitions of ammonia in MHz/Torr.

Prior to fitting the measured data points to the model for ammonia opacity, the intrinsic opacity of the water vapor-hydrogen-helium mixture must be removed. Using the modified Karpowicz and Steffes (2011a) and Karpowicz and Steffes (2011b) model described in Section 3.6.2, the intrinsic opacity of water vapor present in each experiment was removed. Subsequently, data fitting and optimization were performed in a fashion similar to that explained previously. The ammonia, hydrogen, and helium free parameters for the linewidth and coupling parameters are described previously in this work. Water vapor's free parameters are displayed in Table 3.7. The new model fits 66.3% of the 838 data points within 2σ.

Table 3.7: Constants of H_2O-broadening of NH_3

	i=H_2O	Units
γ_i	5.3119	(GHz/bar)
Γ_i	0.6224	
ζ_i	5.2333	(GHz/bar)
Z_i	2.1248	

This is an improvement of 2.5% from the Devaraj et al. (2014) model.

3.6 Water Vapor

Similar to ammonia, previous measurement campaigns have measured the 5–20 cm opacity of water vapor under simulated deep jovian conditions. These measurements reached pressures up to 100 bars and temperatures up to 525 K (Karpowicz and Steffes, 2011a; Karpowicz and Steffes, 2011b). This work extends the temperature range using measurements of pure water vapor made in the 3.5–4.7 bar range.

3.6.1 Measurement Procedure

To measure the opacity of water vapor, reverse osmosis/deionized (RO/DI) liquid water was inserted into the evacuated, heated chamber through a high-pressure clear rubber hose.

To reach pressures above ambient, UHP grade argon was used to pump the liquid water through the hose and into the chamber. The clear hose served as a window to ensure that no argon was added to the chamber. To ensure that no water vapor condensed when the pressure was measured with the pressure sensor at ambient temperature, the pipes in the gas manifold were filled with 10 bars of argon to prevent water vapor from exiting the heated chamber. Since the volume of the pipes was quite small, this had a negligible effect on the accuracy of the pressure measurement. After the opacity and refractivity were measured, some water vapor was immediately released and another measurement was taken. The chamber was evacuated over a period of 15 hours to minimize adsorption, but it was noticed that the quality factor of all the resonances at a vacuum were drastically lower than previous vacuum measurements. This was caused by damage to the resonator probes as the system was evacuated under these extremely high temperature conditions. Due to the decrease in the vacuum quality factor, reliable dielectric matching could not be conducted. As a result, a differential measurement was conducted by comparing the quality factors with 4.734 bars of water vapor present versus that with 3.612 bar pressure.

Using equation 3.4 the differential opacity is calculated by

$$\alpha_{p_1} - \alpha_{p_2} = \frac{\pi}{\lambda}\left(\frac{1}{Q_{gas,p_1}} - \frac{1}{Q_{gas,p_2}}\right) \tag{3.43}$$

where p_1 and p_2 represent the two different pressures, α is the opacity (in dB/km), and Q_{gas} is the quality factor of the resonance. Substituting equation 3.9 into equation 3.43 gives

$$\alpha_{p_1} - \alpha_{p_2} = \frac{\pi}{\lambda}\left(\frac{1-\sqrt{t_{loaded,p_1}}}{Q_{loaded,p_1}} - \frac{1-\sqrt{t_{loaded,p_2}}}{Q_{loaded,p_2}}\right) \tag{3.44}$$

where p_1 and p_2 are the two different pressures, t_{loaded} is the measured transmissivity as per equation 3.6, and Q_{loaded} is the measured quality factor of a resonance in the presence of water vapor at the stated pressure.

While differential measurements have larger uncertainties due to lack of dielectric

matching, these measurements were useful to verify the validity of the revised model for water vapor opacity.

3.6.2 Revisions to Existing Model and Comparison with Laboratory Results

A new model for the intrinsic opacity of water vapor has been developed which is a modification of the model created by Karpowicz and Steffes (2011a) and Karpowicz and Steffes (2011b). This model has two distinct parts: the absorption due to individual resonant lines and the absorption due to water vapor's continuum. While the former is important, it is less significant in the frequency range where the Karpowicz and Steffes (2011a) and Karpowicz and Steffes (2011b) laboratory measurements were conducted. At long wavelengths, the absorptivity is dominated by the continuum absorption, defined as

$$\alpha_{continuum} = \alpha_{c,w} + \alpha_{c,f} \tag{3.45}$$

where $\alpha_{c,w}$ is the continuum term based solely on the water vapor density (self-continuum), and $\alpha_{c,f}$ is the continuum term dependent on the foreign gas influence on the water vapor. As per Rosenkranz (1998), the water vapor self-continuum term is defined as

$$\alpha_{c,w} = C_w P^2_{ideal,H_2O} \Theta^{x_{w,continuum}} f^2 \ \ (\text{km}^{-1}) \tag{3.46}$$

where C_w is an empirically derived constant, $x_{w,continuum}$ is the temperature exponent of the continuum, P_{ideal,H_2O} is the ideal pressure of water vapor, $\Theta_{continuum}$ is the standard $\frac{300}{T}$ where T is in degrees Kelvin, and f is the frequency in GHz. Also Rosenkranz (1998) and Karpowicz and Steffes (2011a) defines the foreign gas contribution as

$$\alpha_{c,f} = C_{H_2} P_{ideal,H_2} P_{ideal,H_2O} \Theta^3 f^2 + C_{He} P_{ideal,He} P_{ideal,H_2O} \Theta^3 f^2 \ \ (\text{km}^{-1}) \tag{3.47}$$

where C_{H_2} and C_{He} are empirically derived constants based upon measurements done by Karpowicz and Steffes (2011a).

The total absorption due to water vapor is written as

$$\alpha_{H_2O} = 4.342945 \times (\alpha_{lines} + \alpha_{continuum}) \text{ (dB/km)} \tag{3.48}$$

The factor 4.342945 is a conversion factor from km^{-1} to dB/km.

The necessary empirically-derived constants are summarized in Table 3.8. These differ slightly from the constants derived in Karpowicz and Steffes (2011a). The biggest change is the removal of a second term present in the Karpowicz and Steffes (2011a) water vapor self-continuum term.

The second term was added to provide additional opacity and subsequently, provide a better fit to data taken at 525K. However, subsequent re-calibration of the temperature data indicate that this term was not required (Karpowicz, private communication, 2012). Moreover, the additional term exhibited non-physical behavior at high temperatures.

The empirically derived constant for water vapor (C_w) and the temperature exponent of the water vapor self-continuum ($x_{continuum}$) have been reset to allow use of the physically-based self-continuum expression from Rosenkranz (1998). Of the 929 measurement points used to develop the Karpowicz and Steffes (2011a) and Karpowicz and Steffes (2011b) model, this model revision fits 670 points within 2σ error bars. This is very similar to the 738 data points fit by the original Karpowicz and Steffes (2011a) and Karpowicz and Steffes (2011b) model.

The laboratory measurements of water vapor conducted at high temperature described in Section 3.6.1 are presented in Figure 3.5. The result of these high temperature measurement of water vapor's microwave opacity are consistent with the modifications made to the Karpowicz and Steffes (2011a) and Karpowicz and Steffes (2011b) model.

Table 3.8: Empirically derived constants for the modified Karpowicz and Steffes (2011a) and Karpowicz and Steffes (2011b) H_2O water vapor model.

C_w	3.1×10^{-7}	$km^{-1} \times (mbars \times GHz)^{-2}$
$x_{continuum}$	12	
C_{H_2}	$5.07722009423 \times 10^{-11}$	$km^{-1} \times (mbars \times GHz)^{-2}$
C_{He}	$1.03562010226 \times 10^{-10}$	$km^{-1} \times (mbars \times GHz)^{-2}$

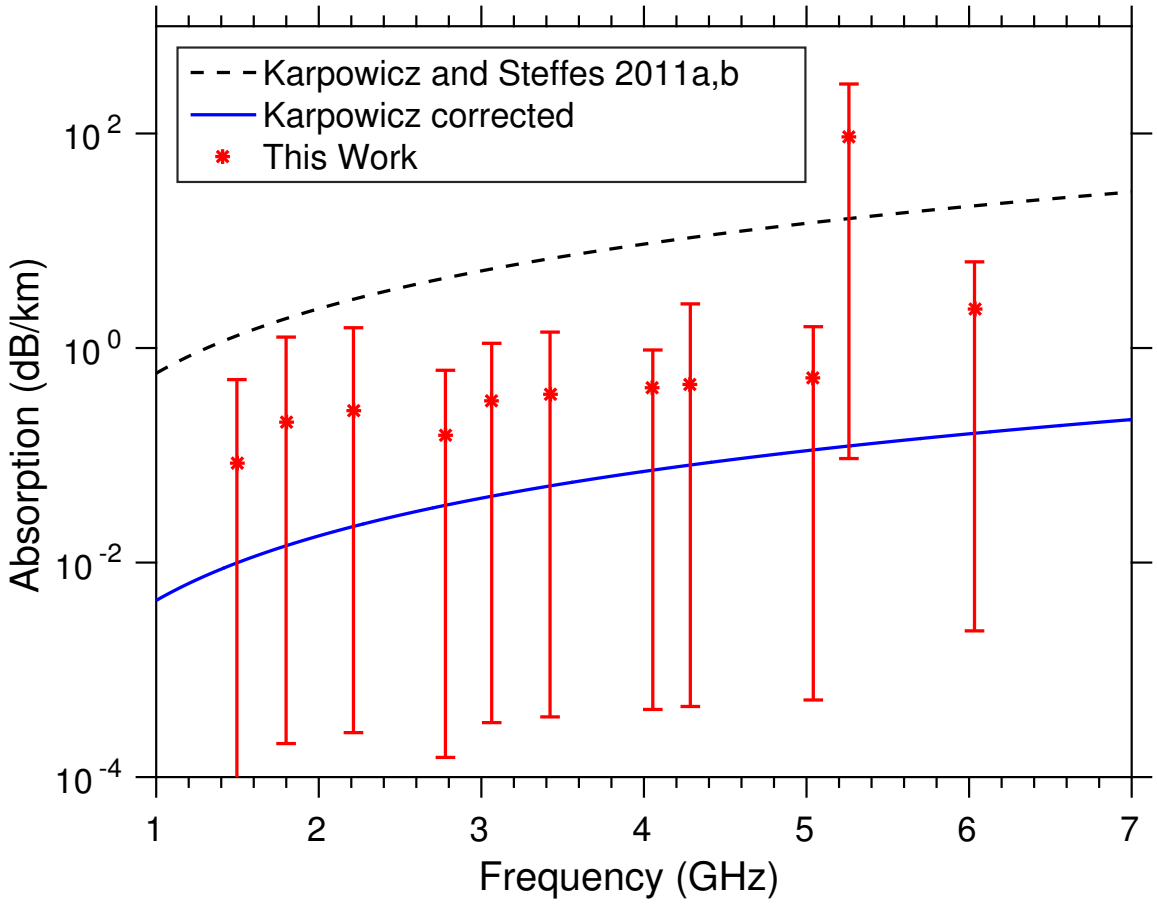

Figure 3.5: Differential water vapor opacity data measured using the high-temperature centimeter-wavelength system at pressures of 4.734 bars and 3.612 bars at a temperature of 597 K.

3.7 Methane

Similar to water vapor's broadening of ammonia's absorption spectrum, the linewidth and coupling parameters for ammonia are modified by adding the contribution of methane to equations 3.37 and 3.38 as follows

$$\begin{aligned}\gamma_j &= \gamma_{CH_4} P_{CH_4} \left(\frac{300}{T}\right)^{\Gamma_{CH_4}} + \gamma_{H_2} P_{H_2} \left(\frac{300}{T}\right)^{\Gamma_{H_2}} + \gamma_{He} P_{He} \left(\frac{300}{T}\right)^{\Gamma_{He}} \\ &\quad + \gamma_{NH_3} \gamma_{(0,j)} P_{NH_3} \left(\frac{295}{T}\right)^{\Gamma_{NH_3}} \text{ (GHz)} \end{aligned} \tag{3.49}$$

$$\begin{aligned}\zeta_j &= \zeta_{CH_4} P_{CH_4} \left(\frac{300}{T}\right)^{Z_{CH_4}} + \zeta_{H_2} P_{H_2} \left(\frac{300}{T}\right)^{Z_{H_2}} + \zeta_{He} P_{He} \left(\frac{300}{T}\right)^{Z_{He}} \\ &\quad + \zeta_{NH_3} \gamma_{(0,j)} P_{NH_3} \left(\frac{295}{T}\right)^{Z_{NH_3}} \text{ (GHz)} \end{aligned} \tag{3.50}$$

where for the inversion line j and constituent $i =$ CH_4, H_2, He, NH_3, γ_i and ζ_i are constant scale terms, Γ_i and Z_i represent the constant temperature dependences of the broadening and coupling of each of the gases, P_i are the ideal partial pressures in bar, and $\gamma_{(0,j)}$ are the self-broadening linewidths of the inversion transitions of ammonia in MHz/Torr.

The optimized free parameters for methane's scaling parameters and temperature dependences for both the linewidth and coupling parameters are derived through fitting the model to the laboratory results from Chinsomboon (2012). The ammonia, hydrogen, and helium free parameters for the linewidth and coupling parameters are described previously in this work. The derived methane line shape coefficients are displayed in Table 3.9.

Table 3.9: Constants for the new microwave opacity model of CH_4-broadened NH_3

	i=CH_4	Units
γ_i	2.6406	(GHz/bar)
Γ_i	1.0	
ζ_i	0.9111	(GHz/bar)
Z_i	1.9200	

This new model for the opacity of ammonia pressure-broadened by methane in the 5–20 cm wavelength range is fitted to opacity measurements at pressures up to 3 bars and a temperature range of 330 to 450 K.

In Figures 3.6 – 3.8, the model for the opacity of ammonia, which has been pressure-broadened by methane, is plotted along with a subset of the opacity measurements taken in the laboratory by Chinsomboon (2012). All 264 measurements taken in the 330-450 K temperature region at pressures of up to 3 bars (including either 100 mbar or 200 mbar of ammonia) in this work were used to evaluate the performance of the model in the 1.5-6 GHz range. The error bars of each data point display the 2σ total uncertainties and uncertainty due to experimental conditions.

The formalism accurately models 89.77% of all data points within the 2σ uncertainty.

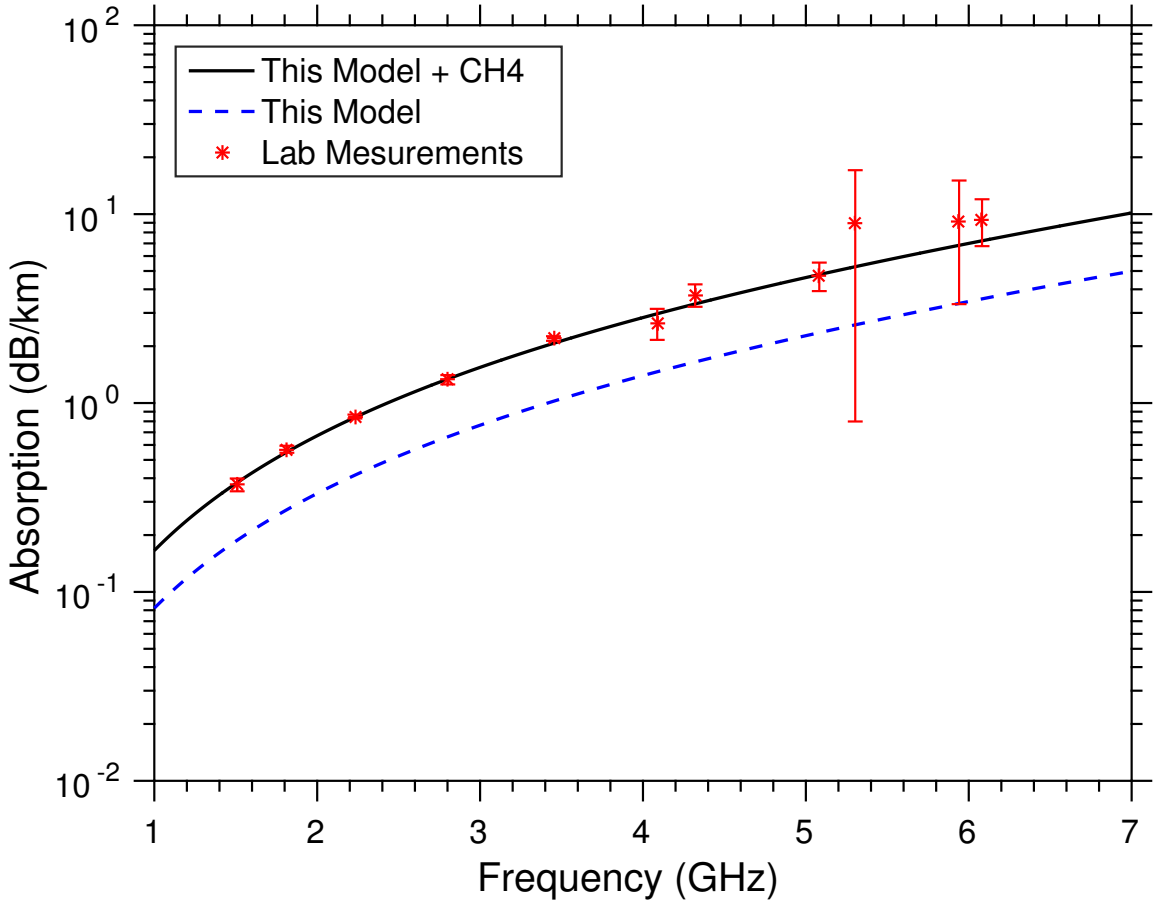

Figure 3.6: Opacity data measured using the high-temperature centimeter-wavelength system for a mixture of NH_3 = 10.78%, CH_4 = 89.22% at a pressure of 1 bar and temperature of 329.4 K (Chinsomboon, 2012) compared to the ammonia model presented in Section 3.5.2 and the ammonia model with methane added.

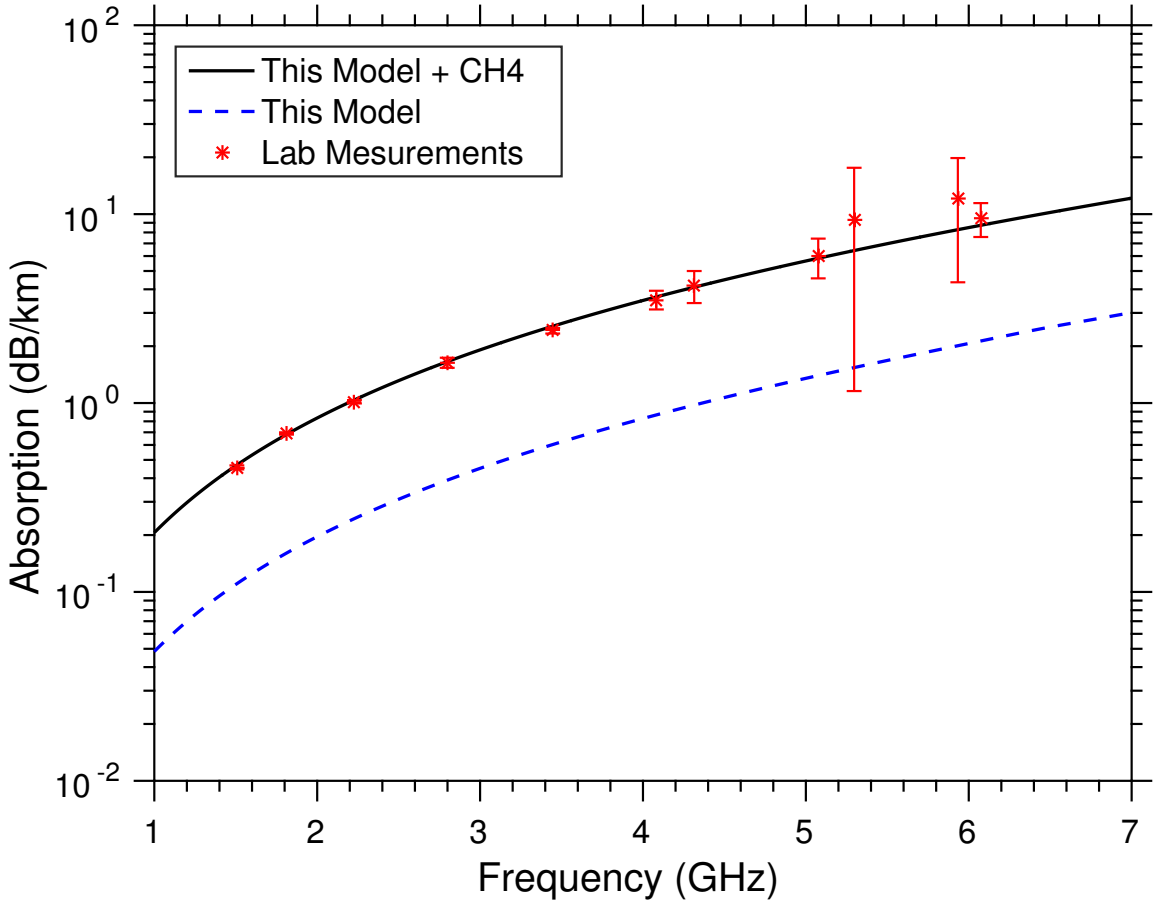

Figure 3.7: Opacity data measured using the high-temperature centimeter-wavelength system for a mixture of NH_3 = 3.39%, CH_4 = 96.61% at a pressure of 2.992 bars and temperature of 375 (Chinsomboon, 2012) compared to the ammonia model presented in Section 3.5.2 and the ammonia model with methane added.

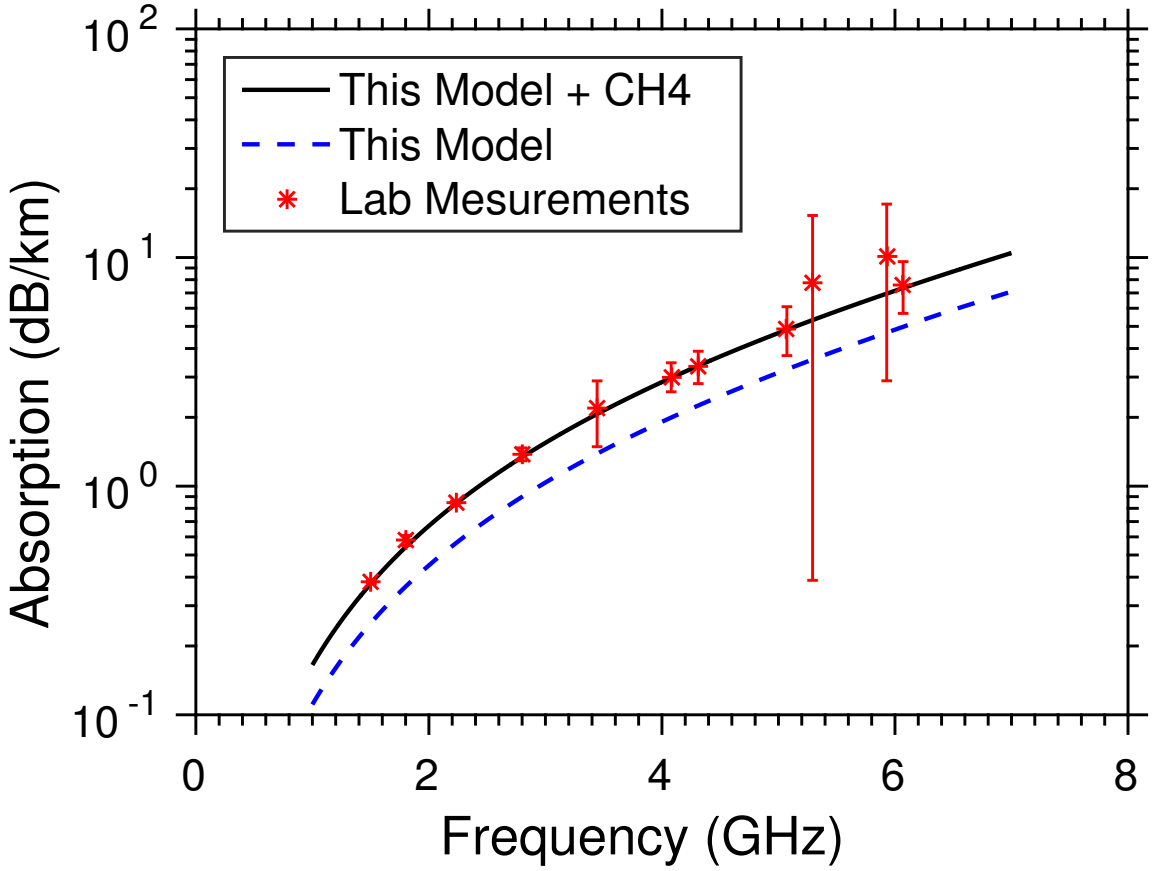

Figure 3.8: Opacity data measured using the high-temperature centimeter-wavelength system for a mixture of NH_3 = 20.37%, CH_4 = 79.63% at a pressure of 1 bar and temperature of 449.8 K (Chinsomboon, 2012) compared to the ammonia model presented in Section 3.5.2 and the ammonia model with methane added.

Part II

Modeling and Theory

CHAPTER 4
ATMOSPHERIC MODELING

Accurate retrievals of the abundance profiles of ammonia and water vapor in Jupiter's atmosphere require accurate atmospheric models. This chapter begins by describing the Jupiter Atmospheric Microwave Radiative Transfer (JAMRT) code. JAMRT computes a model brightness temperature based on a set of input parameters. The Juno MWR does not measure brightness temperature directly, however, but rather it measures antenna temperature. Following the description of JAMRT is an explanation of the process used for deconvolving the antenna beam pattern reflected in the measured antenna temperatures so as to retrieve brightness temperature. A large unknown in the jovian atmosphere is the presence of rain and its effect on the signal retrieved with Juno MWR. The third section in this chapter describes a time-dependent microphysical model of rainfall in the jovian atmosphere and its potential effects on the Juno MWR data.

The next two sections in this chapter address an issue reflected in data from the first perijove. In Li et al. (2017) a possible ammonia abundance profile based on MWR data from perijove 1 is retrieved and presented. While this ammonia abundance profile matches the first perijove's measured brightness temperatures at all channels and limb darkening at Channels 2–6 (24–1.36 cm), an issue occurs with Channel 1's (50 cm) limb darkening. The modeled limb darkening for Channel 1 is, on average, 2-3% higher than the measured limb darkening. While this can be reduced by adding more water vapor, JAMRT does not take into account two deep atmospheric effects that significantly change Channel 1's limb darkening. The first of these effects is the possible presence of a radiative layer at temperatures greater than 1300 K, driven by the infrared opacity at these temperature levels. The second is the ionization of alkali metals and their intrinsic opacity in both the microwave and infrared regime. The ionization of alkali metals produces an infrared opacity strong

enough to remove the possibility of a radiative zone, making these two effects mutually exclusive. Similarly, the last section in this chapter address an issue reflected in data from the fifth perijove. The last section describes the jovian aurora and its potential to effect the jovian microwave emission measured by the Juno MWR.

4.1 JAMRT

The Jupiter Atmospheric Microwave Radiative Transfer (JAMRT) code is the core model behind the work presented in this chapter. JAMRT was developed primarily to use in the Juno mission and is described in Janssen et al. (2013) and Janssen et al. (2017a). The core of JAMRT is the pencilbeam forward model (PBF), which computes brightness temperatures corresponding to a set of atmospheric input parameters. The PBF model is split into distinct parts: the atmospheric model and the radiative transfer code. Section 2.2 describes the radiative transfer theory at the core of JAMRT.

Built atop of the PBF model is the full forward model that computes antenna temperatures. Given a set of observation times, the full forward model determines the position and orientation of the spacecraft and its antennas using SPICE and appropriate kernels. The SPICE toolkit is provided by NASA's Navigation and Ancillary Information Facility to assist scientists in planning and interpreting scientific observations from space-based instruments aboard robotic spacecraft. SPICE allows the user to calculate derived observation geometry such as altitude, latitude, longitude, and spacecraft orientation. The full forward model convolves the antenna pattern with the simulated brightness temperatures from the PBF model over all angles. To generate the observation times for the full forward model, an orbit simulator is added to JAMRT. Together, the full forward model and the orbit simulator are called the Instrument Simulator.

This section will focus on the atmospheric model and its input parameters. Also described are details of the full forward model. Appendix A contains a technical section which will focus on explaining the JAMRT input file, source code, and the core algorithms

in the PBF model. This will serve as a starting point for future students trying to modify and understand the JAMRT code.

4.1.1 Pencilbeam Forward Model

At the core of JAMRT is the pencilbeam forward model (PBF). The PBF model constructs a model atmosphere and carries out radiative transfer calculations at microwave frequencies within the Rayleigh-Jeans limit. While this model can be used for Saturn, it was originally written to support the Juno Microwave Radiometer experiment at Jupiter.

The atmospheric modeling part of JAMRT builds deep convective models using wet adiabatic lapse rates in the cloud forming regions and dry adiabatic lapse rates elsewhere. The gravitational potential is calculated by assuming a fluid with uniform angular velocity with the radius of Jupiter taken to be 71,492 km at the equator. For the purposes of the radiative transfer calculations, the atmosphere is assumed to be stratified. The normal to the stratified layers follow the normal to the equipotential surfaces of Jupiter (Lindal et al., 1981).

A reference temperature pressure point can be selected by the user, but is set to 0.5 bars and 132.79 K, respectively, by default. These values are based on measurements near 6.53°N latitude with the Galileo entry probe (Seiff et al., 1998). Changing this reference temperature allows the user to select which adiabatic pressure-temperature profile the model calculates. The full atmospheric model extends as deep as 1000 bars, but can be controlled by the user. Due to the broad nature of Channel 1's contribution function, the atmospheric model is extended to 5000 bars. Layer thickness is another adjustable parameter set to 100 m by default. Raising this to 1 km produced a substantial decrease in computational time without noticeable difference in the calculated brightness temperatures. The atmospheric model will reduce the layer thickness to account for the transition that occurs in the formation of clouds.

The dry atmosphere consists of hydrogen (H_2), helium (He), methane (CH_4), phos-

phine (PH_3), and argon (Ar). The condensable gases are water vapor (H_2O), hydrogen sulfide (H_2S), and ammonia (NH_3). The deep abundances of these gases are nominally set as shown in Table 4.1, but can be adjusted by the user. The condensates formed in the region of Jupiter's atmosphere are H_2O liquid, H_2O ice, aqueous ammonia (liquid H_2O mixed with NH_3), ammonium hydrosulfide (NH_4SH), and NH_3 ice. Aqueous ammonia is generated when NH_3 is absorbed by the condensing liquid water. NH_4SH is caused by the interactions between H_2S and NH_3. The saturation vapor pressures and moist adiabats for these gases and condensates are given in Atreya (2013). Figure 4.1 shows the calculated pressure-temperature profile along with the vertical mixing ratio as a function of depth for the condensable gases. Note that in this dissertation, the term "mixing ratio" refers to the number of molecules of a specific species relative to the total number of all molecules in a specific volume. Thus it is synonymous with the term "mole fraction".

Table 4.1: Nominal composition of the Jupiter reference model atmosphere (protosolar abundances are from Atreya et al. (2017))

Constituent	Protosolar abundance (Relative to H_2)	Enrichment (Jupiter/Protosolar)	Jupiter mole fraction
H_2	1		0.862
He	0.191	0.82	0.135
CH_4	5.90×10^{-4}	4.02	2.04×10^{-3}
H_2O	1.07×10^{-3}	0.46	4.22×10^{-4}
NH_3	1.48×10^{-4}	4.48	5.72×10^{-4}
H_2S	2.90×10^{-5}	3.08	7.67×10^{-5}
Ar	5.50×10^{-6}	3.31	1.57×10^{-5}
PH_3	5.64×10^{-7}	3.83	1.86×10^{-6}

The equilibrium cloud condensation model (ECCM) used in the JAMRT code is described by Weidenschilling and Lewis (1973). ECCMs are first order descriptions of clouds and their compositions in planetary atmospheres. While this model correctly calculates the atmospheric structure and gas mixing ratios accompanying clouds, the cloud densities calculated by Weidenschilling and Lewis (1973) are inconsistent with the available mass. Wong et al. (2015) improve the cloud density calculation by calculating a "cloud density rate" instead of a cloud density. This rate can be converted to the density based on an up-

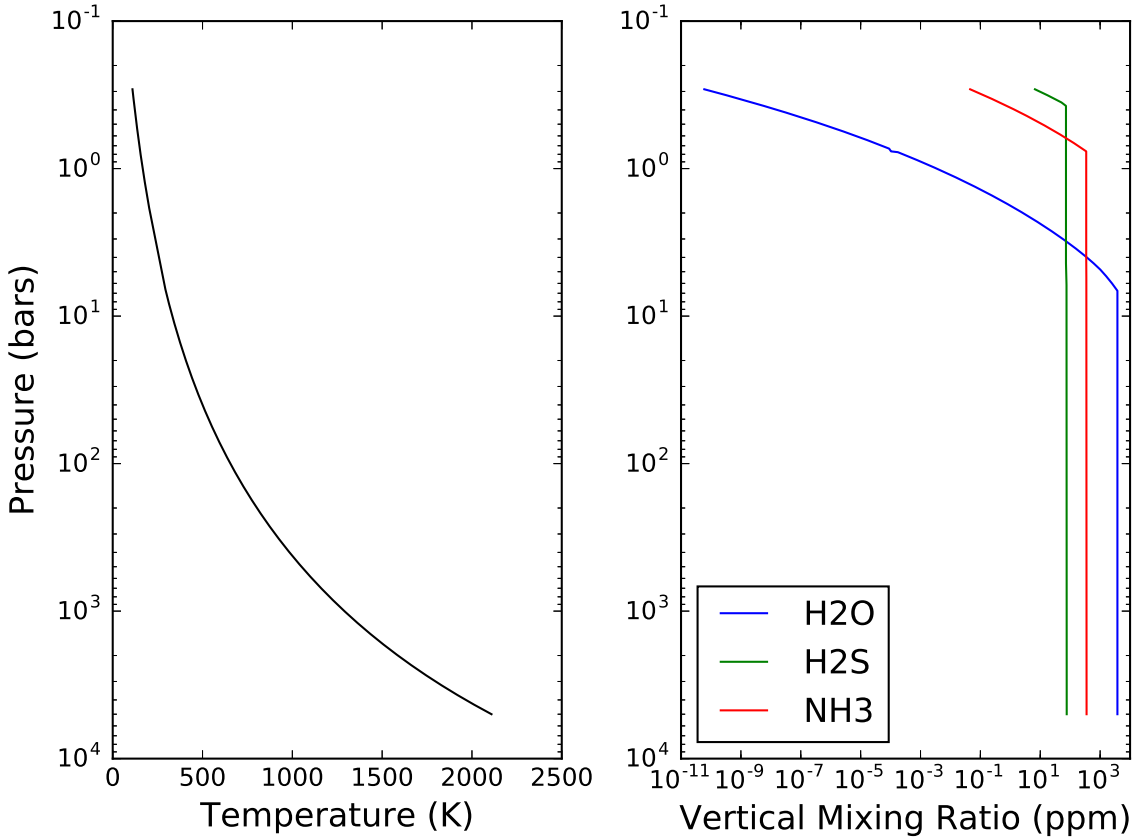

Figure 4.1: Atmospheric model with the input deep abundance of NH_3 and H_2O as 2.7 and 4.0 x solar, respectively. The right graph is the temperature-pressure profile. The left is the vertical mixing ratio (in parts per million) verses pressure.

draft length scale, L, a product of the updraft velocity and a time scale. Wong et al. (2015) validates their approach by using data taken by the Galileo Probe nephelometer (Ragent et al., 1998). The calculated cloud densities using the Wong et al. (2015) model requires an updraft length scale of $L \approx 10^8$ cm to reach the same densities modeled by Weidenschilling and Lewis (1973). The largest updraft scale length seen by the nephelometer aboard the Galileo Probe was $L = 10^6$ cm at the NH_4SH cloud (Wong et al., 2015). By significantly reducing the cloud densities, the absorption from cloud particles is vastly diminished. Since the Wong et al. (2015) cloud model results in cloud bulk densities incapable of generating measurable microwave opacity, its effects can be modeled by "turning off" the opacity due to clouds.

The brightness temperature of the atmosphere depends on the distribution of microwave absorbers with temperature. The major absorbers affecting the Juno MWR are gaseous NH_3, and H_2O. Gaseous NH_3 is the dominate source of microwave opacity. JAMRT uses the centimeter-wavelength absorption models for NH_3 and H_2O, described in Bellotti et al. (2016). The procedure to measure and model these absorption coefficients is discussed in depth in Chapter 3. While H_2S and PH_3 do have an intrinsic opacity, their low abundance in the jovian atmosphere does not significantly affect the brightness temperature at the wavelengths measured by the MWR.

4.1.2 Full Forward Model

While only brightness temperatures are used in the retrievals described in the following sections, forward modeling of data from the Juno MWR can be developed using a convolution of the pencilbeam forward model with the antenna pattern, $G(\nu, \hat{\mathbf{n}} \cdot \hat{\mathbf{n}}')$, to produce antenna temperature:

$$T_A(\nu, \hat{\mathbf{n}}) = \int \frac{d\Omega'}{4\pi} T_B(\nu, \hat{\mathbf{n}}') G(\nu, \hat{\mathbf{n}} \cdot \hat{\mathbf{n}}') \tag{4.1}$$

This integration is called the Full Forward Model. While antenna temperature (T_A) is not used in the remainder of this work, it is important to know how brightness temperatures (T_B) and antenna temperatures are related. Integration over all angles where the antenna pattern is non-negligible requires many evaluations of the pencilbeam forward model. Since this is unreasonable to compute in real time, JAMRT can precompute and tabulate the pencilbeam forward model over the entire range of parameters that contribute to the integration. Gridding is performed in such a way that the interpolation error is bounded by a predetermined value. Note that the number of calculations performed will go as n^k where n is the number of grid points and k is the number of atmospheric parameters allowed to vary. Thus, the size of the table grows exponentially with the number of dimensions.

4.2 Deconvolution

While the pencilbeam forward model computes the brightness temperature emitted by Jupiter, the Juno MWR measures antenna temperature. In order to intercompare the two, beam deconvolution is necessary. The main objective of the deconvolution process is to determine the localized brightness temperatures from the observed antenna temperatures. The method of deconvolution used in the Juno MWR science data pipeline was developed by Oyafuso et al. (2017) and is presented here for reference.

The antenna temperatures $T_i^{(A)}$, a time based measurement indexed by i, can be expressed as a convolution of the beam pattern G and the spatially dependent brightness temperatures $T^{(B)}$ arising from the thermal emission from Jupiter. The goal of the deconvolution is to invert the following equation and solve for $T^{(B)}$:

$$T_i^{(A)} \approx G * T_i^{(B)} \tag{4.2}$$

The convolution can be discretized into a summation over a set of direction vectors, indexed by j, for the reference frame of the spacecraft. The discretized convolution is represented

by:

$$T_i^{(A)} \approx \sum_j G_j A_j T^{(B)}(r_{i,j}, \mu_{i,j}) \tag{4.3}$$

where $r_{i,j}$ denotes the location on Jupiter, $\mu_{i,j}$ denotes the cosine of the emission angle at time i and direction j, and A_j denotes area elements.

The brightness temperatures are then expanded in positional and angular basis functions. The positional basis functions, denoted by $h_p(r)$, are hat functions with peak values of unity located at two dimensional grid points $\theta_{\mathbf{p}}$:

$$h_p(\theta) = \begin{cases} 1 - ||\theta - \theta_{\mathbf{i}}||_2 & \theta_{i-1} \leq \theta \leq \theta_{i+1} \\ 0 & \text{else} \end{cases} \tag{4.4}$$

where θ is a two dimensional vector containing the latitude and longitude of the point and $||X||_2$ is the L-2 norm.

The angular basis functions, denoted by $f_k(\mu)$, are currently chosen from the set: $\{1,\ 1-\mu,\ (1-\mu)^2\ \}$. The brightness temperature in equation 4.3 can thus be expanded in coefficients, c_{kp}, scaling each angular basis function, k, for the position, p.

$$\begin{aligned} T_i^{(A)} &\approx \sum_j G_j A_j \sum_{kp} h_p(r_{ij}) f_k(\mu_{ij}) c_{kp} && (4.5) \\ &= \sum_{kp} \underbrace{\left(\sum_j G_j A_j h_p(r_{ij}) f_k(\mu_{ij}) \right)}_{M_{i,kp}} c_{kp} && (4.6) \\ &= \sum_{kp} M_{i,kp} c_{kp} && (4.7) \end{aligned}$$

The quantity $M_{i,kp}$ represents the contribution of measurement i to the k^{th} angular coefficients at position p. This is precomputed for relevant window of an orbit using SPICE function calls and antenna patterns for each channel (Acton, 1996; Acton et al., 2017).

Equation 4.5 can be written as the least squares problem

$$T^{(A)} \approx Mc \tag{4.8}$$

In practice however, the condition number of M is large; many small singular values amplify measurement noise in the inversion. To mitigate this issue, the deconvolution proceeds in two stages. The first stage simultaneously solves for the coefficients c on a coarse, longitudinally-independent mesh using measurements from all available perijoves. This ignores longitudinal variations but provides a more stable solution of local and zonal averages. The second stage uses the coarse mesh solution as a prior for retrievals on individual perijoves. This is computed by:

$$c^T = c_{prior} + \left(M^T S_{T_A}^{-1} M + S_c^{-1}\right)^{-1} \left(M^T S_{T_A}^{-1} \left(T_A - M c_{prior}\right)\right) \tag{4.9}$$

where c is the coefficient matrix, c_{prior} is the coarse, longitudinally-independent coefficient matrix from the first stage, M is the contribution matrix, S_{T_A} is the covariance matrix of the antenna measurements, S_c is the covariance matrix of the coefficients, and T_A is the antenna temperature matrix.

Characterization of the angular dependence of brightness temperature at large emission angles cannot be entirely neglected. For an ideal instrument, adding more basis functions will improve the fit, but in practice instrument noise limits the dimension of the basis set to three at most, and adding more basis functions increases instability. This results in the brightness temperatures as a function of look angle being given by three coefficients for each position, and can be calculated by

$$T_l^{(B)}(\mu) = \varepsilon(\mu)[c_0 + (1-\mu)c_1 + (1-\mu)^2 c_2] \tag{4.10}$$

where c_0, c_1, and c_2 are the three coefficients, c_k, for the position (p) and $\mu = \cos(\theta)$ is the

cosine of the look angle. Additionally, $\varepsilon(\mu) = 1$ for $\mu > 0.6$. For larger emission angles ($\mu < 0.6$), $\varepsilon(\mu)$ is determined by fitting brightness temperatures for a variety of adiabatic atmospheres using the JAMRT code only over the range of $\mu > 0.6$. The ratio between the extrapolated fit and the "true" brightness temperatures defines $\varepsilon(\mu)$. The key is that for any given channel, $\varepsilon(\mu)$ depends only weakly on details of the atmosphere. However, in this work only measurements where $\mu < 0.6$ are used; therefore the $\varepsilon(\mu)$ can be ignored. Equation 4.10 allows the deconvolved brightness temperatures as a function of look angle and latitude to be calculated quickly and using a minimal amount of hard drive space.

4.3 Rainfall and Virga on Jovian Planets

Clouds are seen on almost every planet in our solar system and can cover entire globes. On Earth, cloud formation starts with a parcel of air warmed by the surface, causing it to rise. If the atmosphere is stable (the surrounding air is warmer than the parcel) the parcel will stop rising and sink back down. However, if it unstable (the surrounding air is cooler than the parcel) the parcel will continue to rise and may form a cloud as condensation occurs in the cooler upper atmosphere.

The modeling of virga (rain that evaporates before reaching the surface) in jovian atmospheres has a very sparse history. The Equilibrium Cloud Condensation Model (ECCM) is a thermochemical model used to predict a multi-layer structure on giant planets (Lewis, 1969; Weidenschilling and Lewis, 1973; Atreya and Romani, 1985). The model calculates the upper limit for cloud densities, which are reduced by one to several orders of magnitude when precipitation is allowed (Rossow, 1978; Lunine and Hunten, 1987; Atreya et al., 1999; Wong et al., 2015). Cloud microphysics are further described by Rossow (1978) and Ackerman and Marley (2001). While experiments and models for the rate, the size, and the duration of the precipitation have been conducted for Earth (Marshall and Palmer, 1948; Chu and Hogg, 1968; Laws and Parsons, 1943; Wexler, 1948; Best, 1950), very little work has been done for precipitation on other celestial bodies.

Toon et al. (1988) found that methane rain is present on Saturn's moon, Titan, but suggests that raindrops would be sparse and grow rapidly to a size larger than 50 μm. Recent detailed models indicate that methane rain is indeed possible in Titan's atmosphere (Barth and Toon, 2003). The properties of rain and hail as they fall through the Titan atmosphere have also been modeled (Graves et al., 2008). Modifying the model described in Graves et al. (2008) to suit the jovian atmosphere and determining how such precipitation affects the microwave emission is part of this work.

The virga model consists of three algorithms: the first calculates the raindrop size and effect on the mole fraction of water vapor as it falls through the atmosphere; the second calculates the complex dielectric constant of aqueous ammonia in the droplets (Duong et al., 2014), and the third computes the Rayleigh scattering (and the accompanying attenuation) due to the raindrops present.

4.3.1 Virga Modeling

A time-dependent microphysical model has been developed as part of this work to study the evolution of water clouds in Jupiter's atmosphere. The model also simulates how the resulting precipitation and its evaporation affect the microwave emission spectrum. The virga model takes four inputs, a complete atmospheric thermochemical model (taken from JAMRT), the initial raindrop size (r), the raindrop number density (ρ_{rain}), and the time step, (Δt, set by default to 1 second), and computes the size and amount of rain in each atmospheric layer.

The algorithm begins at the base of the aqueous ammonia cloud and time, $t = 0$. The velocity of the raindrop is assumed to be the terminal velocity, in m/s,

$$v(t) = \frac{2gr^2 \times \rho_{drop}}{9\eta} \tag{4.11}$$

where ρ_{drop} is the density of the rain drop (kg/m^3), g is the acceleration due to gravity, r

is the radius of the raindrop in m, and η is the dynamic viscosity in kg/(s·m) is calculated below, as described in Hansen (1979).

The relationship starts with the viscosity of hydrogen, η_{H2} and helium, η_{He} in units of micropoise:

$$\eta_{H2} = \frac{90.6 \times (T/300)^{0.6658}}{1 + 4/T} \tag{4.12}$$

$$\eta_{He} = \frac{191.6 \times (T/300)^{0.7176}}{1 + 11.4/T} \tag{4.13}$$

The cross section, in cm^2, for hydrogen, Q_{H2}, helium, Q_{He}, and hydrogen-helium, Q_{H2-He}, are defined as:

$$Q_{H2} = 32.3 \times (1 + 4/T) \times (300/T)^{0.1658} \tag{4.14}$$

$$Q_{He} = 21.5 \times (1 + 11.4/T) \times (300/T)^{0.2176} \tag{4.15}$$

$$Q_{H2-He} = ((Q_{H2}^{0.5} + Q_{He}^{0.5})/2)^2 \tag{4.16}$$

The ratio of pure mixture for hydrogen, L_{H2}, and helium, L_{He}, are defined by Hansen (1979):

$$L_{H2} = 1 + 0.7967 \times (X_{He}/X_{H2}) \times (Q_{H2-He}/Q_{H2}) \tag{4.17}$$

$$L_{He} = 1 + 0.5634 \times (X_{H2}/X_{He}) \times (Q_{H2-He}/Q_{He}) \tag{4.18}$$

Finally, the viscosity of the atmosphere in micropoise is calculated as:

$$\eta = \eta_{H2}/L_{H2} + \eta_{He}/L_{He} \tag{4.19}$$

After the terminal velocity is calculated, the distance the raindrop travels in the current

time step (Δt) is calculated

$$x(t) = x(t - \Delta t) + v \cdot \Delta t \tag{4.20}$$

The change in raindrop mass (normalized by cross-section) over change in time for the current atmospheric layer is calculated by

$$\frac{dM[x]}{dt} = (P_{vapor}[x] - P_{H_2O}[x]) \sqrt{\frac{\text{molecular weight}}{2\pi RT[x]}} \quad \left(\frac{kg}{m^2 s}\right) \tag{4.21}$$

where for the current layer x, $P_{vapor}[x]$ is the saturation vapor pressure of water (bars), $P_{H_2O}[x]$ is the partial pressure of water (bars), R is the ideal gas constant, and $T[x]$ is the temperature (K). This algorithm ensures the raindrop does not grow while descending by forcing $\frac{dM[x]}{dt}$ to be less than or equal to zero.

The mass loss for all raindrops in a unit volume during the current time step is

$$\Delta M[x] = \frac{dM[x]}{dt} \times SA_{drop} \times \rho_{rain} \times \Delta t \quad (kg) \tag{4.22}$$

where SA_{drop} is the surface area of each drop (m^2), Δt is the time step (sec), and ρ_{rain} is the raindrop number density (drops/m^3). From this, the change in pressure due to evaporation can be calculated as

$$\Delta P[x] = \frac{\Delta M[x] \cdot T[x] \cdot R}{\text{molecular weight}} \quad (bars) \tag{4.23}$$

If the change in the partial pressure of water vapor causes the partial pressure of water vapor to exceed its saturation vapor pressure, then

$$\Delta P[x] = P_{vapor} - P_{H_2O} \tag{4.24}$$

where P_{vapor} is the saturation vapor pressure of water and P_{H_2O} is the partial pressure of water vapor, both in bars. In this case, the total mass loss per unit volume is instead

calculated by

$$\Delta M[x] = \frac{\Delta P[x] \cdot \text{molecular weight}}{T[x] \cdot R} \left(\frac{g}{m^3}\right) \tag{4.25}$$

The water vapor volume mixing ratio is updated by

$$X_{H_2O}[x] = X_{H_2O}[x] + \frac{\Delta P[x]}{P[x]} \tag{4.26}$$

where for the altitude layer x, $P[x]$ is the total pressure (in bars) and $X_{H_2O}[x]$ is the volume mixing ratio.

The mass loss for an individual raindrop is calculated by

$$\Delta m[x] = \frac{\Delta M[x]}{\rho_{rain}} \tag{4.27}$$

which, in turn, changes the droplet volume by

$$\Delta v[x] = \frac{\Delta m[x]}{\rho_{drop}} \tag{4.28}$$

The change in radius for an individual raindrop, assuming spherical drops, is calculated by

$$\Delta r[x] = \left(\frac{3}{4\pi}\Delta v[x]\right)^{1/3} \tag{4.29}$$

Finally, the new radius is updated by

$$r_{i+1}[x] = r_i[x] - \Delta r \tag{4.30}$$

where i is the current time step. Using the distance the raindrop has traveled, the current atmospheric layer x is updated. This process is repeated until the raindrop radius reaches zero.

4.3.2 Complex Dielectric of Aqueous Ammonia

Following the simulation of rainfall, the complex dielectric constant of aqueous ammonia is calculated. This was first derived by Duong et al. (2014) and is calculated by

$$\epsilon(T) = \frac{\epsilon_s(T) - \epsilon_1(T)}{1 + j \cdot \frac{\nu}{\nu_1(T)}} + \frac{\epsilon_1(T) - \epsilon_\infty(T)}{1 + j \cdot \frac{\nu}{\nu_2(T)}} + \epsilon_\infty(T) + \Delta_{NH_3}(C, \nu, T) \tag{4.31}$$

where T is the temperature in °C, ν is the frequency in GHz, C is the concentration of ammonia, ν_1 and ν_2 represent the two Debye relaxation frequencies, and $j = \sqrt{-1}$. The other coefficients are described by

$$\epsilon_s(T) = \frac{3.70886 \times 10^4 - 8.216810 \times 10^1 \cdot T}{4.21854 \times 10^2 + T} \tag{4.32}$$

$$\epsilon_1(T) = x_0 + x_1 \cdot T + x_2 \cdot T^2 \tag{4.33}$$

$$\nu_1(T) = \frac{45 + T}{x_3 + x_4 \cdot T + x_5 \cdot T^2} \tag{4.34}$$

$$\epsilon_\infty(T) = x_6 + x_7 \cdot T \tag{4.35}$$

$$\nu_2(T) = \frac{45 + T}{x_8 + x_9 \cdot T + x_{10} \cdot T^2} \tag{4.36}$$

$$\Delta_{NH_3}(C, \nu, T) = \frac{x_{11} \cdot C \cdot \nu^{x_{12}}}{T^{x_{13}}} - j \cdot \left(\frac{x_{14} \cdot C \cdot \nu^{x_{15}}}{T^{x_{16}}} + x_{17} \cdot C \right) \tag{4.37}$$

where x_k are empirically derived parameters given in Table 4.2.

Table 4.2: Parameters for the complex dielectric properties of aqueous ammonia (Duong et al., 2014)

k	x_k		k	x_k
0	5.7230		9	$1.4825E-03$
1	2.2379×10^{-2}		10	2.4166×10^{-4}
2	-7.1237×10^{-4}		11	-78.00
3	5.0478		12	0.0190
4	7.0315×10^{-2}		13	0.0586
5	6.0059×10^{-4}		14	226.4
6	3.6143		15	0.0231
7	2.8841×10^{-2}		16	12.90
8	1.3652×10^{-1}		17	24.77

4.3.3 Rayleigh Scattering

The attenuation due to Rayleigh scattering is calculated by

$$\alpha_{rain} = \frac{246 \cdot N \cdot V \cdot \epsilon''}{\lambda \left[(\epsilon' + 2)^2 + (\epsilon'')^2\right]} \tag{4.38}$$

where α_{rain} is the opacity due to the rain in dB/km, N is the raindrop number density in cm^{-3}, V is the volume of a raindrop in cm^3, λ is the wavelength in km, and ϵ' and ϵ'' are the real and imaginary components, respectively, of the dielectric constant of the drop. This additional attenuation is then added to other sources of opacity in the radiative transfer model to determine the effects on microwave emission.

4.3.4 Effects on the Microwave Brightness Temperature and Limb Darkening

The three algorithms have been implemented and added to JAMRT. The effects of virga, on the brightness temperature and 50° limb darkening, as a function of raindrop radius and raindrop density, are presented in Figures 4.2–4.5 and show that only very heavy rainstorms, or very big, non-physical, raindrops, are visible to the Juno Microwave Radiometer.

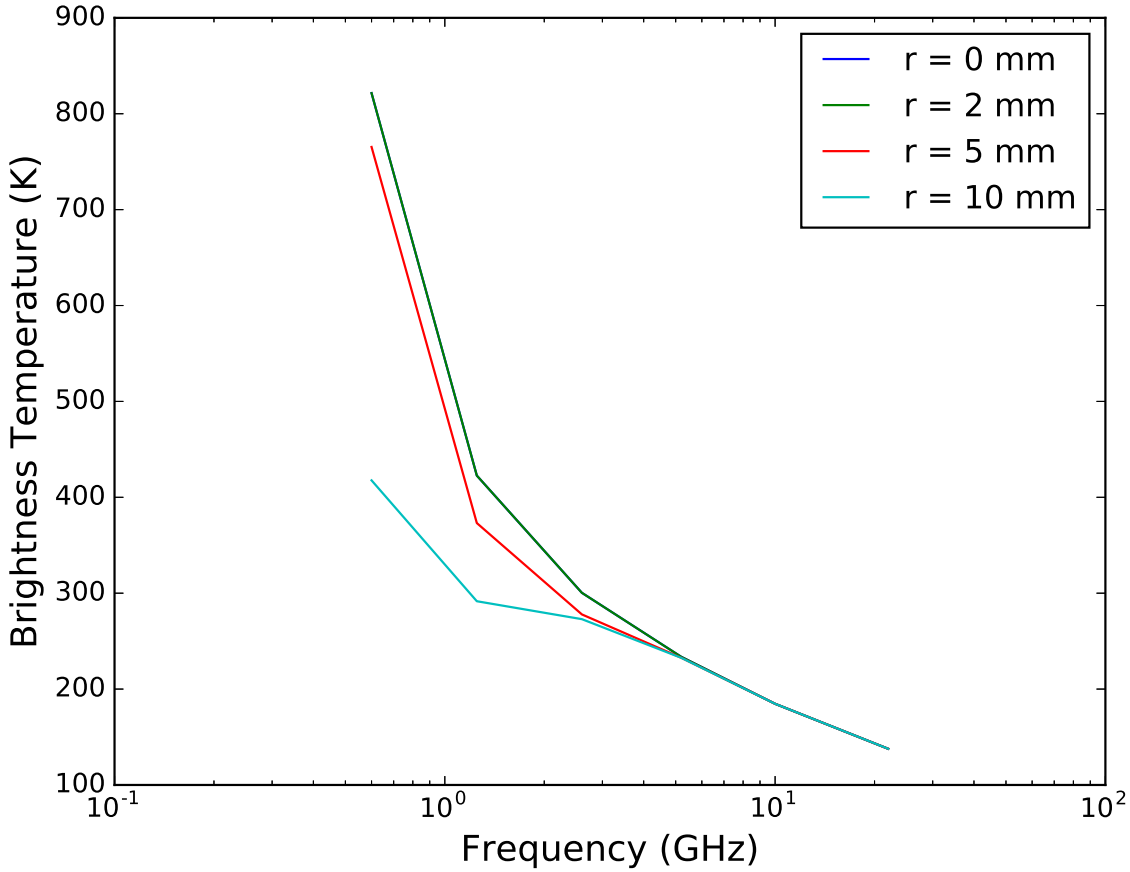

Figure 4.2: Comparison of the simulated nadir microwave brightness temperatures using the virga model and varying the raindrop diameter. A well mixed atmosphere with a deep abundance of 2.7x and 4.0x solar for NH_3 and H_2O, respectively, and a raindrop density of 1E3 m^{-3} is used.

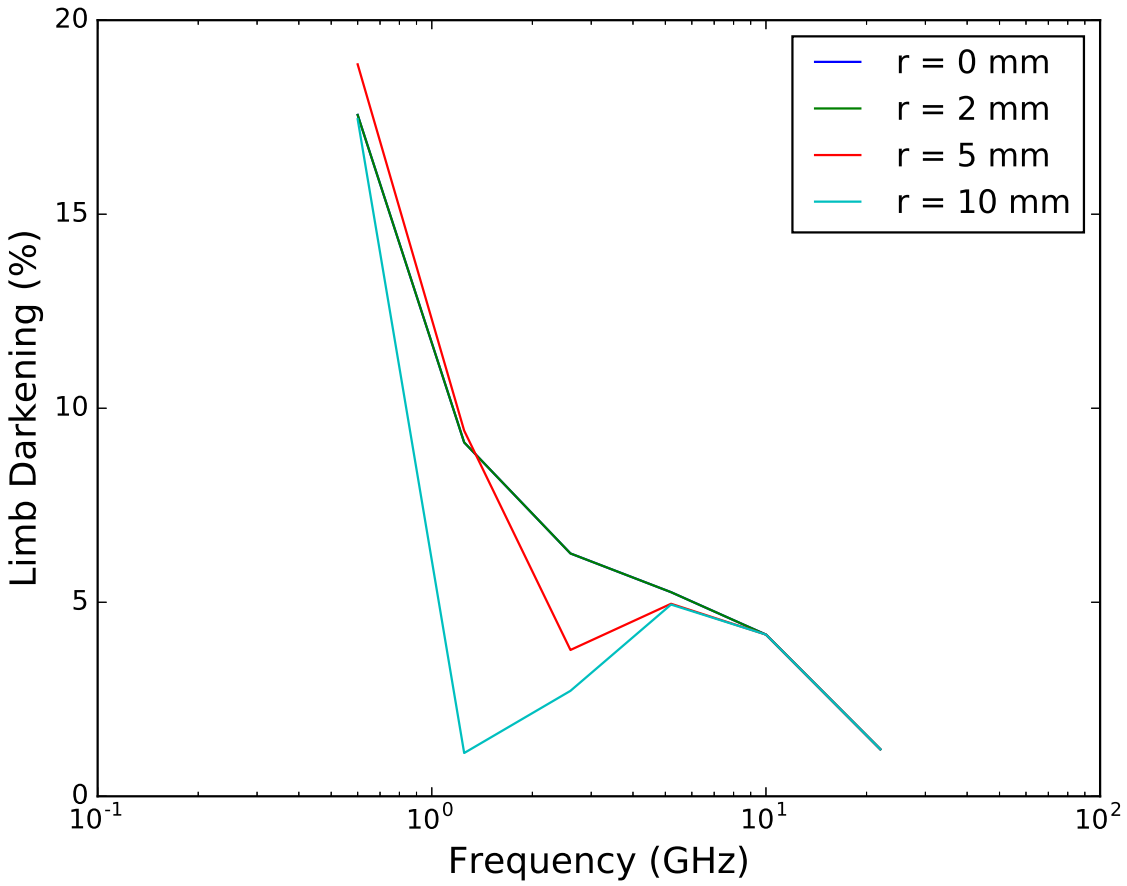

Figure 4.3: Comparison of the simulated 45° limb darkening using the virga model and varying the raindrop density. A well mixed atmosphere with a deep abundance of 2.7x and 4.0x solar for NH_3 and H_2O, respectively, and a raindrop density of 1E3 m^{-3} is used.

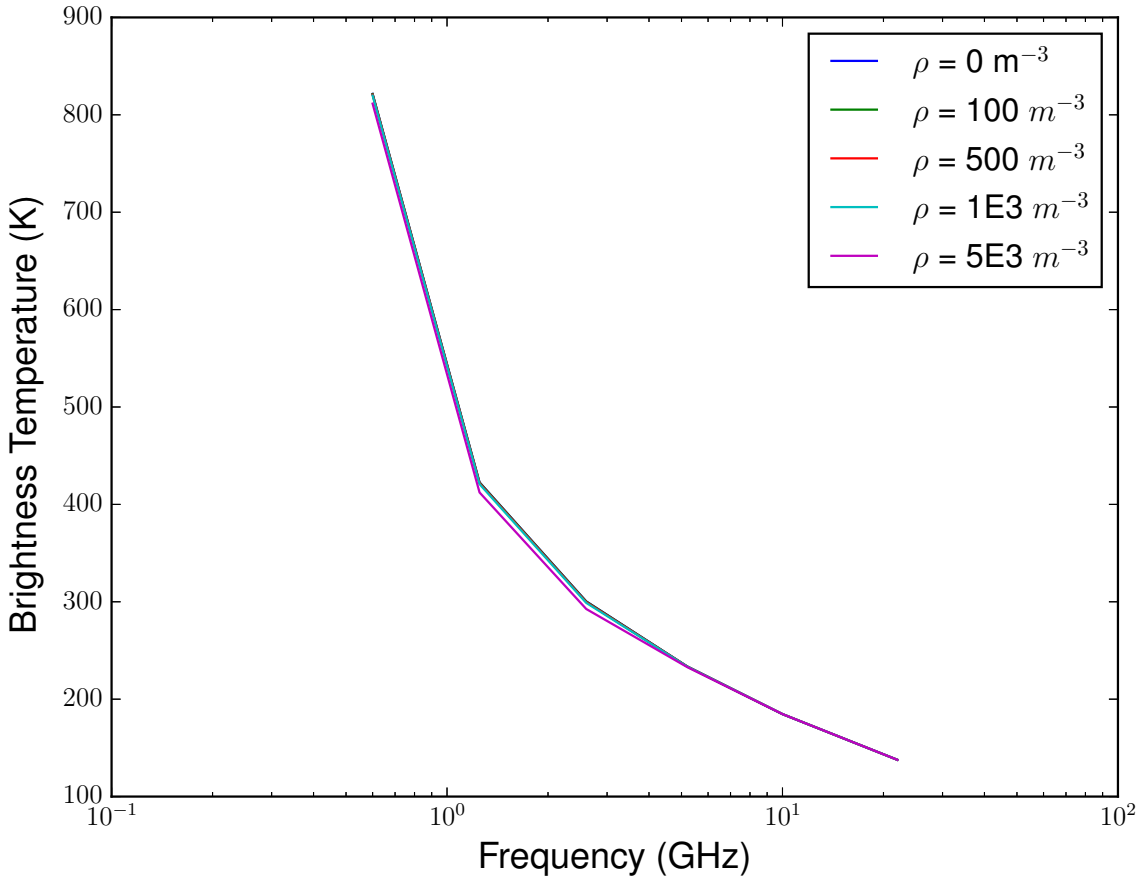

Figure 4.4: Comparison of the simulated nadir microwave brightness temperatures using the virga model and varying the raindrop density. A well mixed atmosphere with a deep abundance of 2.7x and 4.0x solar for NH_3 and H_2O, respectively, and a raindrop diameter of 2mm is used. Note that all of the lines are atop of one another.

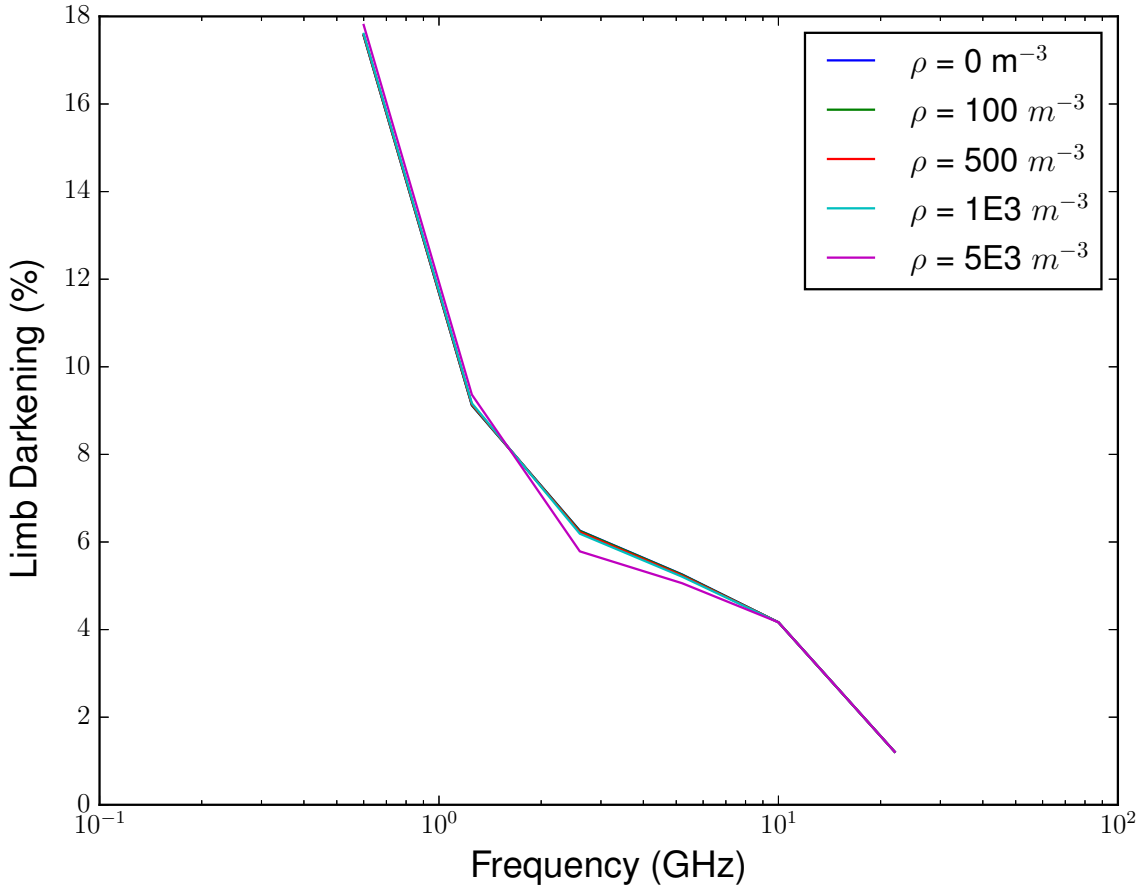

Figure 4.5: Comparison of the simulated 45° limb darkening using the virga model and varying the raindrop density. A well mixed atmosphere with a deep abundance of 2.7x and 4.0x solar for NH_3 and H_2O, respectively, and a raindrop diameter of 2mm is used. Note that all of the lines are atop of one another.

4.4 Radiative Zone

Since the initial work of Hubbard (1968), all models of giant planet interiors assume that the internal energy is transported entirely through convection. Subsequently, Karpowicz and Steffes (2013) improved the equation of state (EOS) for the deep jovian atmosphere so as to better characterize the atmospheric structure, assuming a convective atmosphere. As an alternative, Guillot et al. (1994b) and Guillot et al. (1994a) discuss a potential *radiative* zone that can occur at temperatures near 1300K. This section discusses the theory and structure of this radiative zone as well as its effects on Jupiter's microwave emission as reflected in the Juno MWR data.

According to the Schwarzschild criterion, convection can only occur when

$$\nabla_{rad} > \nabla_{ad} \tag{4.39}$$

where ∇_{rad} and ∇_{ad} are the radiative and adiabatic gradients, respectively, defined by

$$\nabla_{rad} = -\frac{L}{4\pi r^2}\frac{2\rho P}{4acT^4}\left(\frac{dP}{dr}\right)^{-1}\kappa_R \tag{4.40}$$

$$\nabla_{ad} = \left(\frac{d\log T}{d\log P}\right)_S = \frac{P}{T}\frac{dT}{dP} \tag{4.41}$$

where κ_R is the Rosseland mean opacity defined hereafter; P, T, S are the pressure, temperature and entropy respectively; ρ is the atmospheric density, $L = 3.35 \times 10^{17}\ W$ is the internal luminosity, r is the radius, and $ac/4$ is the Stefan-Boltzmann constant.

If the Schwarzschild Criterion is met, heat is transferred through convection (either a wet or dry adiabat), but if not, heat is transferred through radiation. The temperature gradient for the radiative zone is defined by

$$\frac{dT}{dz} = -\frac{3}{4\pi r^2}\frac{L\rho}{16\sigma T^3}\kappa_R \tag{4.42}$$

where, again, T is temperature, κ_R is the Rosseland Opacity, r is radius, L is internal luminosity, ρ is atmospheric density, σ is the Stefan-Boltzmann constant, and dz is the height of the current layer (Kippenhahn et al., 2012).

The Rosseland opacity is calculated by

$$\kappa_R = \left[\frac{\int_0^\infty \frac{1}{\kappa_\sigma} \frac{dB_\sigma}{dT} d\sigma}{\int_0^\infty \frac{dB_\sigma}{dT} d\sigma} \right]^{-1} \tag{4.43}$$

where κ_σ is the monochromatic absorption, B_σ is the Planck function, and σ is the wavenumber, in cm^{-1}. At high densities, the major sources of infrared absorption are collision-induced absorption (CIA) by hydrogen and helium, and the rotovibrational absorption due to H_2O, CH_4, and NH_3. The monochromatic absorption is the sum of these absorbers.

The infrared absorption of H_2O, NH_3, and CH_4 are calculated using a Lorentz lineshape with data from the HITRAN line catalog (Rothman et al., 2013). The Lorentz lineshape is discussed in-depth in Chapter 2. The *HITRAN Application Programming Interface* (HAPI) (Kochanov et al., 2016) is used to calculate the Lorentz profile. The parameters for the Lorentz lineshape under HAPI are pressure, temperature, wavenumber range, and wavenumber cutoff. The first two are determined by the atmospheric model while the third considers all lines from 20–10,000 cm^{-1}. The wavenumber cutoff determines how far each spectral line can affect the spectrum as a whole. For this work the same cutoffs as Guillot et al. (1994b) were used. The cutoffs are 1000 cm^{-1}, 500 cm^{-1}, and 100 cm^{-1} for NH_3, CH_4, and H_2O, respectively.

The collision-induced absorption due to hydrogen and helium is calculated through lookup tables provided by HITRAN (Rothman et al., 2013). These lookup tables are in units of $\text{cm}^5/\text{amagat}^2$ and are ordered primarily, by spectral intervals, and secondly by increasing temperature. The code finds the nearest temperature interval and uses that to calculate the absorption due to CIA.

The effects of this radiative zone on the temperature-pressure profile and Channel 1's

contribution function are shown in Figure 4.6. The radiative zone only occurs deep in the jovian atmosphere (temperatures greater than 1300 K). Table 4.3 shows its effects on the nadir brightness temperatures as well as the 45° limb darkening measurements for all channels.

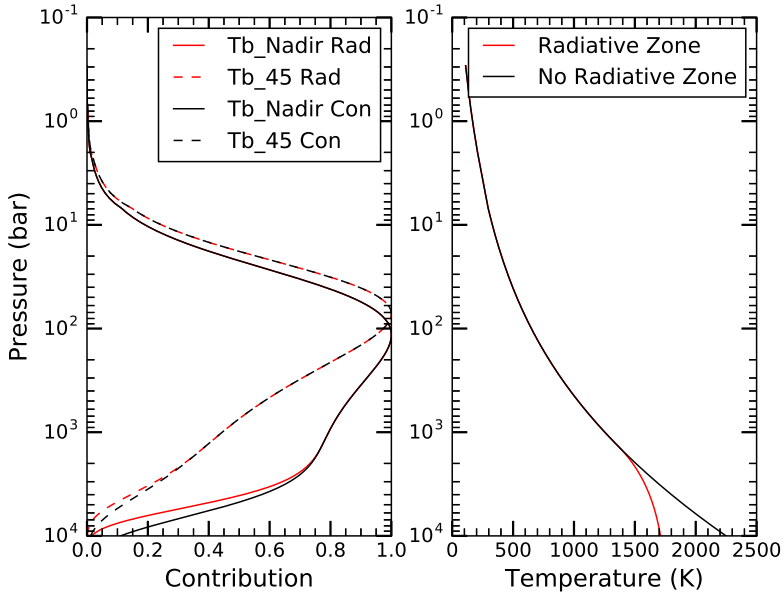

Figure 4.6: The radiative zone's effect on the temperature-pressure profile (right) and Channel 1's contribution function (left). The weighting function is for an atmosphere with NH_3, H_2O deep abundance of 2.7 and 4.0x solar abundance, respectively. The solid line represents the spacecraft pointed at nadir and the dashed line at 45°. The red line is with the inclusion of the radiative zone while the black is a fully convective atmosphere.

Table 4.3: Radiative zone's effects on Juno MWR brightness temperatures assuming a well-mixed atmosphere will a deep abundance of NH_3 and H_2O of 2.7 and 4.0x solar, respectively. The labels Con and Rad are for a fully convective atmosphere and an atmosphere with a radiative zone, respectfully. Also shown is the modeled 45° limb darkening and brightness temperatures for both atmospheres.

	T_b nadir (K)		T_b 45° (K)		45° LD (%)	
Ch	Con	Rad	Con	Rad	Con	Rad
1	**756.80**	**744.19**	**637.11**	**633.69**	**15.82%**	**14.85%**
2	417.90	417.90	380.82	380.82	8.87%	8.87%
3	297.96	297.96	279.28	279.28	6.27%	6.27%
4	231.67	231.67	219.43	219.43	5.27%	5.27%
5	183.05	183.05	175.43	175.43	4.16%	4.16%
6	138.72	138.72	137.17	137.17	1.12%	1.12%

4.5 Ionization of Alkali Metals in the Deep Jovian Atmosphere

In the deep jovian atmosphere where temperatures are very high, it is possible for constituents to ionize and create a cold magnetized plasma. While JAMRT includes an option to calculate the opacity due to the ionization of hydrogen, it does not calculate the opacity due to ionized alkali metals. This section discusses the model used to calculate the opacity due to ionized alkali metals in a jovian atmosphere and its effect on jovian microwave emission and the accompanying Juno MWR measurements. The ionization of these metals creates an intrinsic infrared opacity strong enough to remove the possibility of a radiative zone. As a result, the presence of a radiative zone (described previously) and a deep ionized layer are mutually exclusive (Guillot et al., 2004).

The two most abundant alkali metals in the jovian atmosphere are sodium and potassium (Na and K, respectively). These alkali metals have low ionization energy; 5.14 eV for sodium and 4.33 eV for potassium. Both sodium and potassium primarily react with sulfur at the temperatures as high as 1300K and 1100K, respectively, to form sodium sulfide (Na_2S) and potassium sulfide (K_2S) (Fegley and Lodders, 1994). Since both of these compounds do not ionize at temperatures where they form, this reaction, along with many more described in Fegley and Lodders (1994), depletes the abundance of alkali metals.

Due to the high opacity resulting from ionization, the depletion of alkali metals due to chemical reactions can be simplified by modeling the depletion using a cutoff temperature. This simplified model assumes the alkali metals are present at their deep abundances at altitudes below that of the cutoff temperature. At altitudes above the cutoff level (temperatures lower than the cutoff temperature), the abundance of the alkali metals is set to zero. While this is not a precise calculation, the opacity due to ionization is so high it behaves like a "wall" not allowing the Juno MWR to probe any deeper.

If we assume a solar abundance of sodium (2 ppm) and potassium (0.137 ppm), we can then use the Saha Equation to calculate a free electron density profile. This electron density profile is then used in the Appleton-Hartree equation to calculate the complex refractive index of the cold magnetized plasma. The resulting complex refractive index is used to calculate the absorption due to free electrons. This is then included in the radiative transfer model and used to calculate brightness temperature.

4.5.1 Saha Ionization Equation

The Saha ionization equation relates the ionization state of an element to the ambient temperature and pressure. The equation was originally developed by Saha (1920). For any gas at a high enough temperature, the thermal collisions of the atoms will ionize a fraction of the atoms. When these atoms collide, one of the electrons bound to the atom will be ejected from the atom and form an electron gas that is superimposed with the gas of atomic ions and neutral atoms. This state of matter is called a plasma. The Saha equation describes the degree of ionization of this plasma as a function of temperature, density, and ionization energies of the atoms. This equation is only valid for weakly ionized plasmas where the Coulomb interaction between the ions and elections is negligible.

The Saha equation for a single atomic species can be written as

$$\frac{n_e^2}{n - n_e} = \frac{2}{\lambda^3}\frac{g_1}{g_0}\exp\left[\frac{-\epsilon}{k_B T}\right] \tag{4.44}$$

where n is the number density of a particular atom, n_e is the electron density, g_0 and g_1 are the degeneracy states for the atom, ϵ is the ionization energy, T is the temperature of the gas, k_B is the Boltzmann constant, and λ is the thermal de Broglie wavelength defined as

$$\lambda = \sqrt{\frac{h^2}{2\pi m_e k_B T}} \tag{4.45}$$

where h is Planck's constant and m_e is the electron mass. These physical values can be found in Table 4.4.

By solving the Saha equation from the electron number density, n_e, we can now use the Appleton-Hartree equation to compute the complex refractive index of this plasma.

Table 4.4: Physical values and constants used in the Saha ionization equation.

	Sodium	Potassium	Units
Solar Abundance	2	0.137	ppm
g_0	2	2	
g_1	1	1	
ϵ	5.14	4.33	eV
k_B	8.617×10^{-5}		eV/K
h	4.136×10^{-15}		eV·s
m_e	9.311×10^{-31}		kg

4.5.2 Appleton-Hartree Equation

The Appleton-Hartree equation describes the refractive index for an electromagnetic wave propagating in a cold magnetized plasma. This equation was developed independently by several scientists, but the formulation here is taken from Helliwell (2014). The plasma created by the thermal ionization of alkali metals in the jovian atmosphere can be described as "cold" because the atmosphere is not fully ionized. The same plasma can be considered magnetized due to its location in the jovian atmosphere and the effect of the jovian magnetic field.

The Appleton-Hartree equation can be written as

$$n^2 = 1 - \frac{X}{1 - iZ - \frac{\frac{1}{2}Y^2 \sin^2\theta}{1-X-iZ} \pm \frac{1}{1-X-iZ}\left(\frac{1}{4}Y^4 \sin^4\theta + Y^2\cos^2\theta(1-X-iZ)^2\right)^{1/2}} \tag{4.46}$$

where n is the complex refractive index, θ is the angle between the ambient magnetic field vector and the wave vector; i is $\sqrt{-1}$, and

$$X = \frac{\omega_0^2}{\omega^2} \tag{4.47}$$

$$Y = \frac{\omega_h}{\omega} \tag{4.48}$$

$$Z = \frac{\nu}{\omega} \tag{4.49}$$

where

$$\omega = 2\pi f \quad \text{is the radial frequency,} \tag{4.50}$$

$$\omega_0 = \sqrt{\frac{Ne^2}{\epsilon_0 m}} \quad \text{is the electron plasma frequency,} \tag{4.51}$$

$$\omega_H = \frac{B_0|e|}{m_e} \quad \text{is the electron gyro frequency, and} \tag{4.52}$$

$$\nu = \frac{5}{3}\frac{\pi r^2 P}{k_B T}\sqrt{\frac{3k_b T_e}{m_e}} \quad \text{is the electron collision frequency.} \tag{4.53}$$

in which ϵ_0 is the permittivity of free space, B_0 is the ambient magnetic field, e is the electron charge, m_e is the electron mass, k_b is Boltzmann's constant, r is the average radius of all molecules in the jovian atmosphere, T and T_e, are the ambient and electron temperatures (which are equal in this case), P is the pressure, and N is the electron number density (n_e from the Saha Equation).

The Appleton-Hartree expression is driven by three factors: the plasma frequency, the electron gyro frequency, and the electron collision frequency. Their individual ratios to the radial frequency of the electromagnetic wave also plays an important role. These factors

are presented by the X, Y, and Z terms, respectively. The X term is controlled primarily through the electron density; this term also drives the real part of the refractive index. The Y term is controlled by the magnetic field strength and is scaled by the angle between the magnetic field and the electromagnetic wave (Θ). Finally, the Z term is controlled by the density of the surrounding atmosphere; this term also drives the imaginary part of the refractive index and the absorption. The more dense the surrounding atmosphere, the more microwave opaque the plasma is. This is due to the collision between the neural atmosphere and the electrons.

Also present in the Appleton-Hartree equation is the $\pm$ sign. This gives two separate solutions for the refractive index that represent two different propagation modes relative to the magnetic field. In the case of ionization of alkali metals in the deep jovian atmosphere, the Y term and the $\pm$ sign can be ignored because $Y << Z$, allowing equation 4.46 to be simplified to

$$n^2 = 1 - \frac{X}{1 - iZ} \tag{4.54}$$

4.5.3 Absorption and the Effect on Juno MWR Measurements

From the calculated complex refractive index, n, the loss tangent can be calculated by

$$\tan\delta = \frac{2\Re(n)\Im(n)}{\Re(n)^2 - \Im(n)^2} \tag{4.55}$$

where $\Re(n)$ is the real part of the refractive index and $\Im(n)$ is the imaginary. Since the loss tangent is much less than unity, the absorption coefficient can be calculated by (Hanley, 2008)

$$\alpha = 8.686\frac{\pi}{\lambda}\tan\delta \tag{4.56}$$

where λ is the wavelength in km and 8.686 converts α into dB/km.

The absorption due to the ionization of alkali metals, gaseous NH_3, and water vapor at 600 MHz as a function of altitude (represented as temperature) is shown in Figure 4.7. Ta-

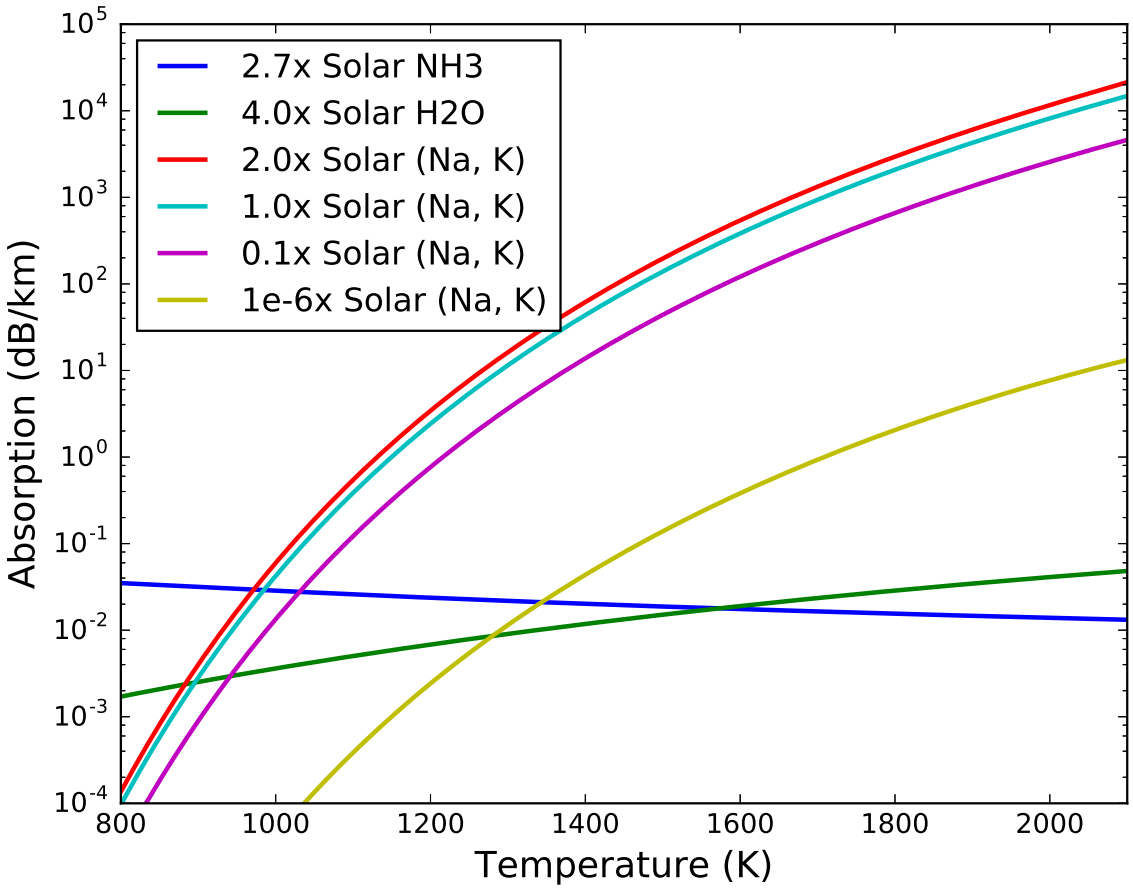

Figure 4.7: Comparison of the 0.6 GHz microwave absorption of 2.7 x solar abundance of NH_3, 4.0 x solar abundance of H_2O, and 2.0, 1.0, 0.1, and 1e-6x solar abundance of ionizing alkali metals, Na and K.

ble 4.5 shows the effects of various alkali abundances on the modeled Channel 1 brightness temperature and 45° limb darkening. Surprisingly, the brightness temperature is not significantly affected by the abundance of alkali metals, the alkali solar abundance drops to 1e-6x solar abundance. This is due to the high opacity of nearly any ionized layer, in comparison to NH_3 and H_2O opacities, producing a "wall" of opacity. Channel 1's brightness temperature and limb darkening are instead controlled by the cutoff temperature determining the altitude at which the alkali metals are depleted, shown in Table 4.6.

Table 4.5: Effects of various alkali abundances on Channel 1 brightness temperature and 45° Limb Darkening. The values here assume a well mixed atmosphere with a deep abundance of 2.7x Solar NH_3 and 4.0x Solar H_2O using a cutoff temperature of 1300K.

Alkali Abundance	T_b Nadir (K)	T_b 45° (K)	45° LD (%)
2.0	732.28	634.78	13.31
1.0	732.48	634.84	13.33
0.1	733.72	635.26	13.42
1e-6	760.44	645.41	15.13
0.0	784.98	653.72	16.72

Table 4.6: Effects of various cutoff temperatures on Channel 1 brightness temperature and 45° Limb Darkening. The values here assume a well mixed atmosphere with a deep abundance of 2.7x Solar NH_3, 4.0x Solar H_2O, and 1.0x Solar alkali metals.

Cutoff Temperature (K)	T_b Nadir (K)	T_b 45° (K)	45° LD (%)
1200	720.80	629.24	12.70
1300	732.48	634.84	13.33
1400	744.08	639.86	14.01
1500	754.39	643.97	14.64
1600	762.79	647.07	15.17
1800	775.06	651.10	15.99
2000	782.44	653.13	16.53

4.6 Auroral Effects on the Jovian Microwave Emission Measured by Juno MWR

As Juno's orbits precess, their perijoves will move farther north and begin to better map the polar regions. While the deep atmospheric composition and dynamics in these regions is largely unknown, the presence of an aurora is well known (Clarke et al., 2002). To properly understand the neutral atmosphere in the polar regions, the aurora, and their effects on the Juno MWR data, modeling has been conducted. An aurora is light emission produced by the impact of any external energetic particles with a planet's atmosphere (Chamberlain and Hunten, 1987). This section will describe the aurora, its potential to effect the jovian microwave emission measured by Juno MWR, and the properties needed to properly model its potential effect on the Juno MWR data using a radiative transfer model.

Jupiter's aurora is one hundred times more energetic, and has ten times higher surface brightness than Earth's. The aurora can be split into three regions: the main ovals, the satellites' auroral footprints, and the transient polar emissions situated within the main ovals, all shown in Figure 4.8. These different regions are physically separated from each other and vary independently, suggesting the presence of independent processes.

The main ovals are bright, narrow, continuous, circular features located approximately 15° from both poles. The ovals are very narrow and very bright, with an overall width of $\approx$ 100-500 km and a brightness exceeding 100 kiloRayleigh (kR) in the UV and visible regions. (One rayleigh (1 R) is defined as a column emission rate of 10^{10} photons per square meter per columns per second.) The physical origins of these emissions are related to both the nature of the precipitating particles and their location. Observations of the emission altitude and UV emission spectra indicate that electrons spanning energy ranges up to many tens of keV are the dominate component (Ajello et al., 1998). Since the UV emission lines from sulfur and oxygen ions, and Doppler shifted H Lyα emission characteristic of fast precipitating protons, have not been observed (Waite et al., 1988; Clarke et al., 1989; Rego et al., 1999), there are a limited number of primary particles other than electrons in the

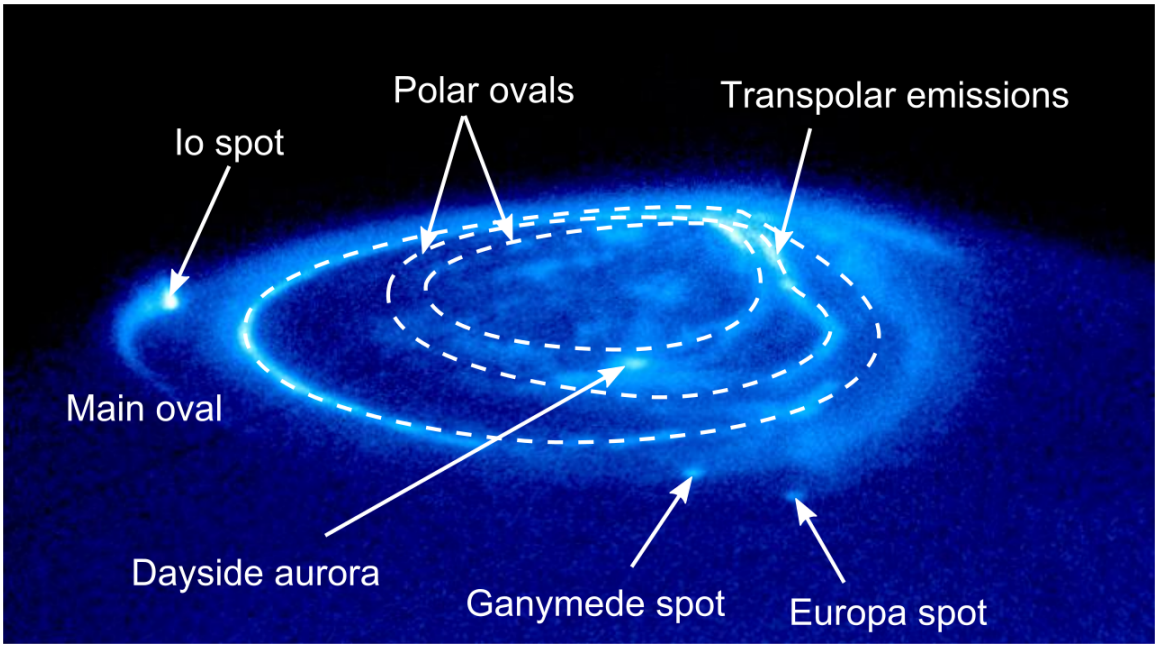

Figure 4.8: Jupiter's northern aurora in November 1998 taken by the Hubble Space Telescope. The main auroral oval and polar ovals are marked with dashed lines. Satellite footprints and other features are shown (Based on Pallier and Prangé (2001)).

main auroral oval. If only electrons exist in the main auroral oval, the plasma density (as described in equation 4.51) would differ when compared to other auroral regions affecting the auroral oval's complex refractive index.

The satellites' auroral footprints correspond to the magnetic field lines connecting Jupiter's ionosphere to its largest moons: Io, Europa, and Ganymede (Clarke et al., 2002). The footprints develop due to the corotation of the plasma slowing down in the vicinity of the moons. The brightest spot belongs to Io, the main source of plasma in the magnetosphere. Europa and Ganymede's footprints are much dimmer because these moons are weaker plasma sources (Blanc et al., 2005).

Bright spots and arcs sporadically appear within the main ovals and create transient polar emissions. These emissions vary independently and much more rapidly than both the satellite footprints and the main oval emissions. These transient phenomena are believed to be related to interaction with the solar wind. The polar aurora emissions are similar to those observed around Earth's poles: both appear when electrons are accelerated towards

the planet during reconnection of the solar magnetic field with that of the planet's (Blanc et al., 2005). This region emits auroral X-rays consisting of spectral lines of highly ionized oxygen and sulfur created by highly energetic (hundreds of keV) S and O ions precipitating into the polar atmosphere of Jupiter (Elsner et al., 2005).

Properly modeling the effect of Jupiter's aurora on the Juno MWR data requires knowledge of three physical properties: the temperature-pressure profile, the charged particle density profile, and the charged particle energy profile. The lack of direct measurements and inaccuracy of models provides a large uncertainty in any model used and is a hindrance to understanding the effects on the MWR data. From coarse estimates of these three properties, the complex refractive index as a function of altitude and the absorption profile can be calculated using the Appleton-Hartree Equation (discussed in depth in Chapter 4.5.2). Using the estimated temperature-pressure profile, the calculated complex refractive index profile, and calculated the absorption profile, a radiative transfer with ray tracing can be calculated using the method described in Chapter 2.2.

It is important to note that when the electron density is above 10^9 cm^3 the aurora exhibits significant backscatter at longer centimeter-wavelengths, reflecting the cosmic background or synchrotron radiation to Channel 1 of the Juno MWR. While this can effect all MWR channels, the electron density would need to be unphysically large to effect the higher frequency channels. This reflection can be modeled by using the Fresnel equations, which for a non-magnetic media is:

$$R_s = \left| \frac{n_1 \cos\theta_i - n_2 \sqrt{1 - \left(\frac{n_1}{n_2}\sin\theta_i\right)^2}}{n_1 \cos\theta_i + n_2 \sqrt{1 - \left(\frac{n_1}{n_2}\sin\theta_i\right)^2}} \right|^2 \tag{4.57}$$

$$R_p = \left| \frac{n_1 \sqrt{1 - \left(\frac{n_1}{n_2}\sin\theta_i\right)^2} - n_2 \cos\theta_i}{n_1 \sqrt{1 - \left(\frac{n_1}{n_2}\sin\theta_i\right)^2} + n_2 \cos\theta_i} \right|^2 \tag{4.58}$$

$$R = \frac{1}{2}\left(R_s + R_p\right) \tag{4.59}$$

where R_s, R_p, and R is the reflectance for s-polarized light, the reflectance for p-polarized light, and the reflectance for unpolarized light, respectively. n_x is the complex refractive index for layer x, and θ_i is the incident angle of the electromagnetic wave between the interface of layer x and layer $x + 1$. The aurora can be considered a non-magnetic media because its relative permeability is unity, $\mu_r = 1$.

Since auroral emissions are strongest at lower frequencies, it was not thought that modeling of auroral emissions as seen by the Juno MWR (600MHz – 22GHz) would be necessary. However, during Perijove 5 an anomaly in emission, shown later in this work, was seen at latitudes greater than 45°N, coinciding with the presence of the northern aurora. This anomaly appeared as a decrease in brightness temperatures in channels 1–3 followed by an increase in brightness temperatures at higher latitudes. In future work, this analysis will be used to begin examining this anomaly.

CHAPTER 5

USE OF NEURAL NETWORKS IN RETRIEVAL OF CONSTITUENT PROFILES FROM JUNO MWR DATA

Machine learning is the subfield of computer science that studies a computer's ability to learn without being explicitly programmed (Samuel, 2000). Evolving from pattern recognition and artificial intelligence, machine learning involves algorithms that can learn and make predictions on data. Machine learning can be split into three paradigms: Supervised, Unsupervised, and Reinforcement learning (Russell and Norvig, 2002). In supervised learning the computer is presented with example inputs and outputs with the goal of generating a function that maps the inputs to the outputs. Conversely, in unsupervised learning, no outputs are given, leaving the algorithm to find its own structure in the inputs. Finally, in reinforcement learning, the computer algorithm interacts with a dynamic environment where it must achieve a certain goal. The algorithm is provided feedback in terms of rewards and punishments as it navigates the problem space; attempting to avoid punishments and gather rewards. While the later two learning paradigms are important to the study of machine learning, supervised learning is the main focus of this work.

Machine learning can also be categorized into five groups based on the desired output of the algorithm: classification, regression, clustering, density estimation, and dimensionality reduction (Russell and Norvig, 2002). In classification, the inputs are divided into two or more classes with the goal of producing a model that correctly classifies unseen inputs into one or more of these classes. Classification algorithms are usually trained using supervised learning. Also a supervised learning problem, regression algorithms have the goal of estimating the relationship between the inputs and continuous outputs. Similar to classification, clustering algorithms are given a set of inputs to be divided into groups. However, the groups are not known beforehand making this an unsupervised task. Density estima-

tion is used to find the distribution of inputs in some sample space. Finally, dimensionality reduction simplifies inputs by mapping them to a lower-dimensional space.

5.1 Supervised Learning

Supervised learning is the machine learning task of inferring a function from a set of training examples. In supervised learning, each example consists of an input object, typically a vector, and a desired output value. The algorithm analyzes the training data and produces an inferred function used to map new examples. The algorithm must be able to generalize from the training data to unseen situations. Supervised learning can be thought of as a "teacher" that provides continuous feedback on the quality of the solutions.

5.1.1 Steps to Solve Supervised Learning Problems

Supervised learning is used to solve a given problem by following six steps (Vapnik, 2013):

1. **Determine the type of training examples.**

   The type of training example depends on the scope of the problem being solved. For the example of handwriting analysis, the scope maybe a single character, a word, or the entire line. For this work, the training data used was the six brightness temperatures associated with a range of possible jovian atmospheres.

2. **Gather together a training set.**

   The data gathered should be representative of the realistic problem space of the function. This work uses modeled brightness temperatures from JAMRT as a training set. It is also important to split the training data into three groups: training, testing and validation. The details of this split are discussed later in this work.

3. **Determine the necessary input feature representation for the learned function.**

   The accuracy of the learned function depends on the input representation. The input is transformed into a feature vector that contains a number of features that are

descriptive of the object. The number of features should not be too large but should contain enough information to properly predict the output.

4. **Determine the structure of the learned function.**

   Choose which learning algorithm best maps the input data to the outputs, and determine the structure of the algorithm. In the case of neural networks, the structure is characterized by the number of inputs, the number of hidden layers, the number of outputs, and the learning rate, discussed later in this chapter.

5. **Complete the design.**

   Execute the learning algorithm on the training data set using the validation data set as a limiting condition. This allows the learning algorithm to stop before over-fitting the data.

6. **Evaluate the accuracy of the learned function.**

   After training, the performance of the learned function should be measured on the testing set. This serves to estimate how well the function will perform on data it has never encountered.

A wide range of supervised learning algorithms are available, each having strengths and weaknesses. The following section describes the main algorithm used in the retrieval of ammonia and water vapor abundance profiles from the Juno MWR data, the artificial neural network. Since no single learning algorithm works best on all supervised learning problems, it is important to understand the limitations of each type of algorithm.

5.1.2 Critical Issues in Algorithm Training

While training a supervised learning algorithm may seem like a trivial task, there are many critical issues that need to be understood. There are no concrete rules available to solve these issues, but some "rules of thumb" are listed to help in navigating these pitfalls.

The first of these pitfalls, the bias-variance tradeoff, is the problem of simultaneously minimizing two sources of error, preventing the algorithm from generalizing beyond its training set. The bias of a function is the error arising from assumptions made in the learning algorithm's structure. The variance of a function is the error caused by small fluctuations in the training set. A learned function must balance these two sources of error to prevent underfitting (high bias) or overfitting (high variance) (James, 2003). This issue can be mitigated by minimizing each error individually. The bias can be reduced by giving the function more information in the form of input features, model structure, or changing the model all together. The variance can be reduced by including more training data and ensuring the training data is representative of the whole domain (Blackwell and Chen, 2009).

The second potential issue is the relationship between the "true" function's complexity and the amount of training data. If the true function is simple, a high bias, low variance learning function will be able to learn the true function using a small data set. Inversely if the true function is complex the learning function must have a low bias and high variance with a very large amount of training data (Blackwell and Chen, 2009).

The third consideration is the dimensionality of the input space. A high dimensional input feature vector can increase the complexity of the learning problem. This is especially true if the true function only depends on a subset of those features. The extra dimensions can "confuse" the learning algorithm thus raising its variance. Usually, the user can manually remove the irrelevant features and improve the accuracy of the learning function. Additionally, the user may utilize a feature selection algorithm which identifies the relevant features and removes the irrelevant ones. More generally the user can implement a strategy of dimensionality reduction where the complex high-dimensional input data is mapped to a lower-dimensional space before running the learning algorithm (Blackwell and Chen, 2009). Similarly to the dimensionality of the input space, the quality of the input data can affect the accuracy of the learned model. Heterogeneity in the training data can affect the

accuracy of the learned model. To fix this the input features are all scaled to similar ranges (e.g [-1,1] or [0,1]).

One final risk is the overfitting of the function to the data. Overfitting occurs when the algorithm "memorizes" the training data and does not generalize to new inputs. Overfitting can occur when noise is present in the training data. If the training data is incorrect due to sensor error or human error, the learning algorithm should not fit the function exactly to the training examples. Doing so will result in overfitting the data. It is also possible to overfit when there are no measurement errors, if the true function is too complex for the learning model. In either situation the algorithm attempts to fit the target function to the portion of the true function that cannot be modeled (e.g. noise). Neural networks have the ability to deal with each of these issues individually. To deal with noise in the training data, the training algorithm has the ability to stop when the errors in the validation set stop improving, avoiding overfitting. The complexity issue can be resolved by adding either more hidden layers or more hidden nodes. For neural networks, the complexity of the trained model is determined by the amount of hidden layers or nodes (Brodley and Friedl, 1999).

While the pitfalls listed here are not exhaustive they do give a good overview of the issues that can occur in any machine learning problem. Recognizing and avoiding these helps with minimizing or avoiding unwanted side-effects.

5.1.3 How Supervised Learning Algorithms Work

Given a set of N training examples in the form

$$(x_1, y_1), \ldots, (x_N, y_N) \tag{5.1}$$

where x_i is the feature vector of the i^{th} example and y_i is the corresponding output, or label. The learning algorithm develops a function

$$g : X \rightarrow Y \tag{5.2}$$

where X is the input space and Y is the output space. The function g is an element of some space of possible functions, G, called the hypothesis space. It is convenient to characterize g using a scoring function (Vapnik, 2013)

$$f : X \times Y \rightarrow \mathbb{R} \tag{5.3}$$

where g returns the y value that gives the highest score:

$$g(x) = \underset{y}{\operatorname{argmax}} \ \ f(x, y) \tag{5.4}$$

and f is a scoring function in the space of all scoring functions, F.

There are two basic approaches for choosing f and g: empirical risk minimization and structural risk minimization. Empirical risk minimization seeks the function that best fits the training data. Structural risk minimization adds a penalty function controlling the bias-variance tradeoff (Vapnik, 2013). Both cases assume the training set consists of a sample of independent and identically distributed pairs, (x_i, y_i). A loss, or cost, function L is used to measure how well a function fits the training data, L is defined as

$$L : Y \times Y \rightarrow \mathbb{R}^{\geq 0} \tag{5.5}$$

where $\mathbb{R}^{\geq 0}$ is the space of real numbers with a dimension greater than or equal to zero. For the i^{th} training example the loss of predicting the value y_i' is $L(y_i, y_i')$. The risk, $R(g)$, of

function g is defined as the expected loss of g and estimated by

$$R_{est}(g) = \frac{1}{N} \sum_{i} L(y_i, g(x_i)) \tag{5.6}$$

In empirical risk minimization, the supervised learning algorithm seeks the function g that minimizes $R(g)$. The supervised learning algorithm is constructed by applying an optimization algorithm to find g. If G contains many candidate functions or the training set is not large enough, empirical risk minimization leads to high variance and poor generalization. In this case, the learning algorithm is able to memorize the training examples, but cannot generalize well, resulting in overfitting (Vapnik, 2013).

Conversely, structural risk minimization seeks to prevent overfitting by applying a regularization penalty into the optimization. This regularization penalty, $C(g)$, forces the supervised learning algorithm to prefer simpler functions over more complex ones. The form of $C(g)$ depends on the function g. The supervised learning algorithm finds the function g which minimizes

$$J(g) = R_{est}(g) + \lambda C(g) \tag{5.7}$$

where λ controls the bias-variance trade off. When $\lambda = 0$, $J(g)$ becomes the empirical risk minimization with low bias and high variance. When λ is large, the supervised learning algorithm will have high bias and low variance. λ can be treated as a free parameter and part of the algorithm's structure (Vapnik, 2013).

Neural networks use the mean-squared error loss function to minimize the average squared error between the network's output, $g(x)$, and the target value y over all training examples. Minimizing this cost using gradient descent produces the backpropagation algorithm which will be discussed later Section 5.2.3. Through minimizing the cost function associated with the neural network, the risk function also becomes minimized.

5.2 Neural Network

Neural networks are computational structures that are inspired by the densely connected neurons in the human brain. In this work, artificial neural networks are used as a surrogate model, emulating the complex non-linearity of JAMRT. This section will briefly describe neural networks and their developments, following is an explanation of the neuron, network topology, and different types of neural networks. A discussion on the training, backpropagation, and using neural networks as surrogate models will follow.

Neural networks are based on a collection of connected units called neurons, represented mathematically as a real number, usually between 0 and 1. The connection between these neurons are called synapses and have a weight attached to them which strengthen or dampen the signal sent forward to other neurons. The neurons are organized in multiple layers where each layer applies a transformation function on their inputs. The signal travels from the first layer (input layer) to the last layer (output layer) while possibly traversing hidden layers multiple times.

Originally the goal of a neural network was the solve problems in the same way as the human brain (Haykin et al., 2009). Over time the focus turned to matching abilities leading to deviations on the training of these networks, such as backpropagation. Just like their biological counterparts, neural networks are able to learn and mold themselves to the presented training data. Neural networks can be used to learn and compute functions for which the analytical relationships between inputs and outputs are unknown or computationally complex. Through their activation function, they can also model the non-linear relationship between two data sets using linear methods, improving computation time (Haykin et al., 2009)

The human brain has been studied for many years, but the neuron in the brain was extensively studied and originally published by Hebb (1949). Hebb (1949) pointed out that neural pathways are strengthened each time they are used. This method of training,

Hebbian learning, led to the original neural networks with just an input and an output layer. While these neural networks could learn to solve the "or" and "and" problems, it was shown that they could not solve the "xor" problem. In the 1980s, Rumelhart et al. (1986) published his work on using backpropagation in relationship to neural networks. This work solved the biggest problem in Hebbian learning, the ability to train a neural network with multiple layers. With the addition of a hidden layer, the neural network utilizes it to find features within the data and allows other layers to operate on those features rather than noisy data. Backpropagation allows the "blame" for the network error to be distributed between neurons.

While there are multiple types of neural networks most of them can be encapsulated into three groups: Feed Forward, Radial Basis Function, and Recurrent neural networks (Haykin et al., 2009). Feed forward neural networks are the simplest types, usually containing multiple layers. Feed forward neural networks use mathematical functions that are continuous and differentiable, which simplifies training and error analysis. Also in the feed forward neural network group are convolutional neural networks, which are designed to respond to variations in a restricted region of the data. Radial Basis Function (RBF) neural networks uses the hidden layer to transform the data to the RBF space and the output layer operates in this non-linear space. Both feed forward and RBF neural networks propagate the data only forward. Recurrent Neural Networks (RNN) have the ability to propagate the data forward and backwards. RNN have long short-term memory that allow the network to process arbitrary series of inputs to model dynamic, temporal behavior. The remainder of this section will focus on feed forward neural networks due to their flexibility, simplicity, and ease of use.

5.2.1 Neuron

The basic element in a feed forward neural network is the neuron. The n inputs to a neuron are weighted, summed and passed through an activation function. The transfer function

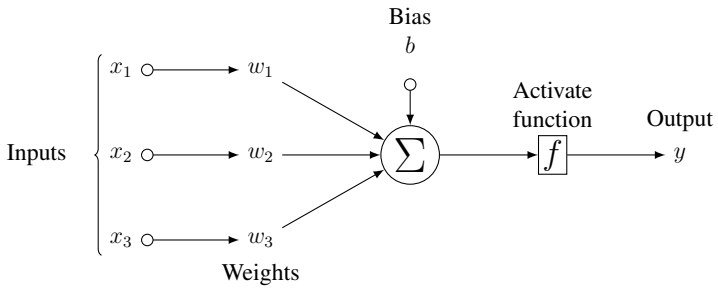

Figure 5.1: A schematic drawing of a neuron

can be written as:

$$y = f\left(\sum_{i=1}^{n} w_i x_i + b\right) \tag{5.8}$$

where y is the neuron output, b is its bias, f is the activation function, and w_i and x_i is the i^{th} element in the neurons weighting vector and input vector, respectively (Blackwell and Chen, 2009). A schematic drawing of a neuron with three inputs is shown in Figure 5.1. Activation functions are generally chosen to be strictly increasing, smooth, and asymptotic (Blackwell and Chen, 2009). The typical activation function used is the logistic function:

$$f(x) = \frac{1}{1 - e^{-x}} \tag{5.9}$$

However, to speed up learning when using backpropagation the hyperbolic tangent function is used:

$$f(x) = \tanh(x) = \frac{e^{x} - e^{-x}}{e^{x} + e^{-x}} \tag{5.10}$$

The activation function can be thought of as a filter that determines when the neuron "fires". While more complicated networks can require more complicated activation functions, the hyperbolic tangent is sufficient for this work.

5.2.2 Topology

The range of functions approximated by a neural network is determined by its topology. Network topology is determined by the number of inputs, the number of hidden layers, and

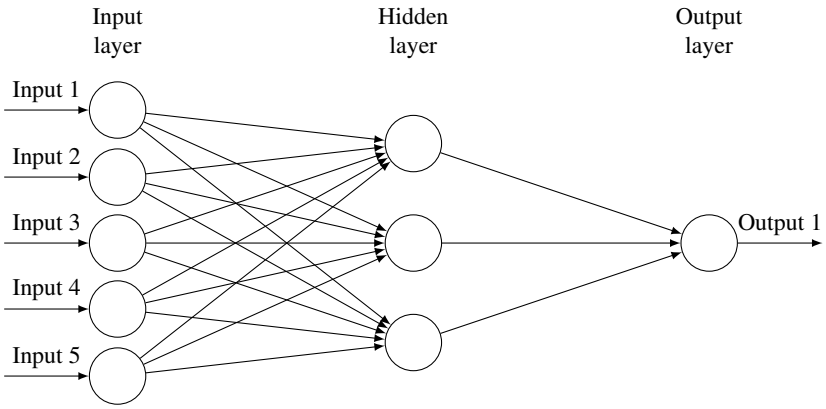

Figure 5.2: A 5-3-1 feed forward neural network with 5 input nodes, 3 hidden nodes, and 1 output node

the number of outputs. One of the surrogate JAMRT model described later in this work uses a network topology of "13-45-45-45-6". The first number is the number of inputs, NH_3 deep abundance, H_2O deep abundance, look angle, and 10 ammonia scale points. The middle numbers represent the number of hidden neurons in that particular layer, in this case three hidden layers with 45 neurons each. The final number is the number of outputs, the brightness temperatures of the six channels. Figure 5.2 shows the topology of a "5-3-1" feed forward neural network.

5.2.3 Training and Backpropagation

Neural Network training (or learning) involves adjusting the neuron weights (w_i in Equation 5.8) in a systemic way to properly minimize the networks cost function. Backpropagation is the method used to calculate the gradient of the cost function with respect to weights in an artificial neural network. The motivation behind the development of this algorithm is to train a multilayered neural network such that it can learn to map any arbitrary set of inputs to outputs. The core of the backpropagation algorithm is the computation of the partial derivative, $\frac{\partial E}{\partial w}$. Where E is the cost function and w is any weight in the neural network.

The cost function maps the value of one or more variables onto a real number repre-

senting the "cost" of a particular event. In the case of backpropagation the cost function calculates the difference between the network output and its expected output for an input example propagated through the network. Two assumptions are made about the cost function to ensure backpropagation will work (Nielsen, 2015). The first is that the cost function can be written as a function of the neural network outputs. The second assumption is that the cost function can be written as an average over multiple cost functions

$$E = \frac{1}{n} \sum_{x} E_x \tag{5.11}$$

This assumption ensures the gradient of the error function calculated by the backpropagation algorithm for a single training example can be generalized to the overall function. The standard choice for a cost function is

$$E(y, y') = \frac{1}{2} ||y - y'||_2^2 \tag{5.12}$$

where y is the target output and y' is the neural network output (Blackwell and Chen, 2009). This measures the square of the Euclidean distance between both vectors, also known as the L-2 norm. The error function over n training examples can be written as an average

$$E = \frac{1}{2n} \sum_{i} ||y_i - y_i'||_2^2 \tag{5.13}$$

Backpropagation can be divided into two phases: propagation and weight update (Haykin et al., 2009). The propagation phase involves two step: forward propagation and backward propagation. In forward propagation, an input vector is propagated through the neural network in order to generate the networks output, y'. In backwards propagation the target vector y is propagated backwards through the network in order to generate the deltas $(y - y')$ for all output and hidden neuron synapses.

The second phase is applied to each weight in the network. The weight's output delta

and input activation function are multiplied to find the gradient of the cost function with respect to the weight, $\frac{\partial E}{\partial w}$. Afterwards, a percentage of the weight's gradient is subtracted from the weight. The percentage, known as the learning rate, determines the speed and quality of the learning. The greater the learning rate the faster the network is trained. However, the smaller the rate, the more accurate is the resulting training.

Phases 1 and 2 are repeated for each data point in the training set consecutively. Afterwards, the validation set is propagated through the network and the total cost is stored. This is repeated until the performance of the network is satisfactory, or as in the case of early stopping, the validation set's cost function stops improving. Finally, the testing set is propagated through the network and the predicted values are used to calculate the network's estimated error.

5.2.4 Neural Networks as Surrogate Models

Numerous computational tasks can benefit from a significant acceleration in their calculations. Here we will present a method for utilizing neural networks as surrogates to the complex radiative transfer model used in interpreting Juno MWR data; providing an accurate prediction in a fraction of the time. This method does not remove the need of a full radiative transfer model. Instead, the surrogate is trained to mimic a subdomain of the results from the radiative transfer model. Once trained the surrogate model is able to quickly and accurately predict results from the radiative transfer model (Bandler et al., 2004). The radiative transfer model used in this work is the Jupiter Atmospheric Microwave Radiative Transfer (JAMRT) code, described in Section 4.1. Many types of machine learning algorithms can be used as surrogates; however, neural network surrogates handle the radiative transfer code best.

Surrogates have a history of use in oceanography and meteorology, allowing a greater understanding of their benefits and drawbacks. An effective surrogate must provide fast evaluations with low computational and memory requirements. Due to the neural network

structure, the surrogate function is capable of dealing with significant non-linearities in the chosen subdomain. The surrogate must also mimic the properties of the full radiative transfer code for all state variables of interest. Finally, it must be trainable from the radiative transfer code simulations. The surrogate model cannot properly mimic the radiative transfer code outside of the given subdomain (Merwe et al., 2007).

The motivation behind this work is to successfully retrieve ammonia and water vapor abundance profiles using data from the Juno MWR. To do this an optimization problem is formulated such that the error between our modeled and measured brightness temperatures is minimized. By using a surrogate instead of JAMRT to model the brightness temperatures in the given subdomain, a significant reduction in the retrieval time will be observed making possible the study of a much broader range of solutions. The subdomain is determined by the training data used in the generation of the surrogate and is described in depth in the next section.

5.3 Training Data

The most fundamental element of any machine learning method is the assembly and organization of the data sets from which the statistical relationships are derived and evaluated. The most complex and well-constructed learning algorithms cannot overcome flaws in the data set on which they operate. The most useful data sets are accurate, comprehensive, and extensive. The absence of any of these attributes severely undermines the overall effectiveness and applicability of the resulting neural network. Poor data sets can lead to poor network generalization.

The phrase “garbage in, garbage out” best explains this issue in the context of machine learning. Inaccuracies, such as noise, present in the data directly effect the quality of the neural network, particularly the flexibility and generalization of the network. Both of these can be improved by ensuring the training data are both extensive and comprehensive. This requires that the entire dynamic range of the input and target space (extensive) and all

relevant feature sets (comprehensive) are included.

The data sets are used in various stages of the neural network training process: adjusting the weights, early stopping, and performance analysis. While it would be convenient to use one data set for all of these tasks, such an approach would lead to poor generalization and overfitting. This is best demonstrated by the bias-variance tradeoff. The bias is the degree to which the model best fits data it has already seen. The variance refers to the deviation of the network learning performance from one data sample to another, as described by the same model. The optimal estimator minimizes both of these jointly, requiring that at least two separate data sets be used to train the neural network: one to evaluate the bias (performance on only the training data) and one to evaluate the variance (performance on a separate data set). Typically a third data set is used to evaluate the ability of the trained network to effectively generalize given unseen inputs.

The terminology for these three data sets are training set, validation set, and testing set. The training set is used to optimize the network weights and biases. The validation set is used to determine when to terminate the training process, to evaluate model complexity, and to evaluate multiple training runs. Finally, the testing set is used to assess the generalization of the network.

The best strategy for reducing both the error bias and the variance is to maximize the amount of training data and to use the simplest network topology required to achieve the desired performance. Given an abundance of data, a 60-20-20 split is often used to construct the training, validation, testing set respectively. However, in this work a 56-24-20 split was used to minimize the computational cost in the training.

5.3.1 Training data generation

The data set usually used in machine learning is measured from actual in-situ data. However, in the case of jovian atmospheric emission this is not possible. Thus the training data needs to be generated using accurate models of the jovian atmosphere. In the jovian atmo-

sphere, turbulence and convection will efficiently reduce the spatial gradient of ammonia concentration below the ammonia cloud layer because ammonia has no major sources or sinks below the cloud. Therefore, accurate models of the jovian atmosphere will converge on a homogenized atmosphere (well mixed) where the ammonia concentration at every level should be less than or equal to the ammonia concentration in an ideal adiabatic profile. An exception would occur in the presence of reevaporation of precipitation. Ignoring such regions keeps the model simple and reduces the amount of data needed to properly train the neural network.

The ammonia abundance profile can be represented as the state vector

$$X = (x_1, x_2, \ldots x_n)^T, 0 \leq x_i \leq 1 \tag{5.14}$$

where x_i is the ammonia scaling factor at pressure level p_i, and n is the number of ammonia scaling factors. The ammonia concentration at pressure p_i is

$$q(p_i) = x_i \times q^*(p_i) \tag{5.15}$$

where $q(p_i)$ is the ammonia concentration at pressure p_i, and $q^*(p_i)$ is the ammonia concentration of an ideal adiabat at pressure p_i. The scaling factor x at any pressure p is given by the linear interpolation of x_i and x_{i+1} with respect to p_i and p_{i+1}. Also important is the pressure level p_{n+1}, where the atmosphere returns to an ideal adiabat. At that pressure level (known as the "anchor" point), the scaling factor is unity ($x_{n+1} = 1.0$). An example of an ideal adiabat and scaled ammonia abundance along with the location of the scaling factors and anchor point is shown in Figure 5.3.

Another factor important in the jovian atmosphere is the presence of an ionized layer due to alkali metals, discussed in depth in Chapter 4.5. The specific abundance of alkali metals, when above 1x solar, has little effect on the modeled brightness temperature. However, the cutoff temperature (which affects the altitude of the ionized layer) does effect

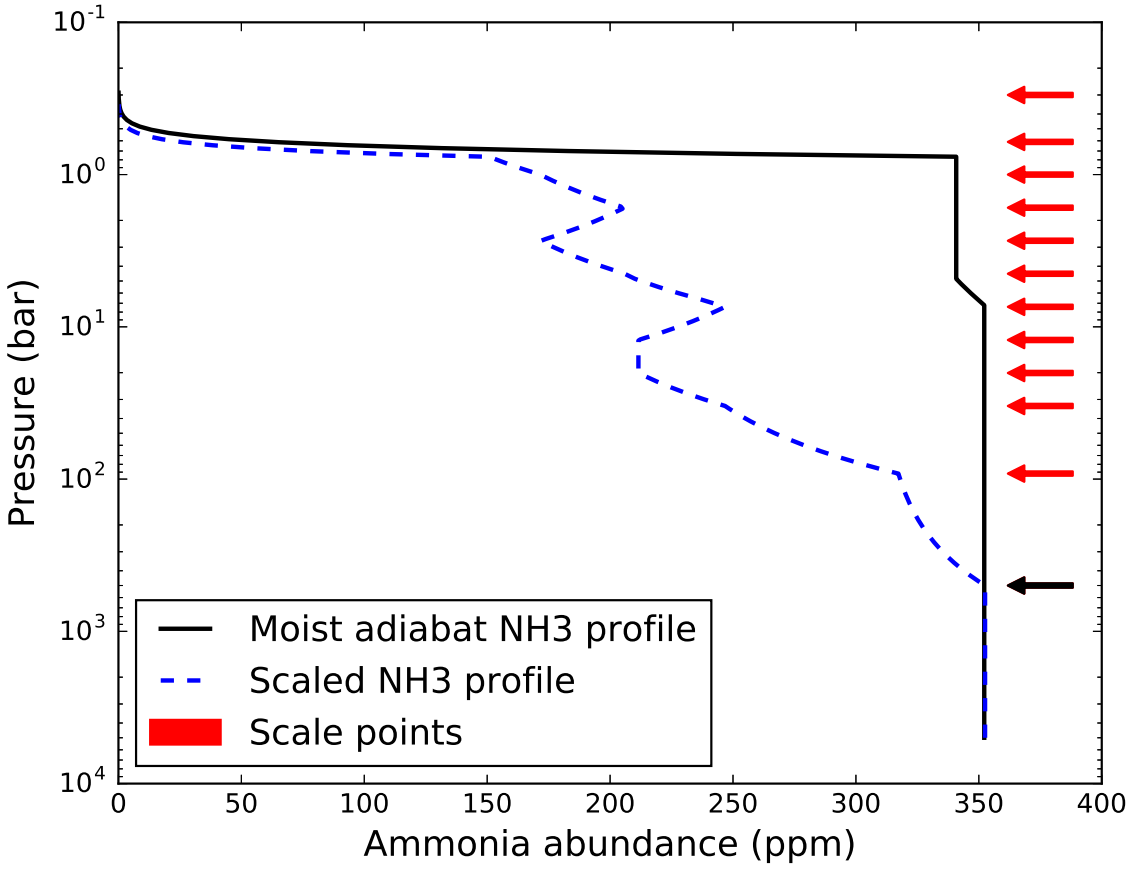

Figure 5.3: The visual representation of the scaling of the ammonia abundance profile. The solid black line is the ideal adiabat distribution of ammonia for a deep ammonia abundance of 2.7x solar (352 ppm) and the blue dashed line is the scaled version. The red arrows show the location of the scaling points, and the black arrow shows the "anchor" point.

the modeled brightness temperature. This simplifies the domain that needs to be generated to ensure the neural network can properly model the effects of an ionized layer on the brightness temperature. The state vector for this thus becomes

$$T_c = (T_{c,1}, T_{c,2}, \ldots, T_{c,k})^T \tag{5.16}$$

where $T_{c,i}$ is the temperature where the abundance of alkali metals goes to zero, and k is the number of cutoff temperatures in the subdomain.

There are three feature spaces shared by all subdomains encapsulated in the surrogate model: deep ammonia abundance, deep water vapor abundance, and look angle. The deep ammonia abundances spans from 1.5–2.8x solar (195–365 ppm), the deep water abundances spans from 1–11x solar (948–10,325 ppm), and the look angle spans from 0–45°.

Two subdomains are used in this work: the first only includes the scaling of ammonia at 10 pressure levels: 33.1, 20.1, 12.2, 7.39, 4.48, 2.72, 1.65, 1.0, 0.61, and 0.30 bars, with an anchor point at 92.0 bars. The second includes the scaling of ammonia concentration at 11 pressure levels: 92.0, 33.1, 20.1, 12.2, 7.39, 4.48, 2.72, 1.65, 1.0, 0.61, and 0.30 bars, with an anchor point at 500.0 bars. The second subdomain also includes the effects of ionized alkali metals with 5 cutoff temperatures: 1300, 1400, 1500, 1600, 2000 K. The PACE cluster at Georgia Tech is used to parallelize the data generation, but this still takes a significant amount of time, ≈12 days for the second subdomain. Table 5.1 shows a list of both subdomains and their free parameters. For a given subdomain, the state vector (or input vector) of a training example is the combination of a single element in the first three columns followed by a scaling value for each pressure level. For subdomain 2 this is followed by a cutoff temperature. For example, in subdomain 1 an input vector would be

$$x_i = (1.5, 1.0, 0, 1.0, 1.0, 1.0, 1.0, 1.0, 1.0, 1.0, 1.0, 1.0, 1.0)^T \tag{5.17}$$

where x_i is the i^{th} training example, the first number is the NH_3 deep abundance, the

Table 5.1: List of all subdomains and their free parameters. For a given subdomain the state vector of a training example is the combination of a single element in each column. Deep abundances are scale factors relative to the solar abundances of the two constituents.

Subdomain	Deep Abundance		Look	Scaling Points		Cutoff
	NH_3	H_2O	Angles (°)	Scales	Pressures (bars)	Temperature (K)
1	1.5, 1.6 1.7, 1.8 1.9, 2.0 2.1, 2.2 2.3, 2.4 2.5, 2.6 2.7	1.0 3.0 7.0 11.0	0 10 20 30 40 45	1.0 0.9 0.8 0.7 0.6 0.5 0.4 0.3 0.2	33.1, 20.1, 12.2, 7.39, 4.48 2.72, 1.65, 1.00, 0.61, 0.30	N\A
2					92.0, 33.1 20.1, 12.2 7.39, 4.48 2.72, 1.65 1.00, 0.61 0.30	1300 1400 1500 1600 2000

second is the H_2O deep abundance, the third is the look angle, and the remainder are the scaling factors for the 10 pressure levels. In this example the modeled atmosphere would be identical to an ideal adiabat with deep abundances of NH_3 and H_2O being 1.5x and 1.0x solar, respectively.

5.3.2 Surrogate Neural Network Accuracy

The accuracy of a neural network is related to the complexity of the problem and the number of training points. The increasing complexity of a problem can be resolved by introducing a more complex network topology along with more training points. For the first subdomain a neural network topology of "13-45-45-45-6" was determined, through trial-and-error, to suitably map the 13 inputs to the 6 brightness temperatures. To accompany this topology, the number of data points used in the training of this network is 9,300,096. By including another scaling point and the effects of ionized alkali metals in the deep atmosphere the complexity of the second domain increased significantly. This increased complexity in the second subdomain required a neural network topology of "15-50-50-50-6" to suitably map the 15 inputs to the 6 brightness temperatures. It also requires 90,848,160 data points to properly train the network. Table 5.2 shows the size and split of the data sets, along with

Table 5.2: Size and split of data sets used to train the neural network surrogate for each subdomain. Also shown is the neural network topology chosen for each subdomain.

Subdomain	Topology	Training Set	Validation Set	Testing set	Total
1	"13-45-45-45-6"	5,952,061	1,488,015	1,860,020	9,300,096
2	"15-50-50-50-6"	50,874,970	21,803,558	18,168,634	90,848,160

the network topology used to train the neural network surrogate for each subdomain.

While speed is the primary benefit of using a surrogate model as a replacement for JAMRT, accuracy determines how successful the surrogate model is. Neural network accuracy is typically characterized by the mean and standard deviation of the errors, specifically the errors in the testing set. The error of a network is calculated as a percent error when compared to the expected value,

$$E_i = \frac{|y_i' - y_i|}{y_i} \times 100\% \tag{5.18}$$

where for the i^{th} data point, E_i is the percent error, y_i' is the neural network output, and y_i is the expected output. These errors are then averaged together to produce the mean percent error (MPE). The standard deviation of the errors, called standard error (SE), provides information as to the spread of the errors. A neural network is considered "correct" if the MPE is close to zero and the SE is small. Figures 5.4 and 5.5 show the histograms of the errors in computed brightness temperatures for the testing set in each subdomain. Table 5.3 shows a tabulated mean and standard deviation of these errors.

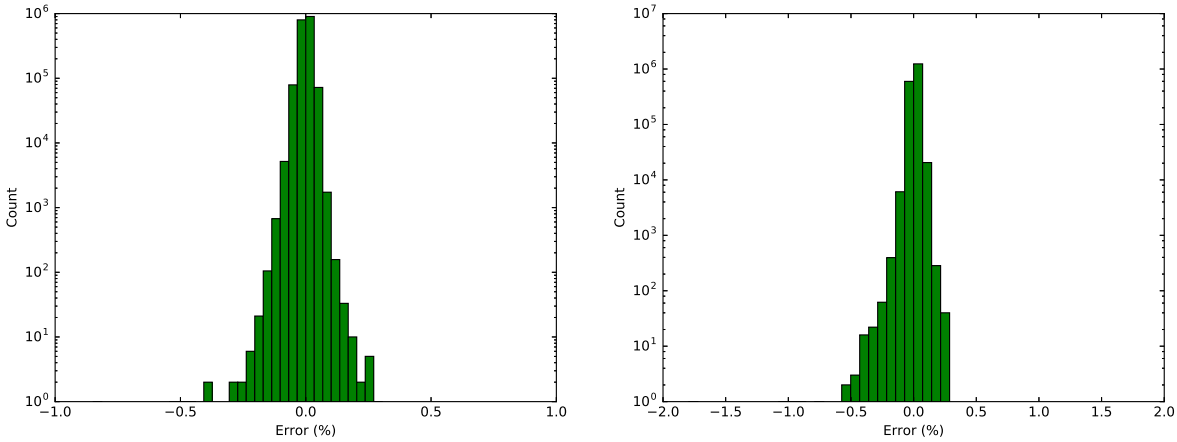

(a) Channel 1

(b) Channel 2

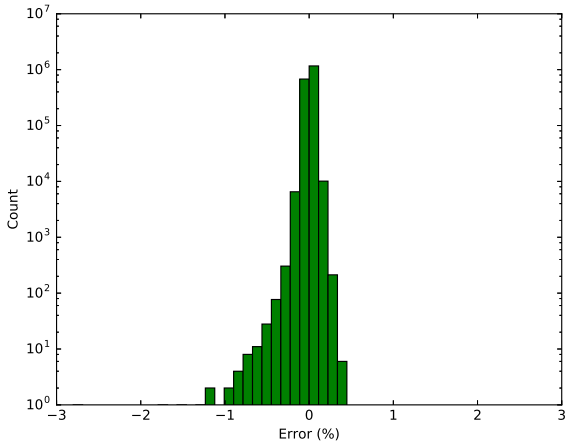

(c) Channel 3

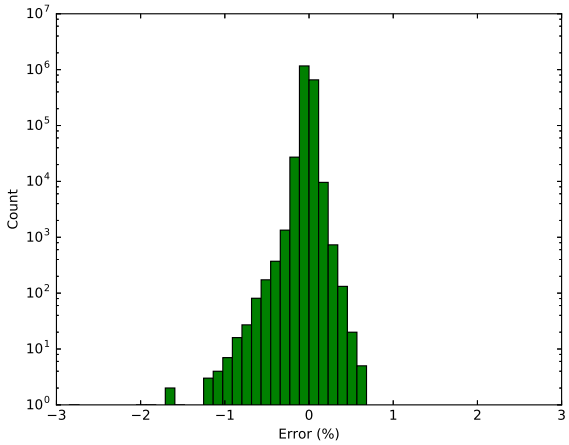

(d) Channel 4

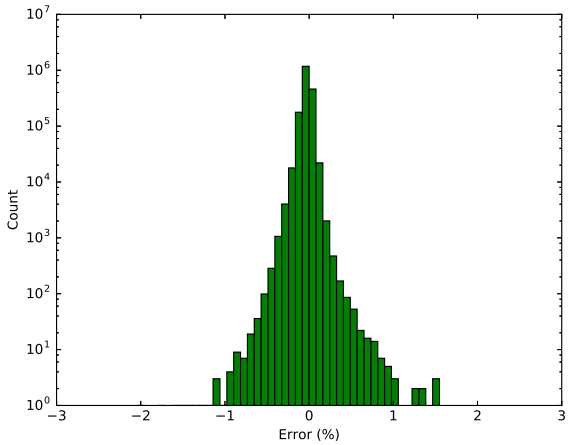

(e) Channel 5

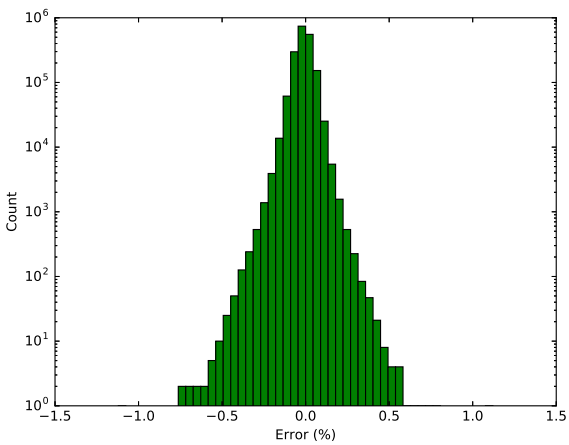

(f) Channel 6

Figure 5.4: Histogram of the percent errors in the testing set for each channel in subdomain 1. The neural network used for this surrogate has a topology of "13-45-45-6".

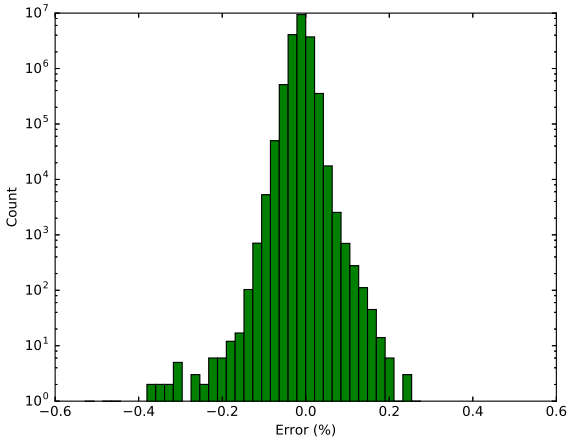

(a) Channel 1

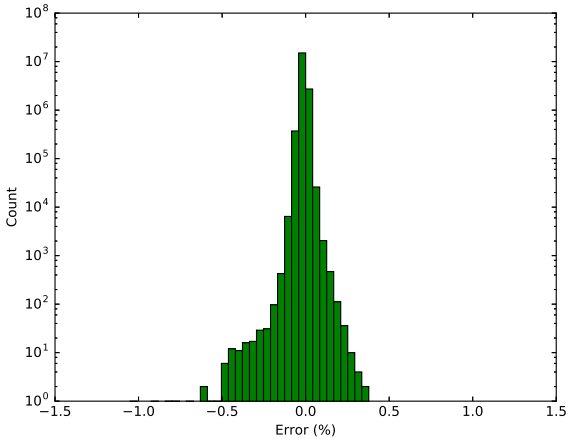

(b) Channel 2

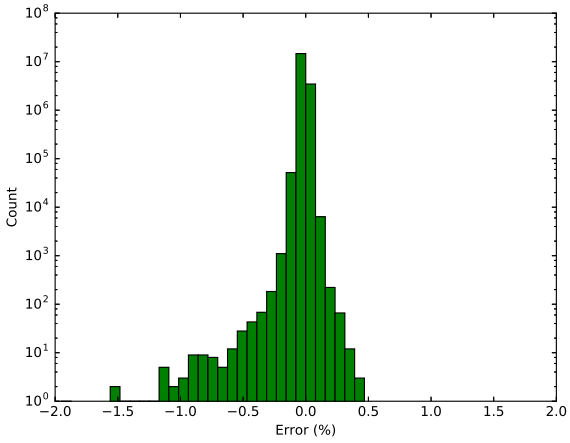

(c) Channel 3

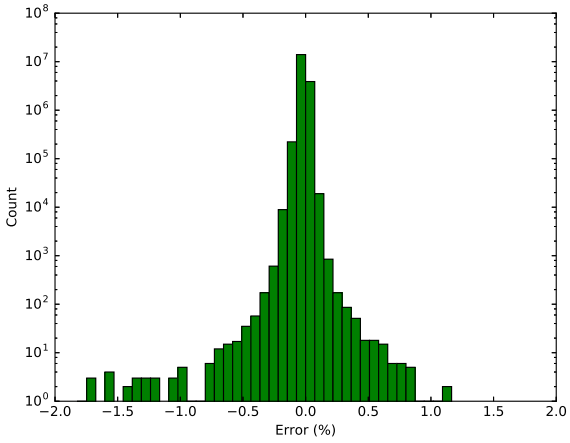

(d) Channel 4

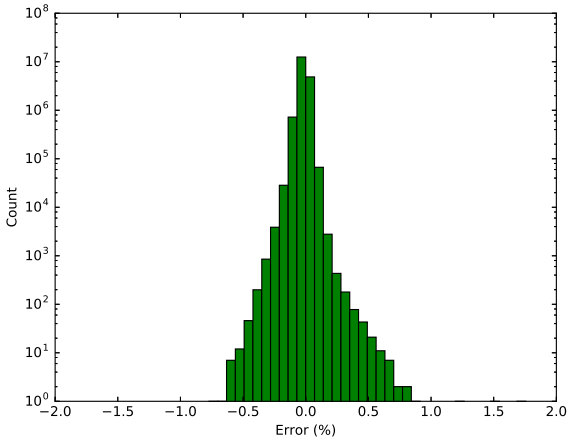

(e) Channel 5

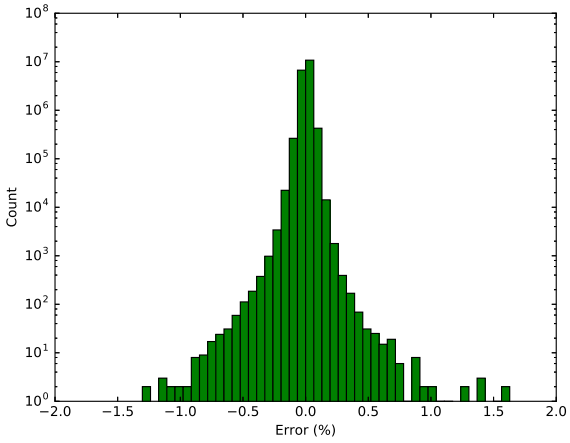

(f) Channel 6

Figure 5.5: Histogram of the percent errors in the testing set for each channel in subdomain 2. The neural network used for this surrogate has a topology of "15-50-50-50-6".

Table 5.3: Mean error and standard deviation for the error in the training set for each channel in each subdomain.

Channel	Subdomain 1		Subdomain 2	
	Mean (%)	Standard Deviation (%)	Mean (%)	Standard Deviation (%)
1	-0.002	0.017	-0.011	0.016
2	0.008	0.024	-0.013	0.014
3	0.001	0.037	-0.014	0.018
4	-0.001	0.048	-0.016	0.023
5	-0.002	0.056	-0.017	0.030
6	0.005	0.063	0.007	0.030

Part III

Results

CHAPTER 6

JUNO MICROWAVE RADIOMETER DATA

The Microwave Radiometer (MWR) instrument onboard the NASA Juno Mission provides unprecedented microwave observations of the thermal emission from Jupiter. The Juno MWR contains 6 channels at frequencies of: 600 MHz (50 cm), 1.248 GHz (24 cm), 2.597 GHz (11.7cm), 5.215 GHz (5.7 cm), 10.004 GHz (3.0 cm), and 21.9 GHz (1.36 cm) (Janssen et al., 2017a). At the publication of this thesis Juno has completed 8 highly elliptical orbits around Jupiter during which microwave radiometer data was taken, with perijoves between 3500–4300 km above the 1 bar pressure level (Shown in Table 1.1). This viewing geometry allows for the Juno MWR to view the thermal emission from Jupiter while avoiding contamination from the synchrotron radiation belts. As the spacecraft moves through each perijove, spinning twice per minute, the Juno MWR scans Jupiter along the subspacecraft track, and observes each latitude over a range of emission angles.

The Juno MWR measures the thermal emission of Jupiter's atmosphere at six wavelengths and multiple emission angles. Due to the finite beam size of the antenna, the measured antenna temperature is a convolution of the antenna gain pattern with the brightness temperature field of the planet, plus calibration error and random instrument noise. Therefore, to intercompare the Juno MWR measurements and the results from the forward model, beam deconvolution is necessary. Beam deconvolution of the antenna brightness temperature was performed by Fabiano Oyafuso at NASA Jet Propulsion Labs and has been included in this work. By using two of the deconvolved brightness temperature observations, one at nadir and the other at 45° emission angle, limb darkening can be computed using

$$LD = 100 \times \frac{T_{b,nadir} - T_{b,limb}}{T_{b,nadir}} \ \ (\%) \tag{6.1}$$

where $T_{b,nadir}$ is the deconvolved nadir brightness temperature and $T_{b,limb}$ is the deconvolved 45° brightness temperature. Because of its polar orbit, the Juno spacecraft makes two measurements of the range of look angles at any given latitude, once when the latitude being observed is in front of the spacecraft (fore), and once when the latitude being observed is behind the spacecraft (aft). The fore and aft antenna temperature measurements can differ due to the planet's rotation, but this effect can be removed through the MWR tilt orbit.

This chapter will show the measured antenna temperatures as a function of emission angle, the deconvolved nadir brightness temperature, and the 45° limb darkening all as a function of latitude for each perijove, with a brief discussion of features and points of interest. Following this a discussion of the measurements taken of the Perijove 5 auroral anomaly, and the Great Red Spot.

6.1 Common Features

There are three specific features in the brightness temperature spectrum common to all perijoves. For this analysis of common features it is useful to define an ideal adiabatic atmosphere. The ideal adiabatic atmosphere behaves as a dry adiabat up to the base of the water cloud. The condensation of water releases latent heat, and the temperature profile becomes a moist adiabat within the cloud. Further up, the moist adiabatic temperature profile gradually approaches that from a dry adiabat, but becomes a moist adiabat again at the base of the ammonia cloud. Figure 6.1 shows this temperature-pressure curve with the moist and dry adiabats differentiated. Thus, the temperature-pressure profile depends on both the deep water vapor abundance and the ammonia abundance. The measured brightness temperatures depend mostly on the ammonia abundance, since ammonia is the main opacity source at microwave frequencies. If we anchor the atmospheric temperature profile to a measured value at 0.5 bar, a lower brightness temperature implies a higher ammonia abundance and vice versa.

The first of the common features is the low brightness temperature occurring in a narrow zone at the equator. Elsewhere, the Juno MWR observations show an excess of brightness temperature from an ideal adiabatic model, suggesting a global depletion of ammonia gas relative to the deep abundance. This is consistent with Very Large Array (VLA) observations (de Pater and Massie, 1985; de Pater et al., 2001; de Pater et al., 2016) made from earth. The depth probed by the VLA observations is limited to a few bars due to synchrotron radiation in the foreground blocking observations at longer wavelengths. The Juno MWR observations show that such depletion is much deeper than any pre-Juno expectations, persisting below 60 bars. This discovery challenges the current understanding of Jovian atmospheric dynamics since ammonia condenses around 0.7 bar and has no known sources or sinks in the atmosphere deeper than the water cloud base. The cause of this deep level depletion is still unknown.

The second prominent feature common in the spectra is the positive brightness temperature anomaly in the North Equatorial Belt (NEB) at 10–20°N in all channels, which can be interpreted as the result of a significantly lower concentration of ammonia. The high brightness temperatures from the NEB in channels 5 and 6 are consistent with ground-based observations at other wavelengths (Bjoraker et al., 2015; Fletcher et al., 2016). The largest part of this anomaly begins on the southern side of the NEB at shallow depths, and gradually shifts to the northern side of the NEB at greater depths. This changing slope with depth was not expected nor observed before. The NEB and South Equatorial Belt (SEB) look similar in visible images and infrared images at 5 μm (Orton et al., 2017). However, they are very different in the microwave regime. A positive brightness temperature anomaly in the NEB is seen on all 6 channels, while the brightness temperature anomaly in the SEB is only seen in channels 5 and 6. The brightness temperature anomaly seen in the NEB when compared to the SEB produces a large unexpected north-south asymmetry. Since this high temperature anomaly in the SEB is not as prominent on all perijoves it is not focused upon here.

Table 6.1: Figure numbers pertaining to each perijove for Antenna Temperature, Brightness Temperature, and 45° Limb Darkening presented in this chapter.

Perijove	Antenna Temperature						Brightness Temperature	45° Limb Darkening
	Ch 1	Ch 2	Ch 3	Ch 4	Ch 5	Ch 6		
1	6.3	6.4	6.5	6.6	6.7	6.8	6.9	6.10
3	6.11	6.12	6.13	6.14	6.15	6.16	6.17	6.18
4	6.19	6.20	6.21	6.22	6.23	6.24	6.25	6.26
5	6.27	6.28	6.29	6.30	6.31	6.32	6.33	6.34
6	6.35	6.36	6.37	6.38	6.39	6.40	6.41	6.42
7	6.43	6.44	6.45	6.46	6.47	6.48	6.49	6.50
8	6.51	6.52	6.53	6.54	6.55	6.56	6.57	6.58
9	6.59	6.60	6.61	6.62	6.63	6.64	6.65	6.66

The third feature common to all perijoves is the uniform brightness temperatures measured at higher latitudes. Over all perijoves measured thus far, save for the perijove 5 auroral anomaly and synchrotron contamination, the deconvolved brightness temperatures at latitudes above 30° are consistent between all perijoves for channels 1, 2, 3, and 4. For channels 5 and 6, the deconvolved brightness temperatures at latitudes above 50° are consistent between all perijoves. This is best illustrated by plotting the deconvolved brightness temperatures for all perijoves atop of one another as shown in Figure 6.2. This feature allows us to split the atmosphere into two regions, the weather and climate region. The weather region is the regions of the atmosphere where channels 5 and 6 probe (pressure less than 5 bars), while the climate region is the area where channels 1, 2, 3, and 4 probe (pressures greater than 5 bars).

Shown in the remainder of this section are the measured antenna temperatures, deconvolved brightness temperatures, and 45° limb darkening for all perijoves. These are shown as a function of planetocentric latitude in the range from 60°N to 60°S. The measured antenna temperatures are also shown as a function of emission angles from 0–50°. A table of each perijove and its associated figures can be found in Table 6.1.

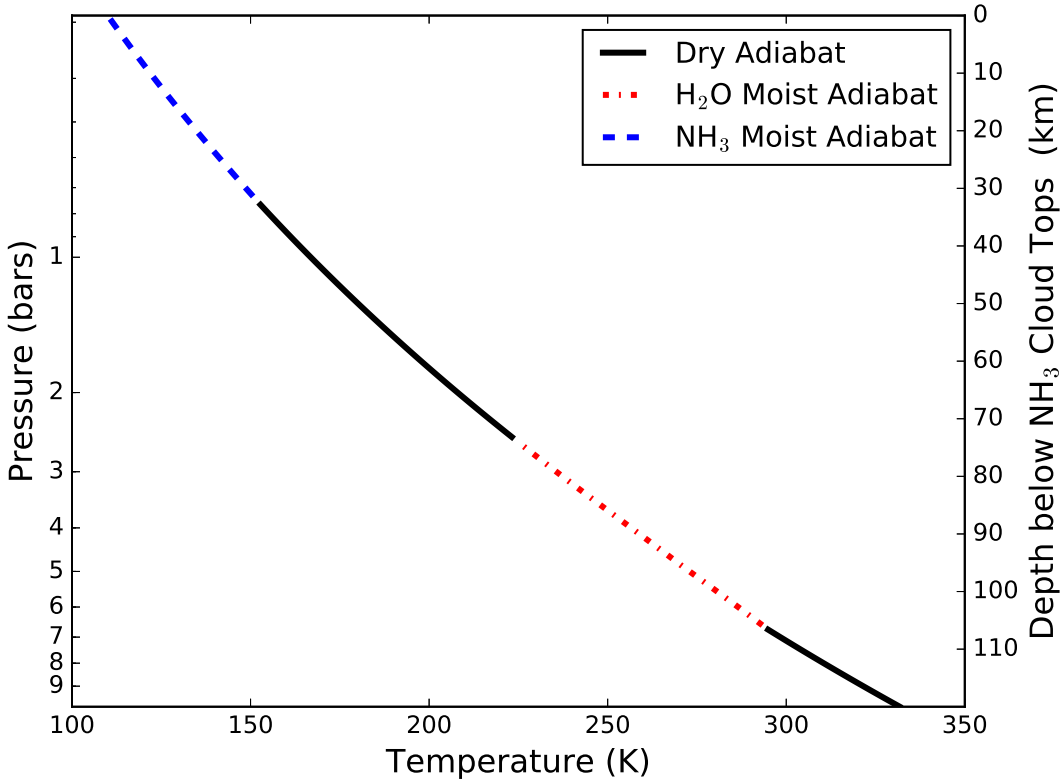

Figure 6.1: Jovian temperature-pressure profile assuming a NH_3 deep abundance of 2.7x solar and a H_2O deep abundance of 4.0x solar. The profile is segmented into three parts: the solid black line represents the portion of the atmosphere where the temperature profile is a dry adiabat, the red dot dashed line represents the portion of the atmosphere where the temperature profile is moist due to the water cloud, and the blue dashed line represents the portion of the atmosphere where the temperature profile is moist due to the ammonia cloud.

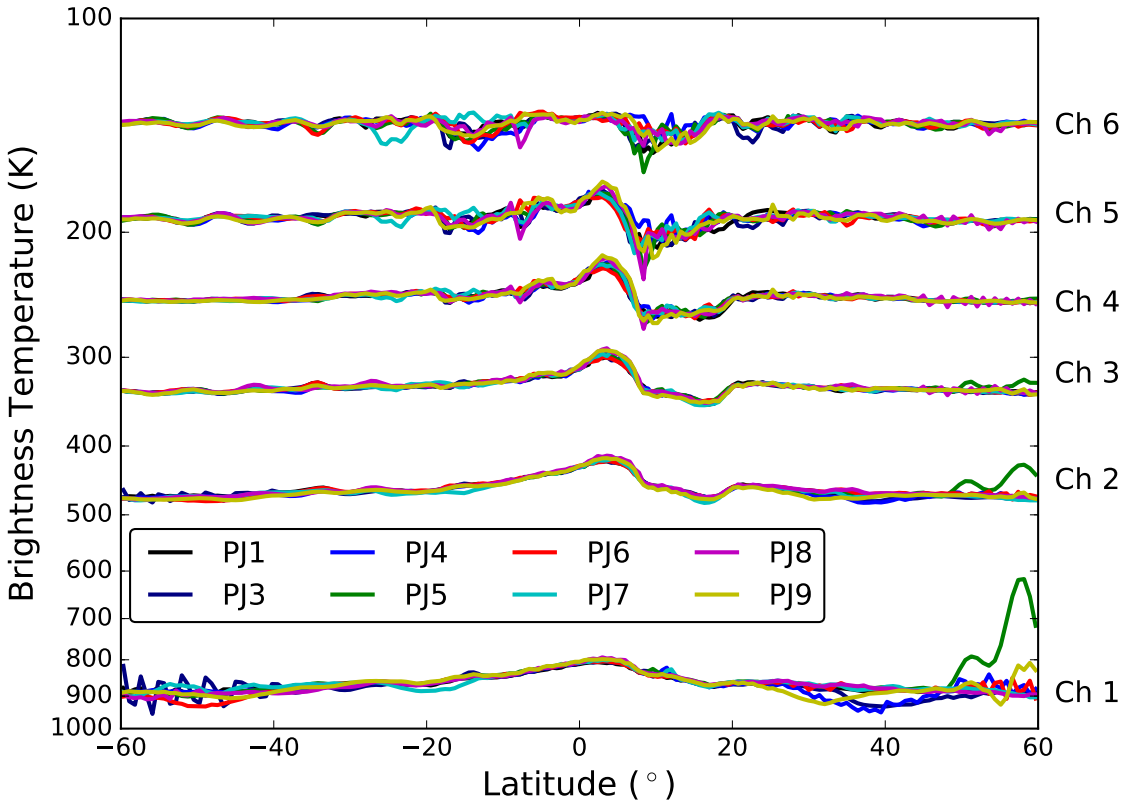

Figure 6.2: Deconvolved nadir brightness temperature as a function of latitude for all six channels and all perijoves.

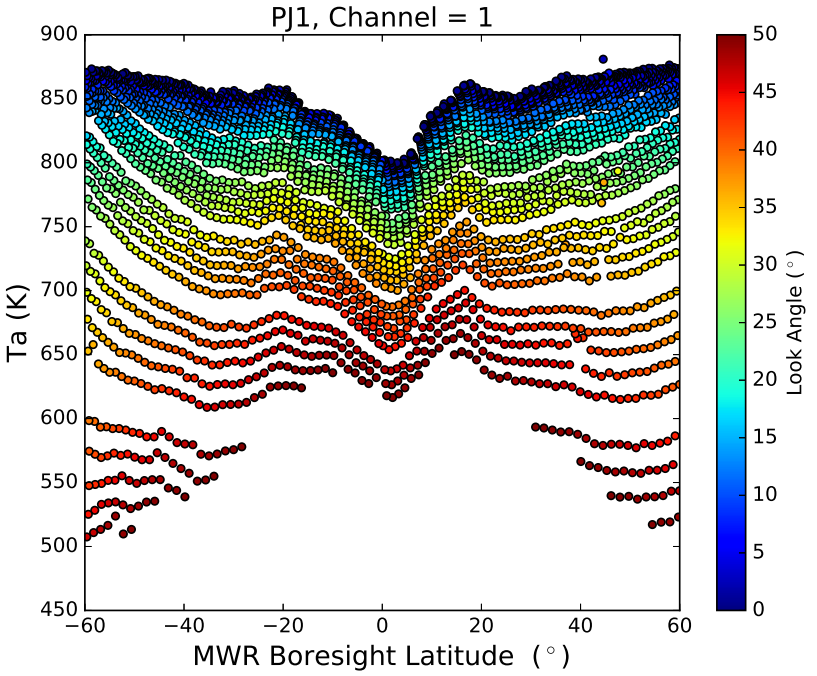

Figure 6.3: Measured antenna temperature as a function of latitude for channel 1 during PJ1 at longitude 97°E with the colors representing the look angle of each measurement.

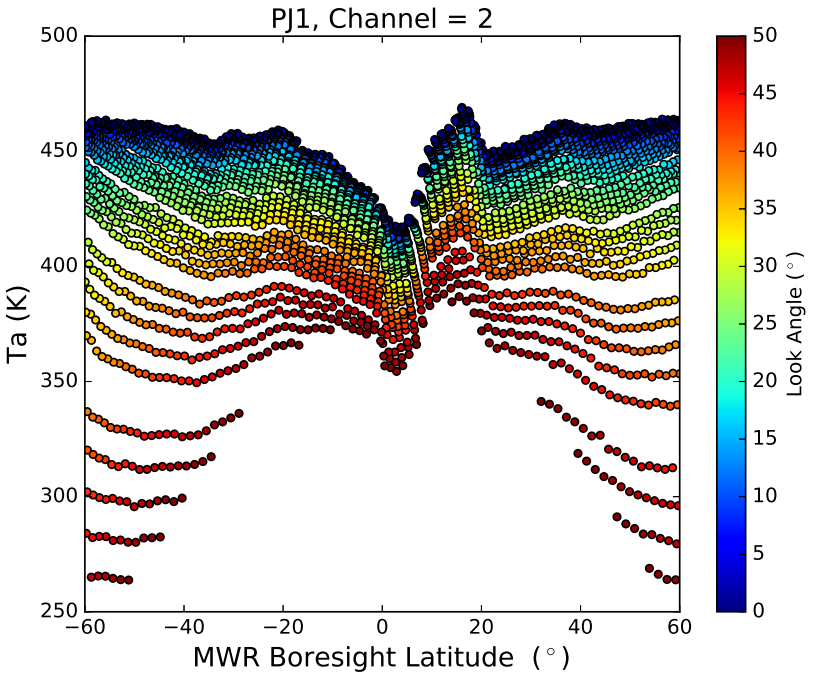

Figure 6.4: Measured antenna temperature as a function of latitude for channel 2 during PJ1 at longitude 97°E with the colors representing the look angle of each measurement.

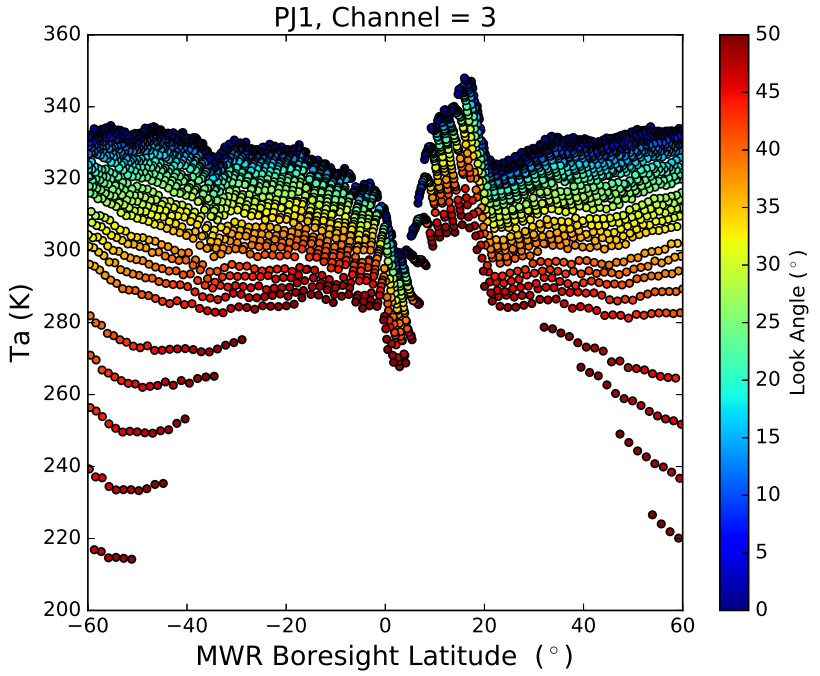

Figure 6.5: Measured antenna temperature as a function of latitude for channel 3 during PJ1 at longitude 97°E with the colors representing the look angle of each measurement.

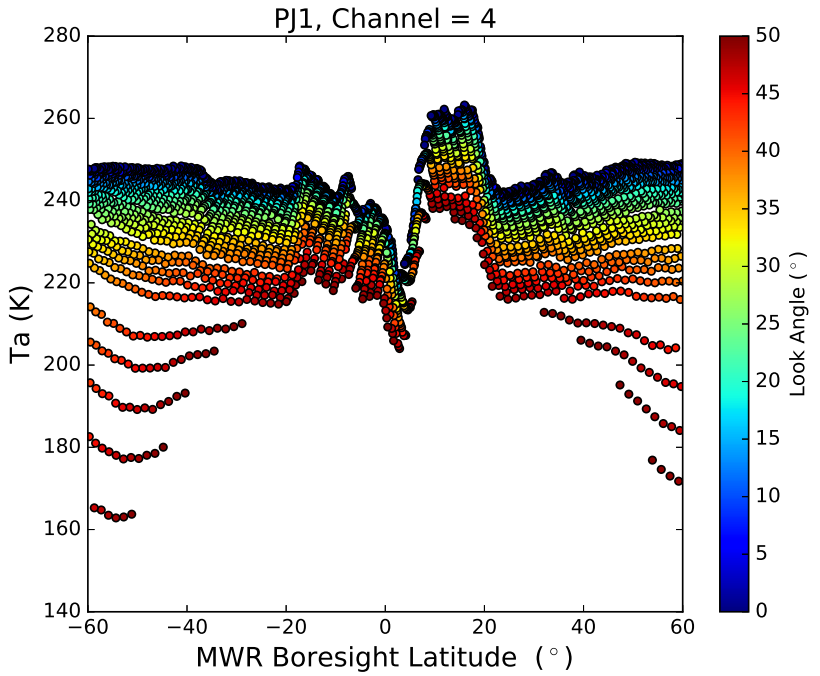

Figure 6.6: Measured antenna temperature as a function of latitude for channel 4 during PJ1 at longitude 97°E with the colors representing the look angle of each measurement.

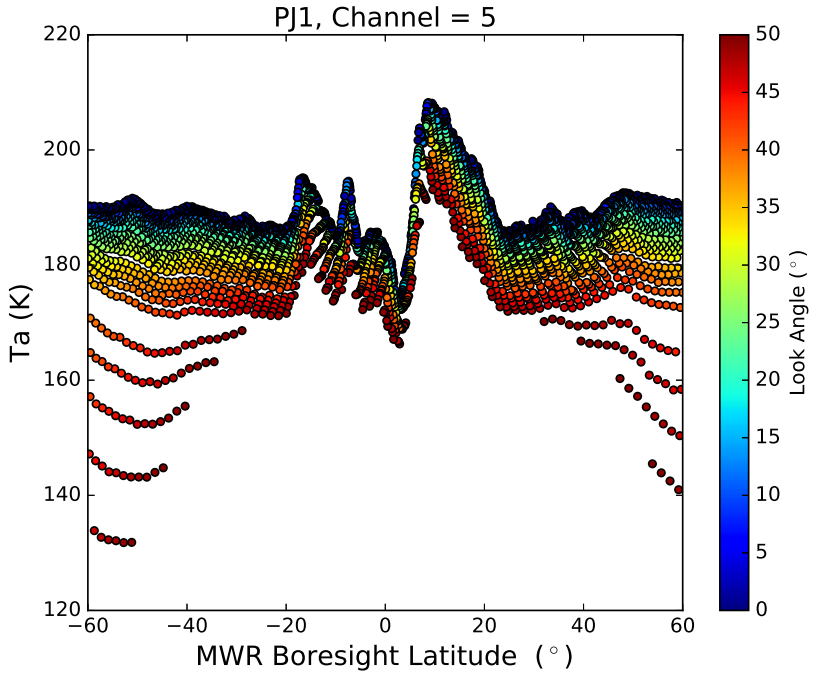

Figure 6.7: Measured antenna temperature as a function of latitude for channel 5 during PJ1 at longitude 97°E with the colors representing the look angle of each measurement.

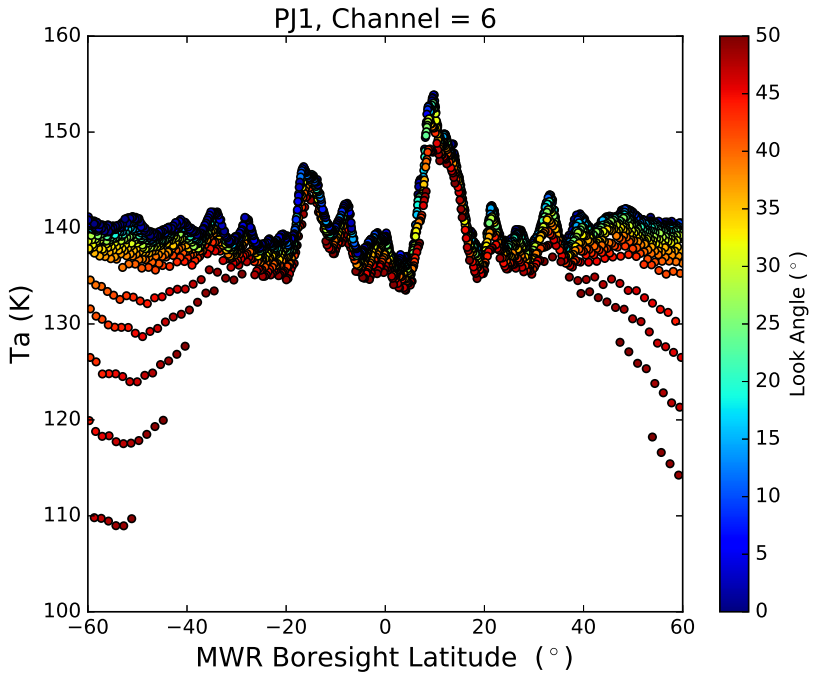

Figure 6.8: Measured antenna temperature as a function of latitude for channel 6 during PJ1 at longitude 97°E with the colors representing the look angle of each measurement.

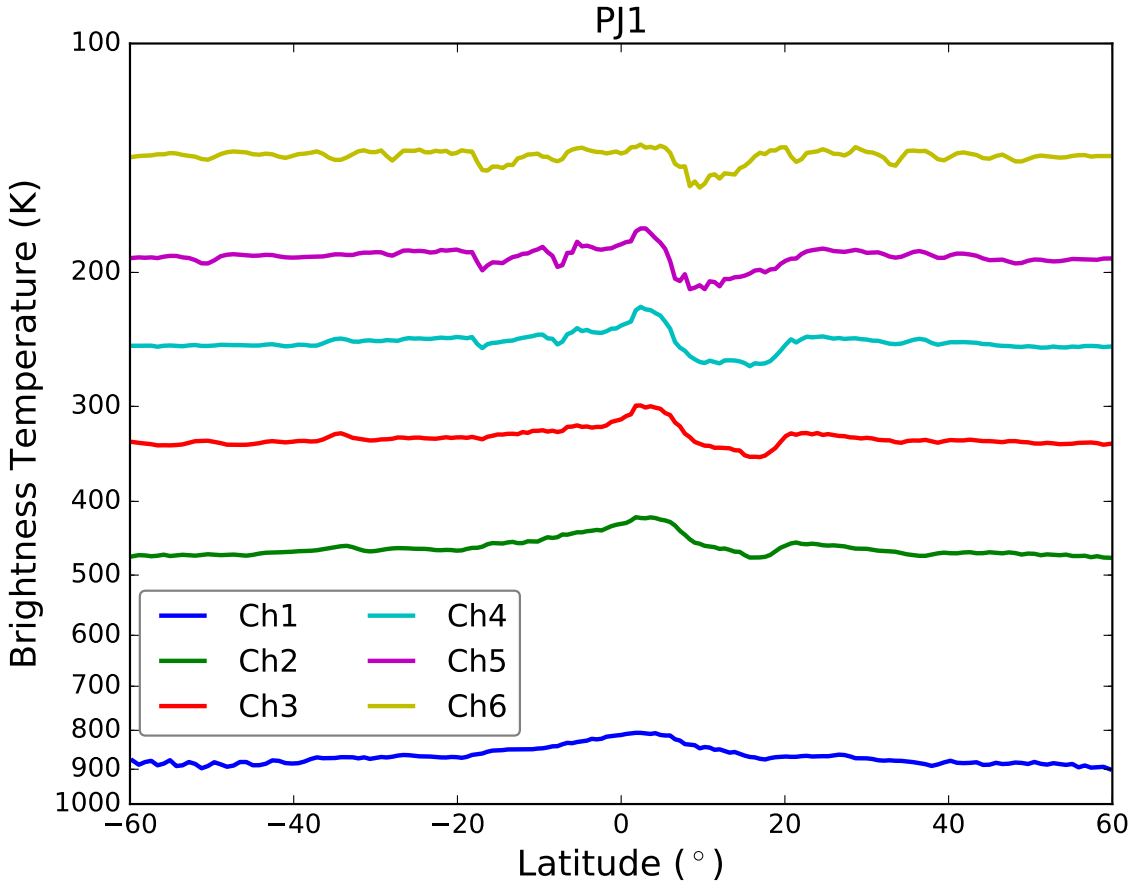

Figure 6.9: Deconvolved nadir brightness temperature as a function of latitude for all six channels for data during PJ1 at longitude 97°E.

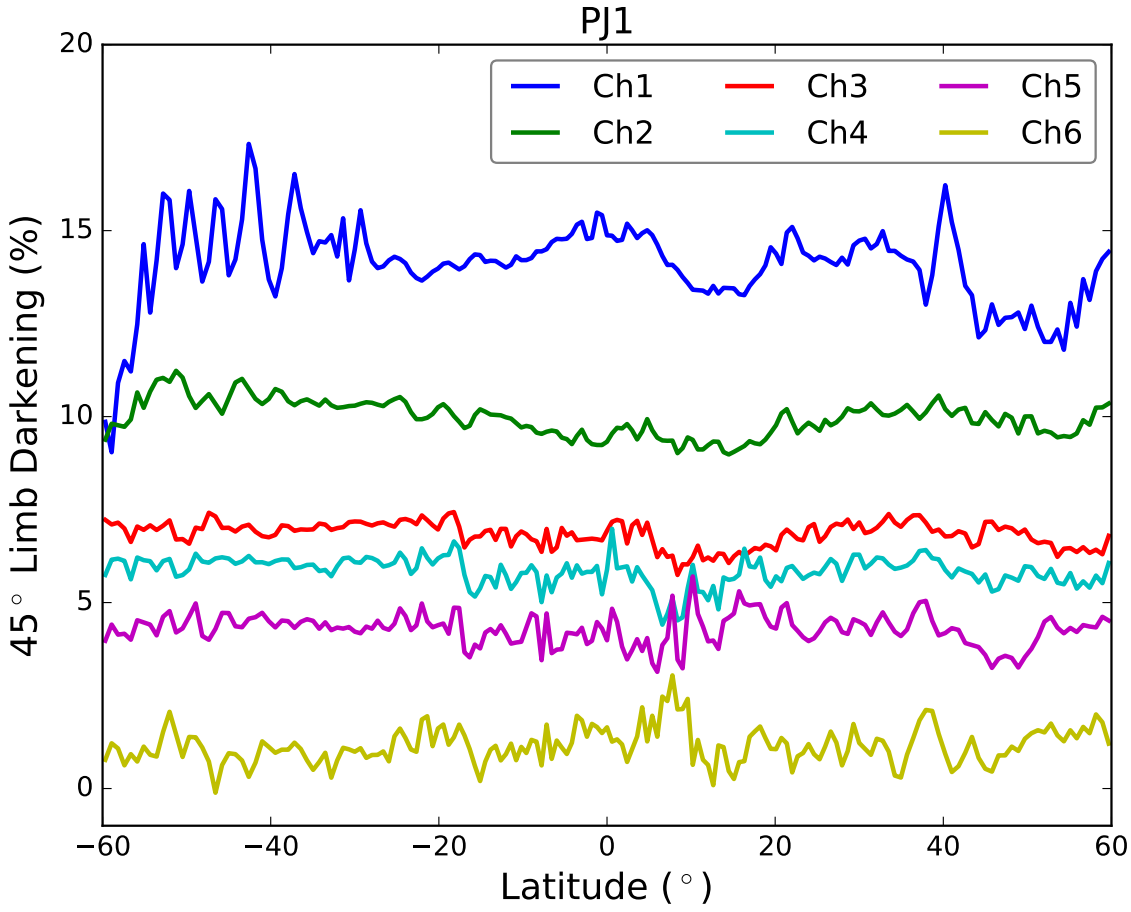

Figure 6.10: 45° limb darkening as a function of latitude for all six channels for data during PJ1 at longitude 97°E.

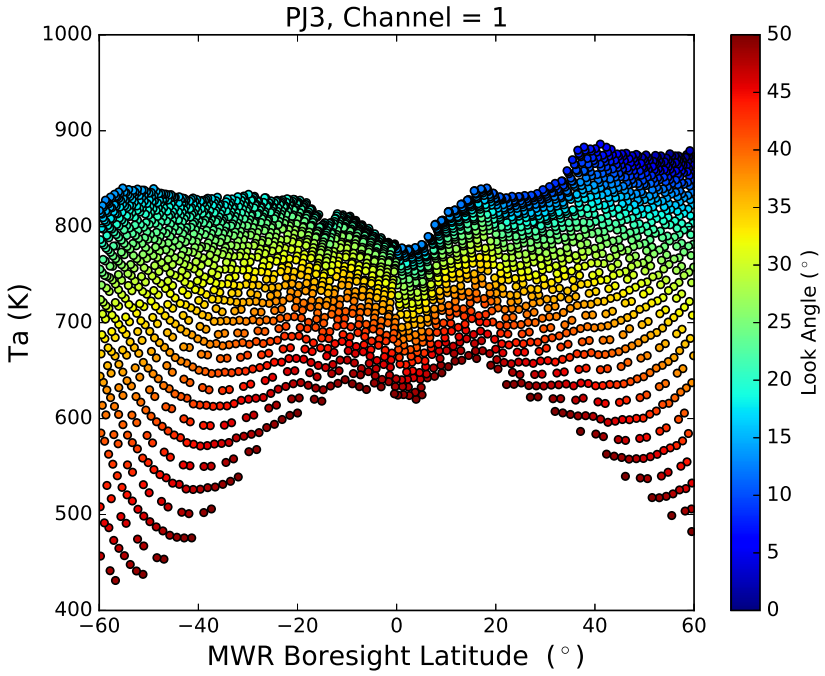

Figure 6.11: Measured antenna temperature as a function of latitude for channel 1 during PJ3 at longitude 7°E with the colors representing the look angle of each measurement.

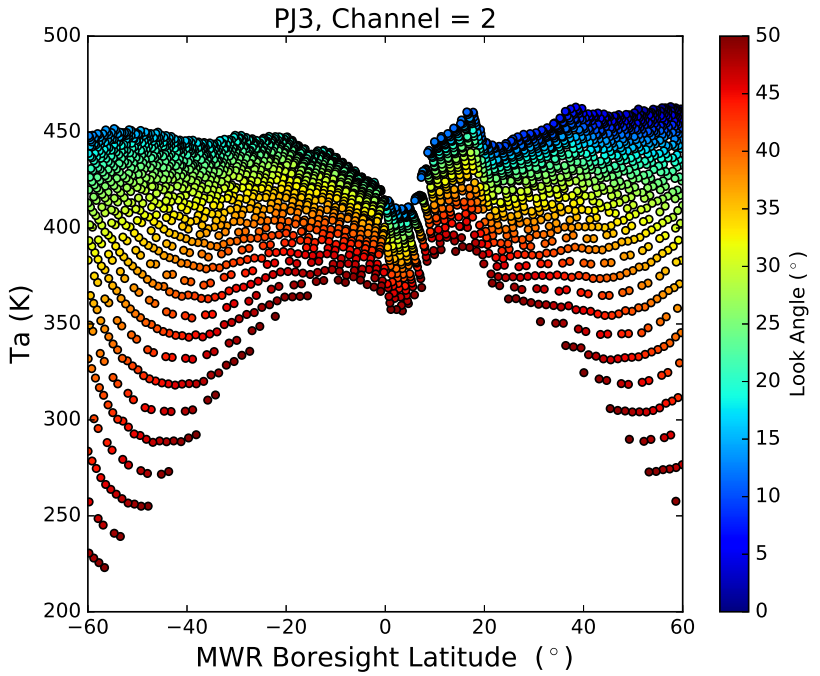

Figure 6.12: Measured antenna temperature as a function of latitude for channel 2 during PJ3 at longitude 7°E with the colors representing the look angle of each measurement.

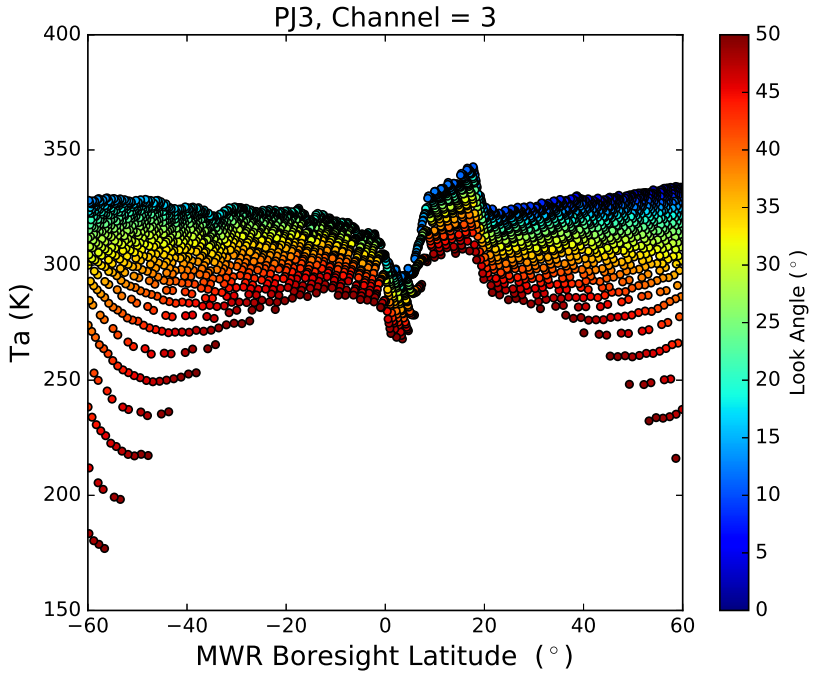

Figure 6.13: Measured antenna temperature as a function of latitude for channel 3 during PJ3 at longitude 7°E with the colors representing the look angle of each measurement.

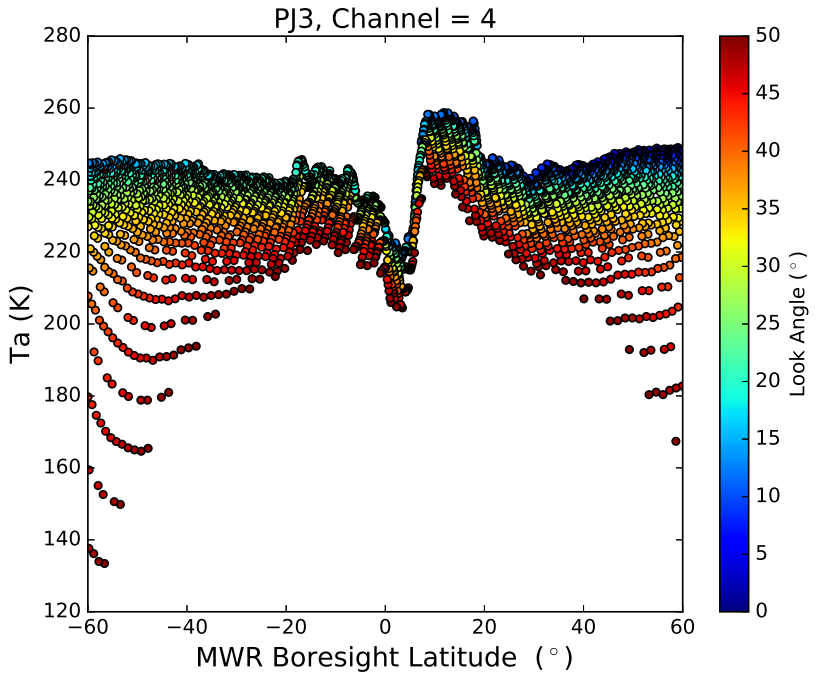

Figure 6.14: Measured antenna temperature as a function of latitude for channel 4 during PJ3 at longitude 7°E with the colors representing the look angle of each measurement.

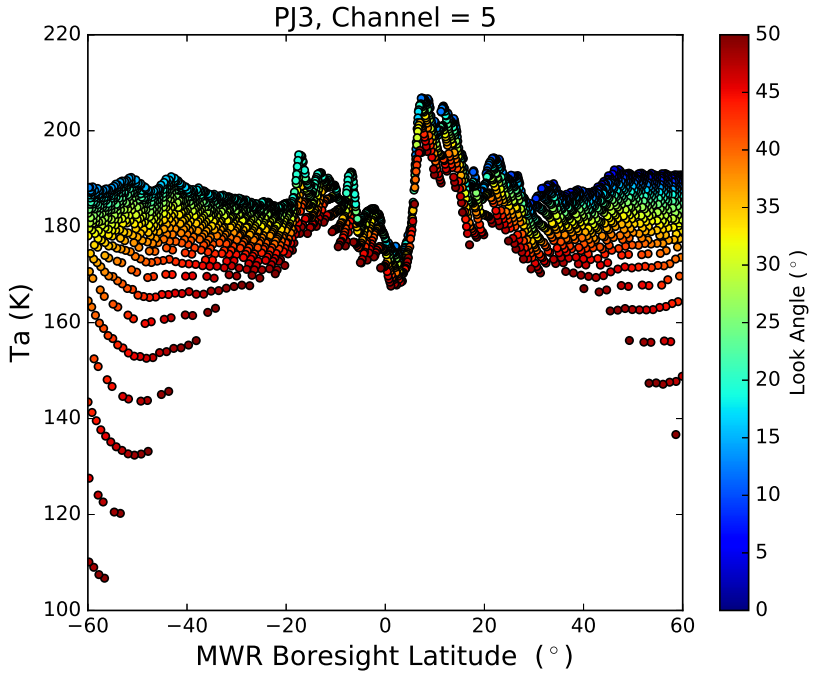

Figure 6.15: Measured antenna temperature as a function of latitude for channel 5 during PJ3 at longitude 7°E with the colors representing the look angle of each measurement.

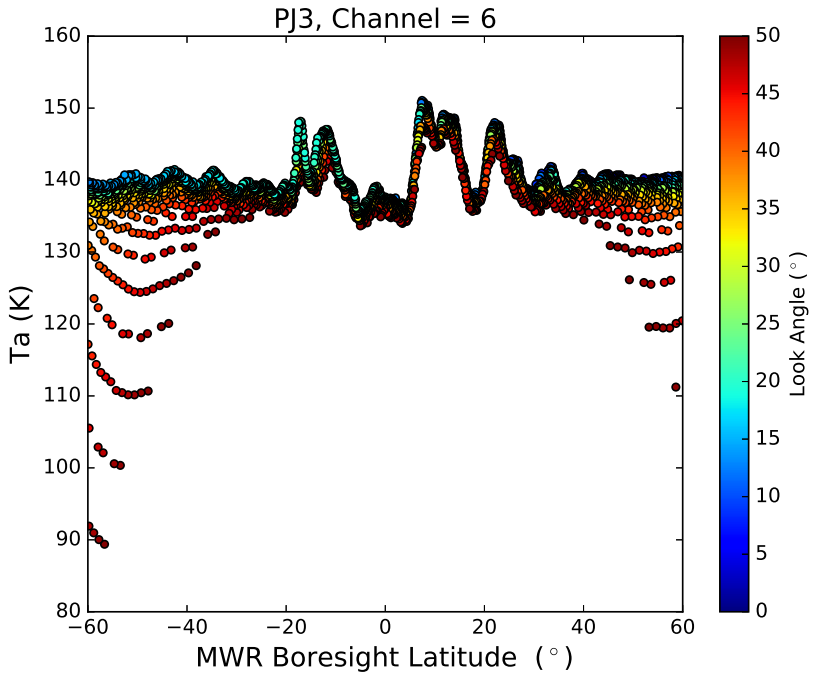

Figure 6.16: Measured antenna temperature as a function of latitude for channel 6 during PJ3 at longitude 7°E with the colors representing the look angle of each measurement.

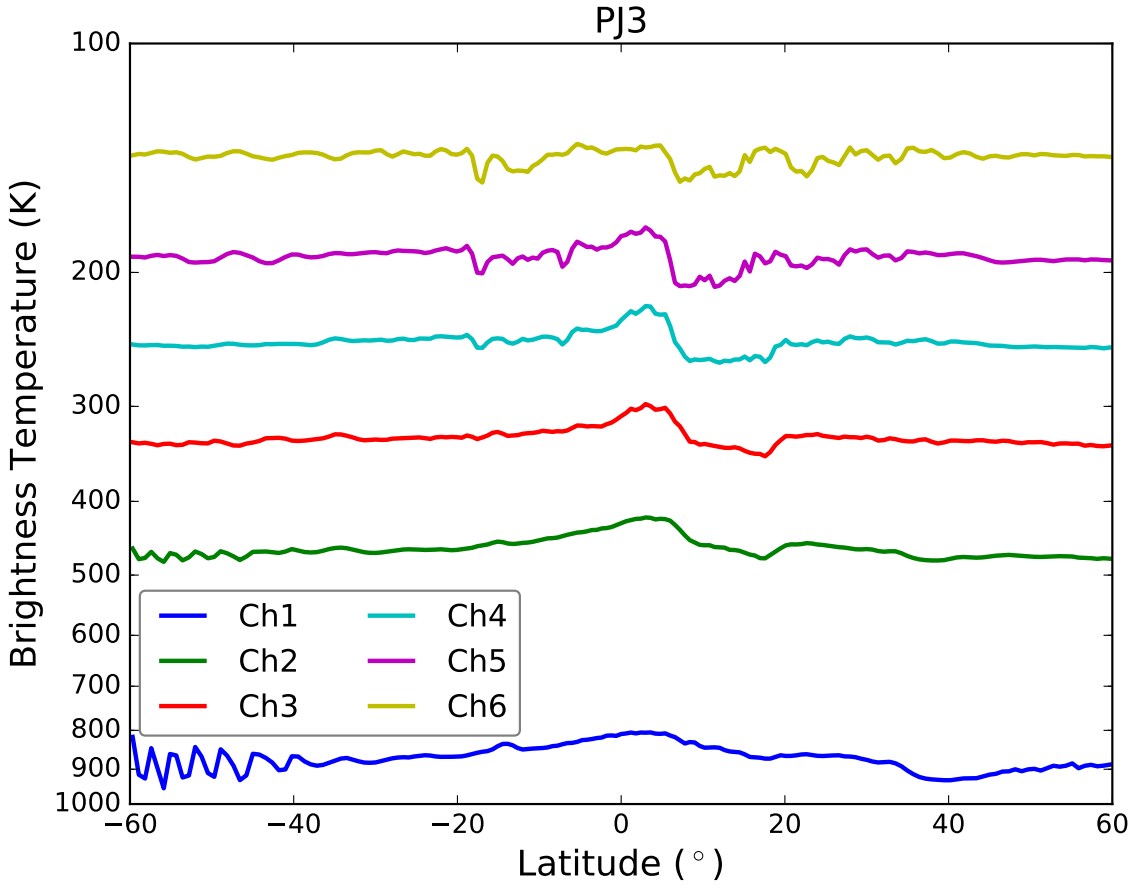

Figure 6.17: Deconvolved nadir brightness temperature as a function of latitude for all six channels for data during PJ3 at longitude 7°E.

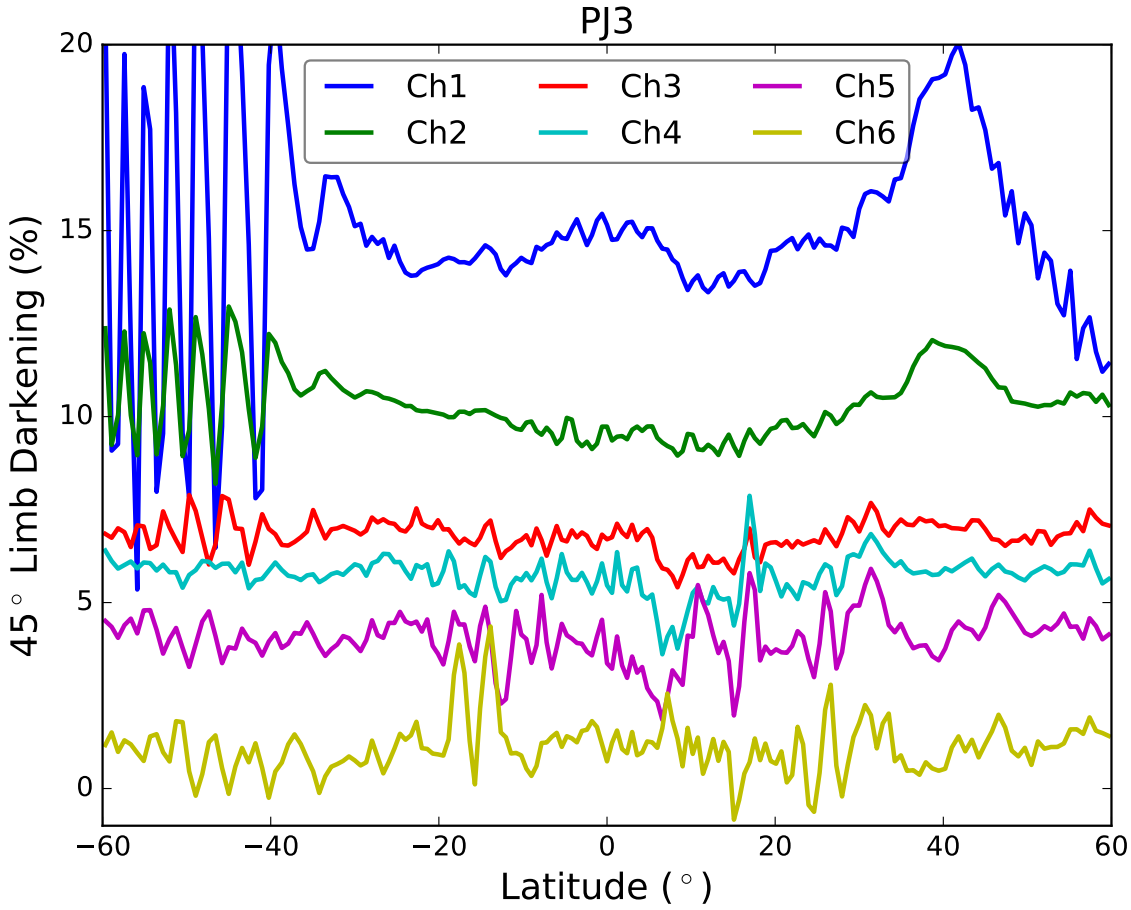

Figure 6.18: 45° limb darkening as a function of latitude for all six channels for data during PJ3 at longitude 7°E.

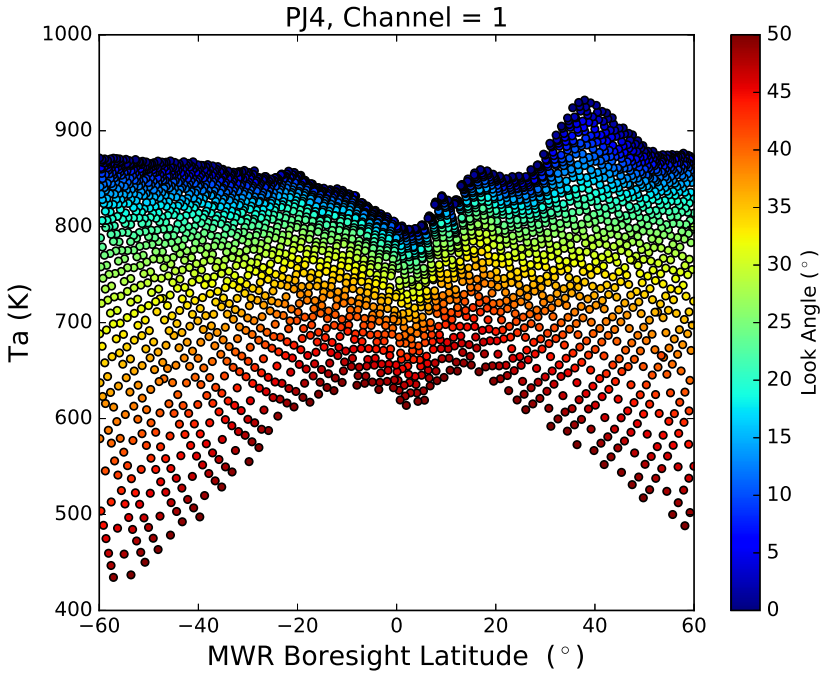

Figure 6.19: Measured antenna temperature as a function of latitude for channel 1 during PJ4 at longitude 276°E with the colors representing the look angle of each measurement.

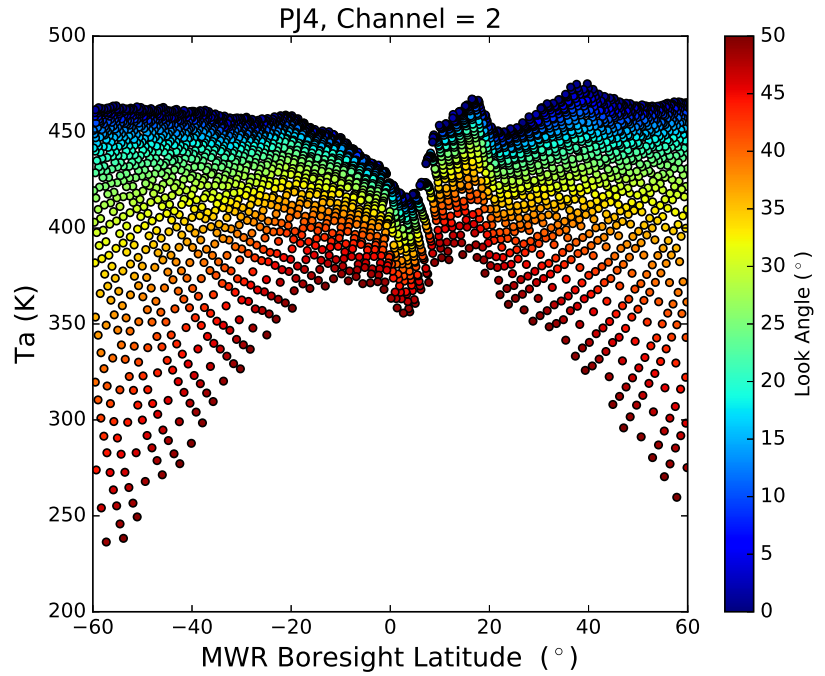

Figure 6.20: Measured antenna temperature as a function of latitude for channel 2 during PJ4 at longitude 276°E with the colors representing the look angle of each measurement.

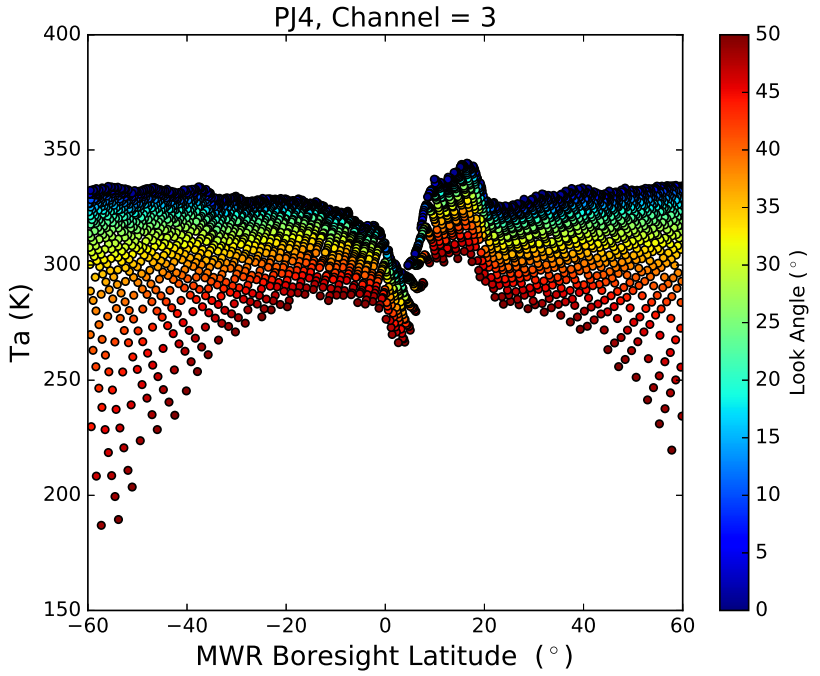

Figure 6.21: Measured antenna temperature as a function of latitude for channel 3 during PJ4 at longitude 276°E with the colors representing the look angle of each measurement.

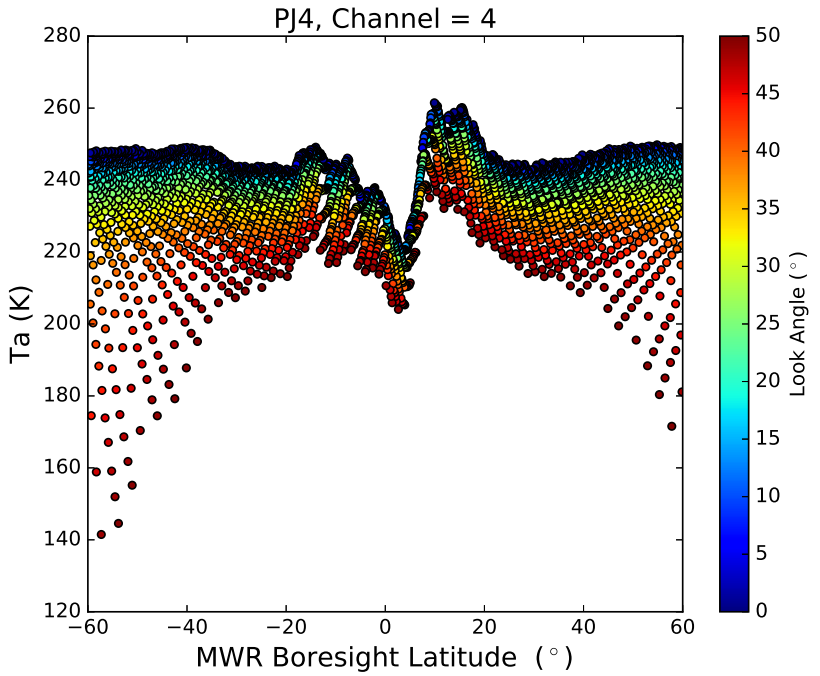

Figure 6.22: Measured antenna temperature as a function of latitude for channel 4 during PJ4 at longitude 276°E with the colors representing the look angle of each measurement.

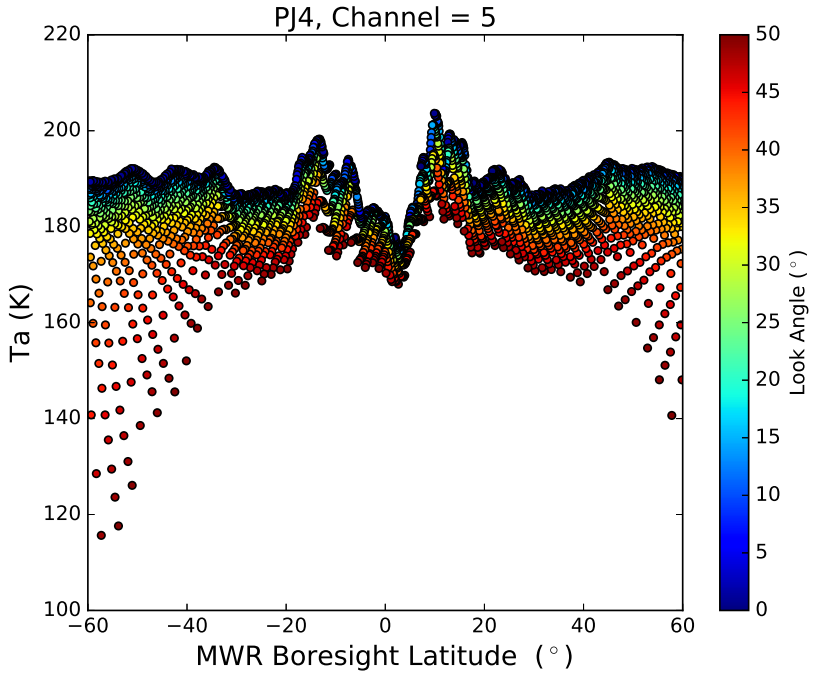

Figure 6.23: Measured antenna temperature as a function of latitude for channel 5 during PJ4 at longitude 276°E with the colors representing the look angle of each measurement.

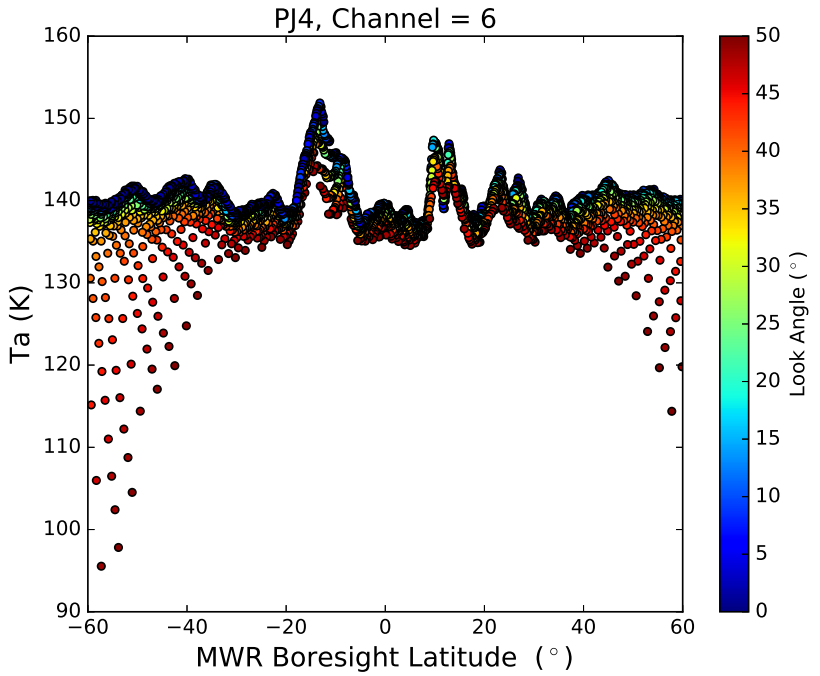

Figure 6.24: Measured antenna temperature as a function of latitude for channel 6 during PJ4 at longitude 276°E with the colors representing the look angle of each measurement.

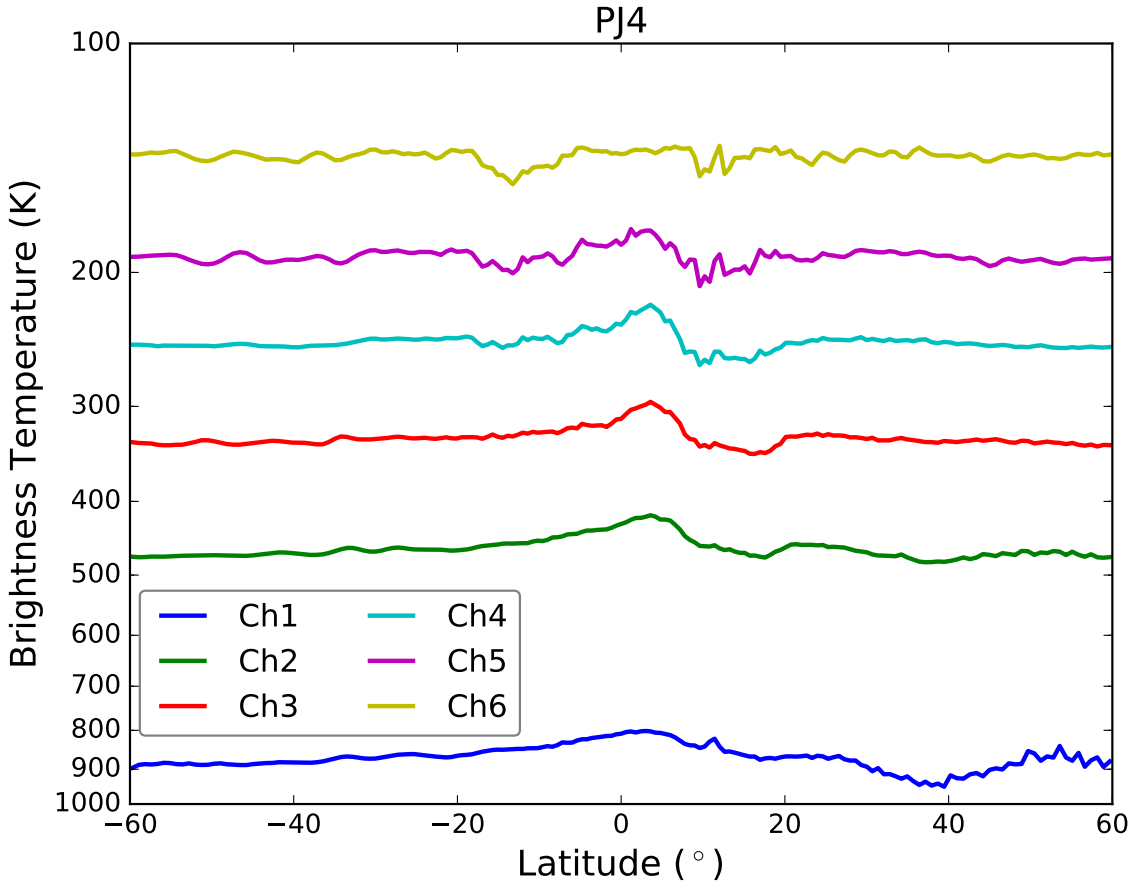

Figure 6.25: Deconvolved nadir brightness temperature as a function of latitude for all six channels for data during PJ4 at longitude 276°E.

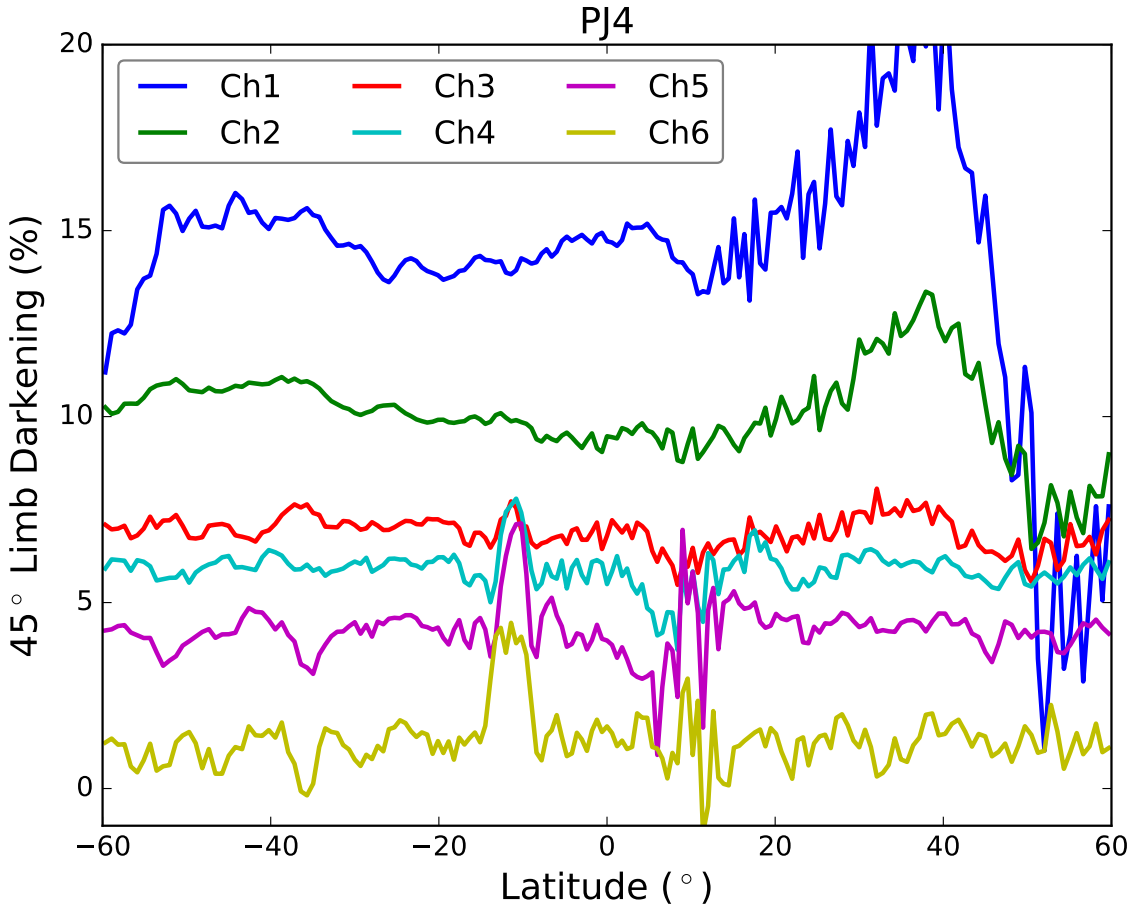

Figure 6.26: 45° limb darkening as a function of latitude for all six channels for data during PJ4 at longitude 276°E.

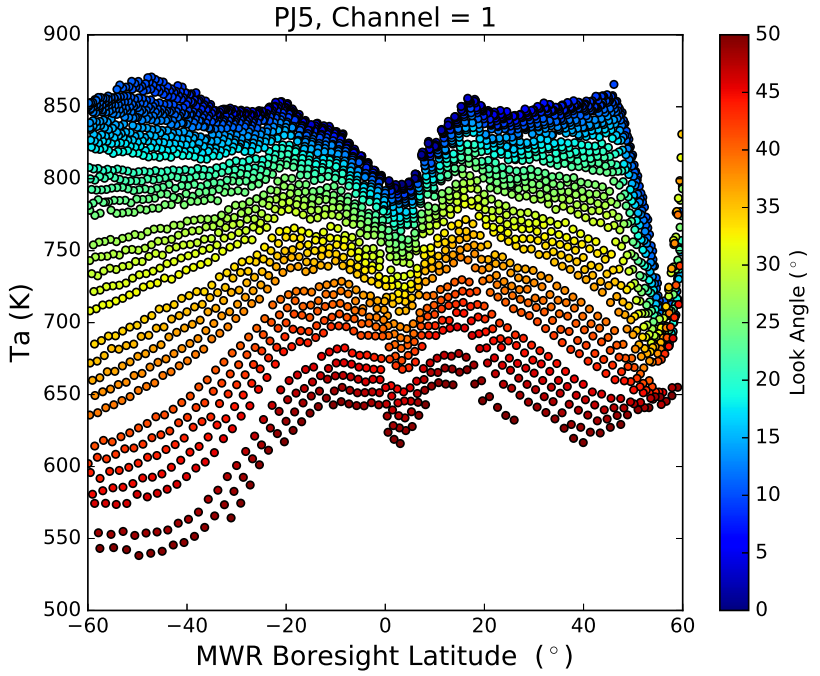

Figure 6.27: Measured antenna temperature as a function of latitude for channel 1 during PJ5 at longitude 187°E with the colors representing the look angle of each measurement.

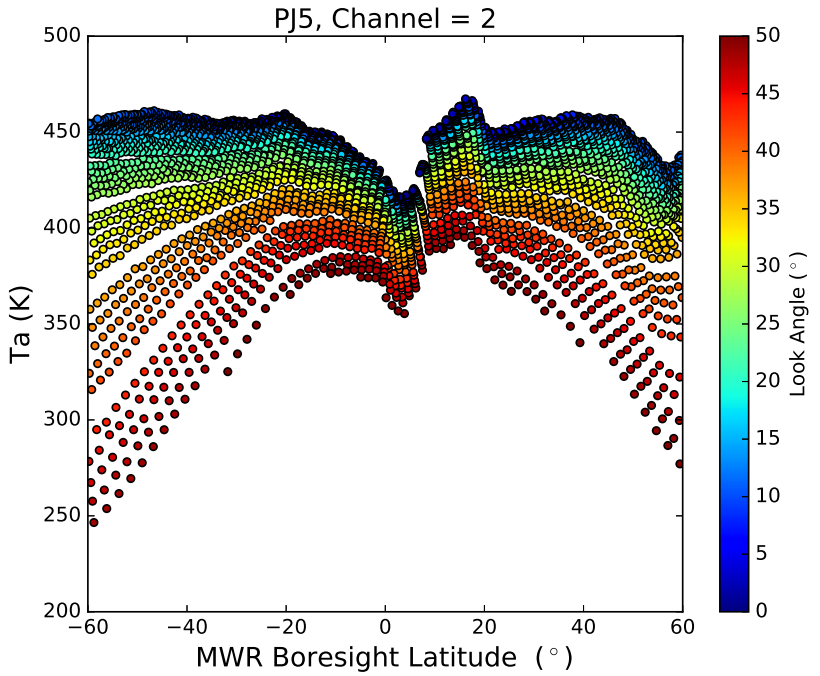

Figure 6.28: Measured antenna temperature as a function of latitude for channel 2 during PJ5 at longitude 187°E with the colors representing the look angle of each measurement.

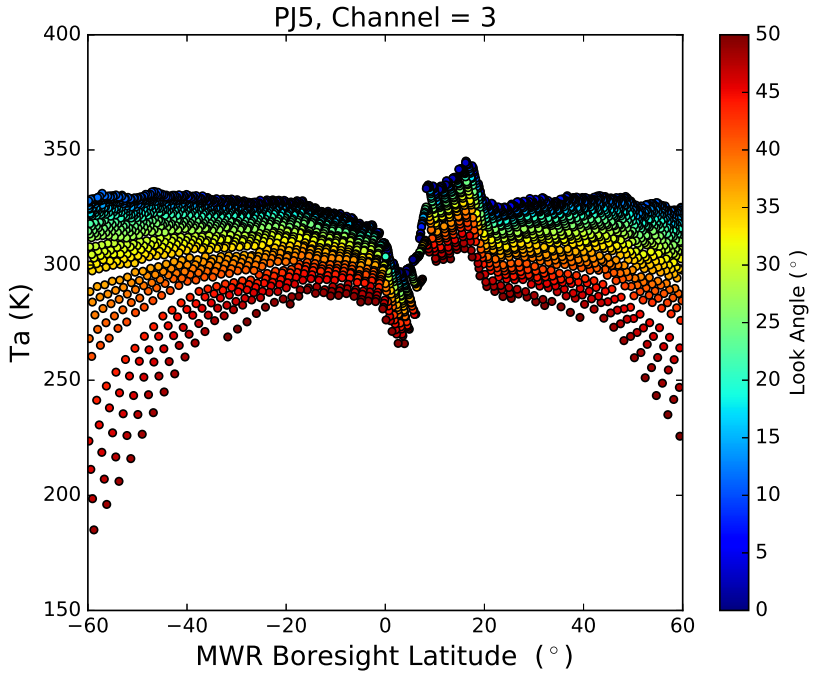

Figure 6.29: Measured antenna temperature as a function of latitude for channel 3 during PJ5 at longitude 187°E with the colors representing the look angle of each measurement.

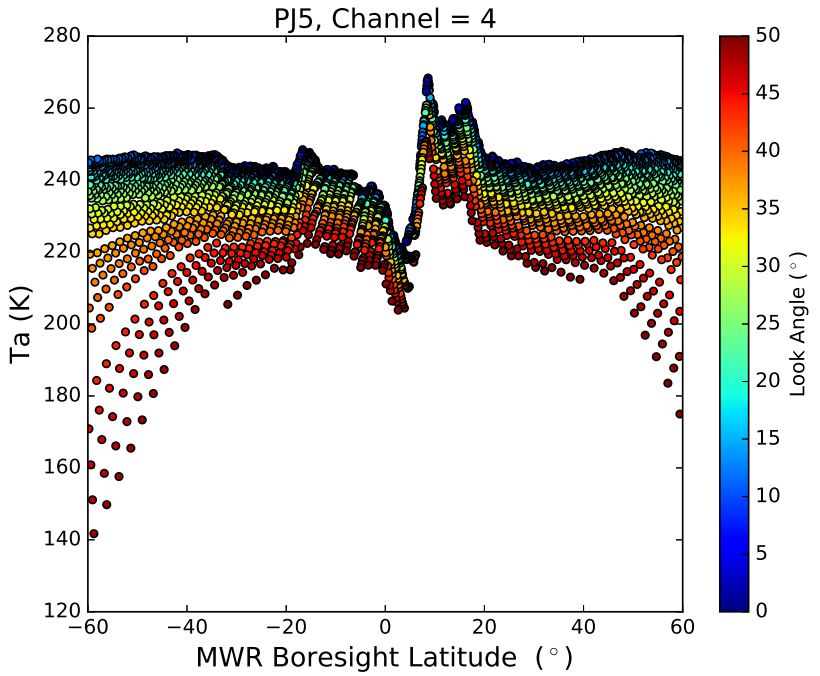

Figure 6.30: Measured antenna temperature as a function of latitude for channel 4 during PJ5 at longitude 187°E with the colors representing the look angle of each measurement.

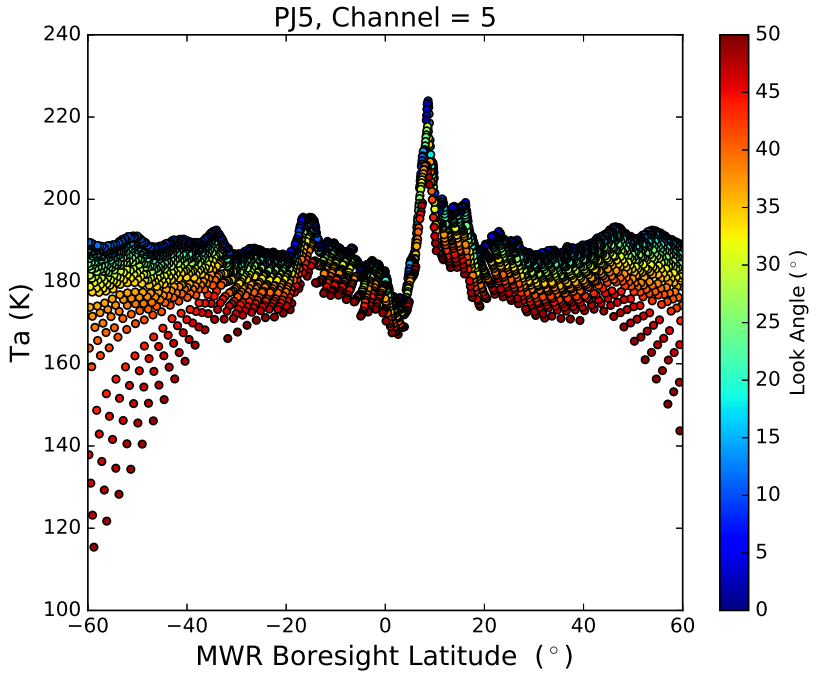

Figure 6.31: Measured antenna temperature as a function of latitude for channel 5 during PJ5 at longitude 187°E with the colors representing the look angle of each measurement.

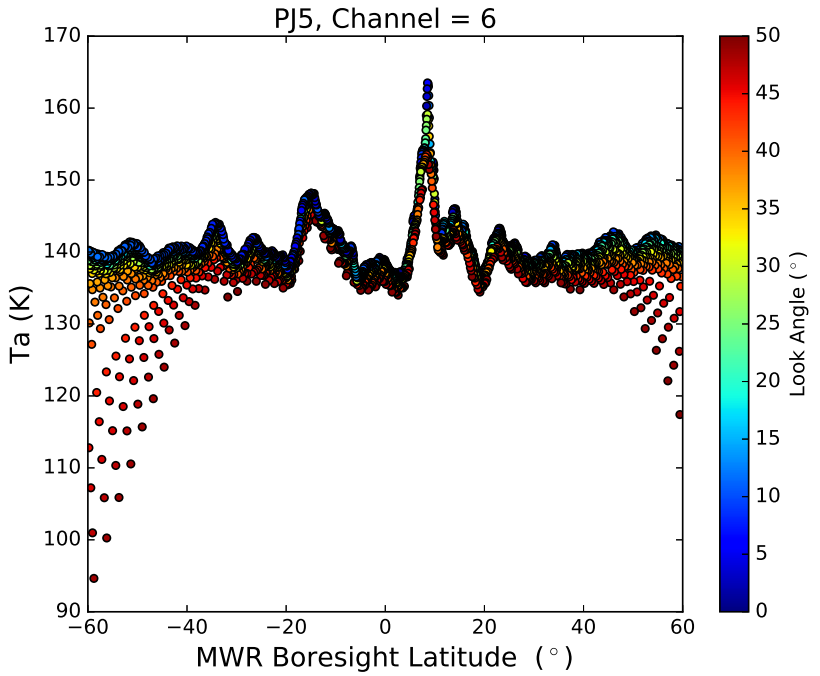

Figure 6.32: Measured antenna temperature as a function of latitude for channel 6 during PJ5 at longitude 187°E with the colors representing the look angle of each measurement.

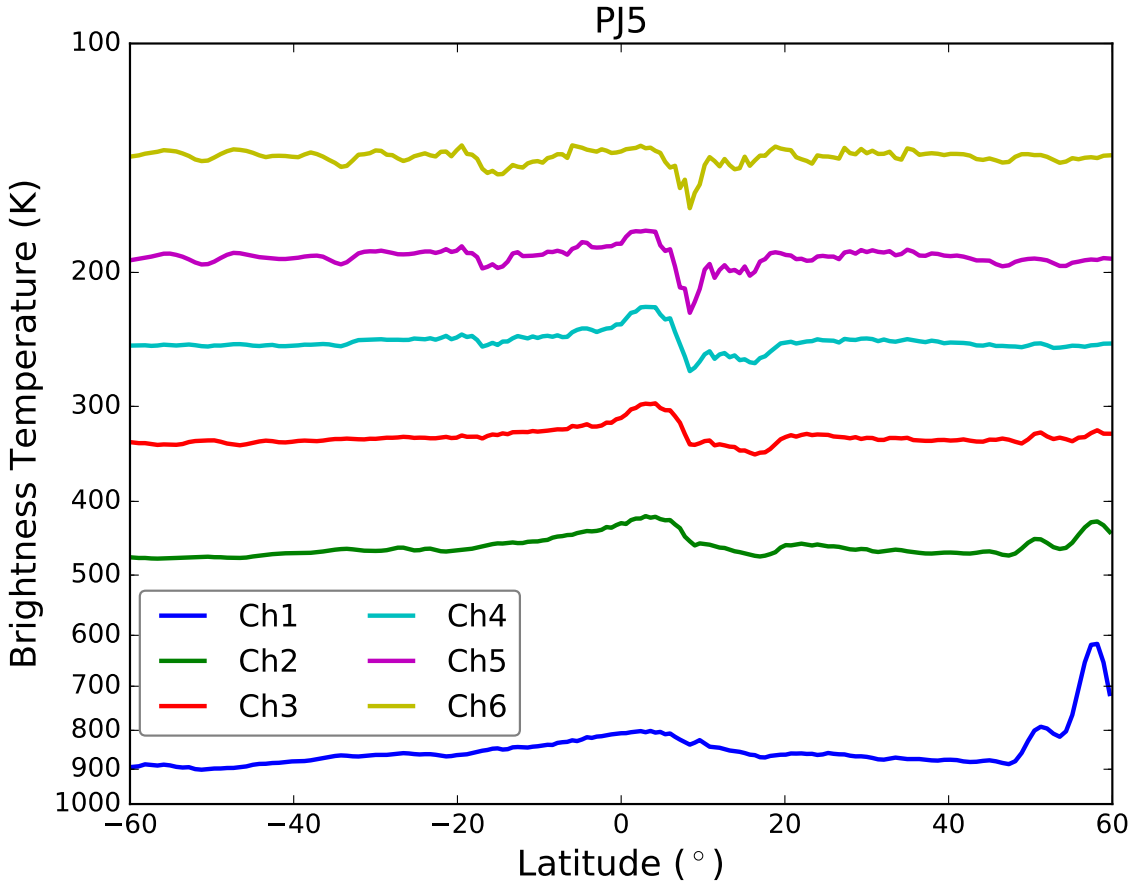

Figure 6.33: Deconvolved nadir brightness temperature as a function of latitude for all six channels for data during PJ5 at longitude 187°E.

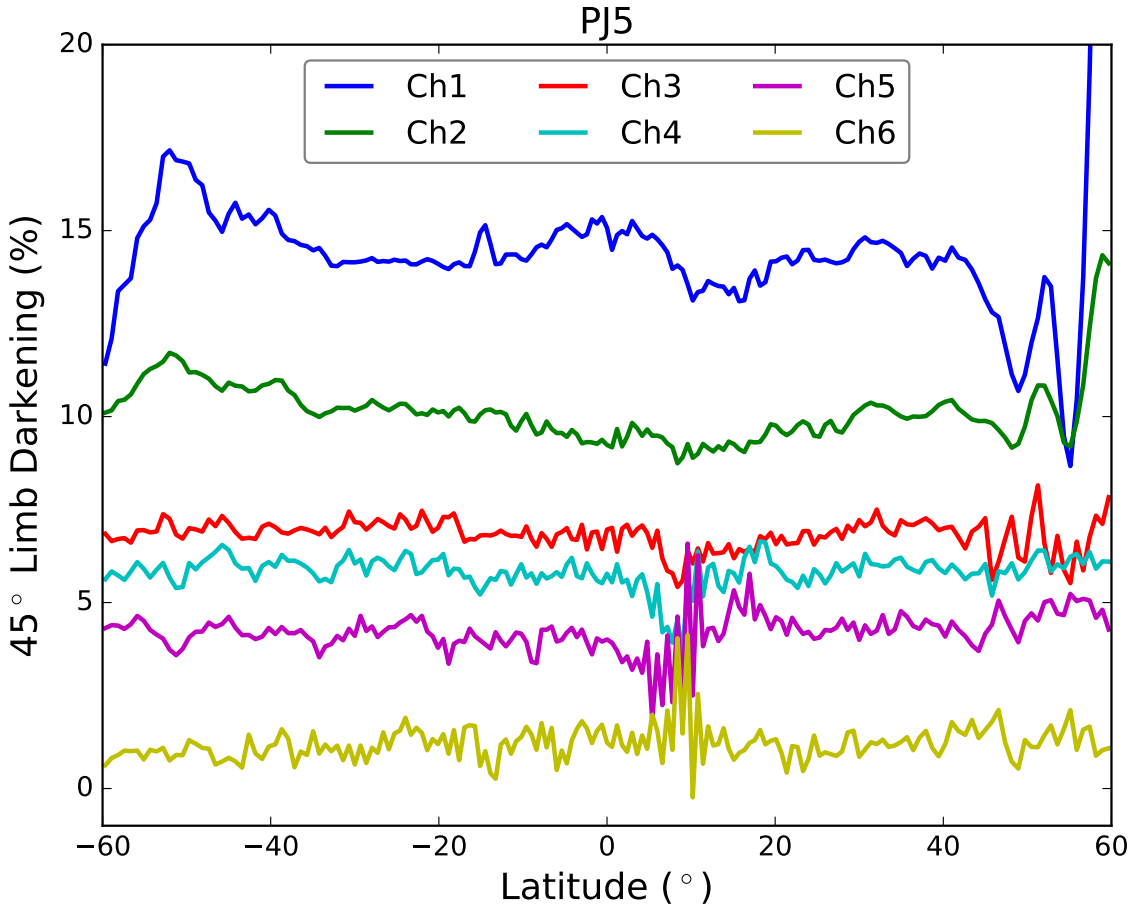

Figure 6.34: 45° limb darkening as a function of latitude for all six channels for data during PJ5 at longitude 187°E.

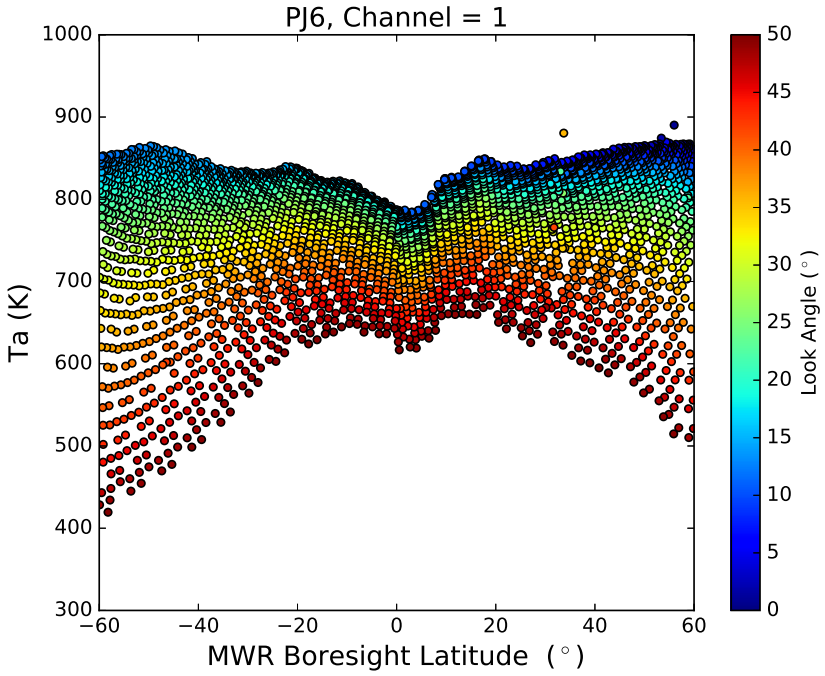

Figure 6.35: Measured antenna temperature as a function of latitude for channel 1 during PJ6 at longitude 142°E with the colors representing the look angle of each measurement.

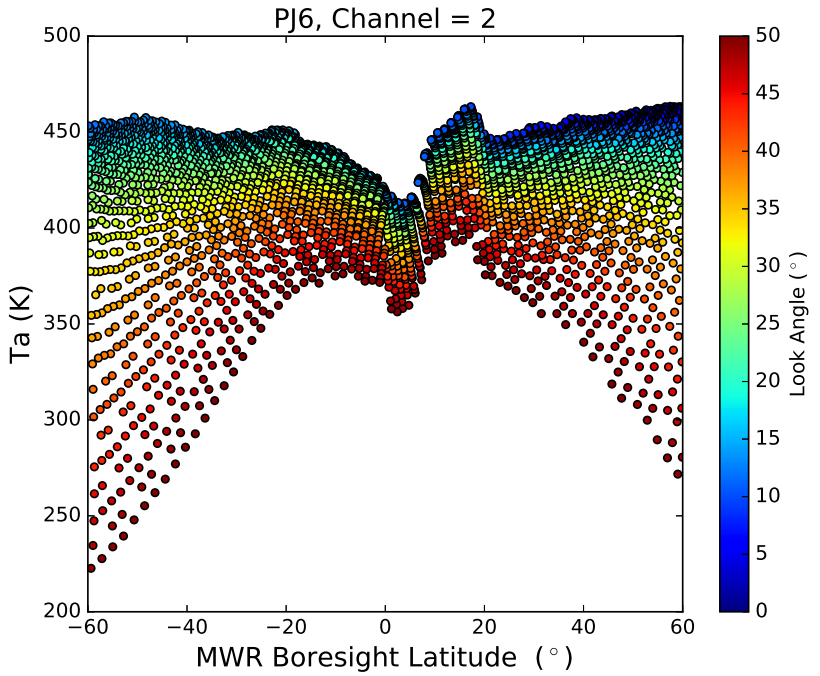

Figure 6.36: Measured antenna temperature as a function of latitude for channel 2 during PJ6 at longitude 142°E with the colors representing the look angle of each measurement.

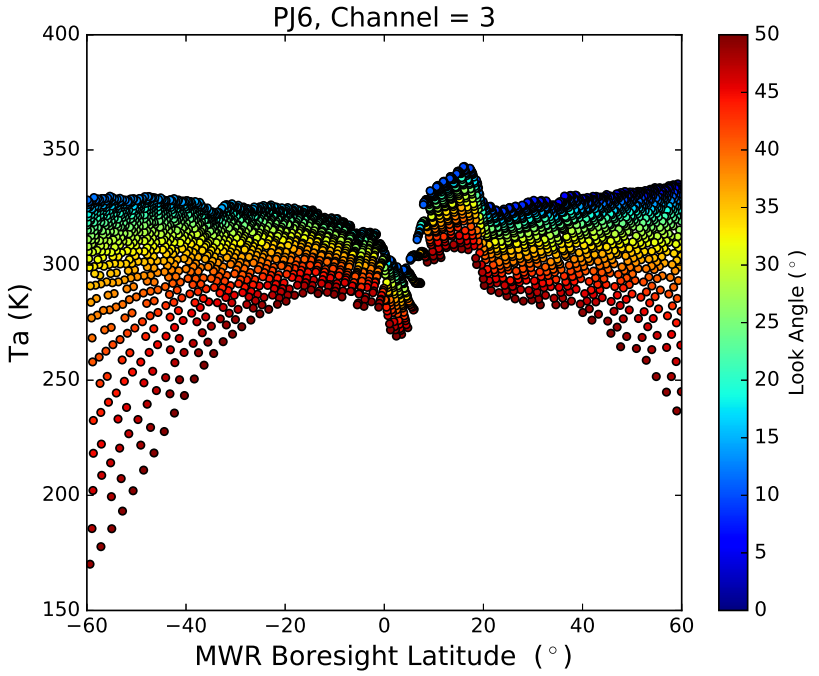

Figure 6.37: Measured antenna temperature as a function of latitude for channel 3 during PJ6 at longitude 142°E with the colors representing the look angle of each measurement.

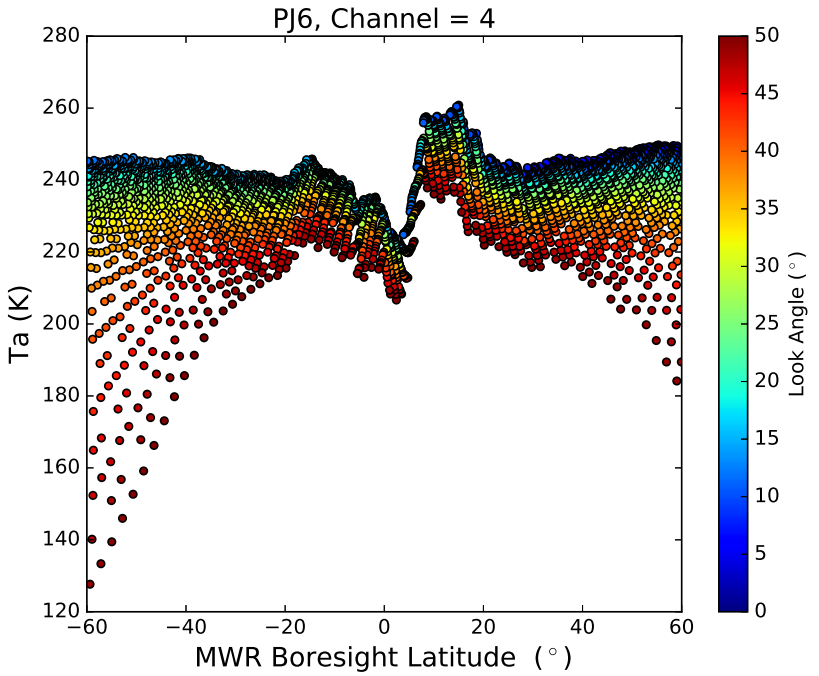

Figure 6.38: Measured antenna temperature as a function of latitude for channel 4 during PJ6 at longitude 142°E with the colors representing the look angle of each measurement.

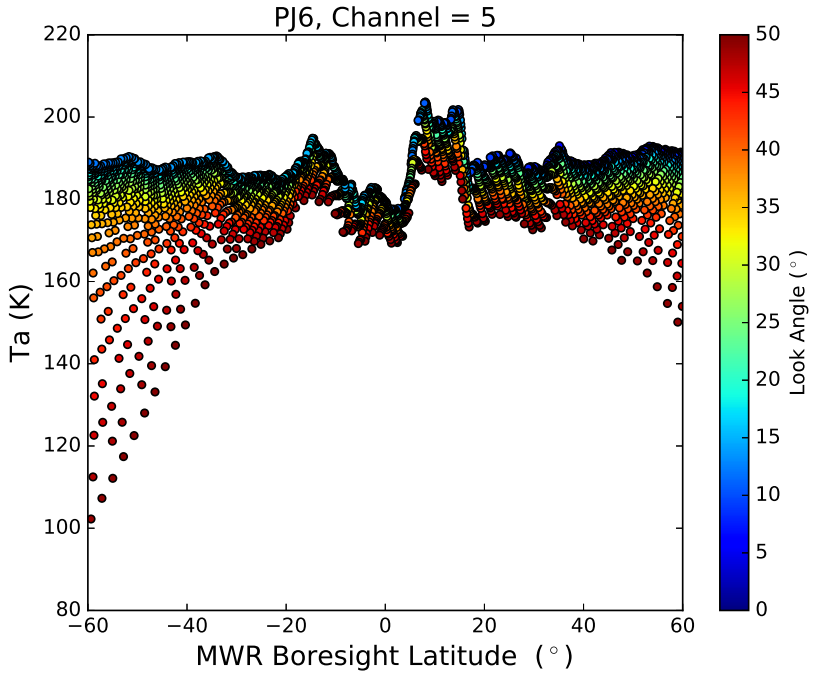

Figure 6.39: Measured antenna temperature as a function of latitude for channel 5 during PJ6 at longitude 142°E with the colors representing the look angle of each measurement.

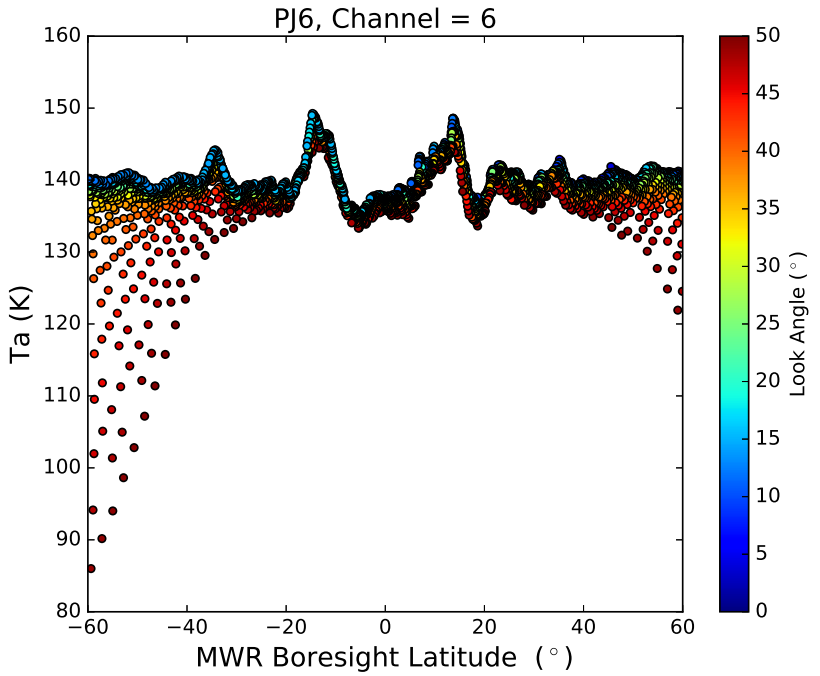

Figure 6.40: Measured antenna temperature as a function of latitude for channel 6 during PJ6 at longitude 142°E with the colors representing the look angle of each measurement.

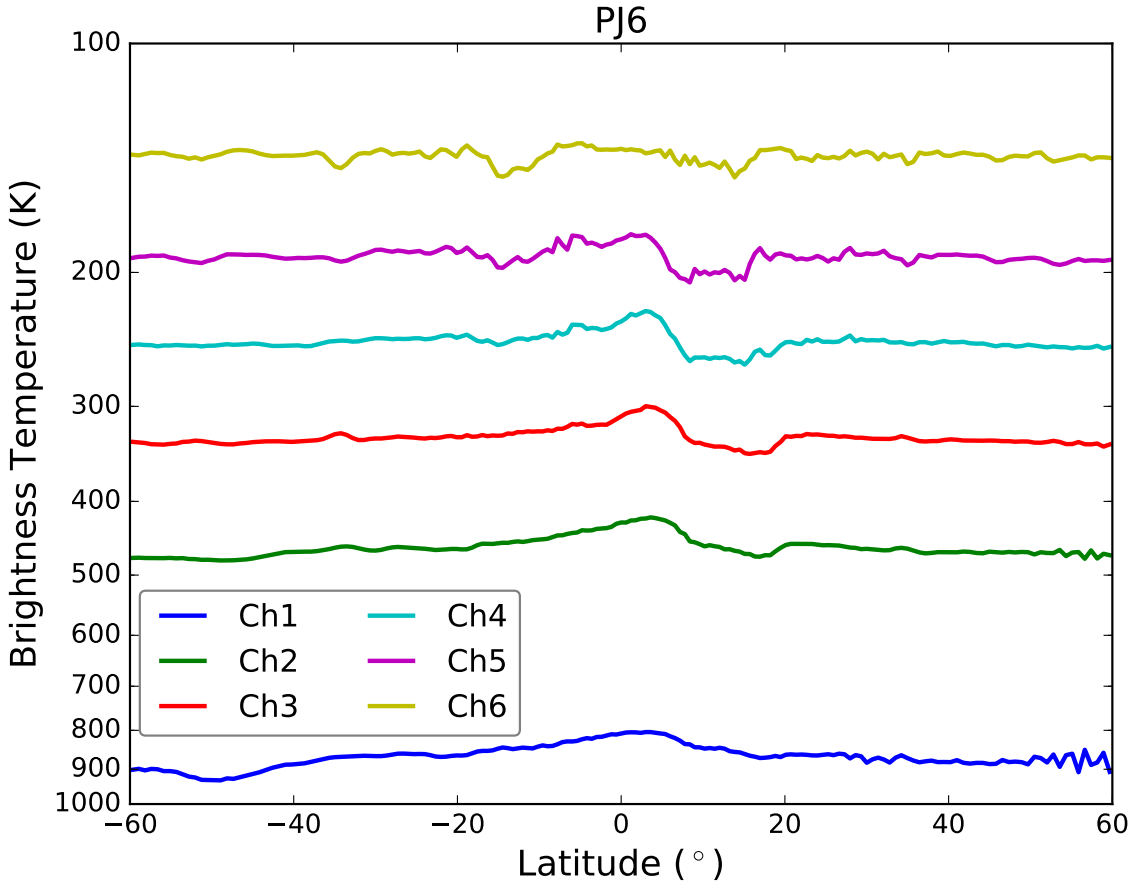

Figure 6.41: Deconvolved nadir brightness temperature as a function of latitude for all six channels for data during PJ6 at longitude 142°E.

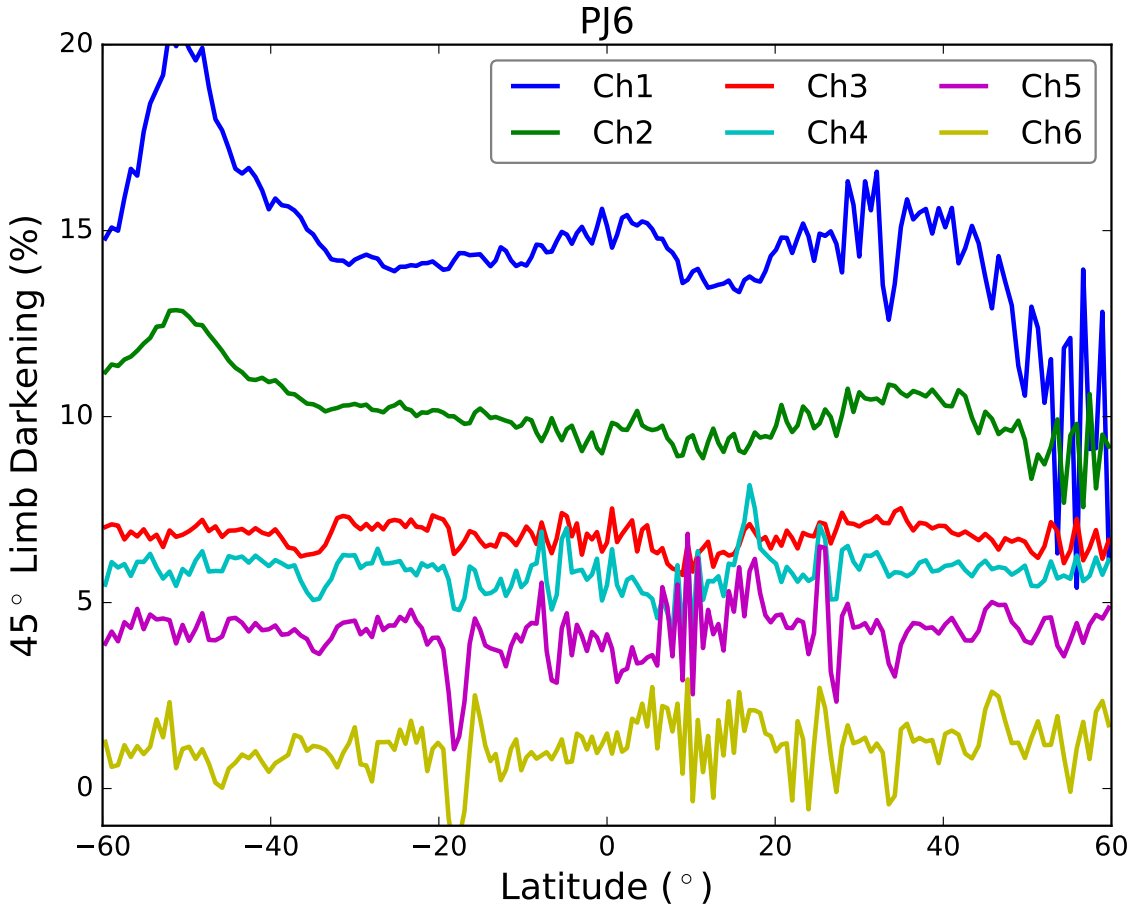

Figure 6.42: 45° limb darkening as a function of latitude for all six channels for data during PJ6 at longitude 142°E.

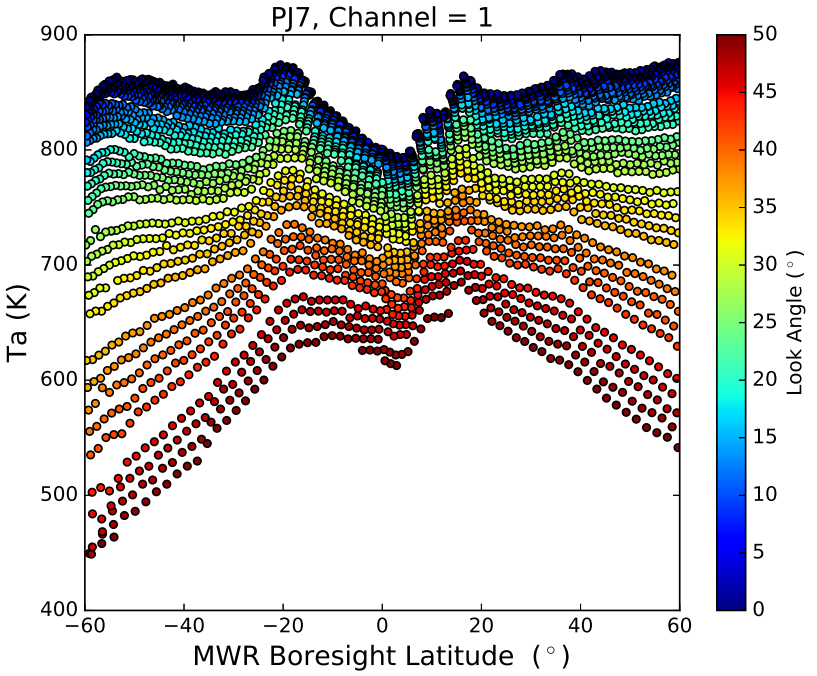

Figure 6.43: Measured antenna temperature as a function of latitude for channel 1 during PJ7 at longitude 52°E with the colors representing the look angle of each measurement.

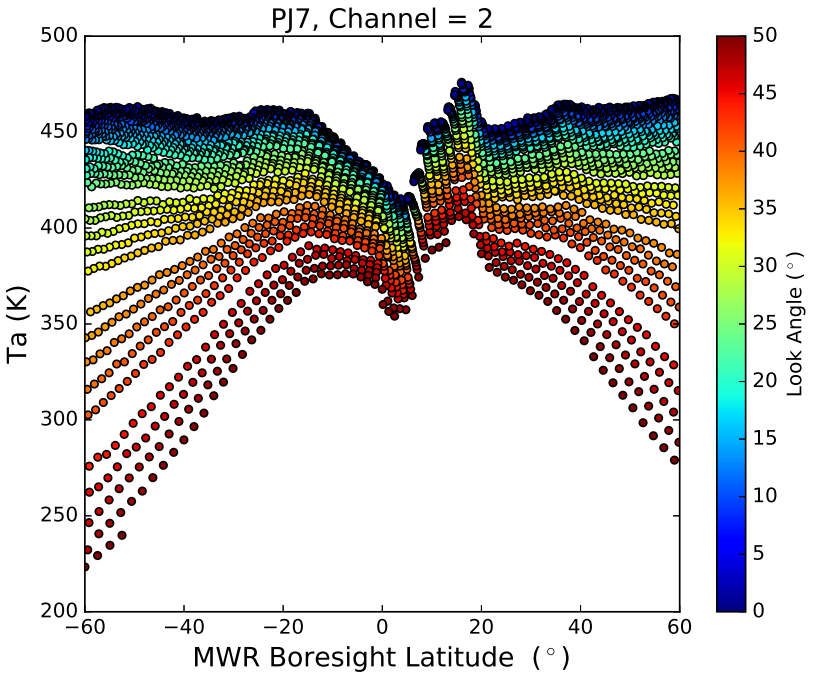

Figure 6.44: Measured antenna temperature as a function of latitude for channel 2 during PJ7 at longitude 52°E with the colors representing the look angle of each measurement.

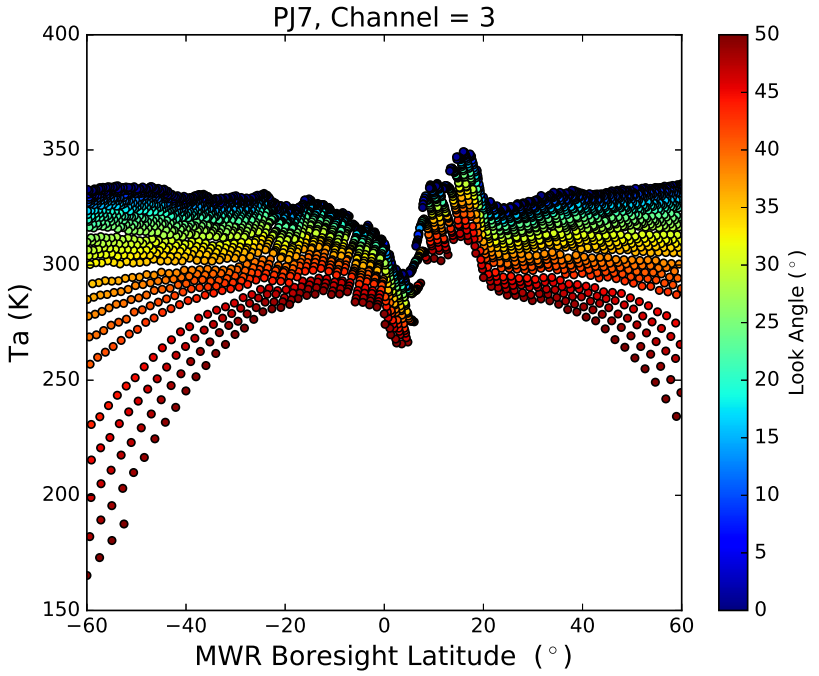

Figure 6.45: Measured antenna temperature as a function of latitude for channel 3 during PJ7 at longitude 52°E with the colors representing the look angle of each measurement.

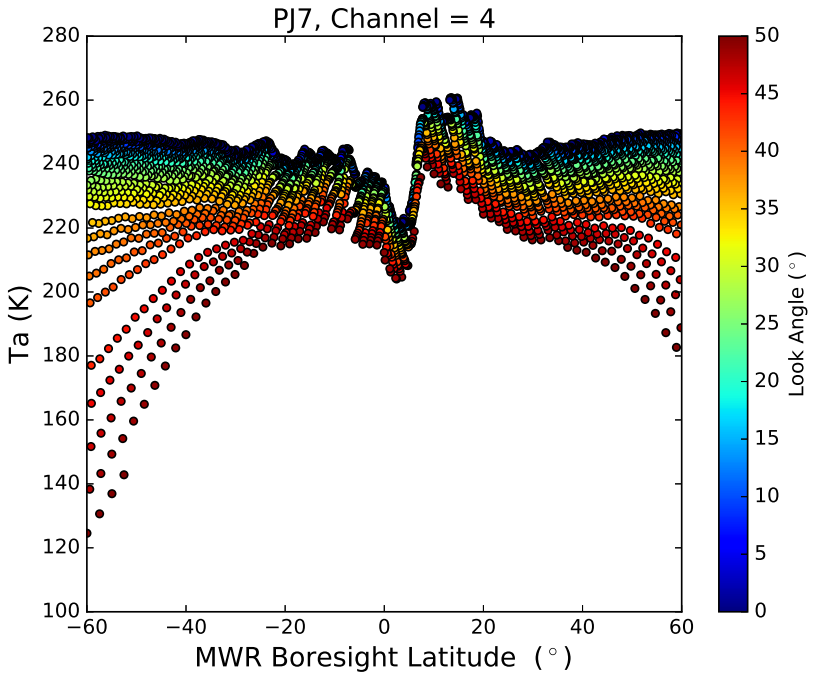

Figure 6.46: Measured antenna temperature as a function of latitude for channel 4 during PJ7 at longitude 52°E with the colors representing the look angle of each measurement.

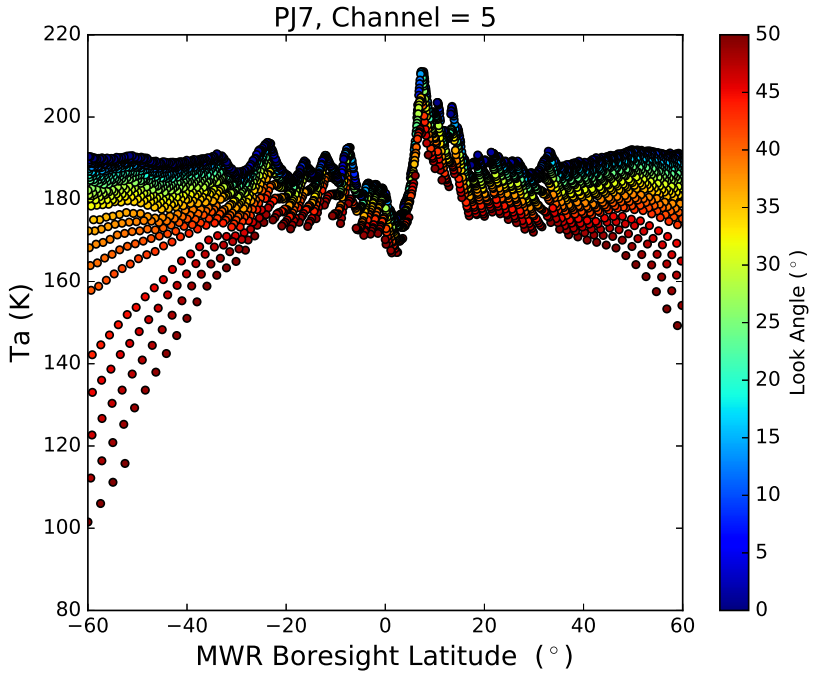

Figure 6.47: Measured antenna temperature as a function of latitude for channel 5 during PJ7 at longitude 52°E with the colors representing the look angle of each measurement.

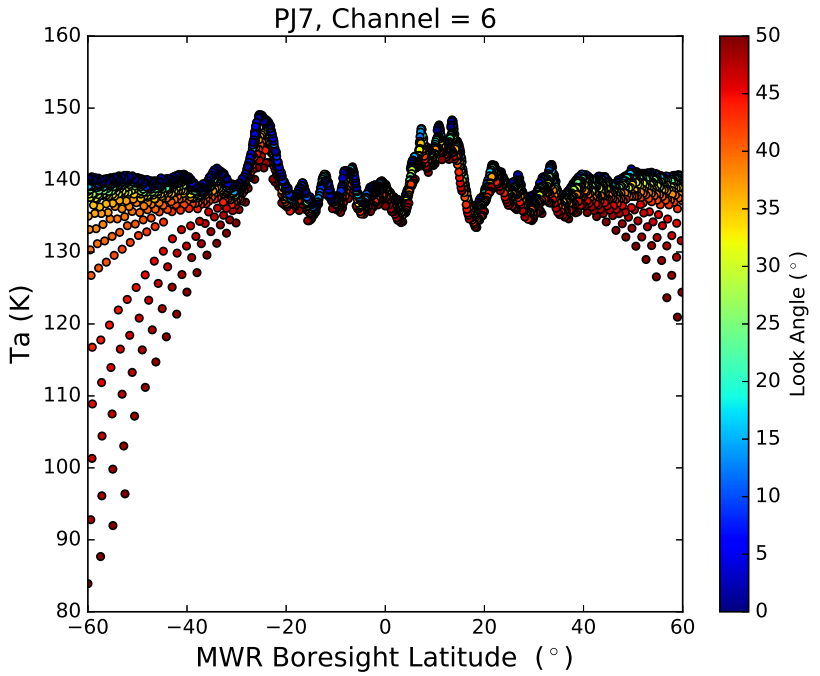

Figure 6.48: Measured antenna temperature as a function of latitude for channel 6 during PJ7 at longitude 52°E with the colors representing the look angle of each measurement.

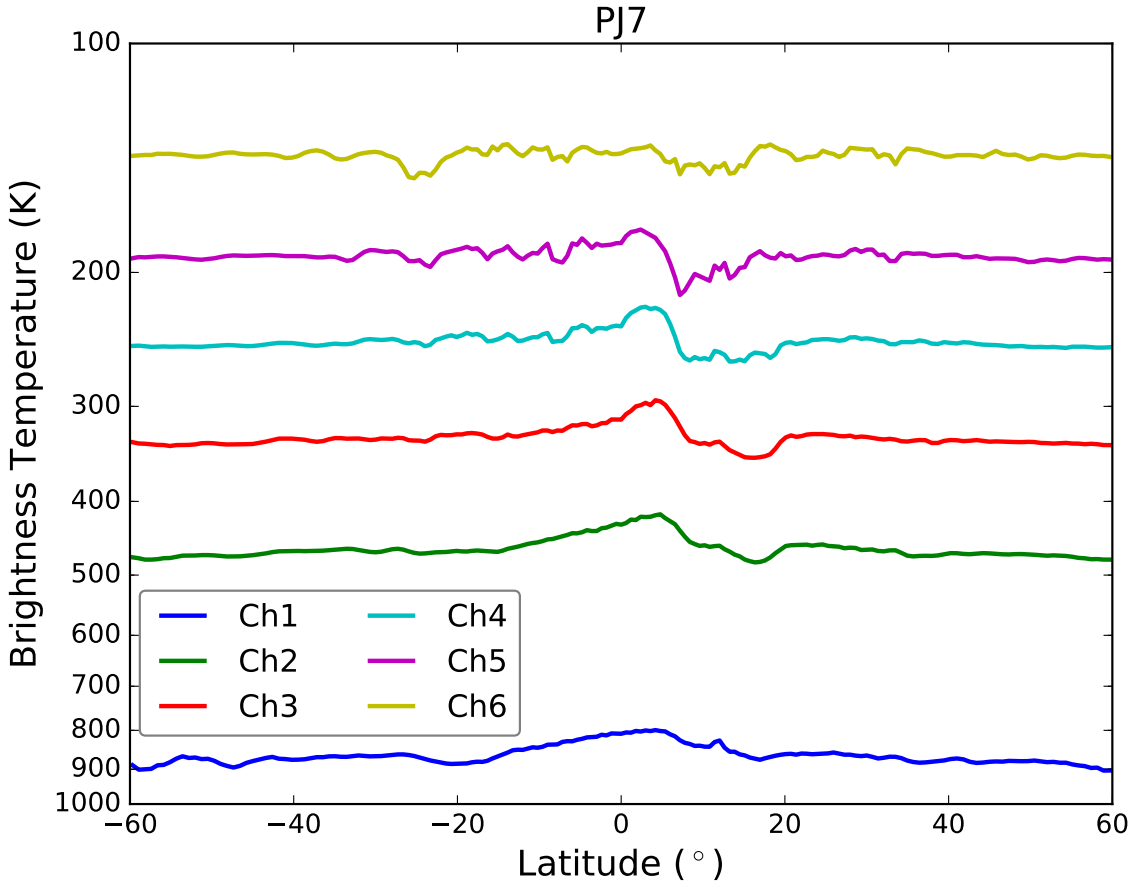

Figure 6.49: Deconvolved nadir brightness temperature as a function of latitude for all six channels for data during PJ7 at longitude 52°E.

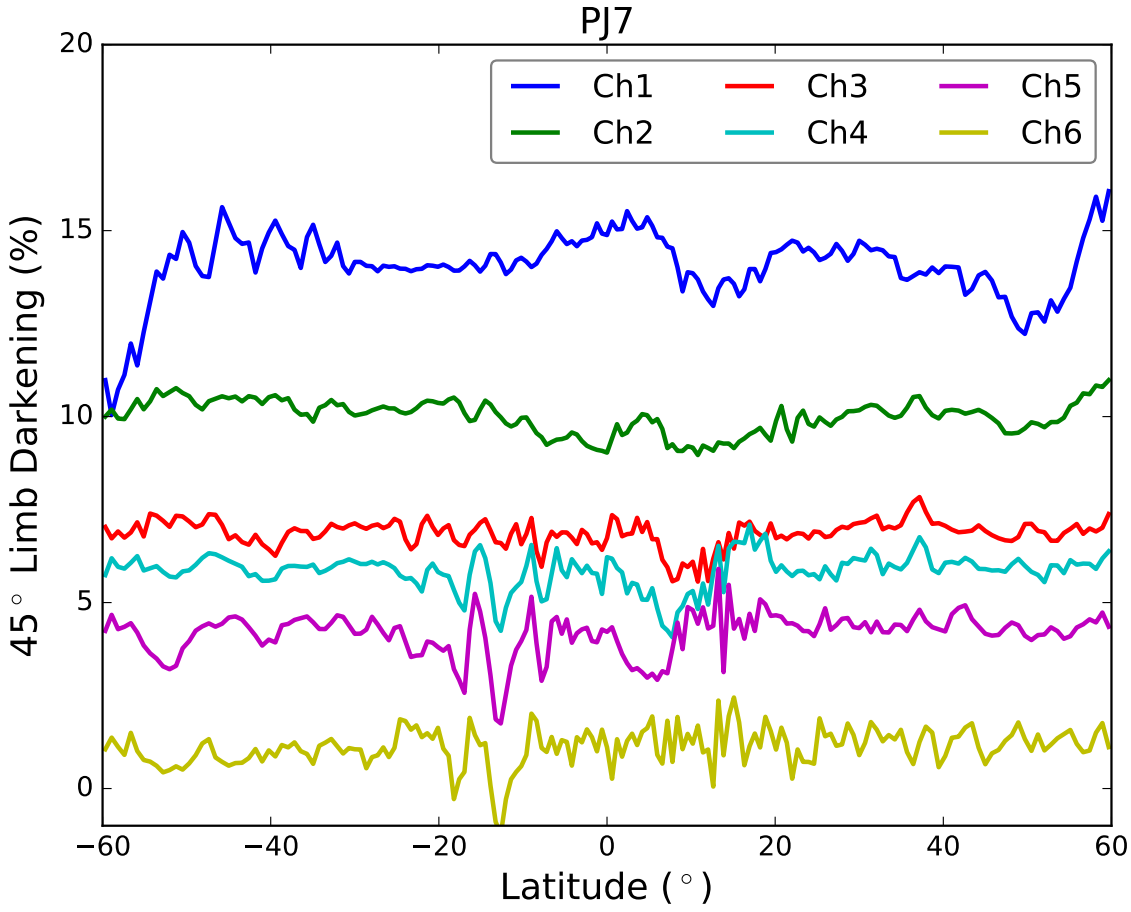

Figure 6.50: 45° limb darkening as a function of latitude for all six channels for data during PJ7 at longitude 52°E.

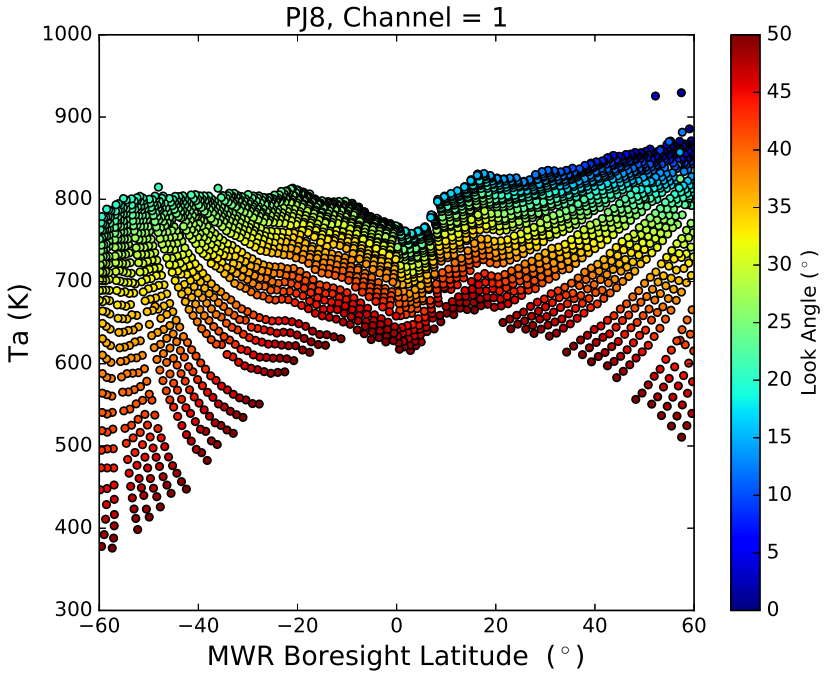

Figure 6.51: Measured antenna temperature as a function of latitude for channel 1 during PJ8 at longitude 322°E with the colors representing the look angle of each measurement.

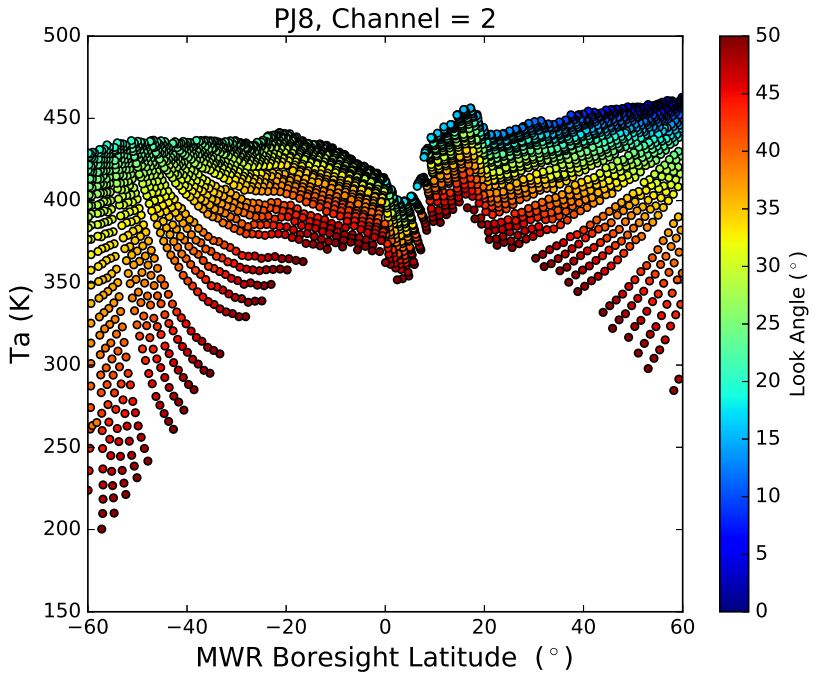

Figure 6.52: Measured antenna temperature as a function of latitude for channel 2 during PJ8 at longitude 322°E with the colors representing the look angle of each measurement.

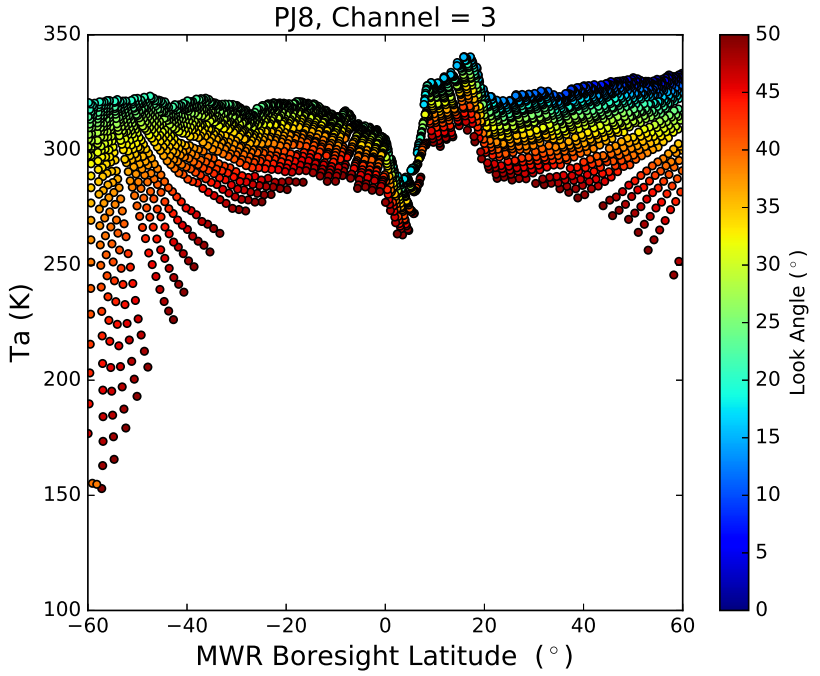

Figure 6.53: Measured antenna temperature as a function of latitude for channel 3 during PJ8 at longitude 322°E with the colors representing the look angle of each measurement.

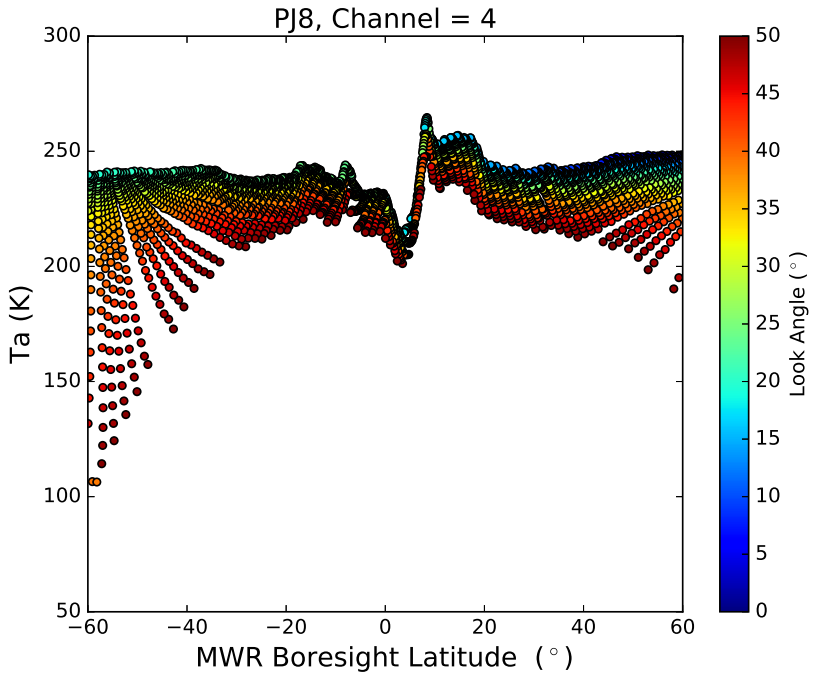

Figure 6.54: Measured antenna temperature as a function of latitude for channel 4 during PJ8 at longitude 322°E with the colors representing the look angle of each measurement.

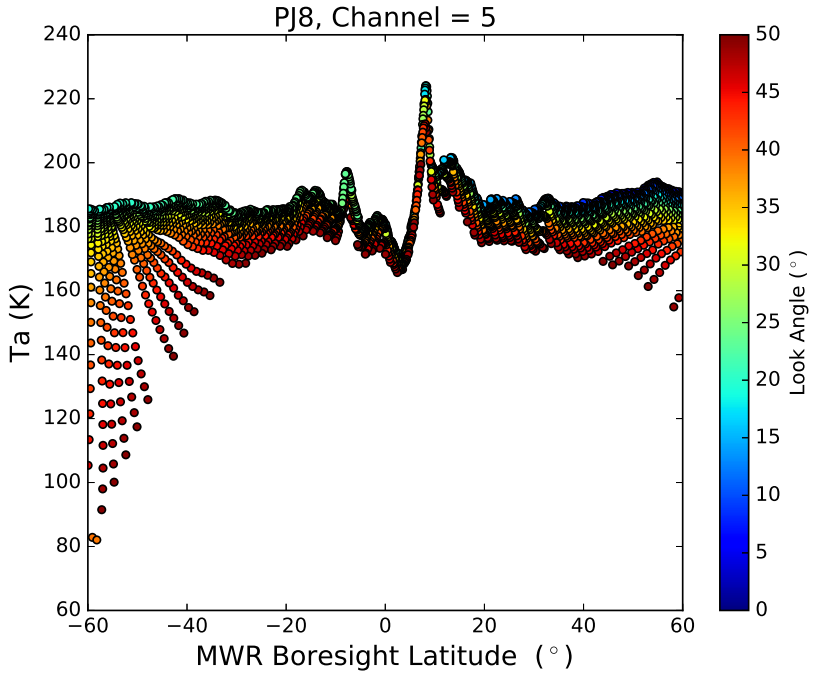

Figure 6.55: Measured antenna temperature as a function of latitude for channel 5 during PJ8 at longitude 322°E with the colors representing the look angle of each measurement.

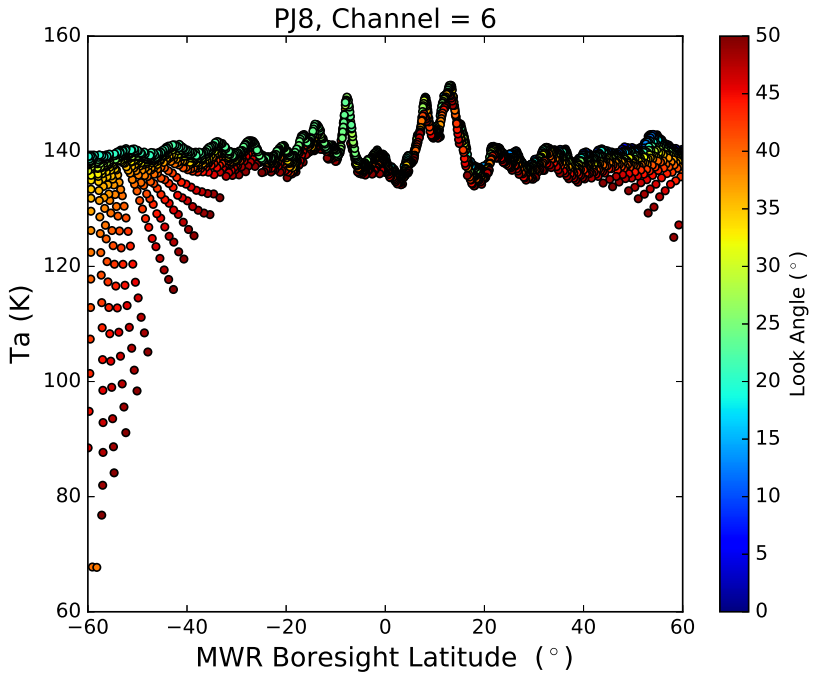

Figure 6.56: Measured antenna temperature as a function of latitude for channel 6 during PJ8 at longitude 322°E with the colors representing the look angle of each measurement.

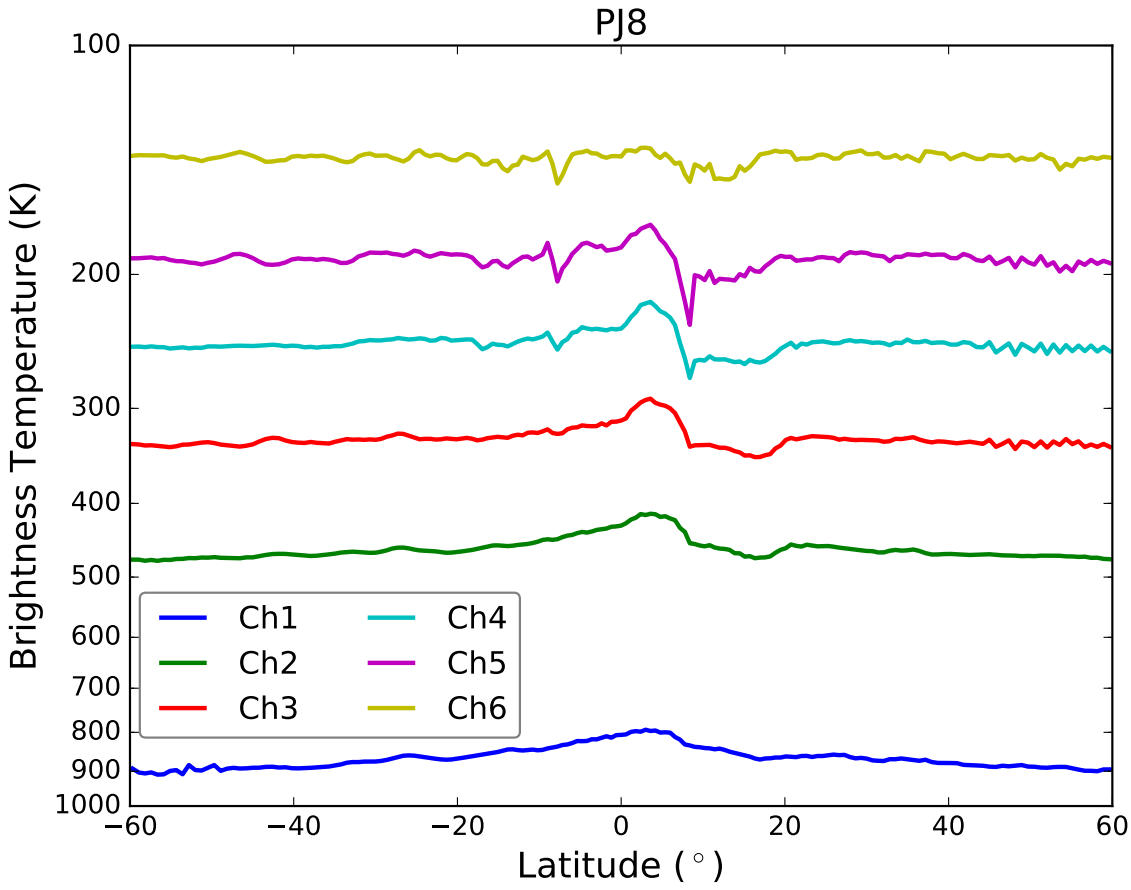

Figure 6.57: Deconvolved nadir brightness temperature as a function of latitude for all six channels for data during PJ8 at longitude 322°E.

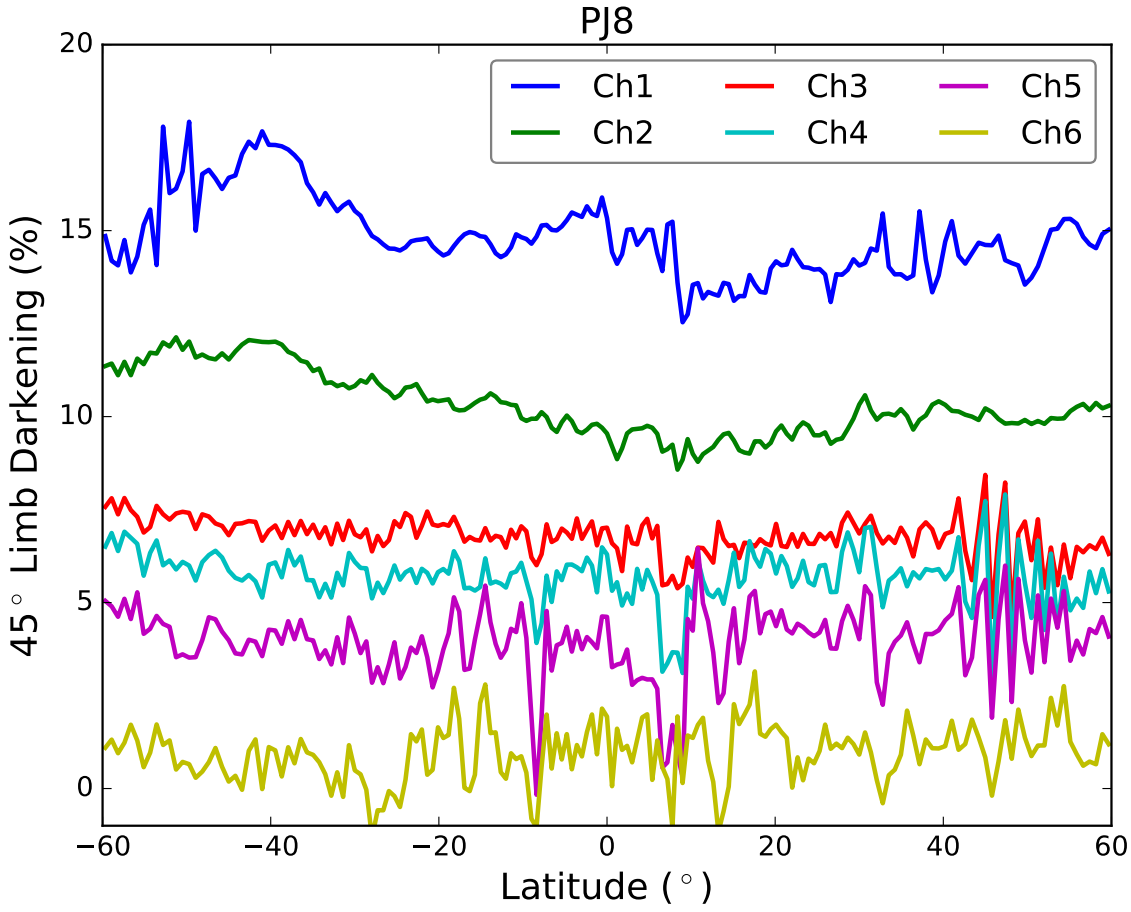

Figure 6.58: 45° limb darkening as a function of latitude for all six channels for data during PJ8 at longitude 322°E.

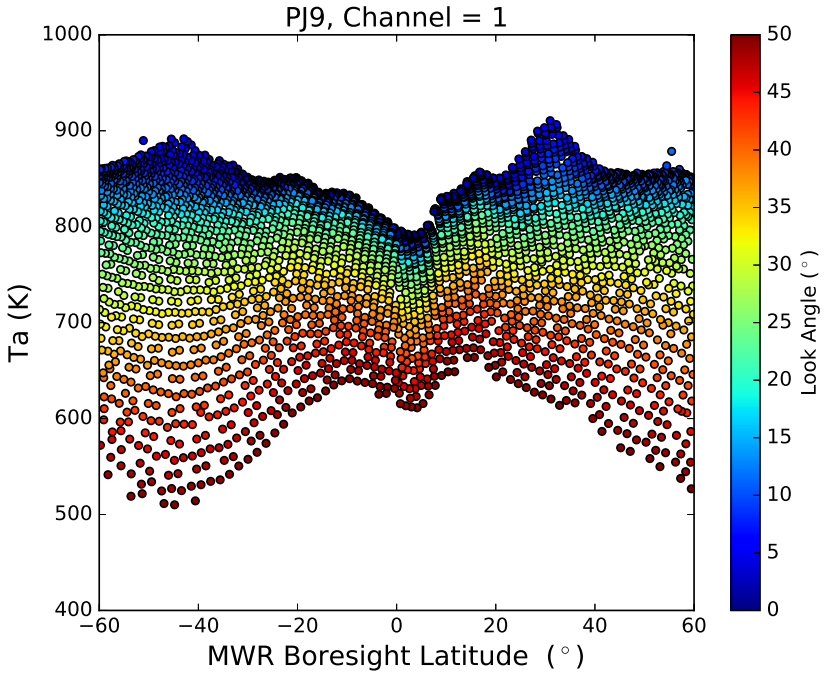

Figure 6.59: Measured antenna temperature as a function of latitude for channel 1 during PJ9 at longitude 232°E with the colors representing the look angle of each measurement.

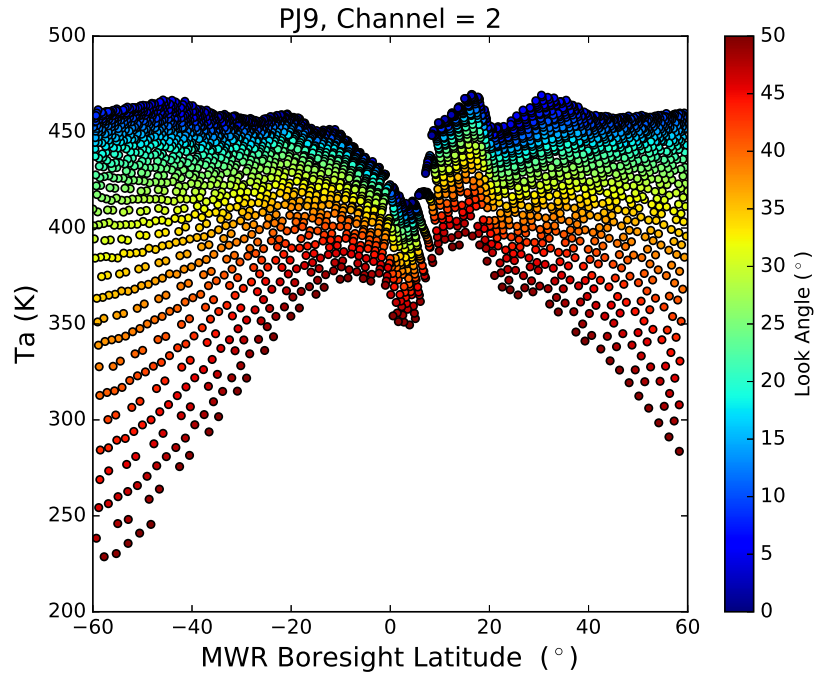

Figure 6.60: Measured antenna temperature as a function of latitude for channel 2 during PJ9 at longitude 232°E with the colors representing the look angle of each measurement.

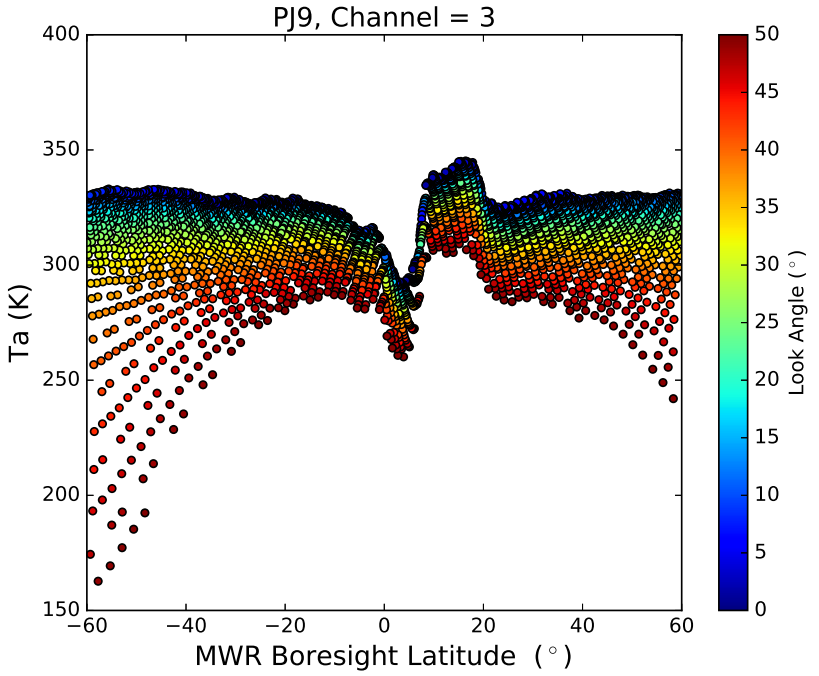

Figure 6.61: Measured antenna temperature as a function of latitude for channel 3 during PJ9 at longitude 232°E with the colors representing the look angle of each measurement.

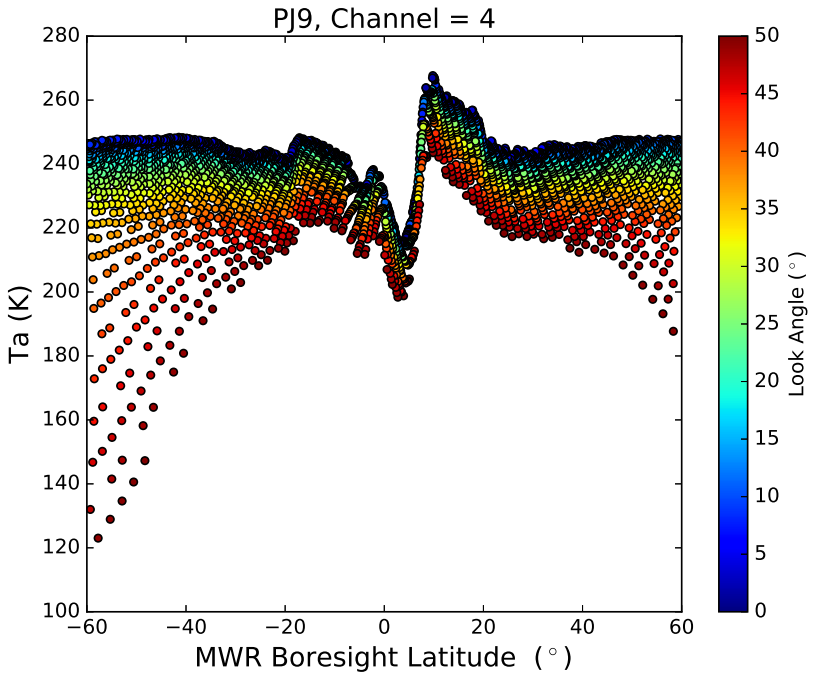

Figure 6.62: Measured antenna temperature as a function of latitude for channel 4 during PJ9 at longitude 232°E with the colors representing the look angle of each measurement.

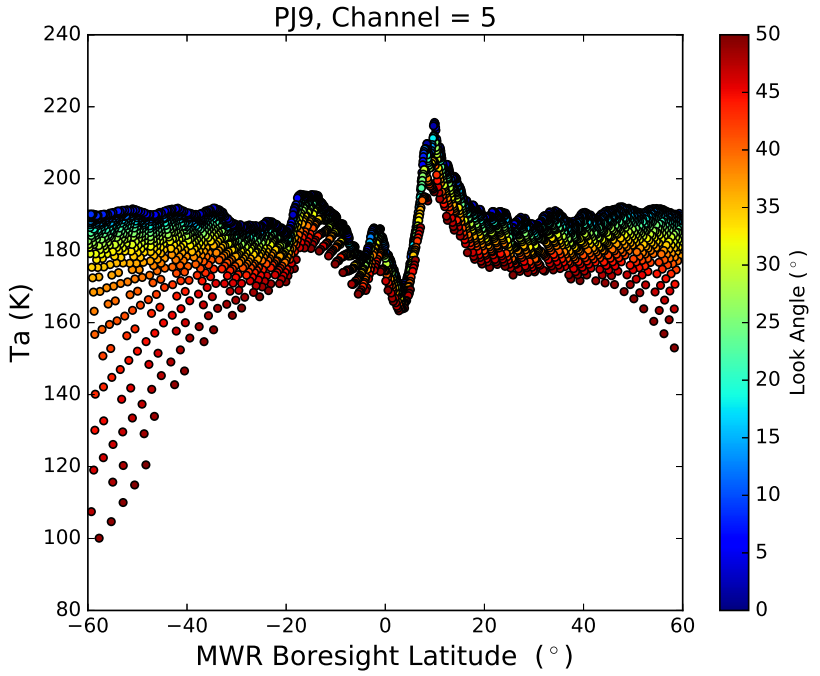

Figure 6.63: Measured antenna temperature as a function of latitude for channel 5 during PJ9 at longitude 232°E with the colors representing the look angle of each measurement.

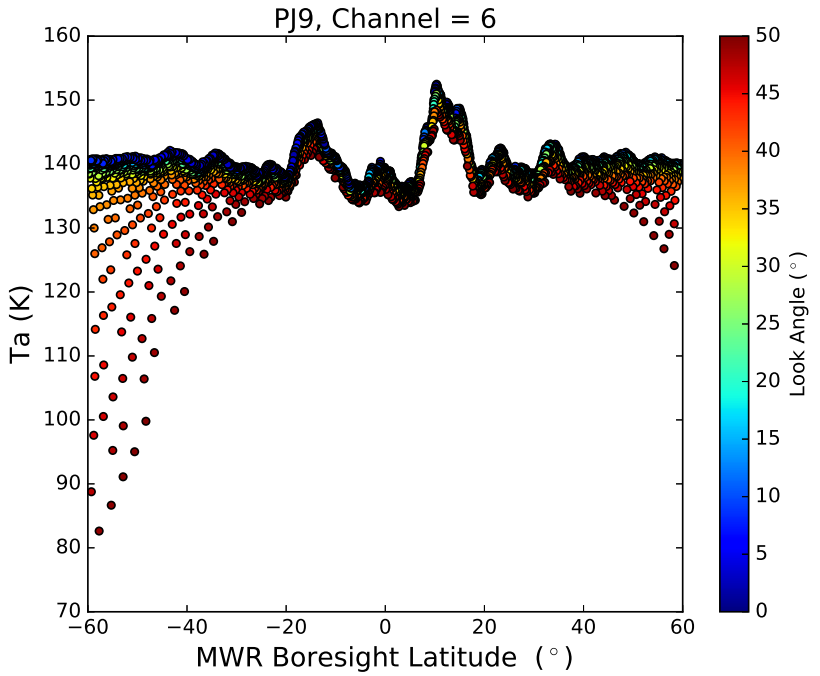

Figure 6.64: Measured antenna temperature as a function of latitude for channel 6 during PJ9 at longitude 232°E with the colors representing the look angle of each measurement.

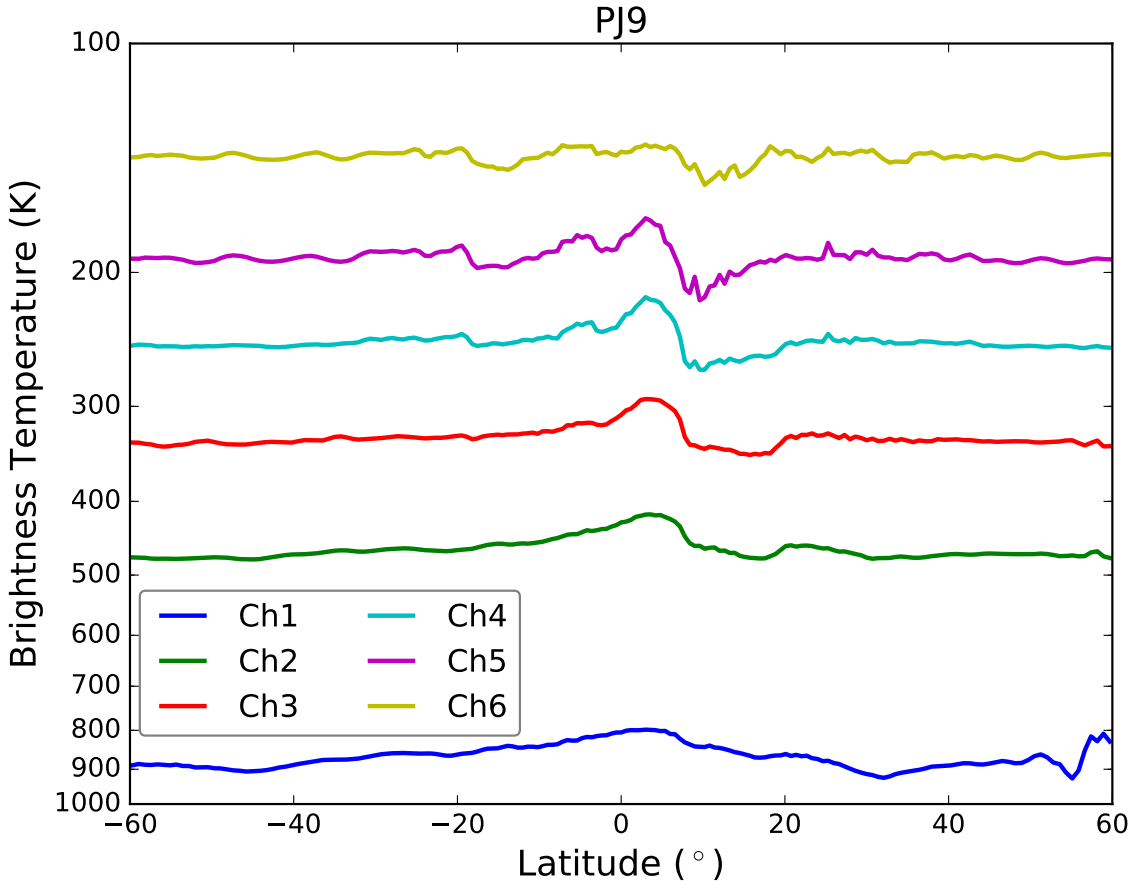

Figure 6.65: Deconvolved nadir brightness temperature as a function of latitude for all six channels for data during PJ9 at longitude 232°E.

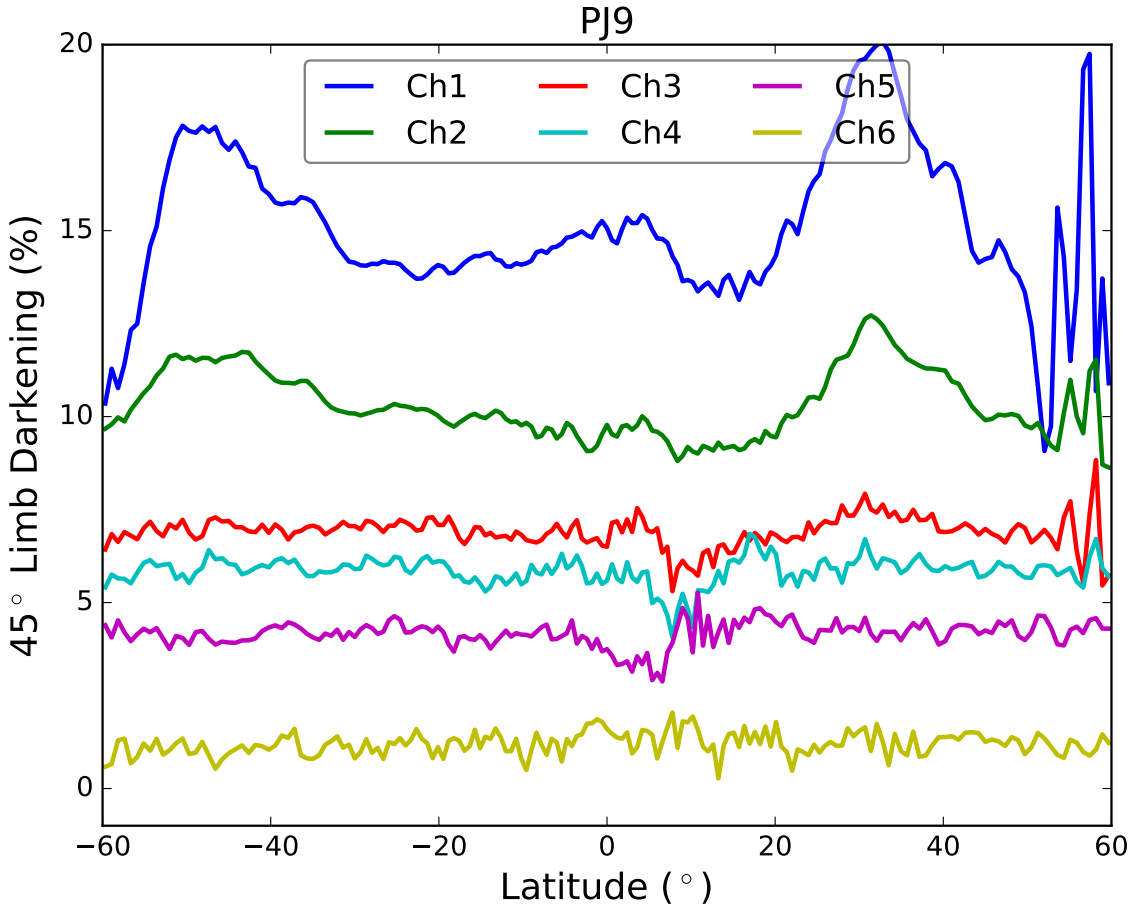

Figure 6.66: 45° limb darkening as a function of latitude for all six channels for data during PJ9 at longitude 232°E.

6.2 Unique Features

The main benefit of the Juno spacecraft's 36 orbits is the ability to map different parts of the atmosphere. This allows the comparison of Juno MWR emission measurements between the different longitudes present at each perijove and study unique features at Jupiter. As of the writing of this thesis, two major features have been observed by the Juno MWR, the Auroral Anomaly seen during PJ5 and the Great Red Spot flyover during PJ7.

6.2.1 Auroral Anomaly

On March 27, 2017, Juno flew, for the first time, in its MWR Tilt orbit, compensating for the longitudinal drift of the MWR footprint due to Jupiter's rotation. By orienting the spacecraft's spin vector approximately 14° out of the equatorial plane of Jupiter, the Juno MWR was able to measure the same parcel of atmosphere at multiple emission angles (Janssen et al., 2017a). The majority of the data taken during this perijove was very similar to the previous 3 perijoves. However, an anomaly in emission was seen at latitudes greater than 45°N and a longitude of 187°E. Originally this was thought to be a combination of contamination due to synchrotron radiation and a thick opaque layer deep in the Jovian atmosphere, but an analysis of the longitude of the orbit showed that Juno flew over an especially bright location in the visible northern aurora. The antenna temperatures as a function of emission angle and latitude pertaining to this anomaly for all channels are plotted in Figures 6.67–6.72.

The anomaly seen during this perijove presents itself in two distinct ways: a cold spot, a decrease in antenna temperature, and a hot spot, an increase in antenna temperature. The cold spot appears on Channels 1, 2, and 3 between 45°N–60°N as a decrease in antenna temperature. The Channel 1 data does not reflect a significant difference between nadir antenna temperature and larger emission angles, indicating a low limb darkening. Prior to detecting the cold spot, the Channel 1 data reflects an increase in brightness temperature

between 60°N–80°N.

While this anomaly is most uniquely seen during PJ5's flyover of the northern aurora, similar effects on Channel 1 can be seen during flyovers of the southern aurora. The southern aurora is more circular around the south pole, thus making the auroral effects visible during multiple perijoves. It is most noticeable in Juno MWR measurements taken during PJ1, PJ3, PJ4, and PJ7, as shown in Figures 6.73–6.76. The southern aurora presents itself differently than the northern aurora; instead of containing both a cold and hot spots, only a cold spot is noticed. The southern aurora decreases Channel 1's brightness temperature at latitudes below 60°S, and shows minimum limb darkening

As discussed in Section 4.6, the physical properties needed to properly model the effects of Jupiter's aurora on the Juno MWR have not been directly measured. Assuming the aurora has a similar temperature-pressure profile as the ionosphere, and the charged particle density profile has a similar shape to that of the ionosphere, the cold spot can be explained as microwave emission from the aurora, and the hot spot can be explained as auroral reflection of the synchrotron radiation from the other side of the planet. The hot spot and cold spot occur as a result of variations in the amount of charged particles present in the aurora at their respective latitudes. In the case of the hot spot, reflection of the synchrotron radiation results from a high density of charged particles. Conversely in the cold spot, a lower number density of charged particles will result in absorption of any upwelling microwave signals. In future work, these effects will be studied by developing a radiative transfer model using the analysis described in Chapter 4.6. Additionally, future measurements of potential auroral effects on the jovian microwave emission measured by the Juno MWR will aid in the development and testing of this theory.

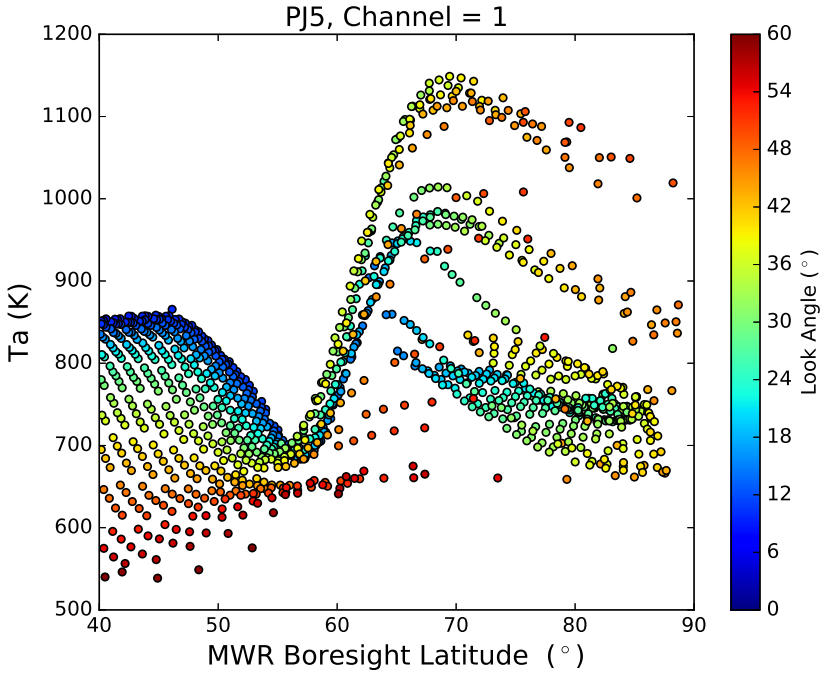

Figure 6.67: Measured antenna temperature as a function of latitude for channel 1 while flying over the PJ5 Auroral anomaly with the colors representing the look angle of each measurement

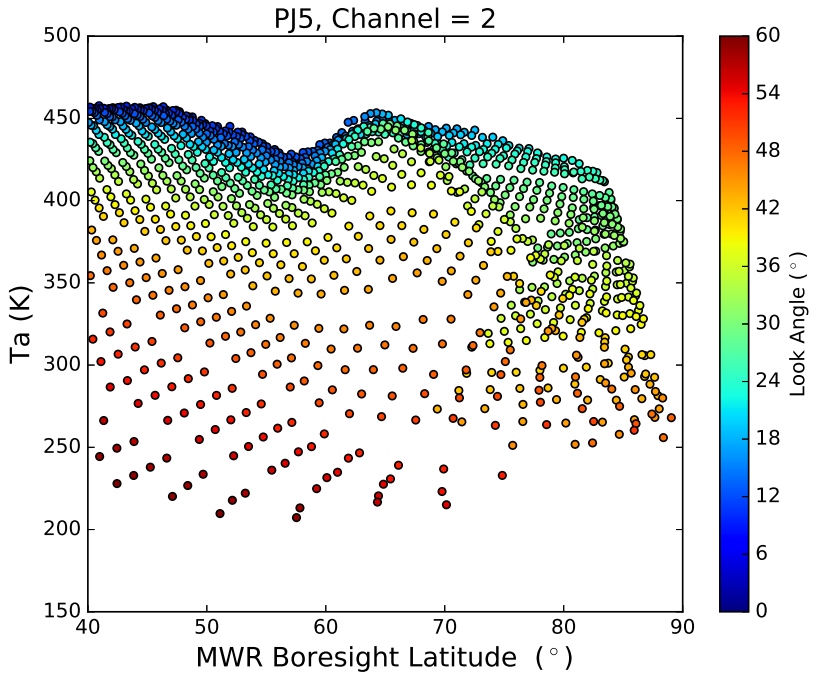

Figure 6.68: Measured antenna temperature as a function of latitude for channel 2 while flying over the PJ5 Auroral anomaly with the colors representing the look angle of each measurement

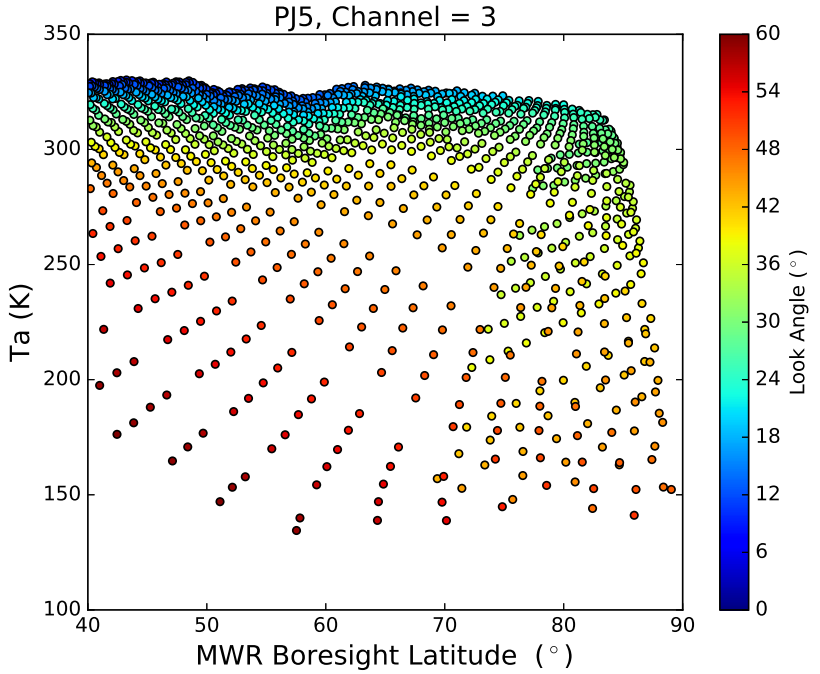

Figure 6.69: Measured antenna temperature as a function of latitude for channel 3 while flying over the PJ5 Auroral anomaly with the colors representing the look angle of each measurement

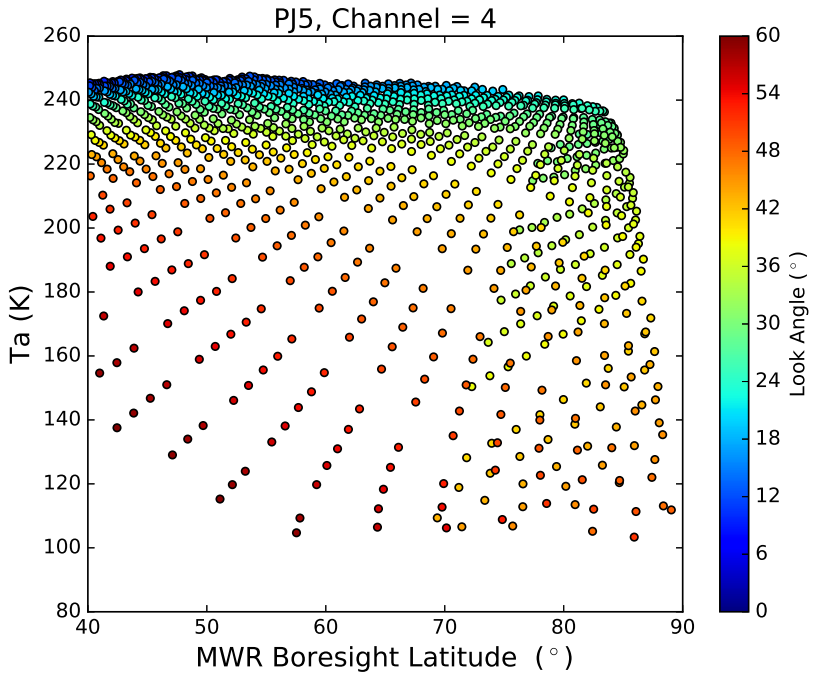

Figure 6.70: Measured antenna temperature as a function of latitude for channel 4 while flying over the PJ5 Auroral anomaly with the colors representing the look angle of each measurement

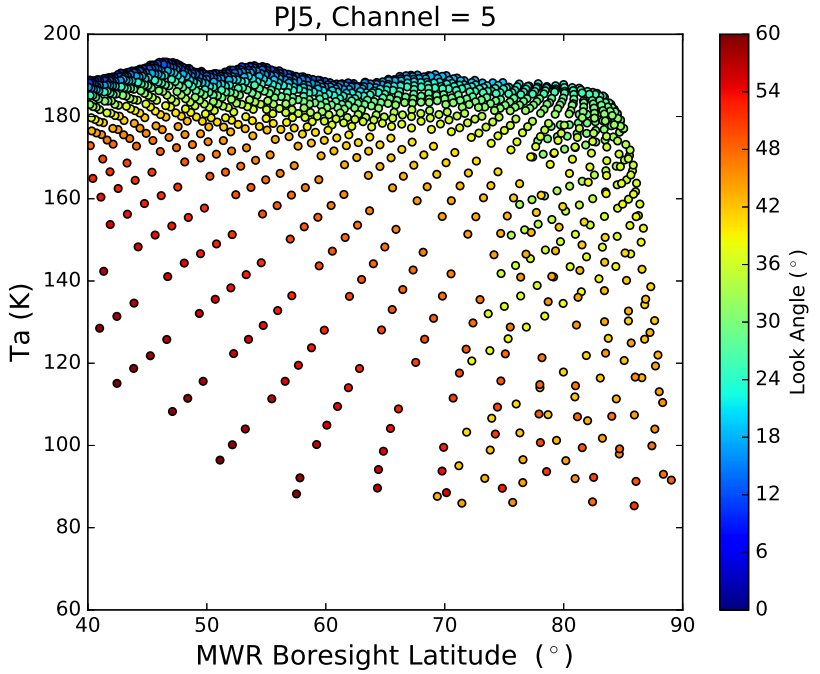

Figure 6.71: Measured antenna temperature as a function of latitude for channel 5 while flying over the PJ5 Auroral anomaly with the colors representing the look angle of each measurement

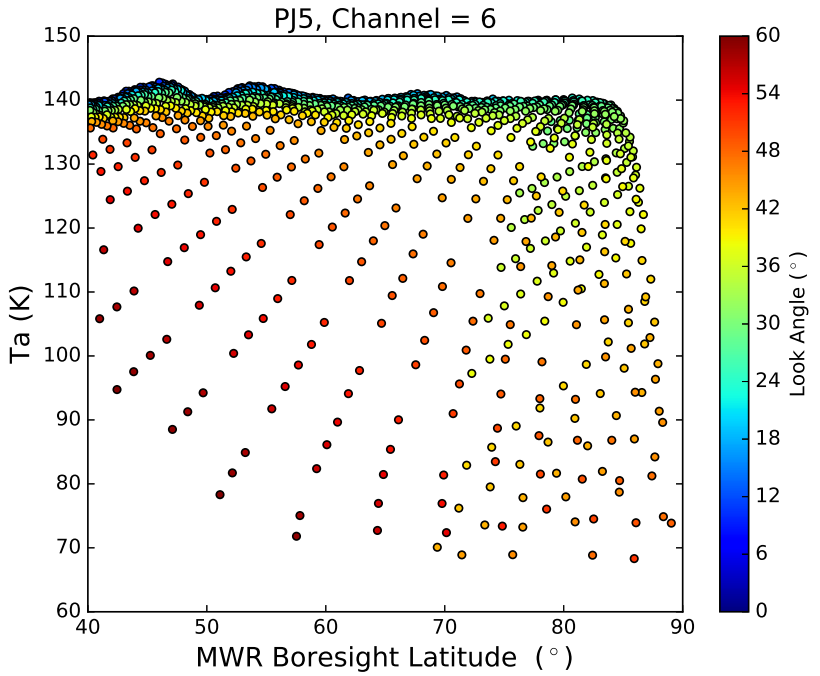

Figure 6.72: Measured antenna temperature as a function of latitude for channel 6 while flying over the PJ5 Auroral anomaly with the colors representing the look angle of each measurement

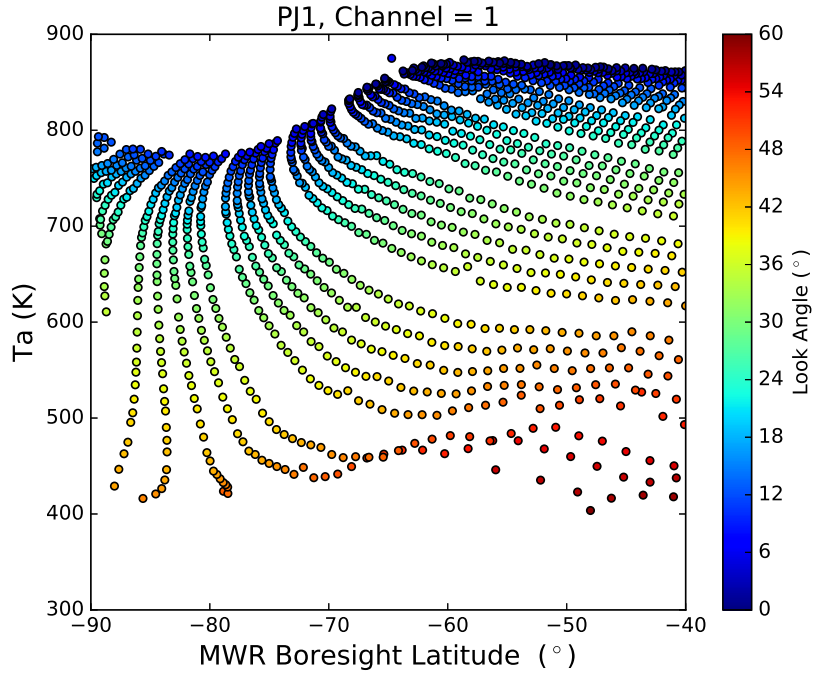

Figure 6.73: Measured antenna temperature as a function of latitude for channel 1 during the PJ1 Southern Auroral anomaly with the colors representing the look angle of each measurement

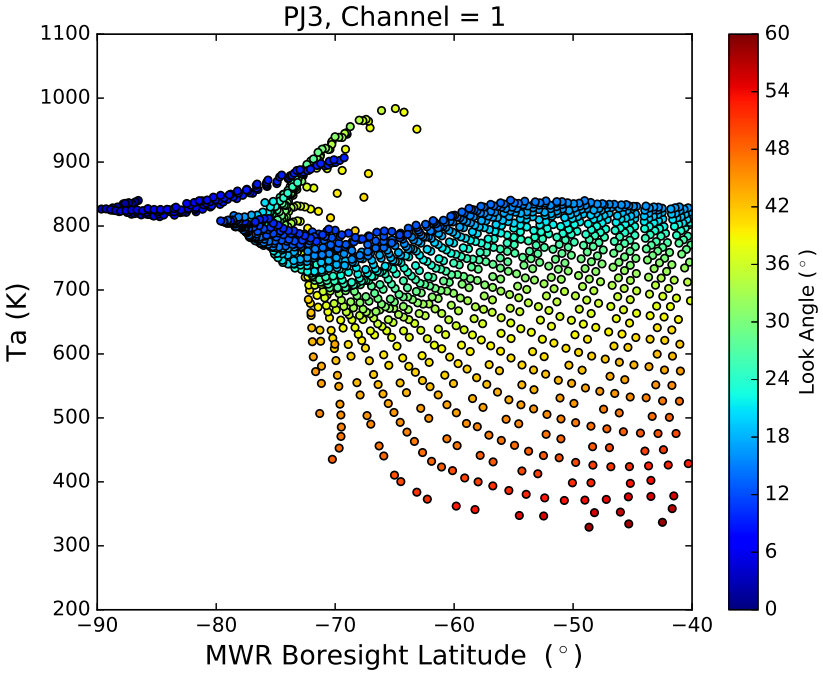

Figure 6.74: Measured antenna temperature as a function of latitude for channel 1 during the PJ3 Southern Auroral anomaly with the colors representing the look angle of each measurement

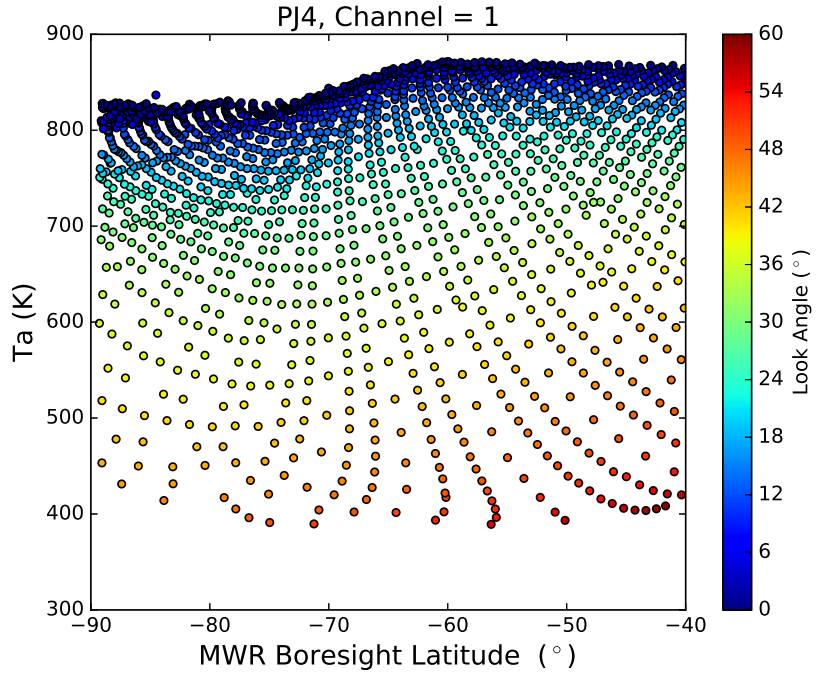

Figure 6.75: Measured antenna temperature as a function of latitude for channel 1 during the PJ4 Southern Auroral anomaly with the colors representing the look angle of each measurement

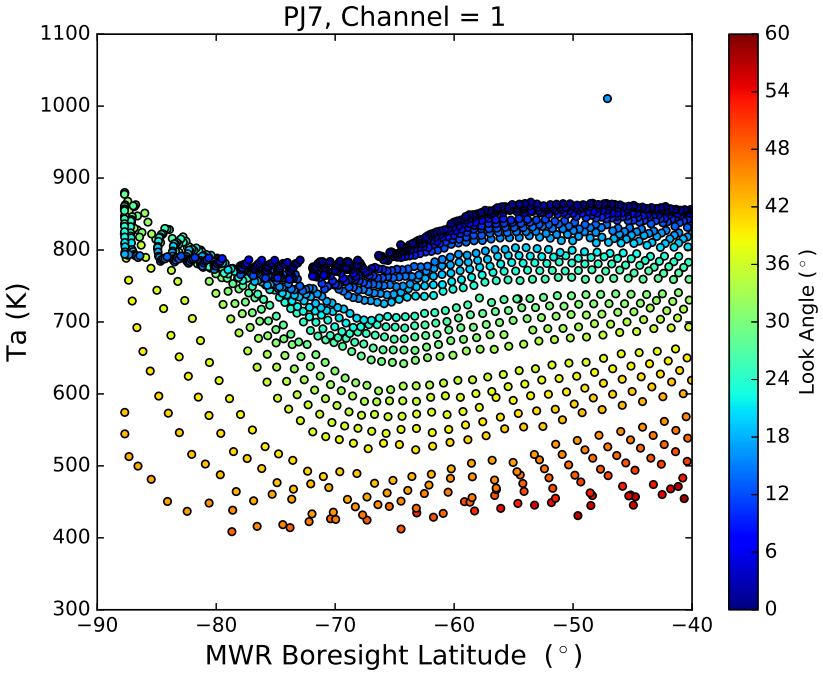

Figure 6.76: Measured antenna temperature as a function of latitude for channel 1 during the PJ7 Southern Auroral anomaly with the colors representing the look angle of each measurement

6.2.2 Great Red Spot Flyover

Jupiter's most well known feature, the Great Red Spot (GRS), is a constant high pressure zone, producing an anticyclonic storm located at 22° south of the equator. The Great Red Spot has been continuously observed since 1830, 187 years (Rogers, 1995) . Earlier observations of a giant storm from 1665 to 1713 have been reported but it is unclear if these are observations of the GRS we know today (Rogers, 1995).

The GRS rotates counter-clockwise with a period of approximately six Earth days, 14 Jovian days, or 144 hours. Measuring at 16,350 kilometers, or 1.3 times as wide as Earth, it is the largest feature seen on Jupiter. While the storm's latitude has been stable for a long time, its longitude is subject to constant variation due to the inconstant rotation of Jupiter's atmosphere. The cause of the GRS's reddish color is unknown but theories suggest that the color may be caused by complex organic molecules, red phosphorus, or a compound containing sulphur.

On July 11, 2017, Juno flew over the GRS at an altitude of approximately 8,000 km above the 1 bar atmospheric level. Juno was flying in the MWR orientation, where the spacecraft's spin plane was oriented so as to contain Jupiter's center ensuring that the MWR instrument will measure viewing nadir at all latitudes. Figure 6.77 shows the deconvolved brightness temperature as a function of latitude, longitude, and depth along with a visible image taken by Junocam (Janssen et al., 2017b). Viewing the data in this 3D-map is useful to understand how the Great Red Spot presents itself in each channel. In channels 6, 5, 4, and 3, the microwave emission of GRS appears as cold in the area of the visible storm and hot south of the visible storm. However, this does not persist to the deeper channels. Channel 2 does not show a signature of the GRS, but the GRS appears again in channel 1 as a hot area directly correlated to the visible storm. Additionally, Figures 6.78–6.83 show the measured antenna temperature as a function of latitude and look angles for all six channels for latitudes associated with the Great Red Spot, and have been included for reference.

Since its first observation 187 years ago, the Great Red Spot's dynamics and longevity

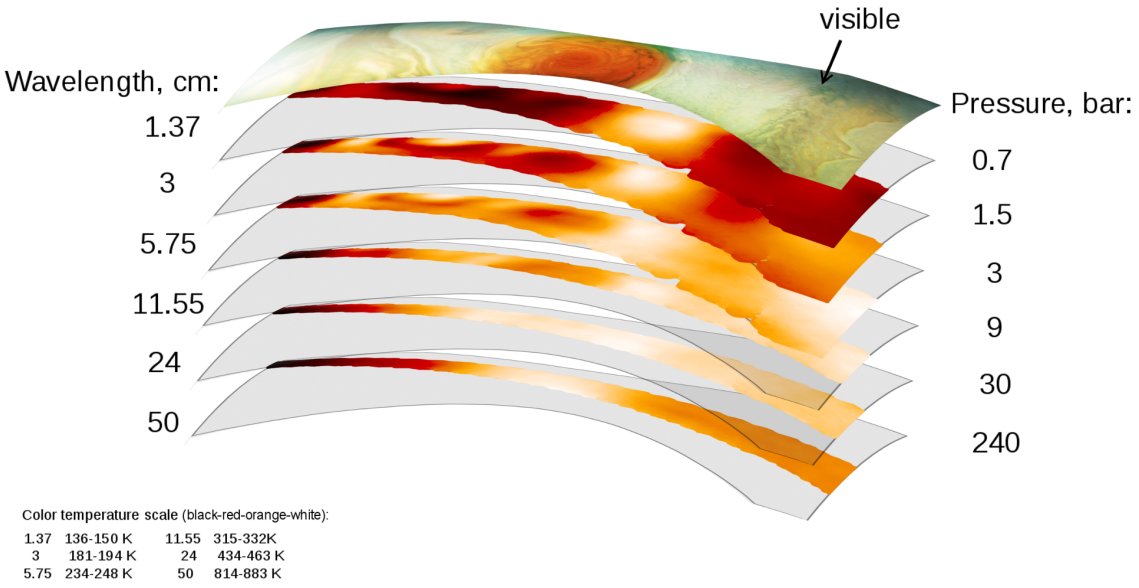

Figure 6.77: 3D map of the Juno MWR deconvolved brightness temperature. The image includes a visible image of the GRS taken by Junocam. Each following layer is related to the brightness temperature at channels 6–1. Each channel is scaled to the same data range to show features at each channel where the red is the coldest temperature and the white is the hottest. The lowest and highest values for each channel are listed in the left hand corner. The south pole is to the right of the image (Janssen et al., 2017b).

has been a mystery to scientists who have only had a cloud top view of this Jovian storm. Juno's MWR measures radio waves originating from pressures 100 times greater than the cloud tops, indicate that the GRS originates from deep in the Jovian atmosphere. In future work, the dynamics and development of the Great Red Spot will be studied and expanded by the Juno MWR measurements.

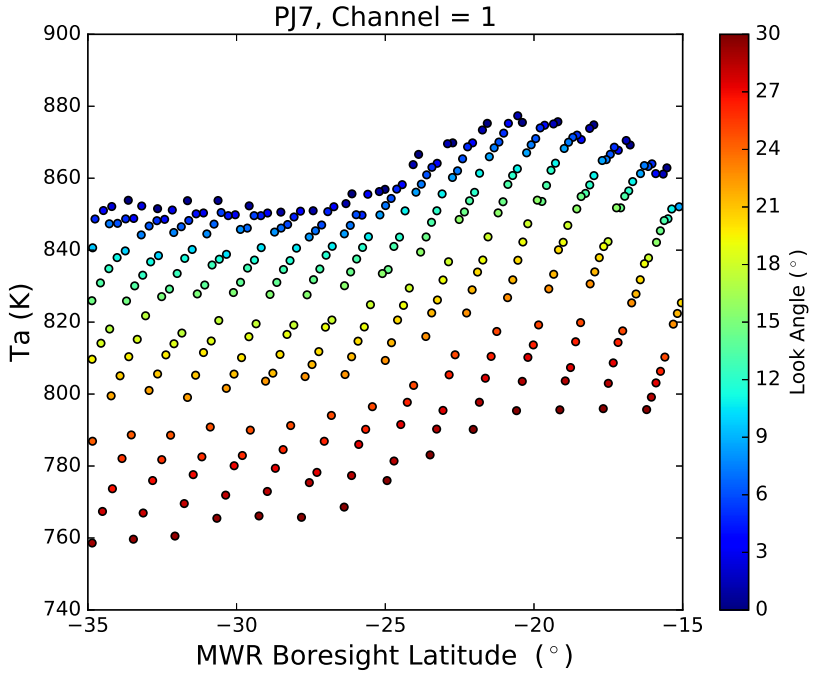

Figure 6.78: Measured antenna temperature as a function of latitude for channel 1 during the PJ7 Great Red Spot flyover with the colors representing the look angle of each measurement

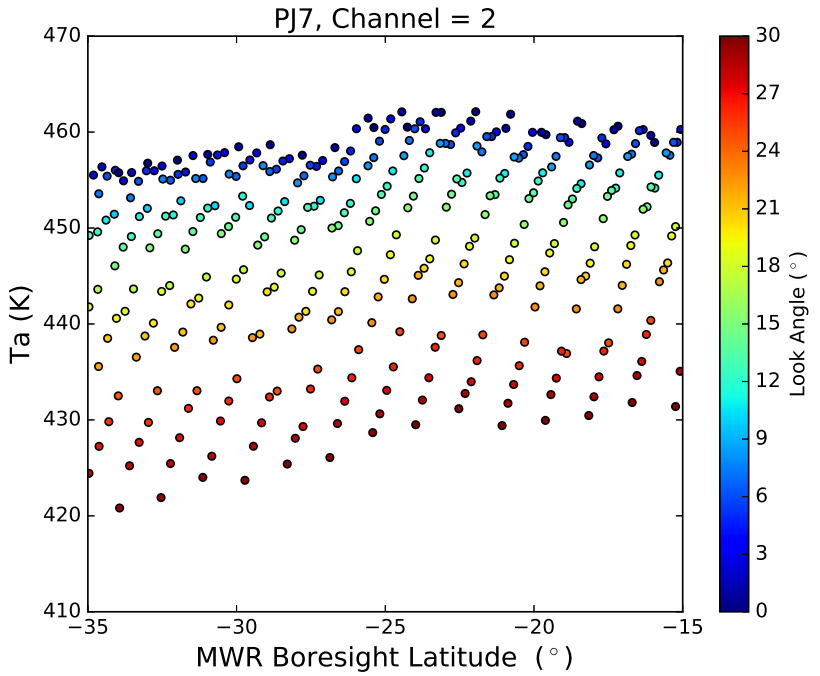

Figure 6.79: Measured antenna temperature as a function of latitude for channel 2 during the PJ7 Great Red Spot flyover with the colors representing the look angle of each measurement

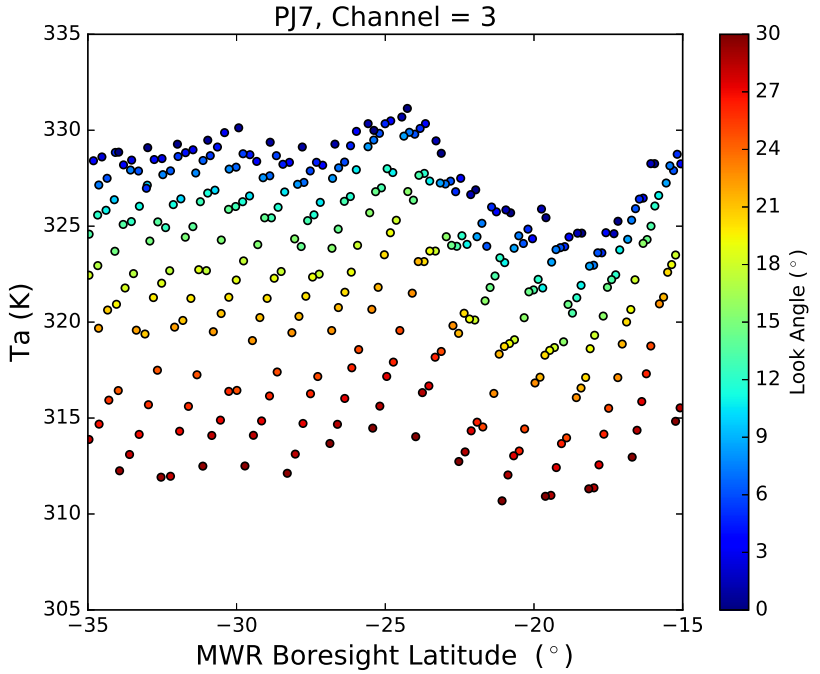

Figure 6.80: Measured antenna temperature as a function of latitude for channel 3 during the PJ7 Great Red Spot flyover with the colors representing the look angle of each measurement

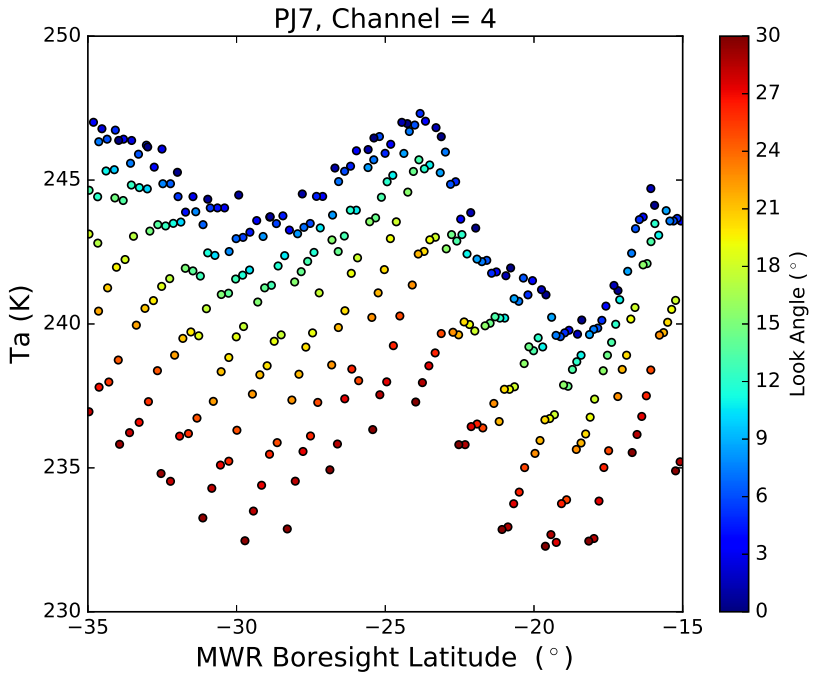

Figure 6.81: Measured antenna temperature as a function of latitude for channel 4 during the PJ7 Great Red Spot flyover with the colors representing the look angle of each measurement

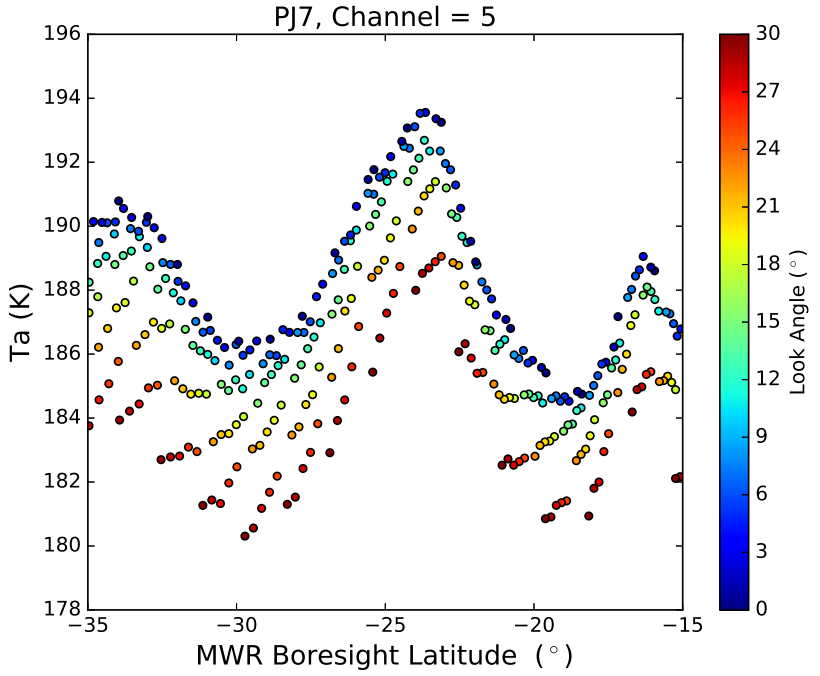

Figure 6.82: Measured antenna temperature as a function of latitude for channel 5 during the PJ7 Great Red Spot flyover with the colors representing the look angle of each measurement

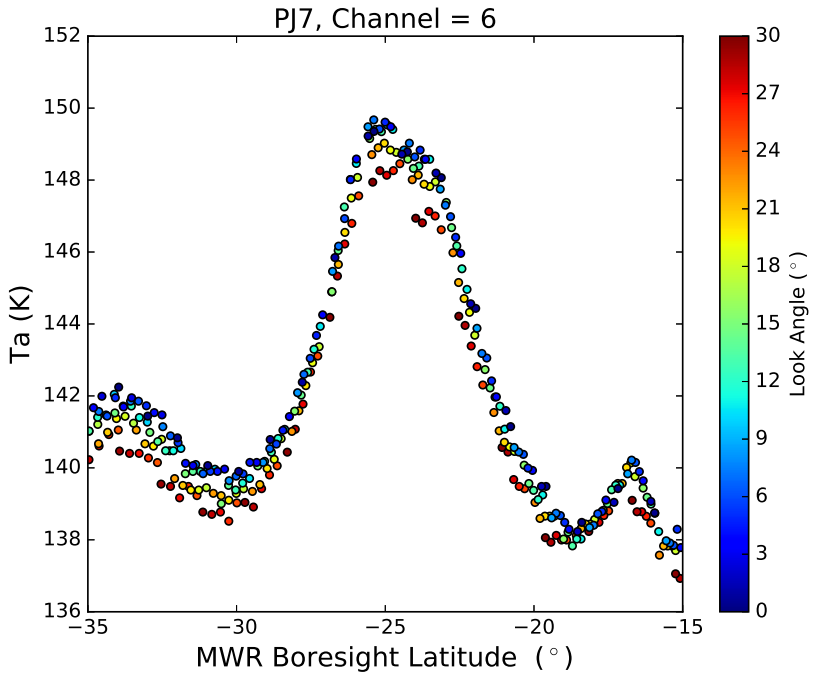

Figure 6.83: Measured antenna temperature as a function of latitude for channel 6 during the PJ7 Great Red Spot flyover with the colors representing the look angle of each measurement

CHAPTER 7
ABUNDANCE PROFILE RETRIEVALS

One of the primary objectives of this work has been to develop a consistent retrieval algorithm for deriving the abundance of ammonia and water vapor in Jupiter's deep atmosphere using emission measurements from the Juno MWR. Through the analysis of the data it was discovered that the distribution of ammonia was not uniform with respect to altitude (Li et al., 2017). This requires the retrieval algorithm to solve not only for the deep abundance, but also the distribution of ammonia with respect to altitude. Li et al. (2017) proposed a possible retrieval algorithm and ammonia abundance profile based on emission measurements from the first perijove. However, the modeled limb darkening for Channel 1 is on average 2-3% higher than that measured. While this discrepancy can be reduced by increasing the deep water vapor abundance, the retrieval algorithm presented in this work considers the presence of alkali metals ionizing deep in the jovian atmosphere and their resulting intrinsic microwave opacity. The retrieval algorithm does not allow the cutoff temperature, discussed in depth in Chapter 4.5, to vary as a function of latitude. The developed retrieval algorithm initially solves for the deep abundance of ammonia and water vapor, and the presence of ionizing alkali metals at latitudes near 2.4°N. It then uses these retrieved values to solve for the distribution of ammonia at pressures less than 92 bars over a wide range of latitudes. 2.4°N was used as a reference location because it has the lowest brightness temperature across all perijoves.

This chapter begins by presenting a formalism for the retrieval algorithm developed in this work. Afterwards, retrieval results near 2.4°N latitude with and without the presence of ionizing alkali metals are presented. Finally, a complete retrieval of the deep abundance of ammonia and water vapor, along with the vertical distribution of ammonia at pressures less than 92 bars, with and without the presence of ionizing alkali metals is presented.

Both of these retrievals use the measurements taken at 2.4°N to initially solve for the deep abundances for ammonia and water vapor and the location of the ionizing alkali metals (when needed). Finally, the errors associated with this retrieval technique are discussed.

7.1 Retrieval Method

The prevailing method of fitting microwave spectra is done manually by forwarding modeling and trial-and-error to find models that reproduce the data. In this work, the process is automated by using the Limited-memory BFGS (Boyden-Fletcher-Goldfarb-Shanno) technique with simple box constraints (L-BFGS-B) as the optimization technique (Byrd et al., 1995). This algorithm's target problem is to minimize $f(\mathbf{x})$, defined hereafter, over a constrained state vector $\mathbf{x}$. The L -BFGS -B algorithm requires that f is a differentiable scale function and uses the Hessian matrix to navigate through the variable state. The Hessian matrix is defined as the second derivative of the function f. Unlike other minimization algorithms the L-BFGS-B algorithm uses an estimation of the Hessian matrix, saving on memory requirements and allowing for a larger state vector. This section describes the numerical approach to retrieving jovian atmospheric profiles using deconvolved microwave brightness measurements from the Juno MWR. The method presented here can be extended in a straightforward manner to other multi-wavelength, spatially resolved observations of Jupiter or any other planet.

The algorithm begins with an initial estimate of the optimal value of the state vector, $\mathbf{x_0}$, and iteratively refines the estimate with a sequence of better estimates $\mathbf{x_1}, \mathbf{x_2}, \ldots \mathbf{x_k}$. In this work the initial estimate is determined randomly, and the algorithm is run multiple times to ensure the solution represents a global minimum. The derivative of the function

$$g_k = \nabla f(\mathbf{x_k}) \tag{7.1}$$

is used as the driver of the algorithm, determining the direction of the steepest descent,

and used to form the estimate of the Hessian matrix. At each iteration, k, the algorithm identifies the fixed and free variables at each step and only minimizes the free variables. A variable is defined as an element in the state vector and is considered free if

$$l_i \leq x_i \leq u_i \tag{7.2}$$

where for element i, $\mathbf{l}$ and $\mathbf{u}$ are the lower and upper bound constraint vector, respectively.

The minimization function used in this work is

$$f(\mathbf{x}) = \left|\left|\frac{\Delta_{Tb}}{\sigma_{Tb}}\right|\right| + (\lambda)\left|\left|\frac{\Delta_{LD}}{\sigma_{LD}}\right|\right| + \alpha||\mathbf{Ds}|| \tag{7.3}$$

where

$$\Delta_{Tb} = T_{b,nn}(\mathbf{x}, \Theta_{Tb}) - T_{b,meas}(\Theta_{Tb}) \tag{7.4}$$

$$\Delta_{LD} = LD_{nn}(\mathbf{x}, \Theta_{LD}) - LD_{meas}(\Theta_{LD}) \tag{7.5}$$

and, $\mathbf{x}$ is the state vector defined hereafter, $T_{b,meas}$ is the measured brightness temperature at look angle Θ_{Tb}, LD_{meas} is the measured limb darkening at look angle Θ_{LD}, λ is the limb darkening weight, $T_{b,nn}$ and LD_{nn} are the neural network surrogates of the brightness temperature and limb darkening model, respectively, σ_{Tb} and σ_{LD} is the uncertainty in the measured brightness temperature and limb darkening, respectively, α is the regularization scale, $\mathbf{s}$ is the scaling matrix which is part of the state vector, and $\mathbf{D}$ is the Tikhonov regularization matrix. The minimization function can be split into three distinct parts: the error between the modeled and measured brightness temperature, the error between the modeled and measured limb darkening, and a regularization term which imposes a penalty for a large variance in the $\mathbf{s}$ with respect to altitude. Regularization is included to represent prior knowledge of the climatological state.

The state vector $\mathbf{x}$ is defined as

$$\mathbf{x} = [NH_3,\ H_2O,\ \mathbf{s},\ T_c] \tag{7.6}$$

where NH_3 and H_2O, are the deep abundances of ammonia and water vapor, respectively, for the entire perijove, $\mathbf{s}$ is the ammonia abundance scaling matrix for the perijove with the size $n \times l$ where n is the number of scaling points in the vertical direction and l is the number of latitudes measured, and T_c is the ionizing alkali metal cutoff temperature.

The uncertainty in measured brightness temperature is defined as

$$\sigma_{Tb} = 0.02 \times T_{b,meas} \tag{7.7}$$

and the uncertainty in measured limb darkening for each channel are

$$\sigma_{LD} = [0.3,\ 0.3,\ 0.3,\ 0.3,\ 0.3,\ 0.3]\% \tag{7.8}$$

Both of these uncertainties are derived from Janssen et al. (2017a) and Li et al., 2017.

A unique benefit of the L-BFGS-B algorithm is that the same minimization function can be used for any subdomain of the state vector. This is accomplished by setting the constraints ($\mathbf{l}$ and $\mathbf{u}$) of the state vector to a determined value. For example if the desired subdomain was one where the deep water vapor abundance was preset to 9.0x solar, the constraints for deep water vapor abundance can be set to 9.0x solar. Table 7.1 shows the $\mathbf{l}$ (lower) and $\mathbf{u}$ (upper) vectors used in the retrievals main domains presented in this work. This, along with the use of a neural network surrogate, allows for multiple retrievals of the domain and subdomains to be performed quickly. It is important to note that the constraints on the scaling factor are wider than the data used to train the surrogate neural network (Table 5.1). This retrieval pushes the surrogate neural network to its limits. However, the errors between the surrogate and JAMRT in this extended domain space are comparable to

Table 7.1: Table of free parameter constraints used in the retrieval algorithm.

	NH_3	H_2O	Scaling amount at Pressure (bar)											T_c
			92.0	33.1	20.1	12.2	7.39	4.48	2.72	1.65	1.0	0.61	0.3	
u	2.7	11.0	1.0	1.0	1.0	1.0	1.0	1.0	1.4	1.4	1.4	1.4	1.4	2000
l	1.8	1.0	1.0	0.1	0.1	0.1	0.1	0.1	0.1	0.1	0.1	0.1	0.1	1300

those inside the two subdomains presented in Chapter 5.3.

In the deconvolution, described in Chapter 4.2, the deconvolved brightness temperatures at each latitude can be represented as a function of look angle and three constants, reducing the complexity of the deconvolved brightness temperatures to three dimensions. To properly encapsulate these three dimensions in the retrieval process, multiple look angles should be used for either brightness temperature (Θ_{Tb}) or limb darkening (Θ_{LD}). At least three separate look angles, including nadir, should be used to ensure the three dimensional representation of the brightness temperature is not projected to a lower dimension.

Tikhonov regularization is an important factor in the retrieval algorithm. By imposing a penalty for large variances in s_l (which are not physical), it forces the solution to have a small variance. The regularization matrix used is the difference matrix:

$$D = \begin{bmatrix} 1 & -1 & 0 & 0 & 0 \\ 0 & 1 & -1 & 0 & 0 \\ 0 & 0 & \dots & \dots & 0 \\ 0 & 0 & 0 & 1 & -1 \end{bmatrix} \tag{7.9}$$

The regularization scale, α, from equation 7.3, provides the ability to tune the strength of the regularization; trading off between goodness of fit and variances in $\mathbf{s}$.

7.2 Retrievals

This section describes retrievals of the deep abundances of ammonia and water vapor and the cutoff temperature of the ionizing alkali metals at latitudes near 2.4°N for all perijoves.

We then present the parameter space used and accompanying results of the retrievals for both subdomains. The retrieval of the ammonia distribution maps with and without deep atmospheric ionizing alkali metals are also described. Only perijoves 5 and 9 are presented in the retrievals without ionized alkali metals. However, ammonia distribution maps from retrievals using ionized alkali metals are presented for all perijoves. Also presented are the parameter space and accompanying errors for each perijove in each subdomain. For clarity the subdomains defined in Chapter 5.3 are referenced here as "without ionized alkali metals" (Subdomain 1) and "with ionized alkali metals" (Subdomain 2).

7.2.1 Equatorial Zone

We have assumed for each subdomain that ammonia and water are well mixed below a sufficiently deep level in the jovian atmosphere. Finding a special place on Jupiter that resembles an ideal adiabat allows us to connect the deep abundances to the shallower levels where they are measured by the Juno MWR. Figure 6.2 shows that the Equatorial Zone (EZ) is a candidate for such a place. The lowest brightness temperature is consistently measured to be at 2.4°N during every perijove. While the measured brightness temperature has the lowest RMS at the equator (0°), it is very difficult to physically model the decreased brightness temperature seen at Channels 1 and 2 near 2.4°N latitude if the equator is used to develop the deep abundances. Therefore, the 2.4°N latitude is the better candidate for this special spot. The mean brightness temperature and RMS for 2.4°N and the equator is shown in Table 7.2. The 2.4°N latitude is consistent in Channels 1, and 2 but varies more in Channels 3, 4, 5, and 6. This can be attributed to "weather" in the upper atmosphere of Jupiter. By picking a latitude that most resembles an ideal adiabat we can assume the temperature-pressure profile and any variation from that will be attributed to the presence of water as is discussed later in this section.

After running preliminary tests, it was found that an ideal adiabat can match the measured brightness temperatures of Channels 1, 2, and 3 but overestimates those of Chan-

Table 7.2: Table showing the average measured brightness temperatures and RMS between all perijoves for both the 2.4°N latitude band and the equator.

Channel	2.4°N			Equator		
	Mean T_b (K)	RMS (K)	RMS (%)	Mean T_b (K)	RMS (K)	RMS (%)
1	802.87	7.47	0.93	807.86	3.03	0.38
2	419.45	7.18	1.71	427.57	0.87	0.20
3	298.79	8.39	2.81	310.47	2.31	0.74
4	222.50	5.57	2.50	233.58	3.01	1.29
5	175.91	3.52	2.00	182.41	2.91	1.60
6	136.92	0.68	0.50	138.92	0.75	0.54

nels 4 and 5. This discrepancy suggests that ammonia is more concentrated in the upper atmosphere than the uniformly mixed deep layers, probably due to the reevaporation of precipitated ammonia (Li et al., 2017). Using the retrieval method described earlier in this chapter, this increase of ammonia can be modeled by allowing the ammonia abundance to increase above adiabat at pressure points greater than 2.72 bars.

The parameter space and accompanying results of the retrievals of deep abundance of ammonia and water vapor both with and without the presence of ionizing alkali metals at 2.4°N latitude are presented in the remainder of this section. Both results are presented here to show the affect of the including the ionizing alkali metals to the retrieval results. The measurements and parameters used in both kinds of retrievals are identical and shown in Table 7.3. The regularization penalty is removed to allow the upper atmosphere to vary without constraints; this is done by setting α to zero. Table 7.4 shows the upper and lower bounds of the allowable state vector for the L-BFGS-B algorithm. The difference between the retrieval with and without ionizing alkali metals is indicated by the presence of the cutoff temperature.

Table 7.5 shows the results of the retrieval algorithm for deep abundance of ammonia and water vapor and the cutoff temperature at 2.4°N at all perijoves for both types of retrievals. **While these deep abundances are used in the following retrieval as the global deep abundances, the deep abundances are solved using only data for a single latitude band and are NOT representative of the whole planet.** Figures 7.1–7.4 shows the abso-

lute brightness temperature, brightness temperature percent error, 45° limb darkening and 45° limb darkening error as a function of frequency for each perijove using the retrieved parameters assuming no ionization of alkali metals. Figures 7.5–7.8 shows the absolute brightness temperature, brightness temperature percent error, 45° limb darkening and 45° limb darkening error as a function of frequency for each perijove using the retrieved parameters assuming ionization of alkali metals.

The deep abundance of ammonia retrieved with and without ionized alkali metals are very similar, 2.40x solar (312 ppm) and 2.35x solar (306 ppm) respectively. This is attributed to ammonia being the largest microwave absorbing gas in Jupiter's atmosphere and primarily having an effect on the nadir brightness temperature. However, the intrinsic opacity of water vapor only becomes significant deep in the jovian atmosphere and only affects Channel 1's brightness temperature. The largest effect of water vapor in the jovian atmosphere is its effect on the temperature pressure profile due to water vapor's high latent heat. This affects the measured limb darkening at channels probing below the water cloud (Channels 1, 2, and 3).

The retrieved deep water abundance with and without ionized alkali metals differ significantly, 5.2x solar (0.49%) and 8.7x solar (0.82%) respectively. The introduction of ionizing alkali metals affects primarily the limb darkening at Channel 1 by introducing a "wall" of opacity deep in the jovian atmosphere. This wall is located at a temperature of 1640K (pressure of 2.3 kbar and an altitude of 750 km below the 1 bar level). The difference in the retrieved deep water vapor abundance is attributed to the ionizing alkali metals; by lowering Channel 1's limb darkening the water vapor abundance can be significantly lower and better match the higher altitude channels. This is best explained by comparing the error between limb darkening without ionizing alkali metals (Figure 7.4) and with ionizing alkali metals (Figure 7.8). When ionizing alkali metals are included in the retrieval the modeled limb darkening fits the measured data better not only in Channel 1 but also in Channel 3.

Table 7.3: Table showing the parameter space used in the retrieval of the deep abundance of ammonia and water vapor and the cutoff temperature at 2.4°N with all perijoves.

Parameter	Value	Unit
α	0.0	
λ	1.0	
Θ_{Tb}	0	$^\circ$
Θ_{LD}	20, 30, 45	$^\circ$

Table 7.4: Table of free parameter constraints used in the retrieval of deep ammonia and water vapor abundance and cutoff temperature.

	NH_3	H_2O	Scaling amount at Pressure (bar)											T_c
			92.0	33.1	20.1	12.2	7.39	4.48	2.72	1.65	1.0	0.61	0.3	
u	2.7	11.0	1.0	1.0	1.0	1.0	1.0	1.0	1.4	1.4	1.4	1.4	1.4	2000
l	1.8	1.0	1.0	1.0	1.0	1.0	1.0	1.0	1.0	1.0	1.0	1.0	1.0	1300

Table 7.5: Table showing retrieved deep abundance of ammonia and water vapor and the cutoff temperature at 2.4°N using all perijoves.

State Vector	Value		Unit
	w/o alkali	w/ alkali	
NH_3	2.35	2.40	solar
H_2O	8.70	5.20	solar
T_c	N/A	1640	K

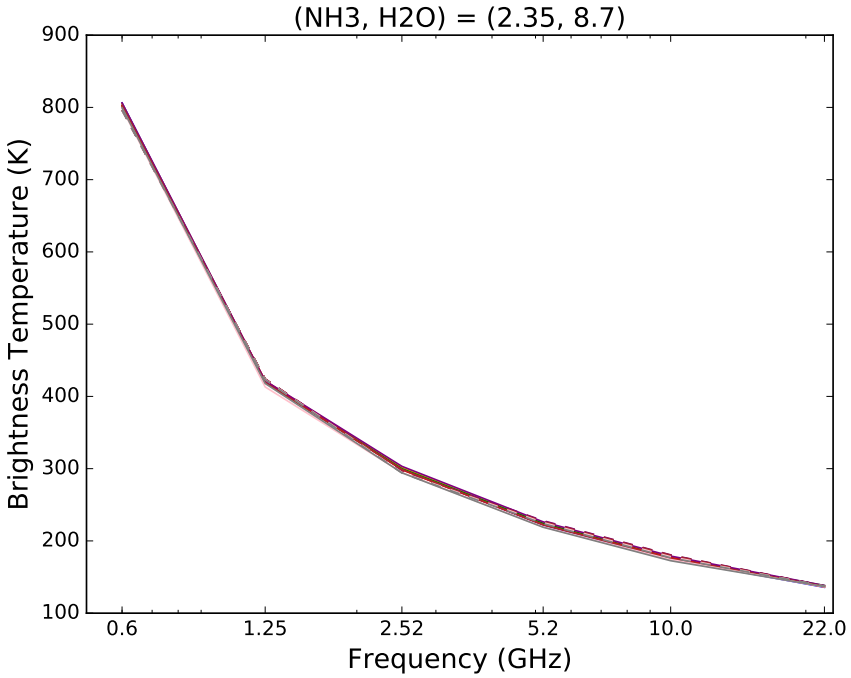

Figure 7.1: Brightness temperature as a function of frequency for each perijove. The solid line represents the measured value and the dashed line is the modeled brightness temperature using the retrieved values without the presence of ionizing alkali metals.

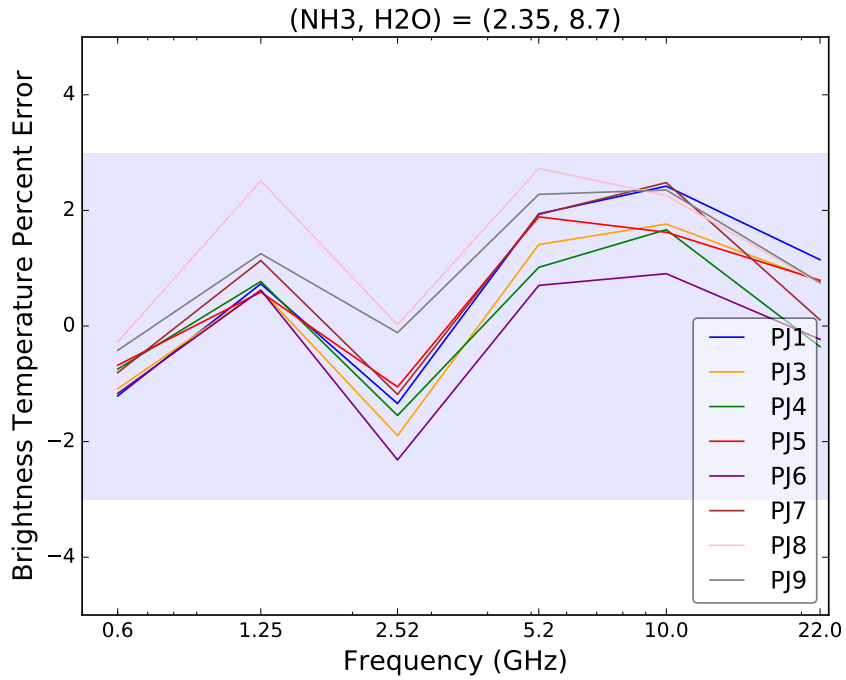

Figure 7.2: Percent error between the measured brightness temperature and modeled brightness temperature as a function of frequency for each perijove without the presence of ionizing alkali metals. The shaded region is the 3% error box.

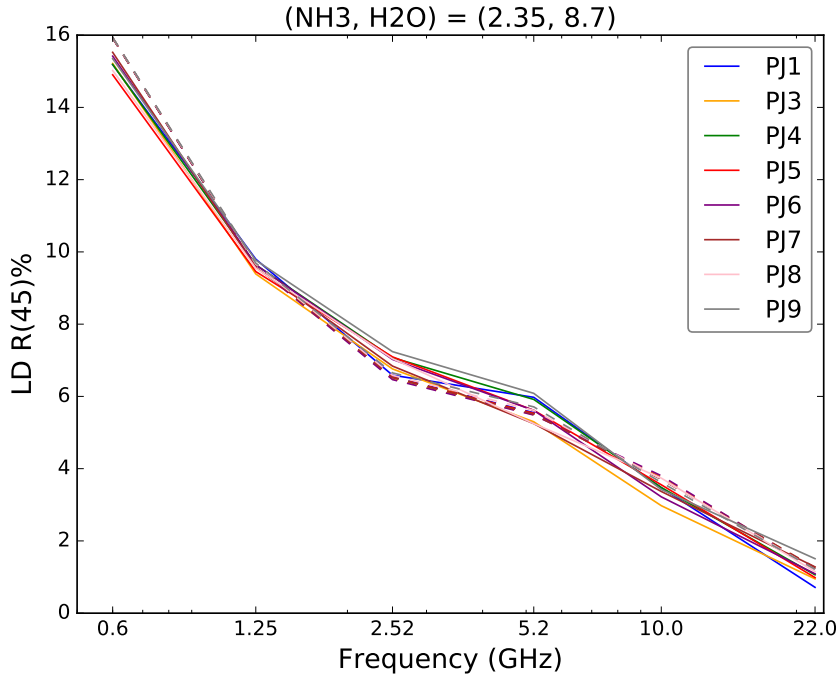

Figure 7.3: 45° Limb Darkening as a function of frequency for each perijove. The solid line represents the measured value and the dashed line is the modeled limb darkening using the retrieved values without the presence of ionizing alkali metals.

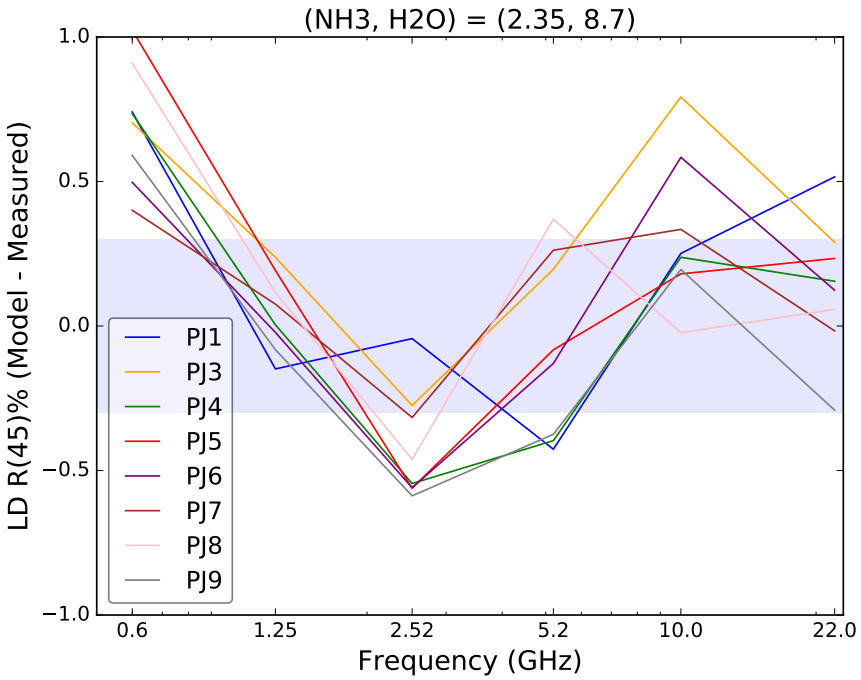

Figure 7.4: Difference between the measured and modeled 45° limb darkening as a function of frequency for each perijove without the presence of ionizing alkali metals. The shaded region is the 0.3% error box.

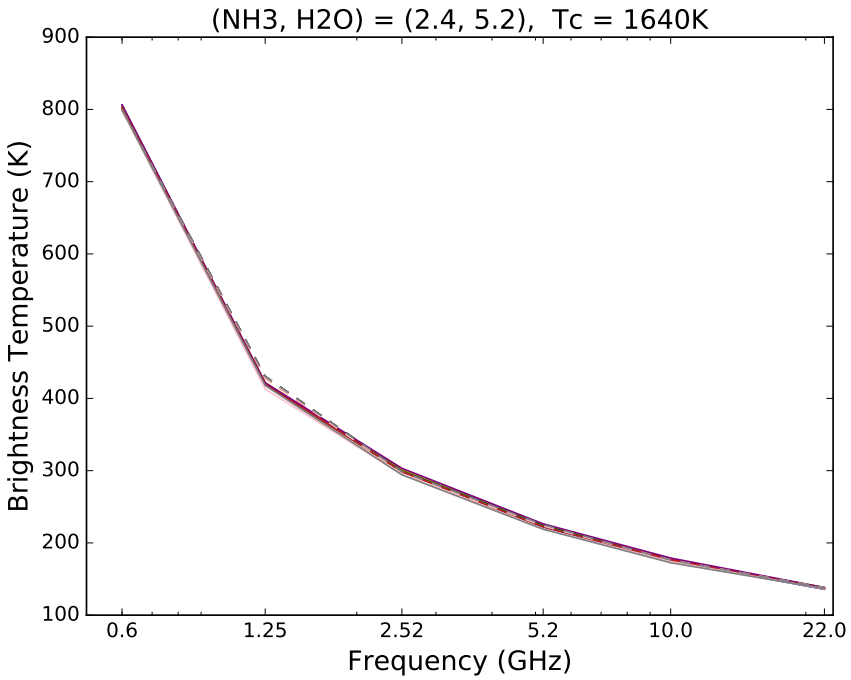

Figure 7.5: Brightness temperature as a function of frequency for each perijove. The solid line represents the measured value and the dashed line is the modeled brightness temperature using the retrieved values with the presence of ionizing alkali metals.

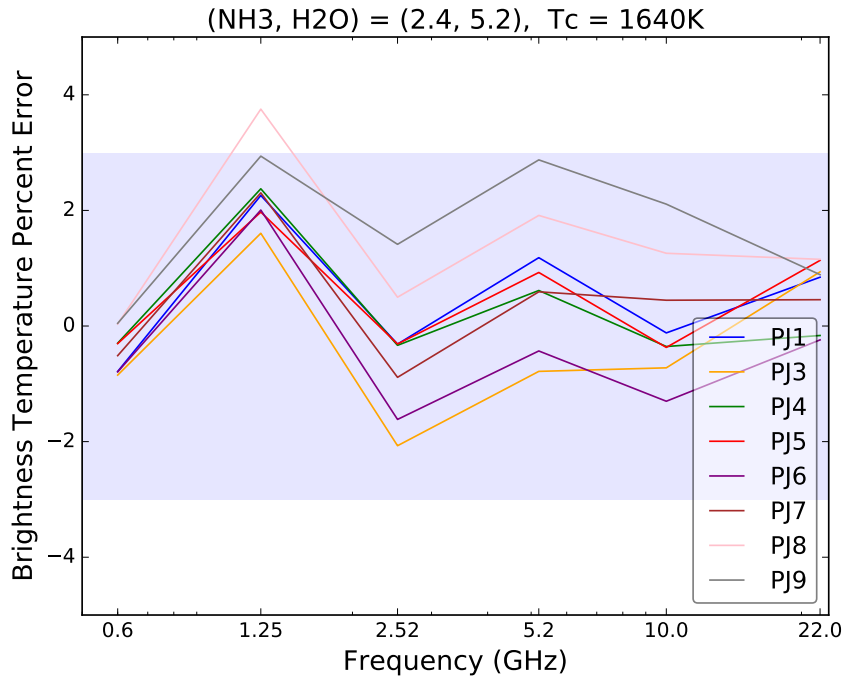

Figure 7.6: Percent error between the measured brightness temperature and modeled brightness temperature as a function of frequency for each perijove with the presence of ionizing alkali metals. The shaded region is the 3% error box.

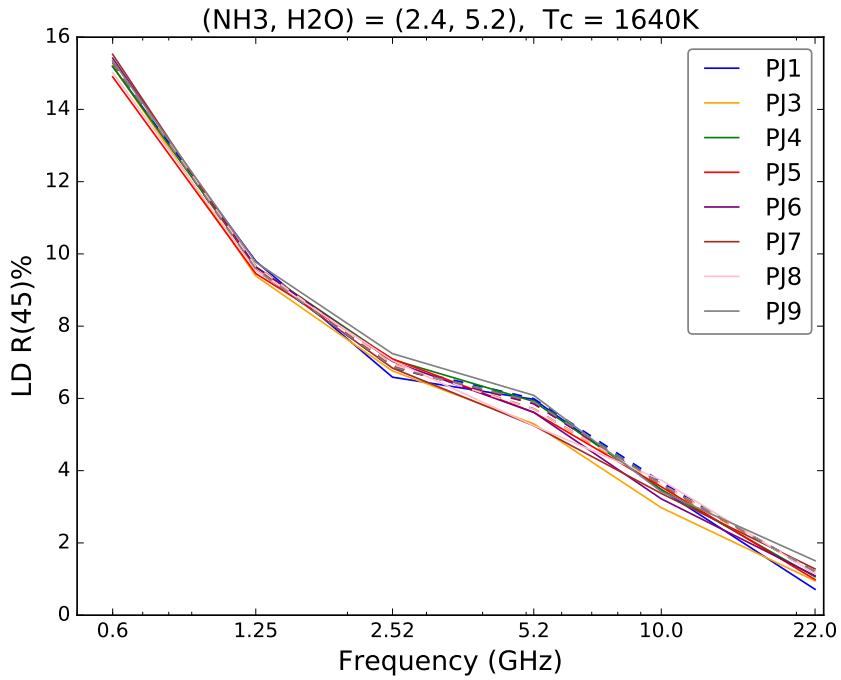

Figure 7.7: 45° Limb Darkening as a function of frequency for each perijove. The solid line represents the measured value and the dashed line is the modeled limb darkening using the retrieved values with the presence of ionizing alkali metals.

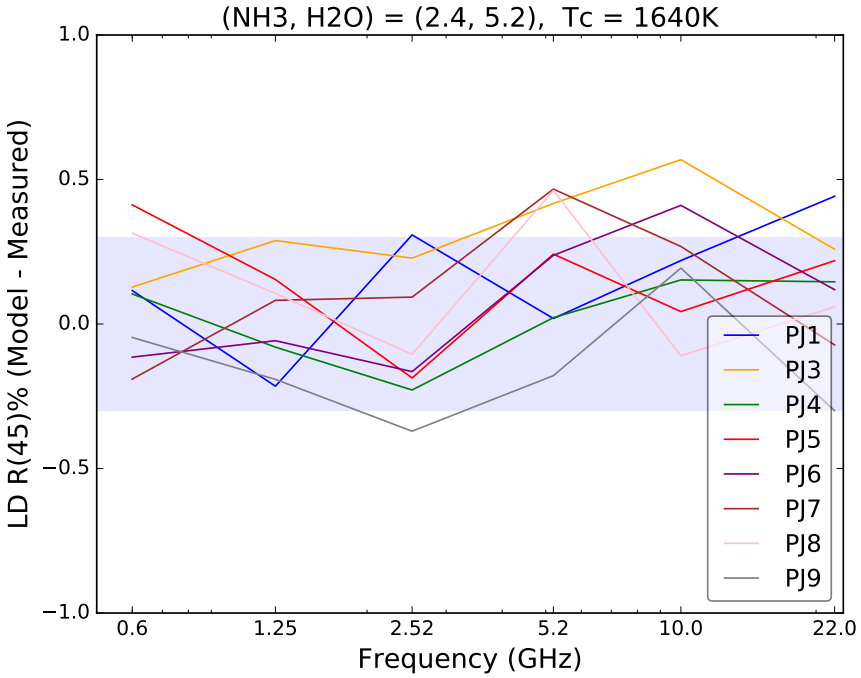

Figure 7.8: Difference between the measured and modeled 45° limb darkening as a function of frequency for each perijove with the presence of ionizing alkali metals. The shaded region is the 0.3% error box.

7.2.2 Ammonia Abundance Profiles

The constrained problem of the ideal adiabat can only be applied to latitudes near 2.4°N. At other latitudes one must solve for the vertical abundance profile of ammonia. Occurring in all profile retrievals of atmospheric sounding is the problem of having an ill-conditioned problem. This can amplify any experimental error and result in fitting the results to the noise instead of the signal, regardless of the optimization method. Rodgers (2000) suggests using a mean value and standard deviation of the state vector as a-priori information to regularize the solution. While this method is suitable for the remote sounding of Earth's atmosphere (due to our prior knowledge of the climatological state), the Juno MWR is exploring unknown territory where the climatological state is unknown. This makes Rodger's regularization method less useful.

The process of applying our prior knowledge of the state vector has been described in Chapter 5.3 but is reiterated here for reference. We expect that turbulence and convection will remove the spacial gradient of ammonia concentration because ammonia has no sources or sinks below the cloud. The solution is therefore guided such that (1) it converges to a homogenized atmosphere in the absence of factors indicating that the ammonia should be inhomogeneous and (2) that the ammonia concentration is equal to or less than that in an ideal adiabatic atmosphere, unless there is evidence showing the presence of reevaporation of precipitation. These constraints are applied in two ways, the first is done using the Tikhonov regularization matrix ($\mathbf{D}$), and the second is done by setting the constraints of the solution ($\mathbf{l}$, $\mathbf{u}$).

Retrievals without Ionized Alkali Metals

Using both brightness temperature and limb darkening measurements from all latitudes between 40°S - 40°N, an ammonia distribution map can be generated. The parameter space and accompanying retrieved ammonia abundance profiles are presented here. Table 7.6 presents the parameters used in this retrieval. The regularization penalty α is set to 20.0 to ensure that the retrieval converges on a homogenized atmosphere in the absence of factors indicating ammonia to be inhomogeneous. Since the solution without ionizing alkali metals is smaller in dimension than the solution with ionizing alkali metals, the regularization penalty (α) assigned to the retrieval without ionizing alkali metals is larger. Table 7.7 shows the upper and lower bounds of the allowable state vector for the L-BFGS-B algorithm. The deep abundance of ammonia and water vapor are set to the values retrieved from the 2.4°N latitude band, and the scaling amounts are allowed to vary from 10%–100% in the deep atmosphere and from 10%–140% in the upper atmosphere.

Shown in the Figures are the retrieved ammonia abundance profiles, nadir brightness temperature errors, and 45° limb darkening errors for perijoves 5 and 9 in absence of ionized alkali metals in the deep atmosphere (Note that Perijoves 5 and 9 used a "tilted" spacecraft attitude so as to assure the comparison of the same atmospheric parcel at different look angles). These are shown as a function of planetocentric latitude in the range from 40°N to 40°S. Figures 7.9–7.13 show the retrieved ammonia abundance profiles, nadir brightness temperature errors, and 45° limb darkening errors for perijove 5. Figures 7.14–7.18 show the retrieved ammonia abundance profiles, nadir brightness temperature errors, and 45° limb darkening errors for perijove 9.

Table 7.6: Table showing the parameter space used in the retrieval of the ammonia abundance profile with all perijoves.

Parameter	Value	Unit
α	20.0	
λ	1.0	
Θ_{Tb}	0	$^\circ$
Θ_{LD}	20, 30, 45	$^\circ$

Table 7.7: Table of free parameter constraints used in the retrieval of the ammonia abundance profiles.

	NH_3	H_2O	Scaling amount at Pressure (bar)											T_c
			92.0	33.1	20.1	12.2	7.39	4.48	2.72	1.65	1.0	0.61	0.3	
u	2.35	8.7	1.0	1.0	1.0	1.0	1.0	1.0	1.4	1.4	1.4	1.4	1.4	N/A
l	2.35	8.7	1.0	0.1	0.1	0.1	0.1	0.1	0.1	0.1	0.1	0.1	0.1	N/A

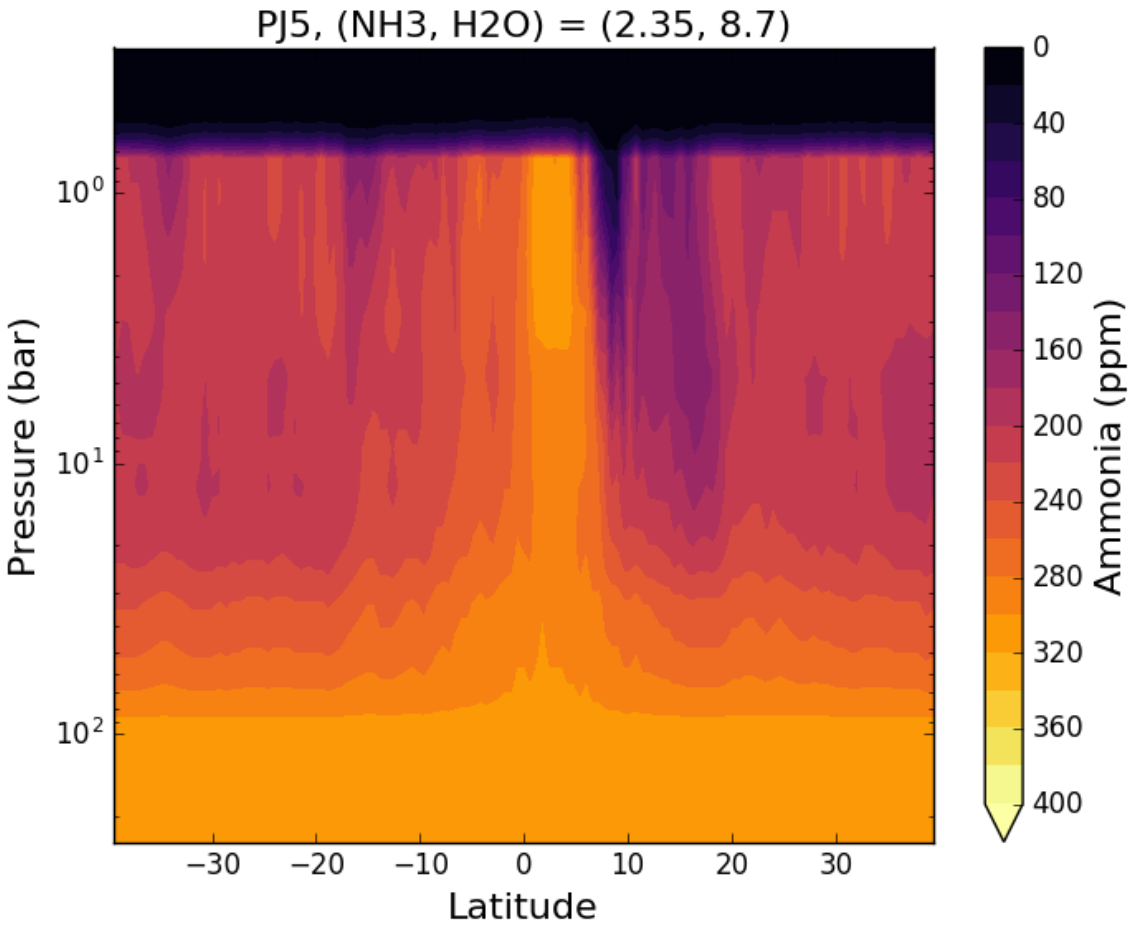

Figure 7.9: Colored contours show the ammonia concentration in parts per million retrieved from nadir brightness temperatures and limb darkening during PJ5 flyby. The assumed deep ammonia abundance is 2.35x solar, the assumed deep water vapor abundance is 8.7x solar.

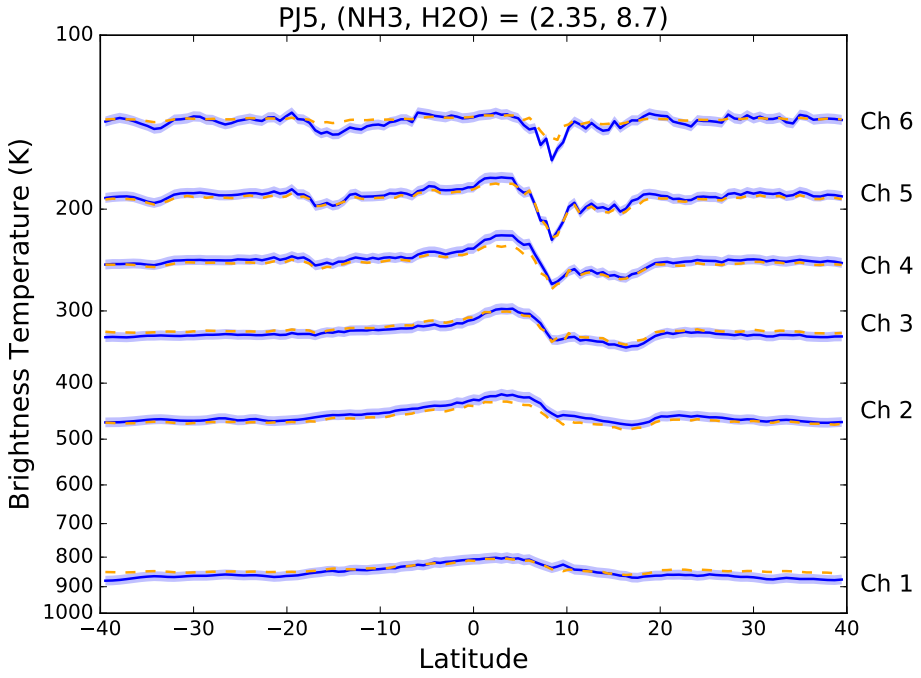

Figure 7.10: Nadir brightness temperature as a function of latitude for PJ5. The solid blue line represents the measured nadir brightness temperature and the dashed orange line is the modeled nadir brightness temperature using the retrieved values. The shaded region represents the 2% measurement error.

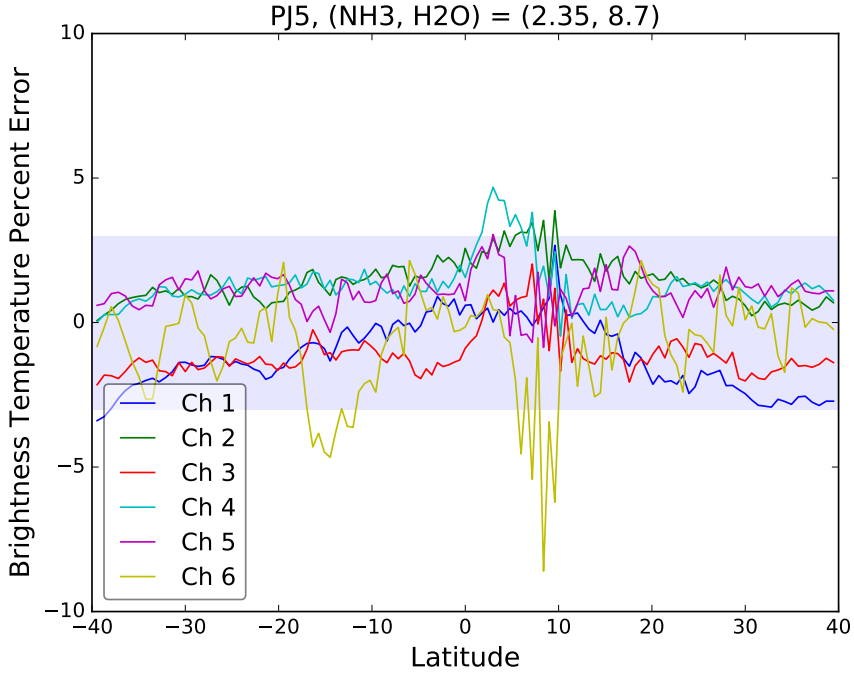

Figure 7.11: Percent difference between the measured and the modeled nadir brightness temperature for each channel. The shaded region represents the 3% error box.

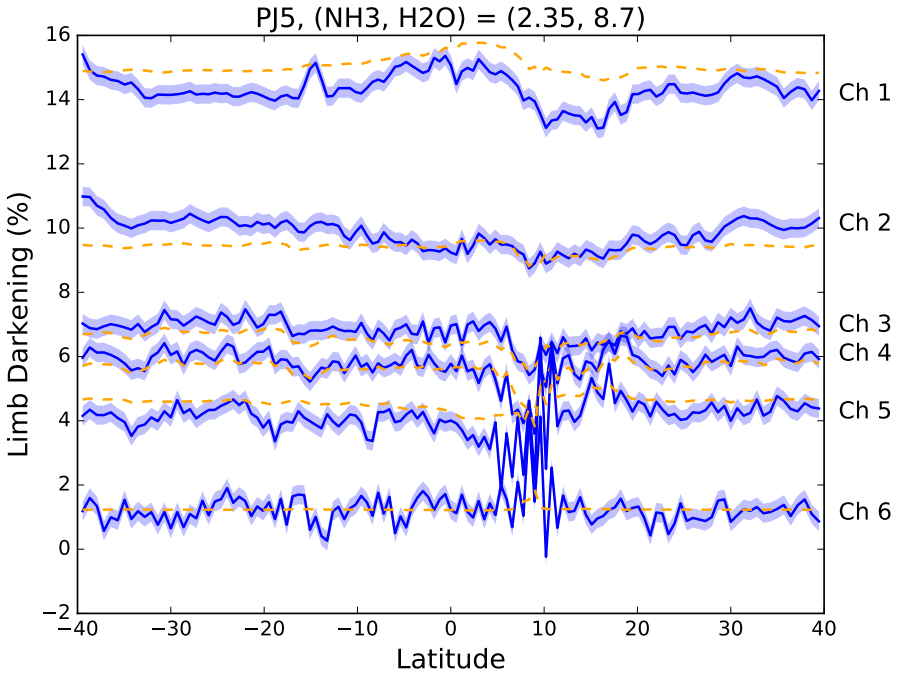

Figure 7.12: 45° Limb Darkening as a function of frequency for each perijove. The solid line represents the measured limb darkening and the dashed line is the modeled limb darkening using the retrieved values. The shaded region represents the 0.3% measurement error.

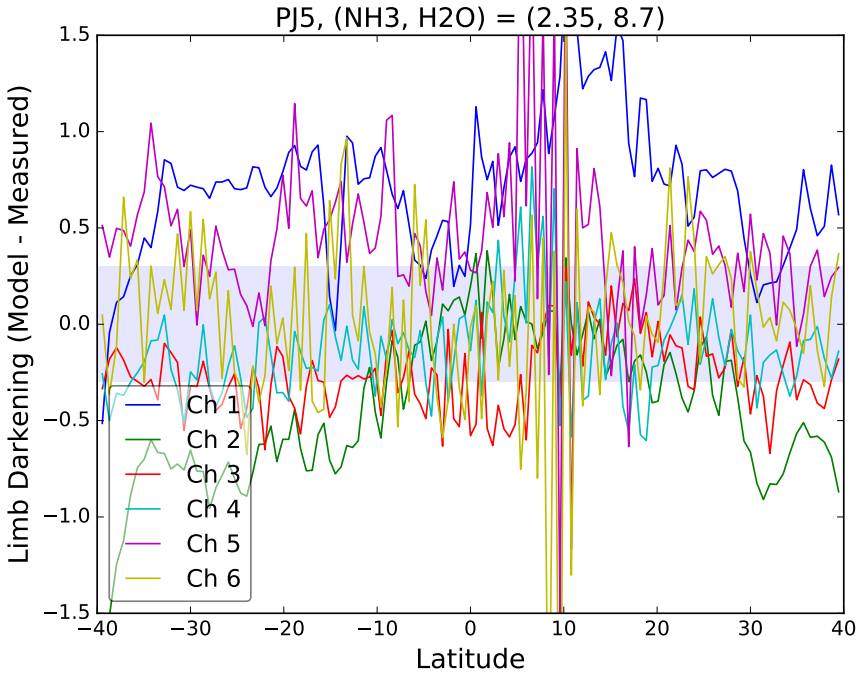

Figure 7.13: Difference between the measured and modeled 45° limb darkening as a function of frequency for each perijove. The shaded region is the 0.3% error box.

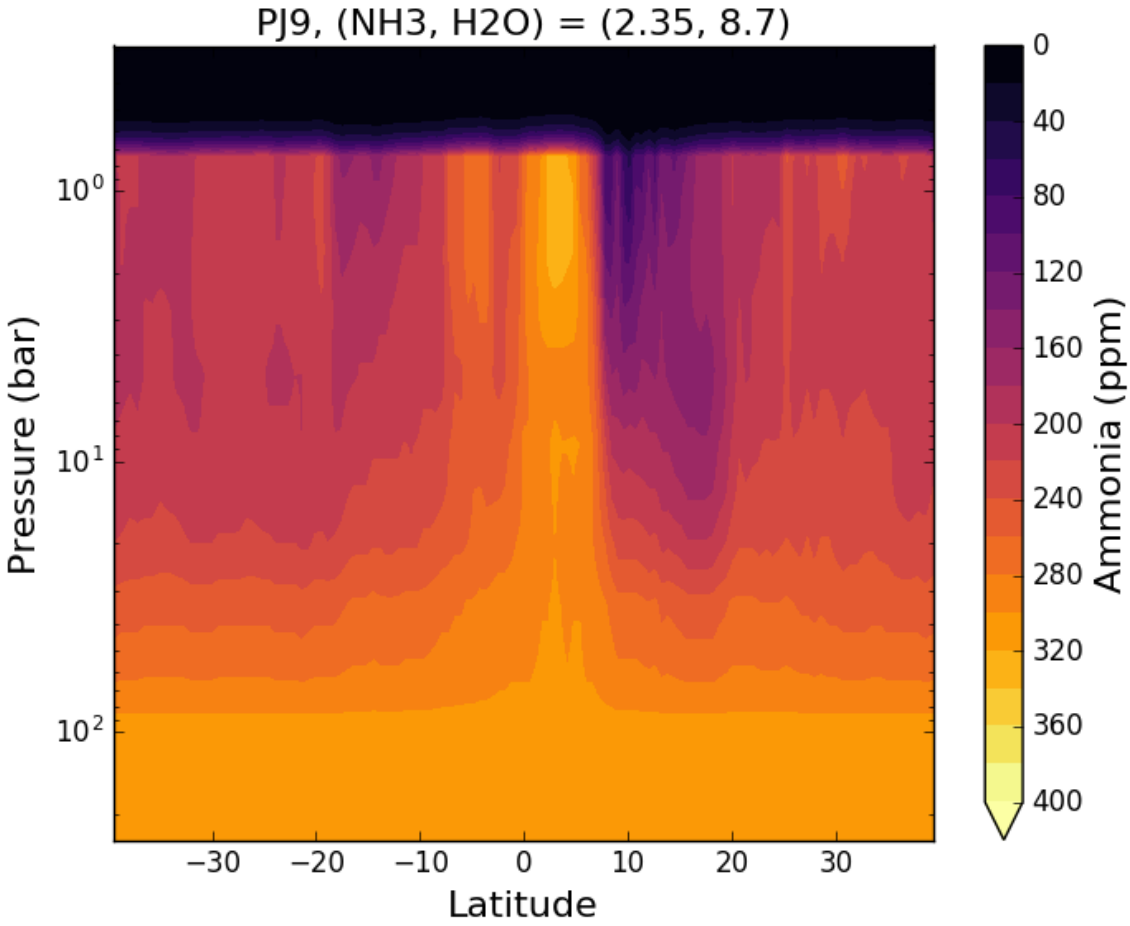

Figure 7.14: Colored contours show the ammonia concentration in parts per million retrieved from nadir brightness temperatures and limb darkening during PJ9 flyby. The assumed deep ammonia abundance is 2.35x solar, the assumed deep water vapor abundance is 8.7x solar.

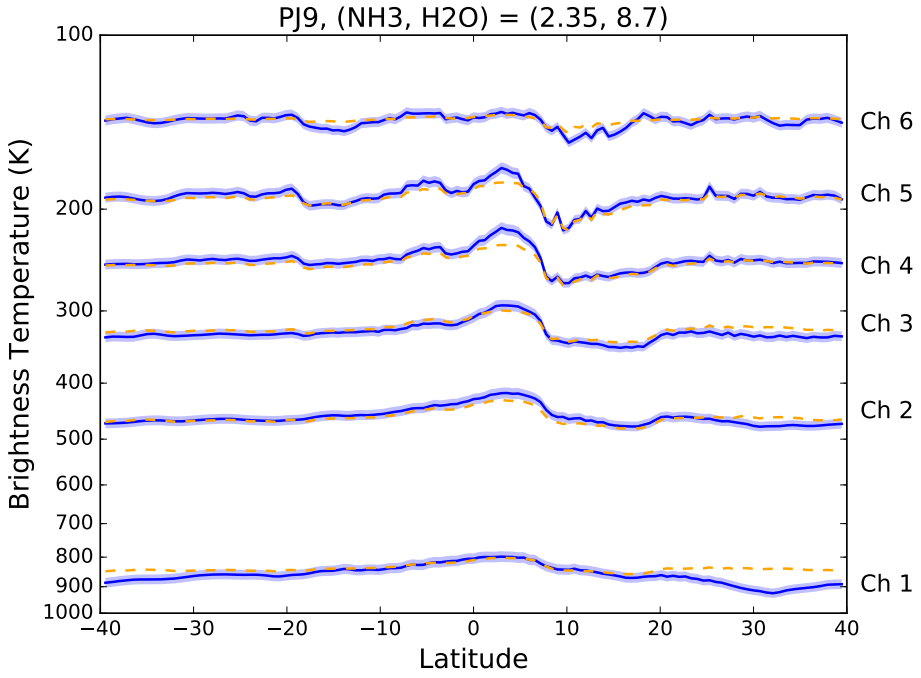

Figure 7.15: Nadir brightness temperature as a function of latitude for PJ9. The solid blue line represents the measured nadir brightness temperature and the dashed orange line is the modeled nadir brightness temperature using the retrieved values. The shaded region represents the 2% measurement error.

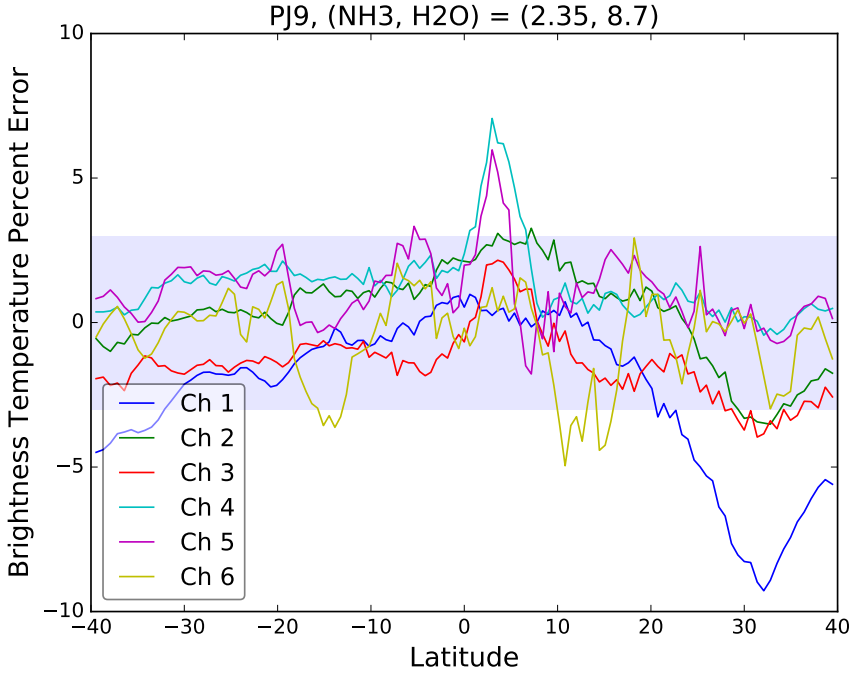

Figure 7.16: Percent difference between the measured and the modeled nadir brightness temperature for each channel. The shaded region represents the 3% error box.

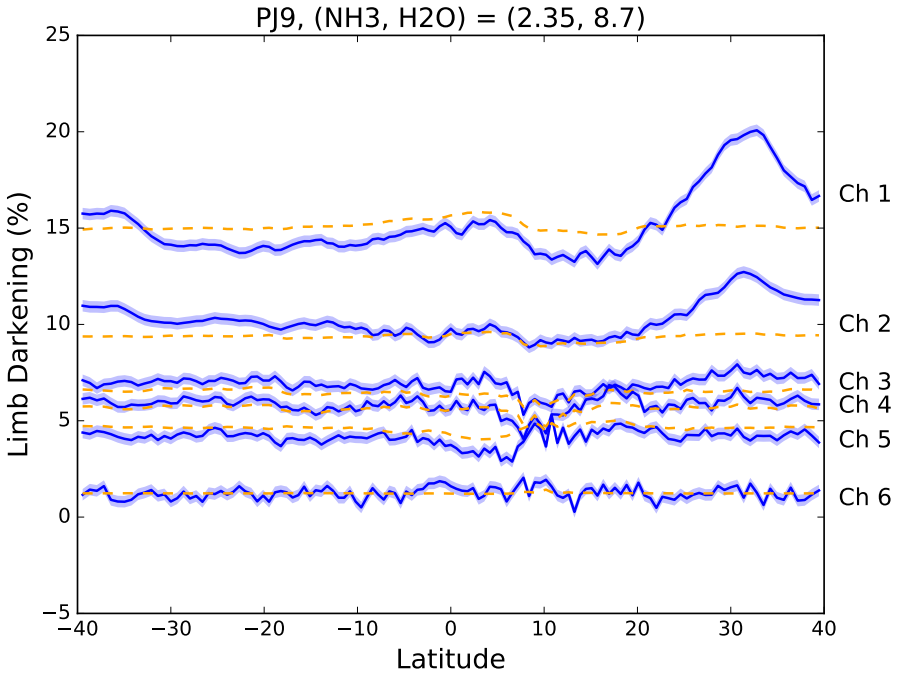

Figure 7.17: 45° Limb Darkening as a function of frequency for each perijove. The solid line represents the measured limb darkening and the dashed line is the modeled limb darkening using the retrieved values. The shaded region represents the 0.3% measurement error.

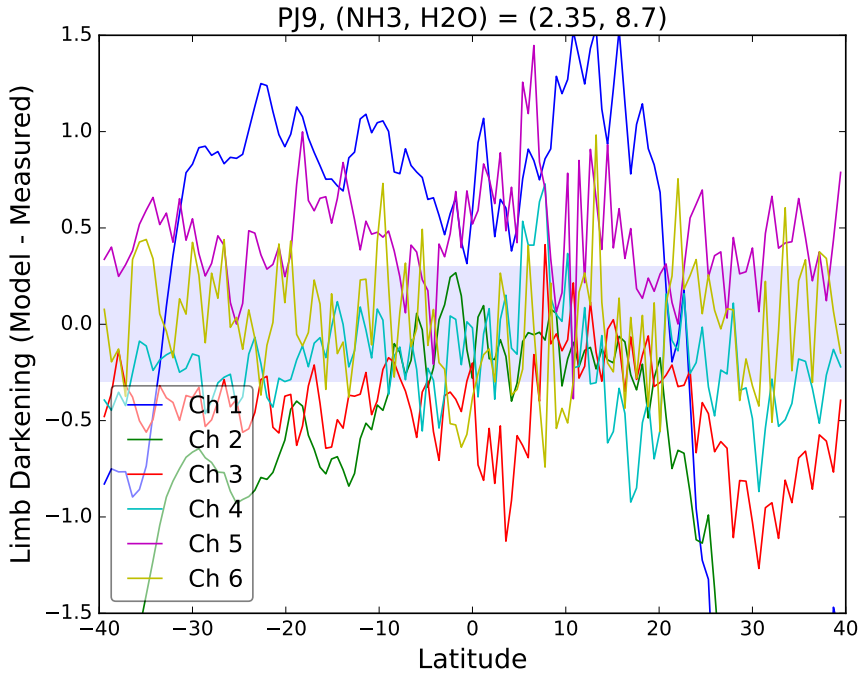

Figure 7.18: Difference between the measured and modeled 45° limb darkening as a function of frequency for each perijove. The shaded region is the 0.3% error box.

Retrievals with Ionized Alkali Metals

The addition of a deep layer of ionized alkali metals provides a better fit to the measured data from all perijoves. Using both brightness temperature and limb darkening measurements from all latitudes between 40°S - 40°N, an ammonia distribution map can be generated. The parameter space and accompanying retrieved ammonia abundance profiles are presented here. Table 7.8 presents the parameters used in this retrieval. The regularization penalty α is set to 5.0 to ensure that the retrieval converges on a homogenized atmosphere in the absence of evidence showing ammonia to be inhomogeneous. Since the solution with ionizing alkali metals is larger in dimension than the solution without ionizing alkali metals the regularization penalty (α) assigned to the retrieval with ionizing alkali metals is smaller. Table 7.9 shows the upper and lower bounds of the allowable state vector for the L-BFGS-B algorithm. The deep abundance of ammonia and water vapor, and the alkali metal cutoff temperature are set to the values retrieved from the 2.4°N latitude band, and the scaling amounts are allowed to vary from 10%–100% in the deep atmosphere and from 10%–140% in the upper atmosphere.

Shown in the remainder of the section are the retrieved ammonia abundance profiles, nadir brightness temperature errors, and 45° limb darkening errors for all perijoves. These are shown as a function of planetocentric latitude in the range from 40°N to 40°S. A table of each perijove and its associated figures can be found in Table 7.10.

Table 7.8: Table showing the parameter space used in the retrieval of the ammonia abundance profile with all perijoves.

Parameter	Value	Unit
α	5.0	
λ	1.0	
Θ_{Tb}	0	°
Θ_{LD}	20, 30, 45	°

Table 7.9: Table of free parameter constraints used in the retrieval of the ammonia abundance profiles.

	NH_3	H_2O	Scaling amount at Pressure (bar)											T_c
			92.0	33.1	20.1	12.2	7.39	4.48	2.72	1.65	1.0	0.61	0.3	
u	2.4	5.2	1.0	1.0	1.0	1.0	1.0	1.0	1.4	1.4	1.4	1.4	1.4	1640
l	2.4	5.2	1.0	0.1	0.1	0.1	0.1	0.1	0.1	0.1	0.1	0.1	0.1	1640

Table 7.10: Figure numbers pertaining to each perijove for NH_3 abundance profile, Nadir Brightness Temperature, and 45° Limb Darkening presented in this chapter.

Perijove	Abundance Profile	Nadir Brightness Temperature		45° Limb Darkening	
		Absolute	Percent Error	Absolute	Percent Error
1	7.19	7.20	7.21	7.22	7.23
3	7.24	7.25	7.26	7.27	7.28
4	7.29	7.30	7.31	7.32	7.33
5	7.34	7.35	7.36	7.37	7.38
6	7.39	7.40	7.41	7.42	7.43
7	7.44	7.45	7.46	7.47	7.48
8	7.49	7.50	7.51	7.52	7.53
9	7.54	7.55	7.56	7.57	7.58

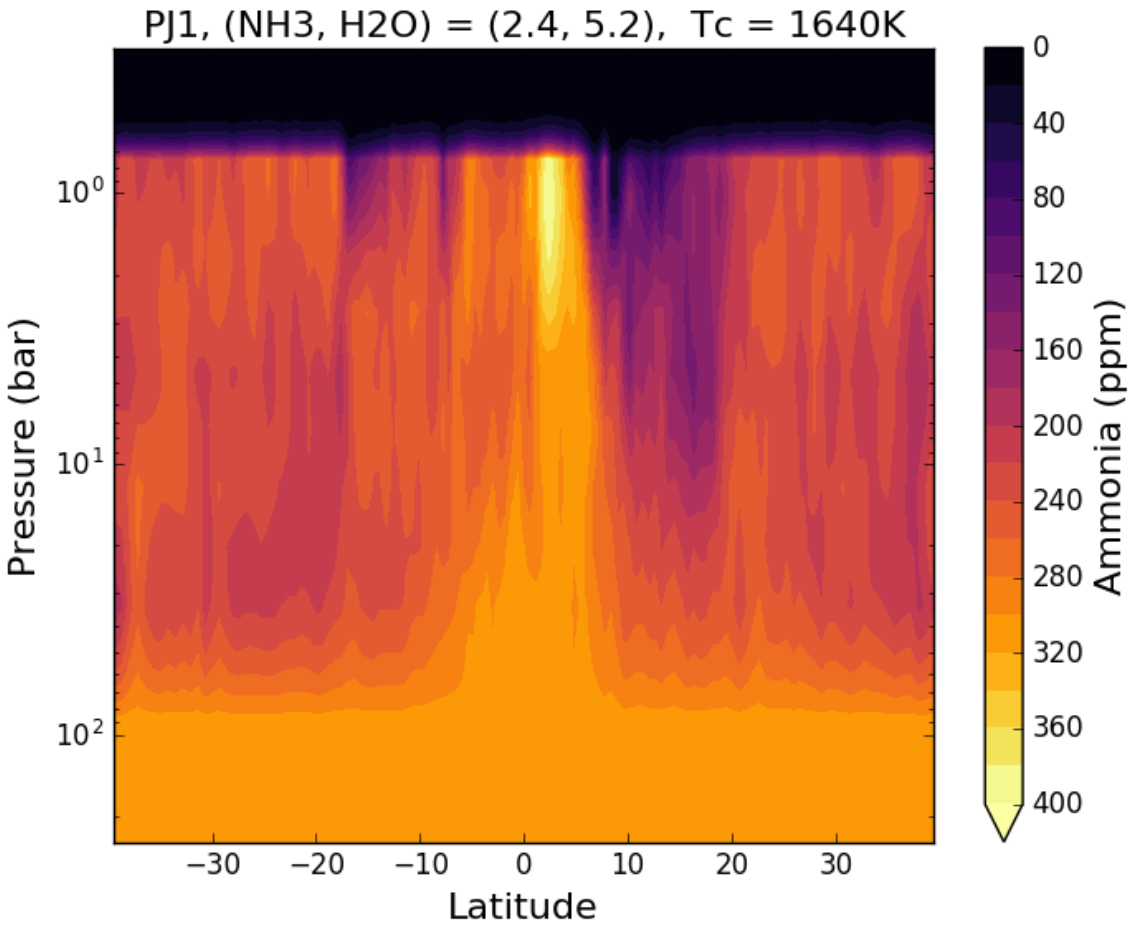

Figure 7.19: Colored contours show the ammonia concentration in parts per million retrieved from nadir brightness temperatures and limb darkening during PJ1 flyby. The assumed deep ammonia abundance is 2.4x solar, the assumed deep water vapor abundance is 5.2x solar, and the assumed alkali metal cutoff temperature is 1640K.

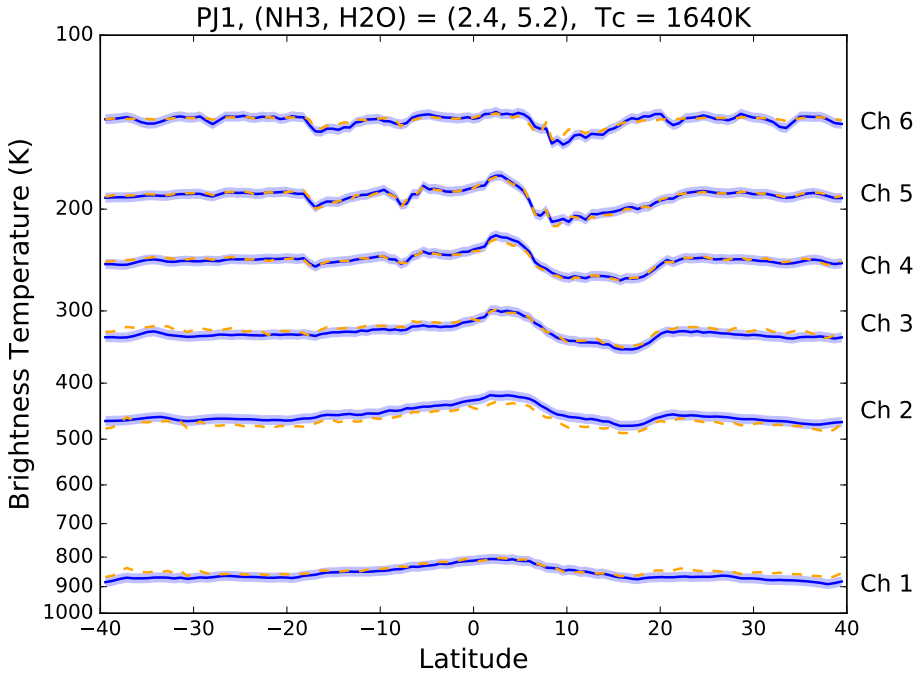

Figure 7.20: Nadir brightness temperature as a function of latitude for PJ1. The solid blue line represents the measured nadir brightness temperature and the dashed orange line is the modeled nadir brightness temperature using the retrieved values. The shaded region represents the 2% measurement error.

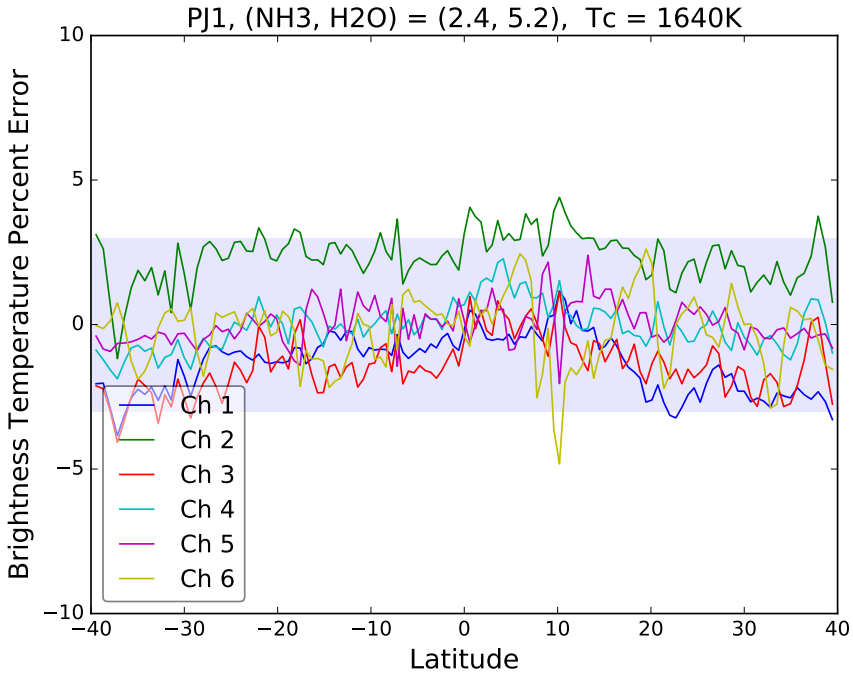

Figure 7.21: Percent difference between the measured and the modeled nadir brightness temperature for each channel. The shaded region represents the 3% error box.

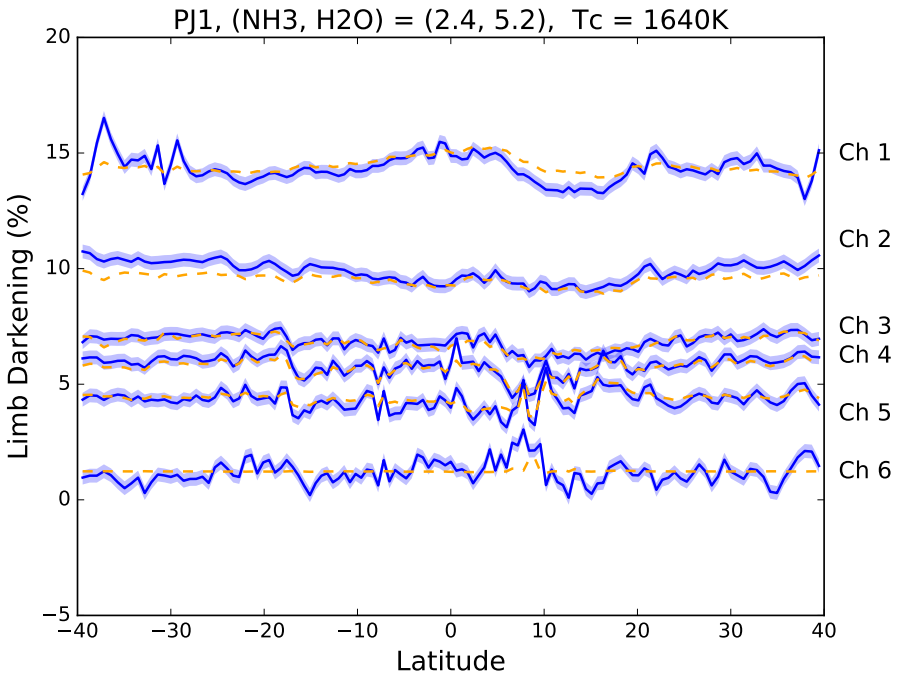

Figure 7.22: 45° Limb Darkening as a function of frequency for each perijove. The solid line represents the measured limb darkening and the dashed line is the modeled limb darkening using the retrieved values. The shaded region represents the 0.3% measurement error.

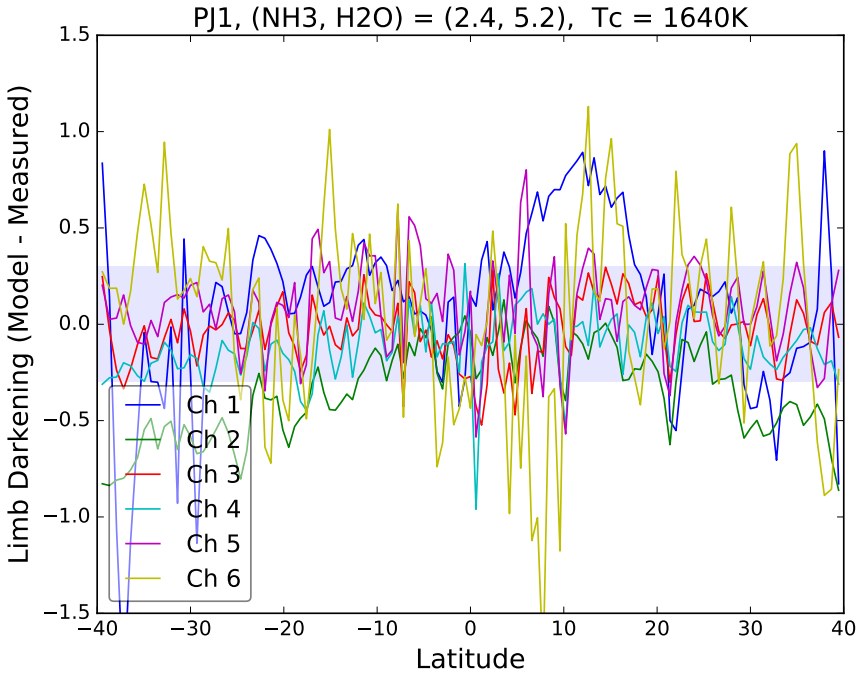

Figure 7.23: Difference between the measured and modeled 45° limb darkening as a function of frequency for each perijove. The shaded region is the 0.3% error box.

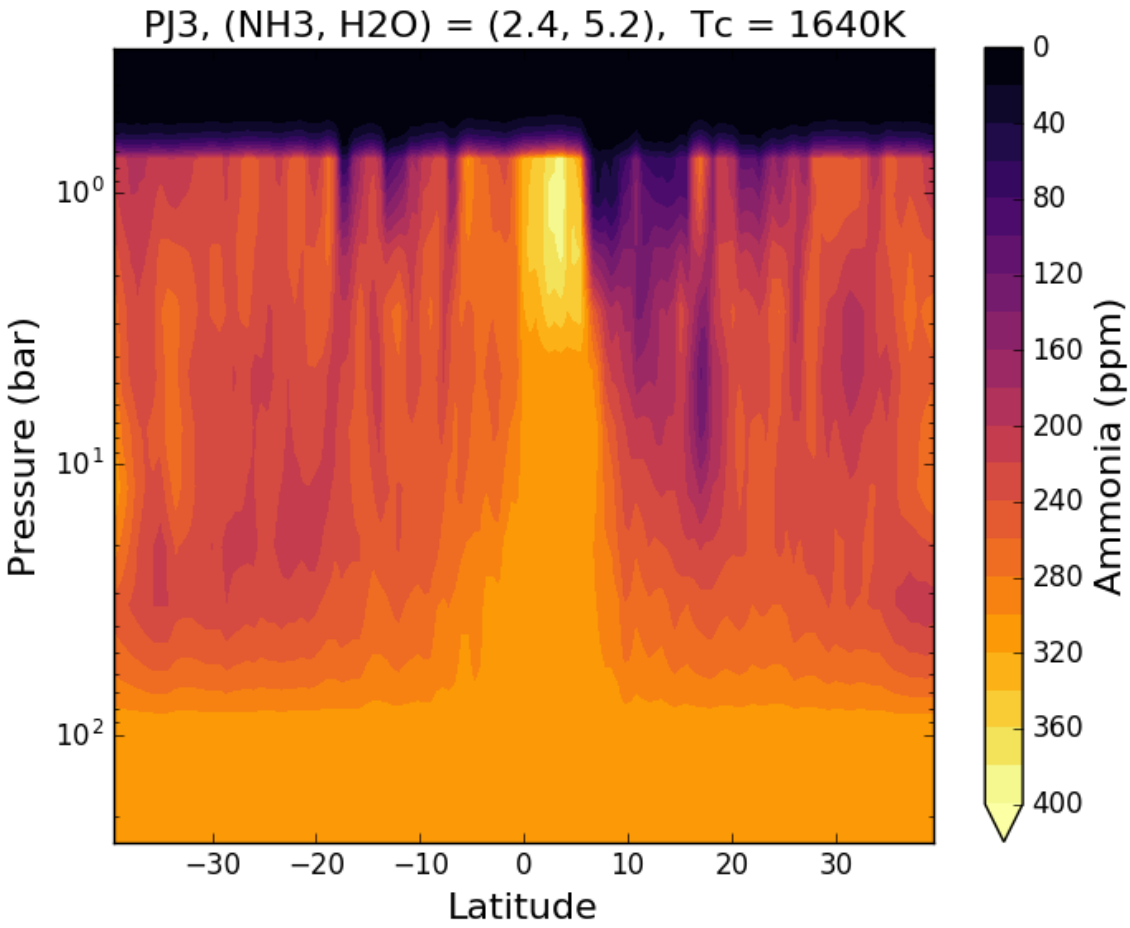

Figure 7.24: Colored contours show the ammonia concentration in parts per million retrieved from nadir brightness temperatures and limb darkening during PJ3 flyby. The assumed deep ammonia abundance is 2.4x solar, the assumed deep water vapor abundance is 5.2x solar, and the assumed alkali metal cutoff temperature is 1640K.

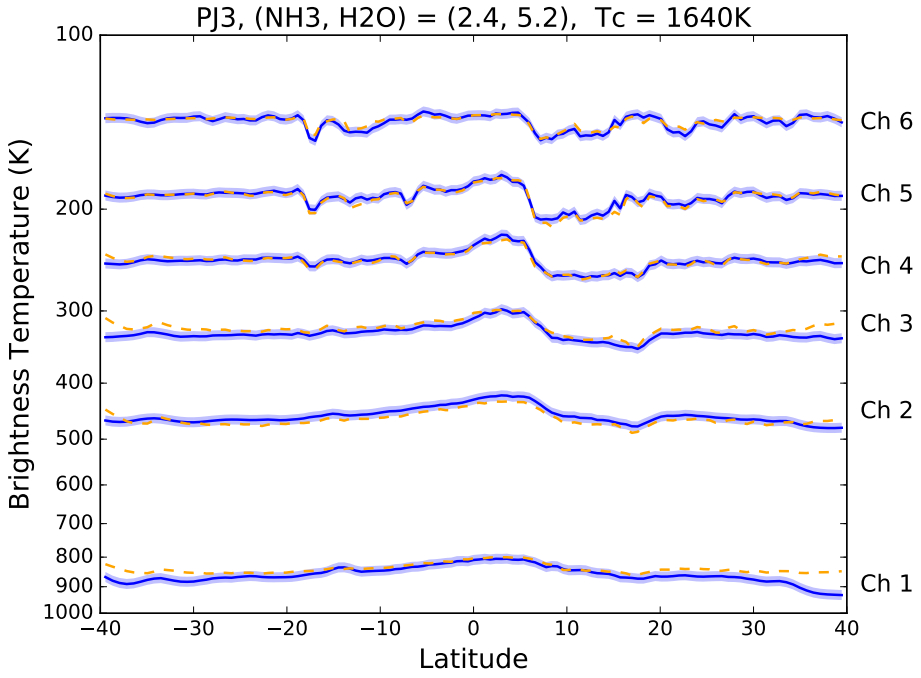

Figure 7.25: Nadir brightness temperature as a function of latitude for PJ3. The solid blue line represents the measured nadir brightness temperature and the dashed orange line is the modeled nadir brightness temperature using the retrieved values. The shaded region represents the 2% measurement error.

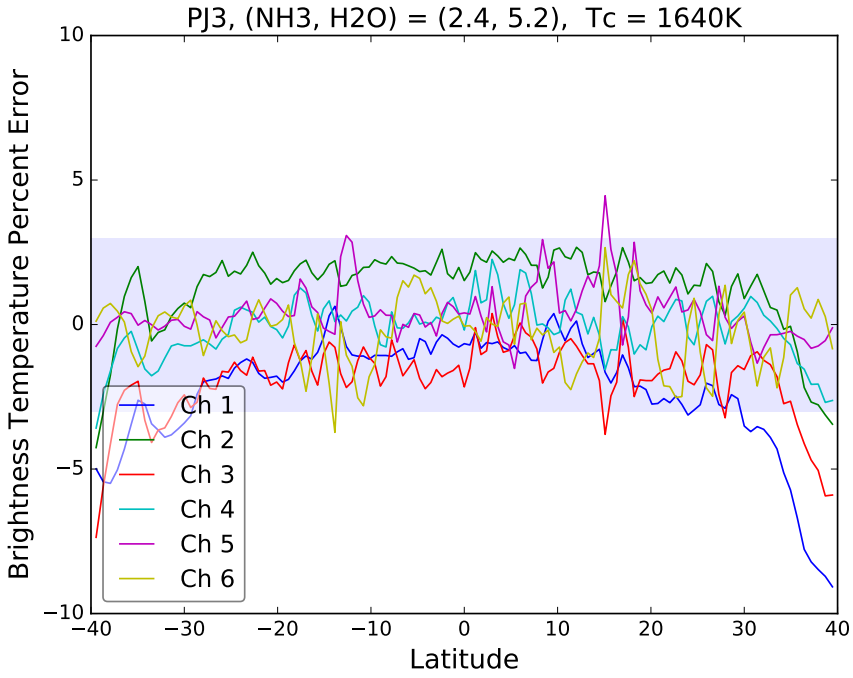

Figure 7.26: Percent difference between the measured and the modeled nadir brightness temperature for each channel. The shaded region represents the 3% error box.

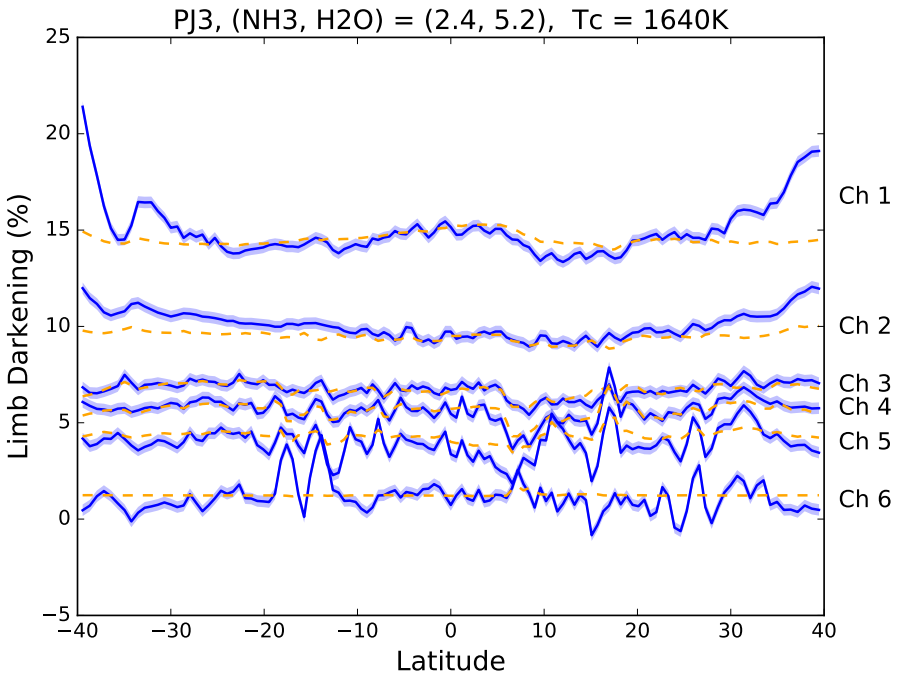

Figure 7.27: 45° Limb Darkening as a function of frequency for each perijove. The solid line represents the measured limb darkening and the dashed line is the modeled limb darkening using the retrieved values. The shaded region represents the 0.3% measurement error.

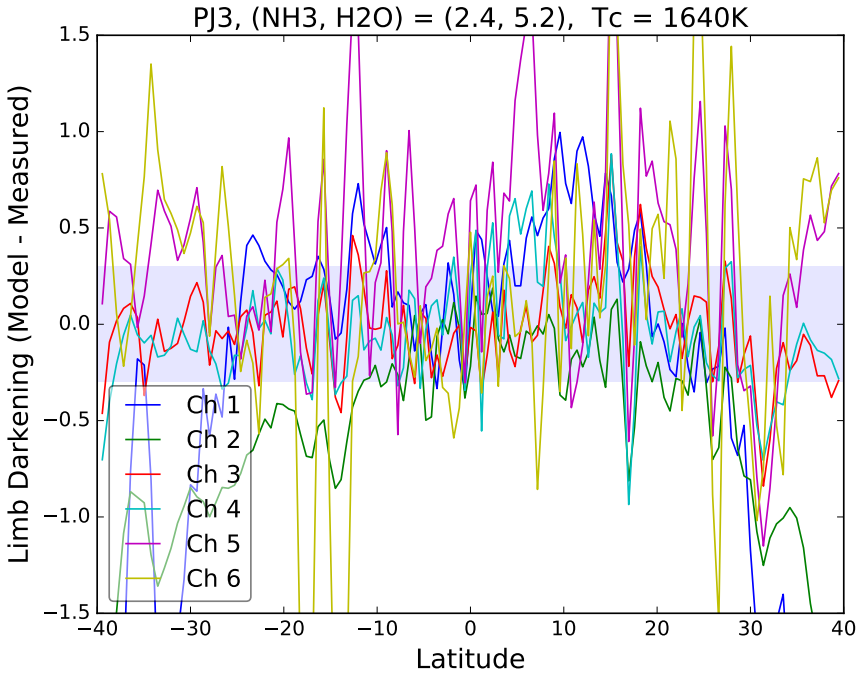

Figure 7.28: Difference between the measured and modeled 45° limb darkening as a function of frequency for each perijove. The shaded region is the 0.3% error box.

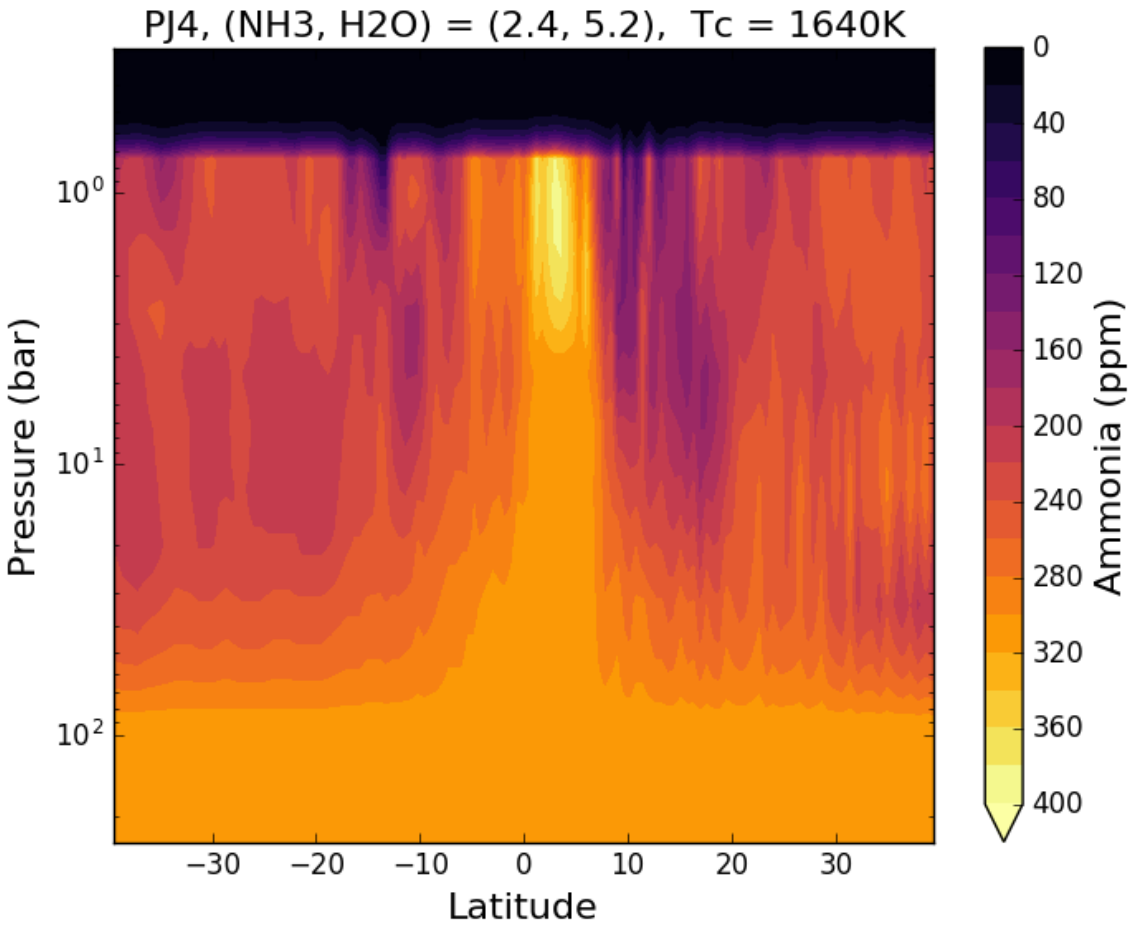

Figure 7.29: Colored contours show the ammonia concentration in parts per million retrieved from nadir brightness temperatures and limb darkening during PJ4 flyby. The assumed deep ammonia abundance is 2.4x solar, the assumed deep water vapor abundance is 5.2x solar, and the assumed alkali metal cutoff temperature is 1640K.

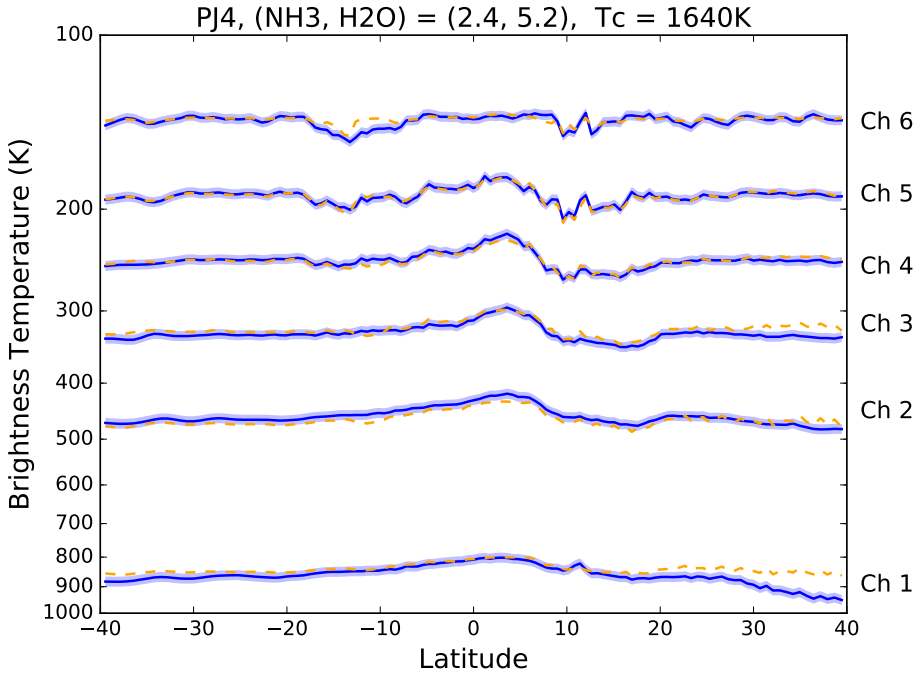

Figure 7.30: Nadir brightness temperature as a function of latitude for PJ4. The solid blue line represents the measured nadir brightness temperature and the dashed orange line is the modeled nadir brightness temperature using the retrieved values. The shaded region represents the 2% measurement error.

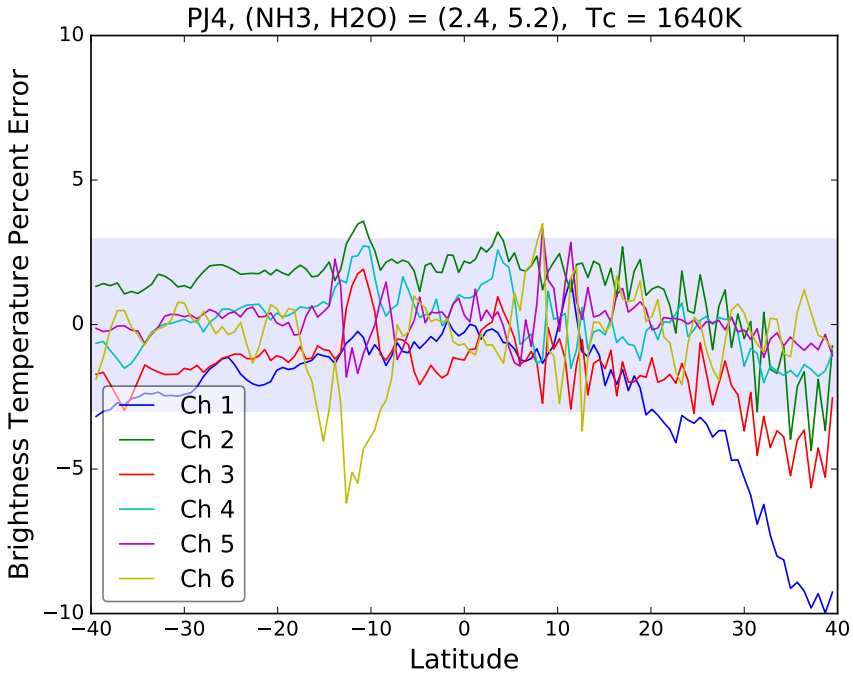

Figure 7.31: Percent difference between the measured and the modeled nadir brightness temperature for each channel. The shaded region represents the 3% error box.

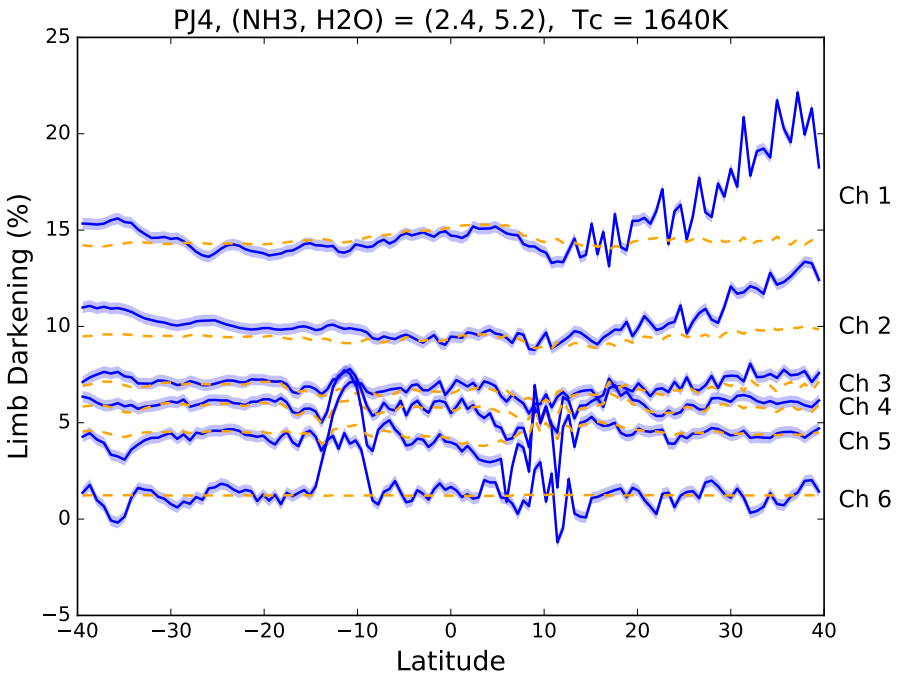

Figure 7.32: 45° Limb Darkening as a function of frequency for each perijove. The solid line represents the measured limb darkening and the dashed line is the modeled limb darkening using the retrieved values. The shaded region represents the 0.3% measurement error.

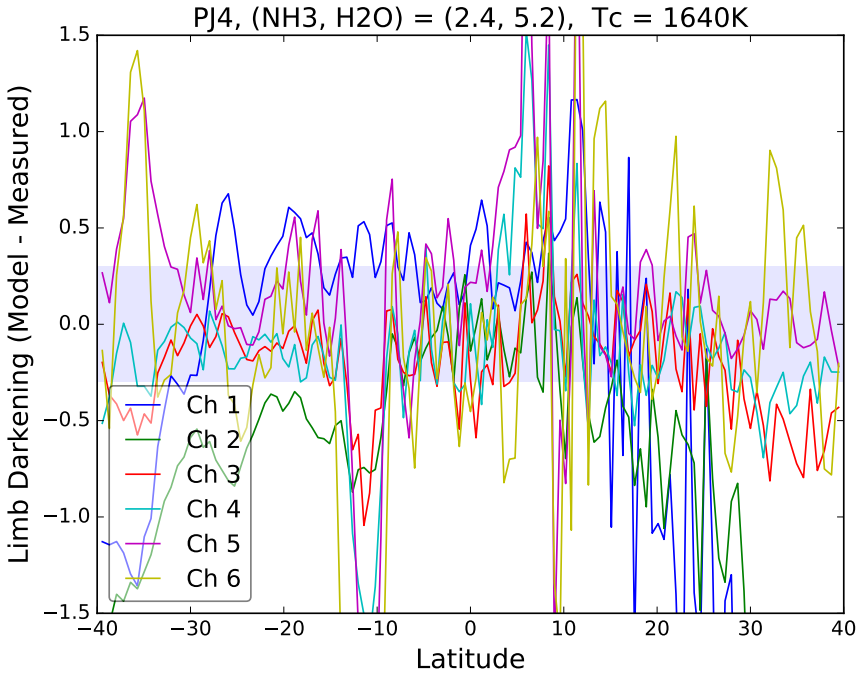

Figure 7.33: Difference between the measured and modeled 45° limb darkening as a function of frequency for each perijove. The shaded region is the 0.3% error box.

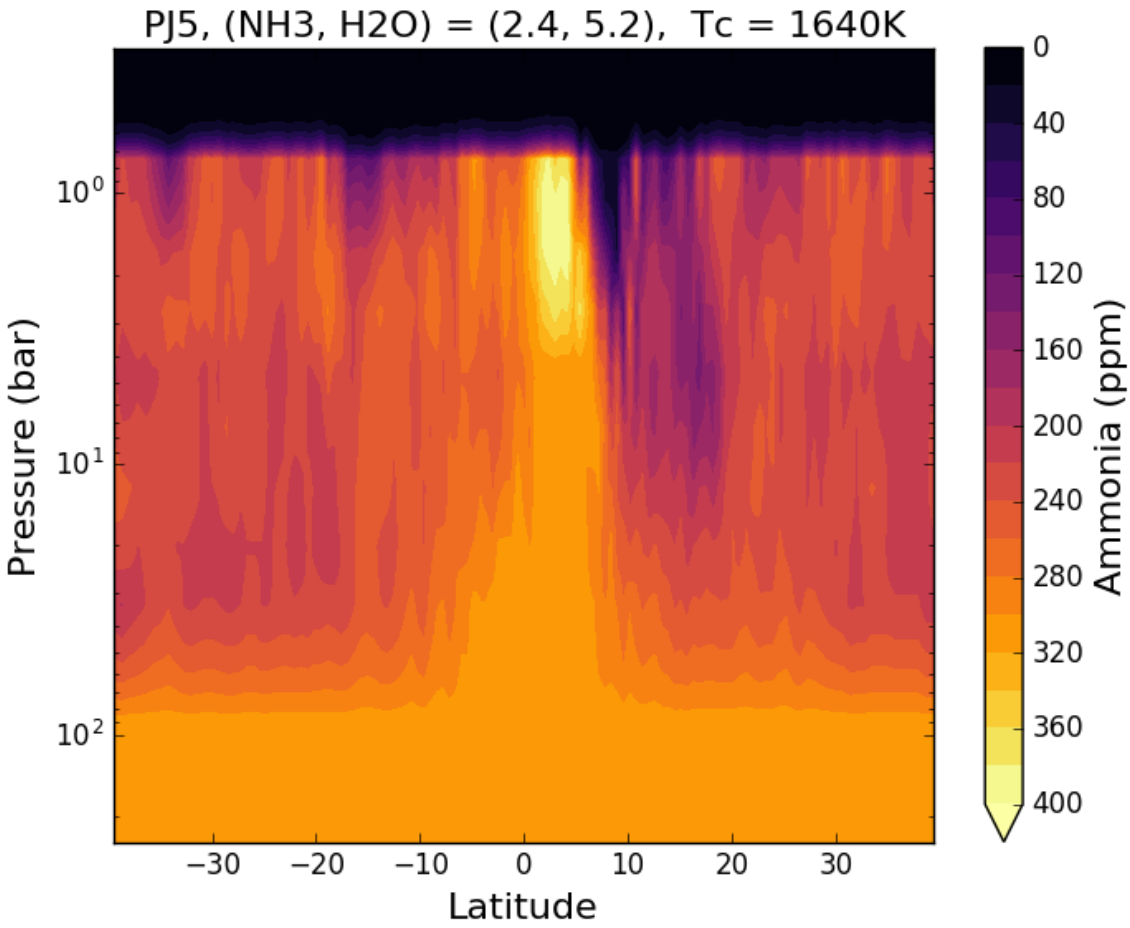

Figure 7.34: Colored contours show the ammonia concentration in parts per million retrieved from nadir brightness temperatures and limb darkening during PJ5 flyby. The assumed deep ammonia abundance is 2.4x solar, the assumed deep water vapor abundance is 5.2x solar, and the assumed alkali metal cutoff temperature is 1640K.

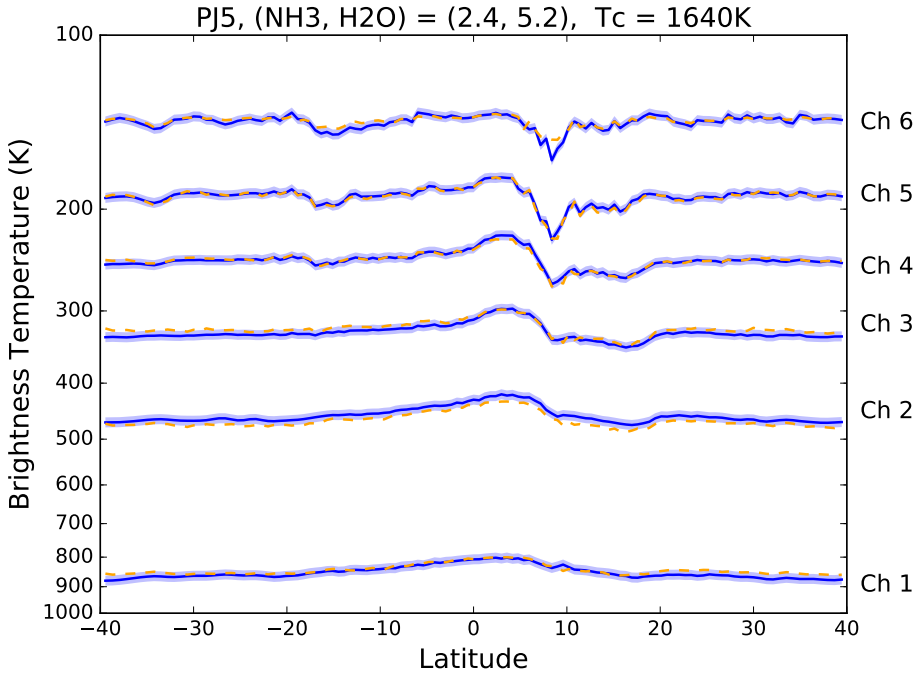

Figure 7.35: Nadir brightness temperature as a function of latitude for PJ5. The solid blue line represents the measured nadir brightness temperature and the dashed orange line is the modeled nadir brightness temperature using the retrieved values. The shaded region represents the 2% measurement error.

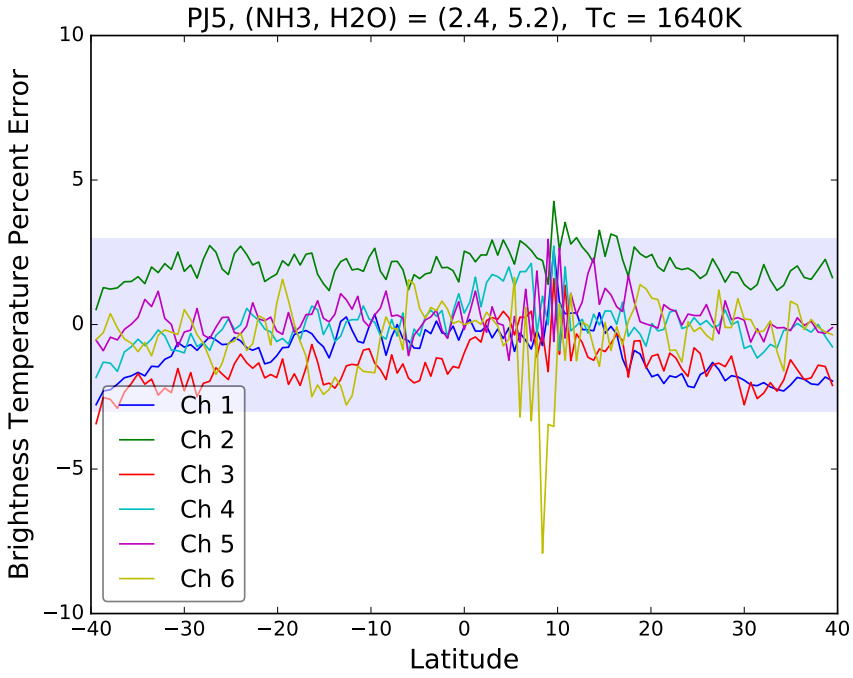

Figure 7.36: Percent difference between the measured and the modeled nadir brightness temperature for each channel. The shaded region represents the 3% error box.

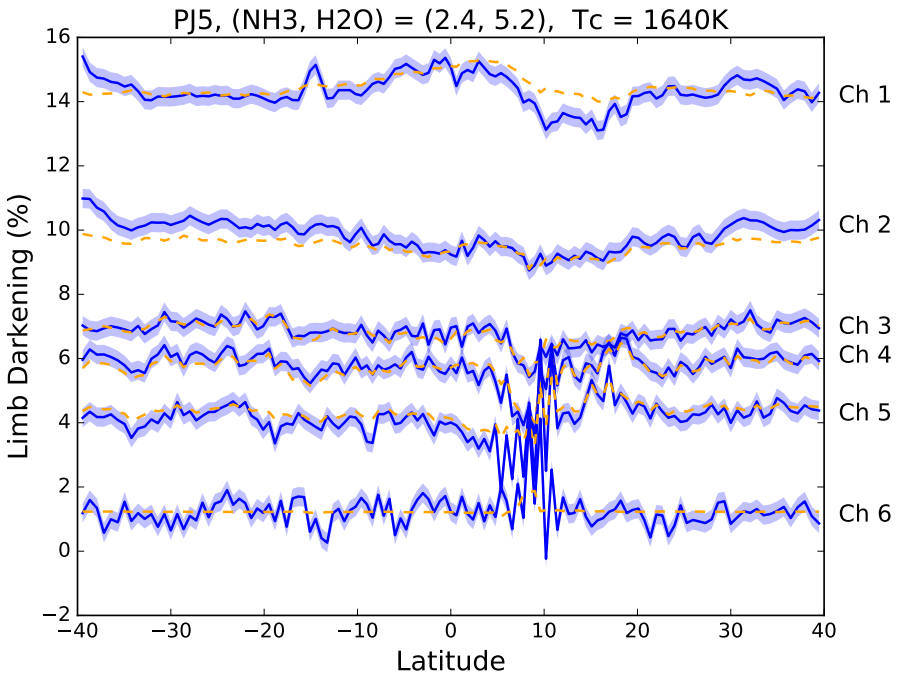

Figure 7.37: 45° Limb Darkening as a function of frequency for each perijove. The solid line represents the measured limb darkening and the dashed line is the modeled limb darkening using the retrieved values. The shaded region represents the 0.3% measurement error.

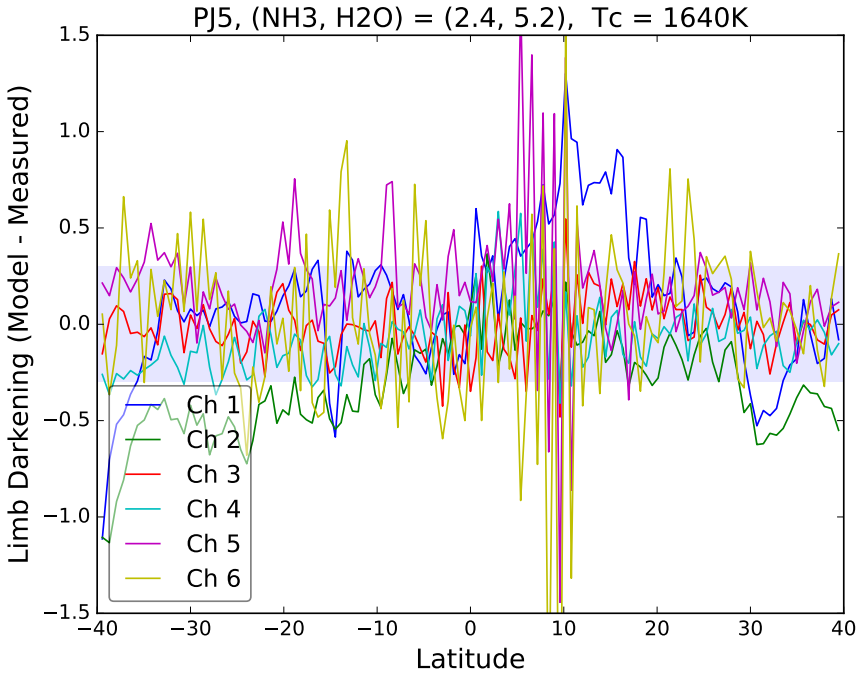

Figure 7.38: Difference between the measured and modeled 45° limb darkening as a function of frequency for each perijove. The shaded region is the 0.3% error box.

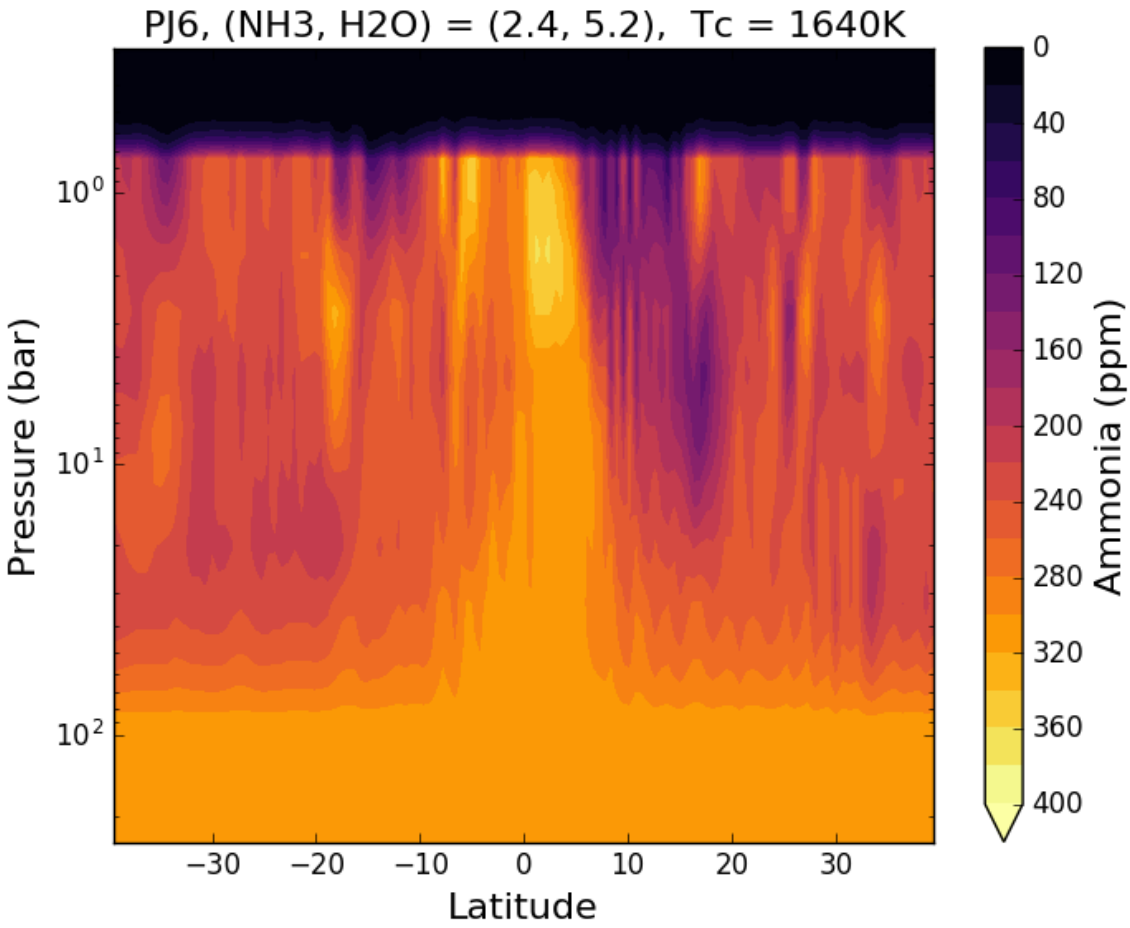

Figure 7.39: Colored contours show the ammonia concentration in parts per million retrieved from nadir brightness temperatures and limb darkening during PJ6 flyby. The assumed deep ammonia abundance is 2.4x solar, the assumed deep water vapor abundance is 5.2x solar, and the assumed alkali metal cutoff temperature is 1640K.

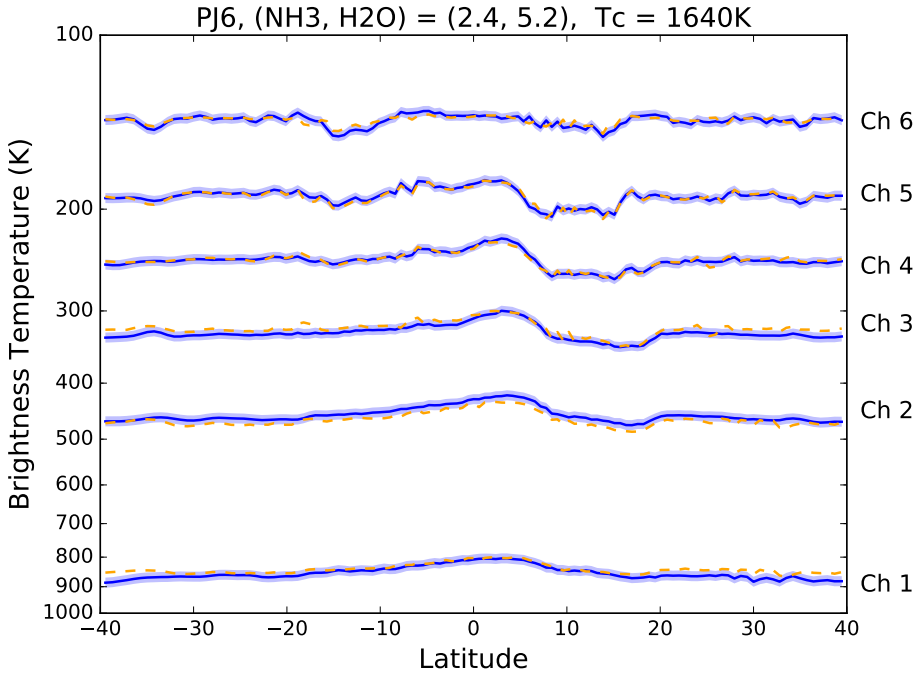

Figure 7.40: Nadir brightness temperature as a function of latitude for PJ6. The solid blue line represents the measured nadir brightness temperature and the dashed orange line is the modeled nadir brightness temperature using the retrieved values. The shaded region represents the 2% measurement error.

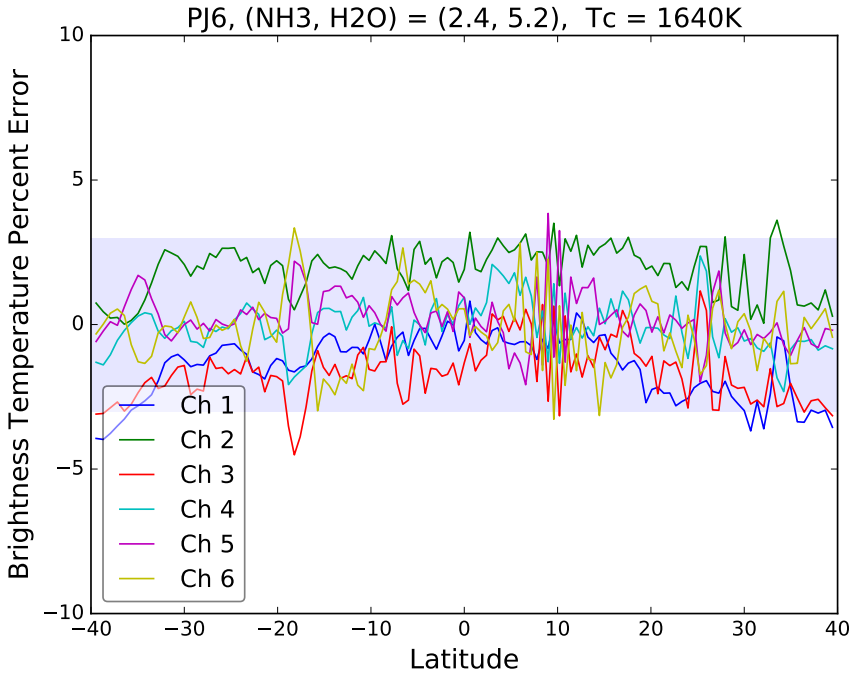

Figure 7.41: Percent difference between the measured and the modeled nadir brightness temperature for each channel. The shaded region represents the 3% error box.

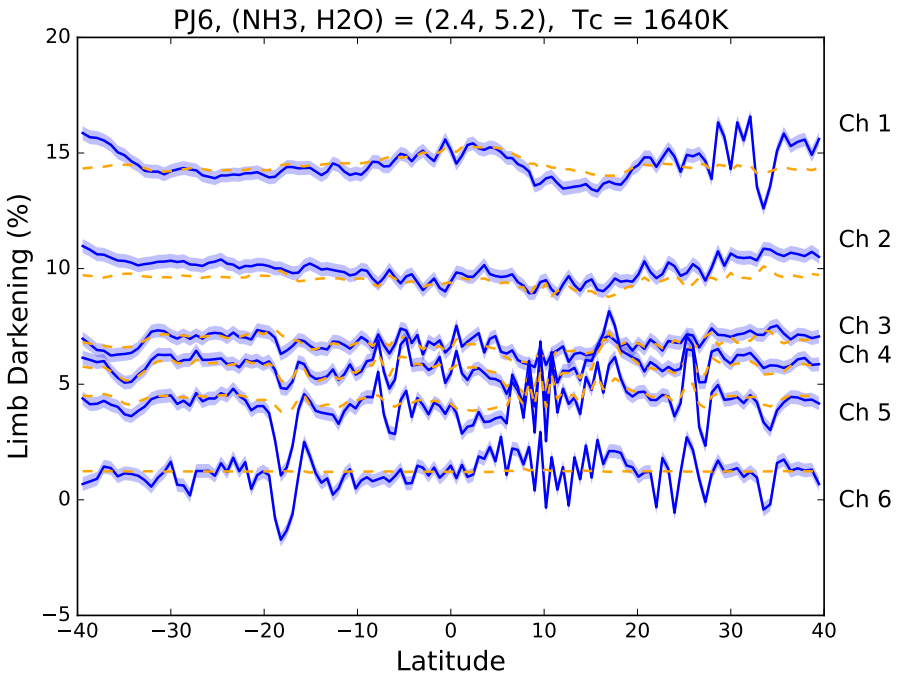

Figure 7.42: 45° Limb Darkening as a function of frequency for each perijove. The solid line represents the measured limb darkening and the dashed line is the modeled limb darkening using the retrieved values. The shaded region represents the 0.3% measurement error.

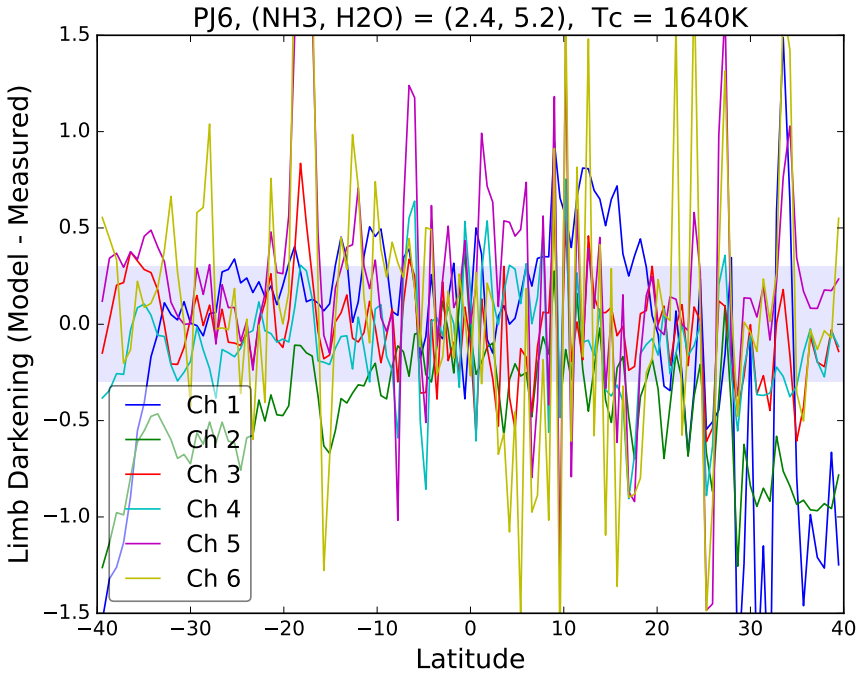

Figure 7.43: Difference between the measured and modeled 45° limb darkening as a function of frequency for each perijove. The shaded region is the 0.3% error box.

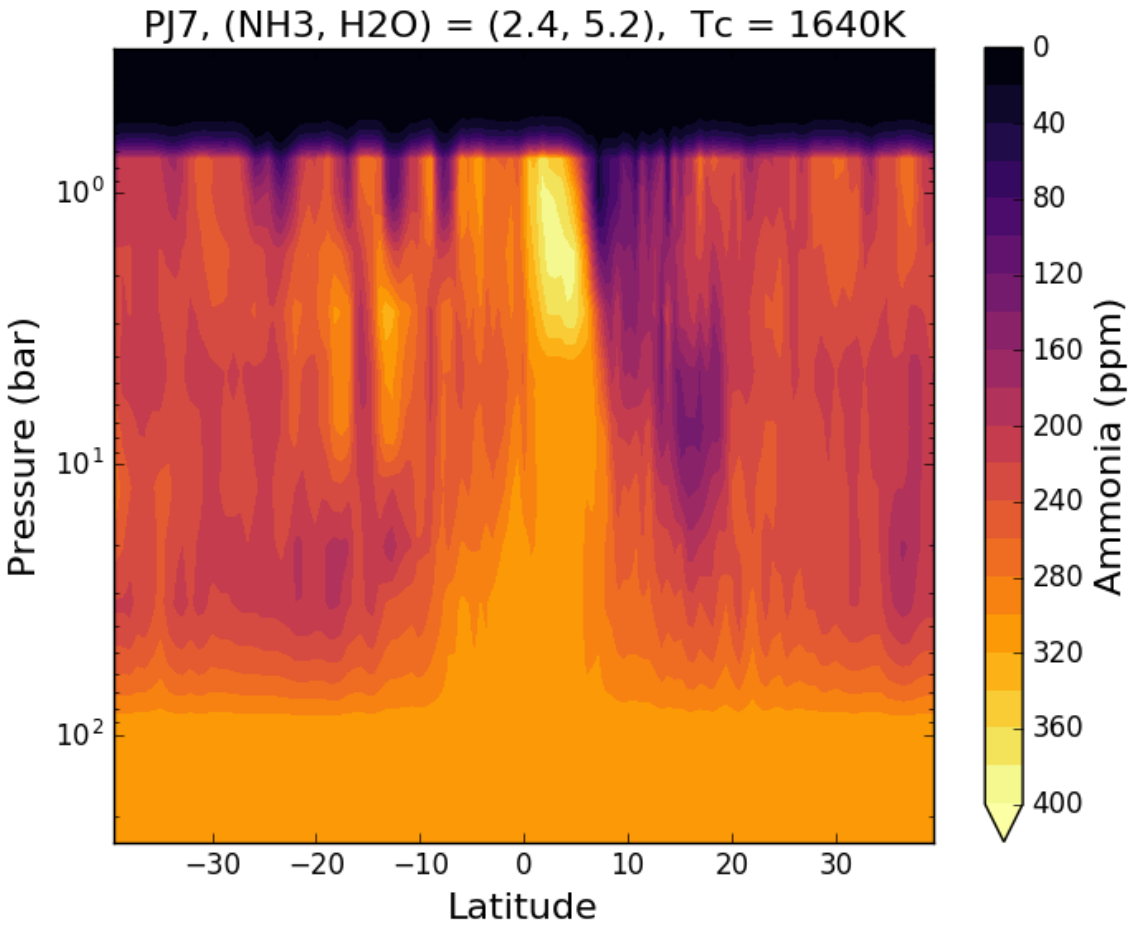

Figure 7.44: Colored contours show the ammonia concentration in parts per million retrieved from nadir brightness temperatures and limb darkening during PJ7 flyby. The assumed deep ammonia abundance is 2.4x solar, the assumed deep water vapor abundance is 5.2x solar, and the assumed alkali metal cutoff temperature is 1640K.

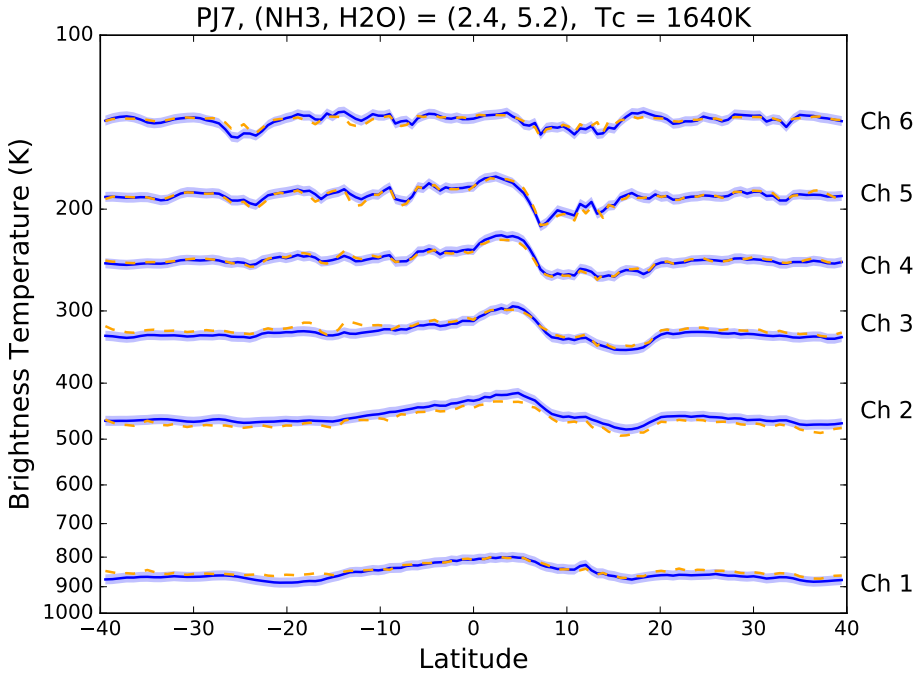

Figure 7.45: Nadir brightness temperature as a function of latitude for PJ7. The solid blue line represents the measured nadir brightness temperature and the dashed orange line is the modeled nadir brightness temperature using the retrieved values. The shaded region represents the 2% measurement error.

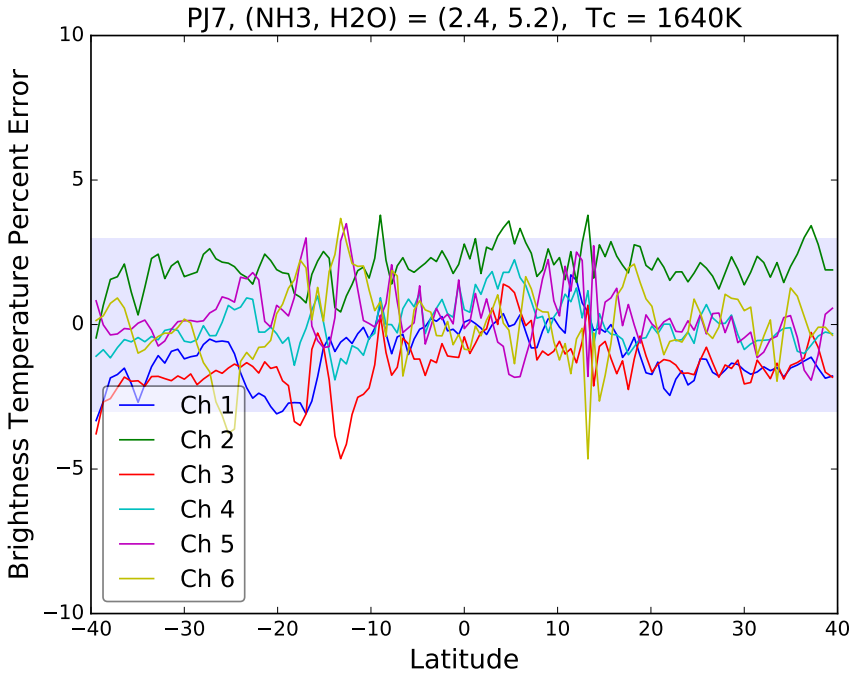

Figure 7.46: Percent difference between the measured and the modeled nadir brightness temperature for each channel. The shaded region represents the 3% error box.

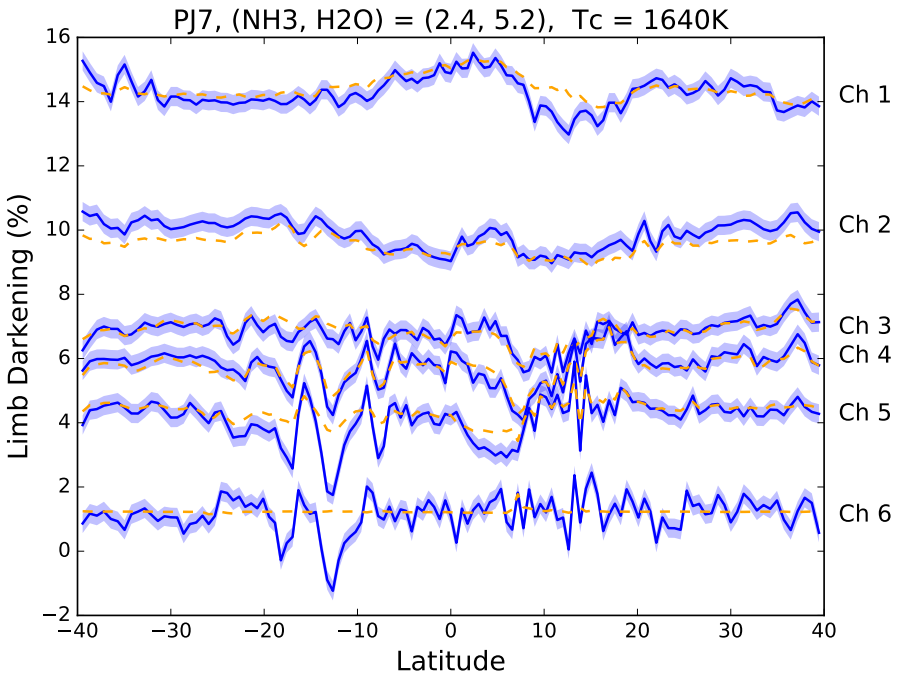

Figure 7.47: 45° Limb Darkening as a function of frequency for each perijove. The solid line represents the measured limb darkening and the dashed line is the modeled limb darkening using the retrieved values. The shaded region represents the 0.3% measurement error.

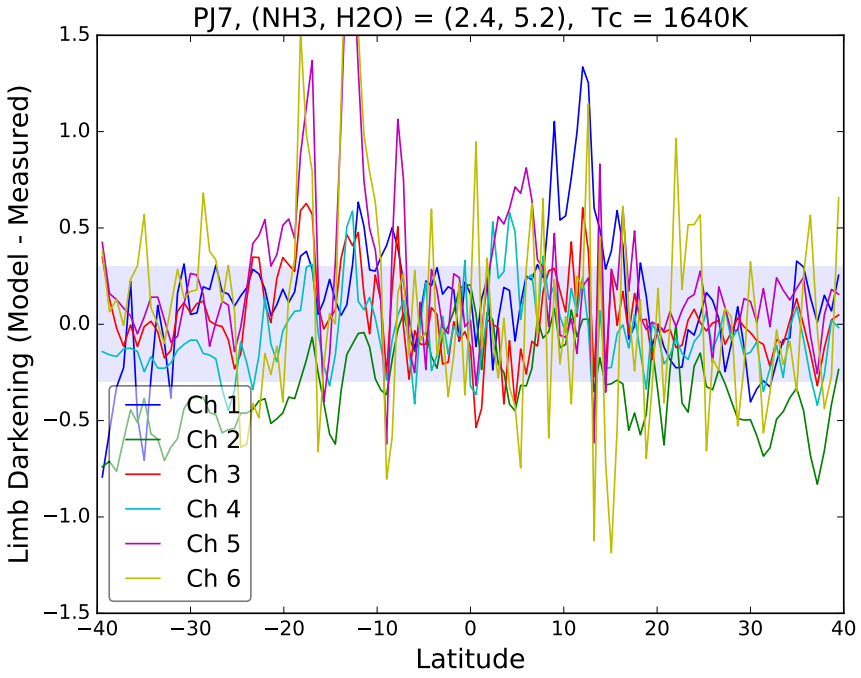

Figure 7.48: Difference between the measured and modeled 45° limb darkening as a function of frequency for each perijove. The shaded region is the 0.3% error box.

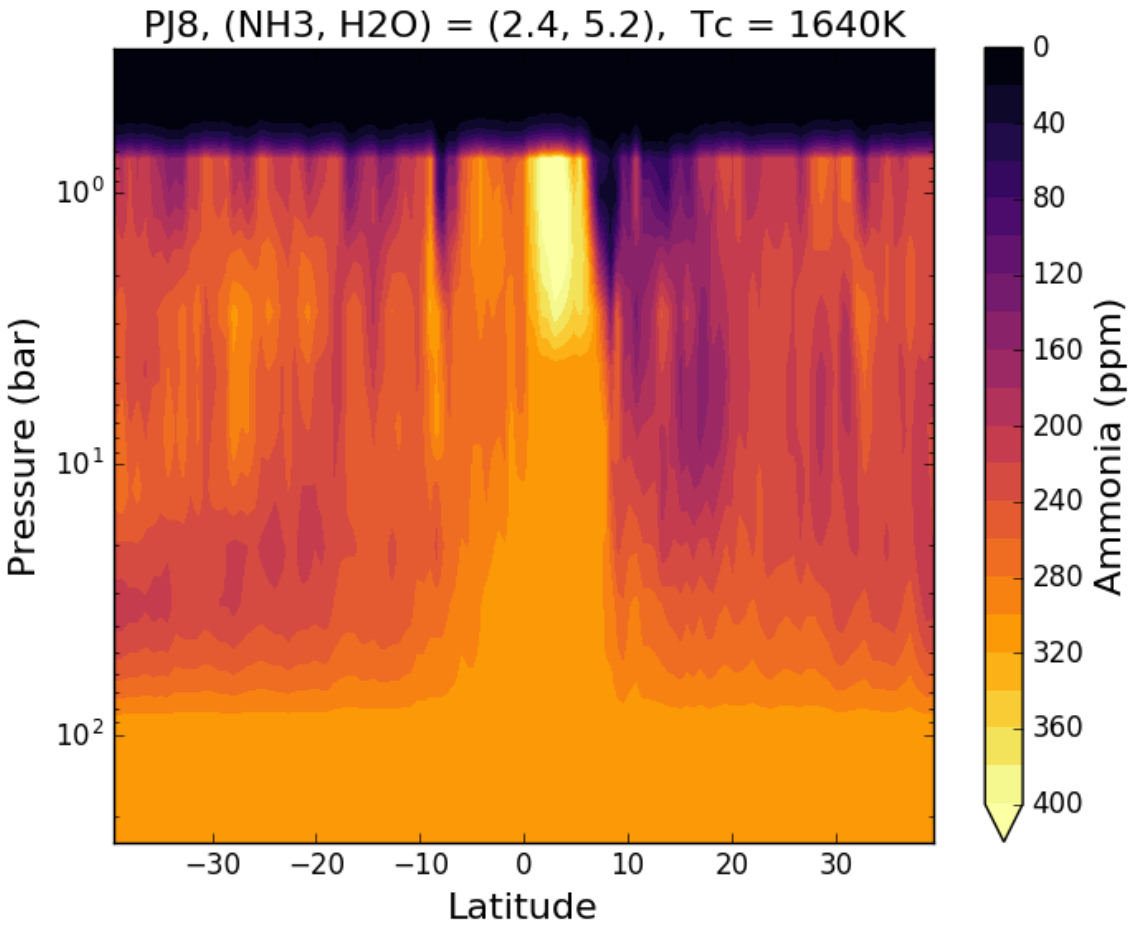

Figure 7.49: Colored contours show the ammonia concentration in parts per million retrieved from nadir brightness temperatures and limb darkening during PJ8 flyby. The assumed deep ammonia abundance is 2.4x solar, the assumed deep water vapor abundance is 5.2x solar, and the assumed alkali metal cutoff temperature is 1640K.

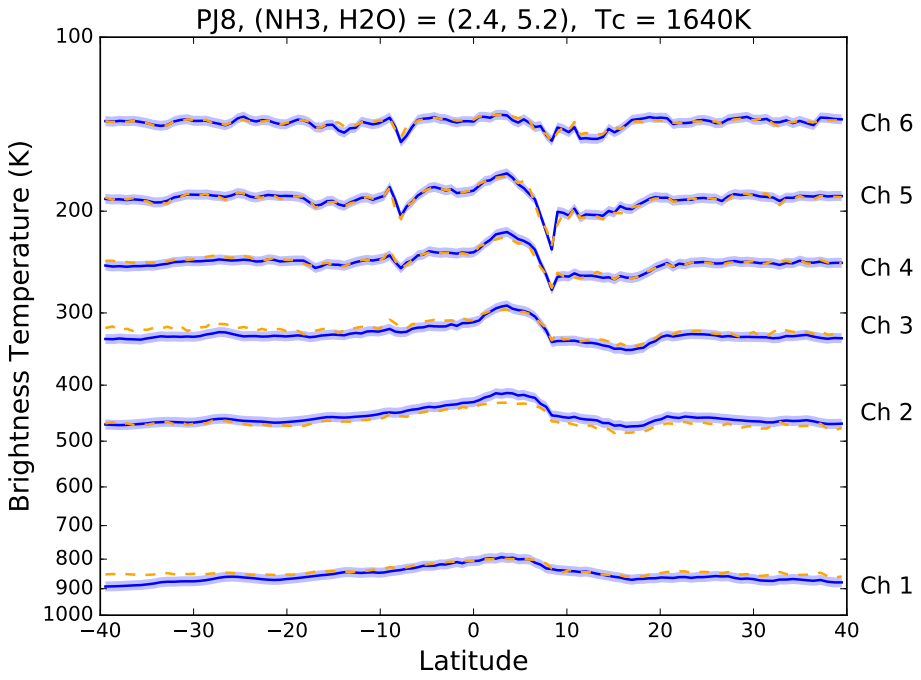

Figure 7.50: Nadir brightness temperature as a function of latitude for PJ8. The solid blue line represents the measured nadir brightness temperature and the dashed orange line is the modeled nadir brightness temperature using the retrieved values. The shaded region represents the 2% measurement error.

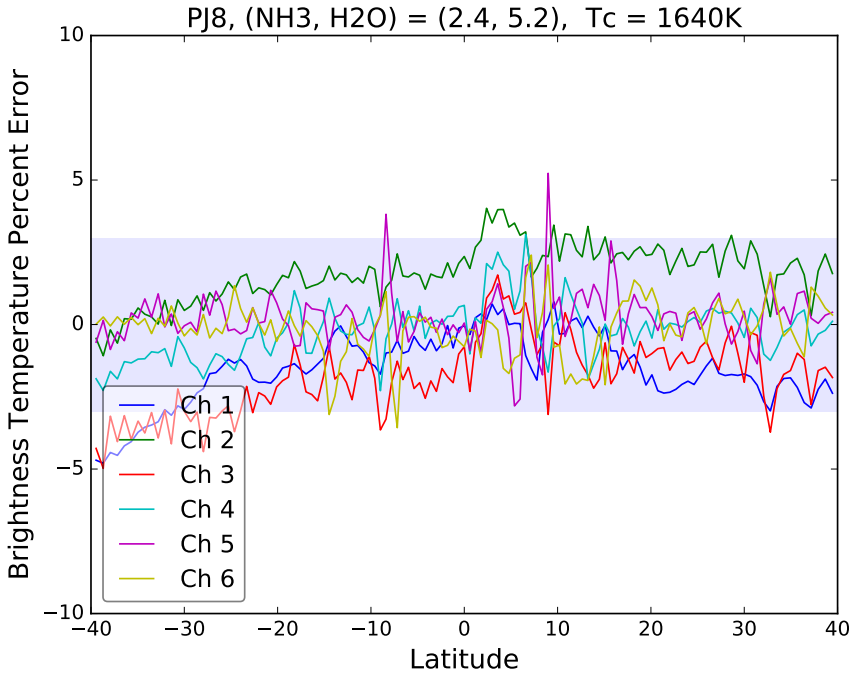

Figure 7.51: Percent difference between the measured and the modeled nadir brightness temperature for each channel. The shaded region represents the 3% error box.

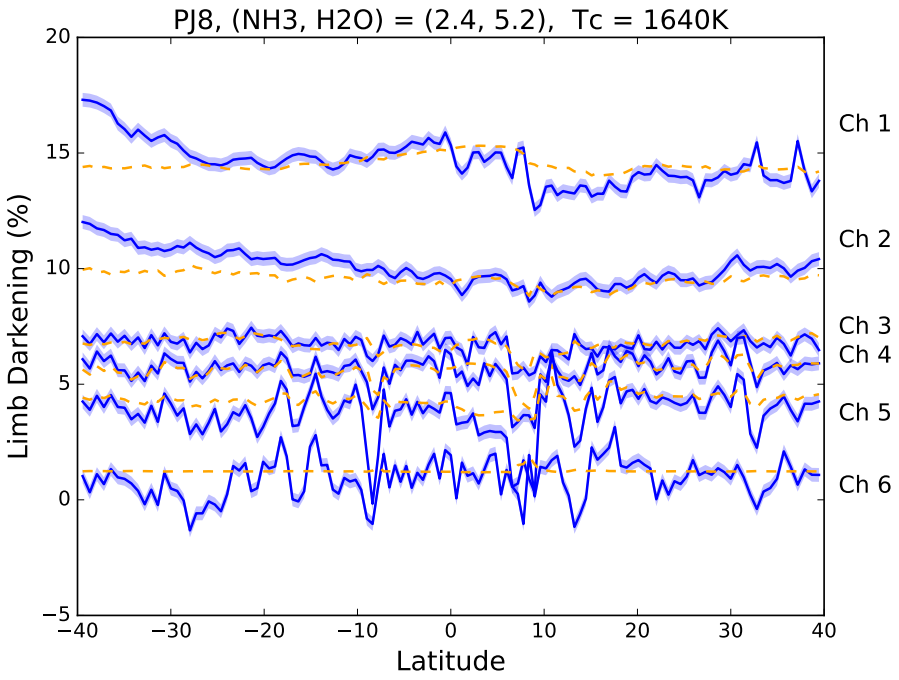

Figure 7.52: 45° Limb Darkening as a function of frequency for each perijove. The solid line represents the measured limb darkening and the dashed line is the modeled limb darkening using the retrieved values. The shaded region represents the 0.3% measurement error.

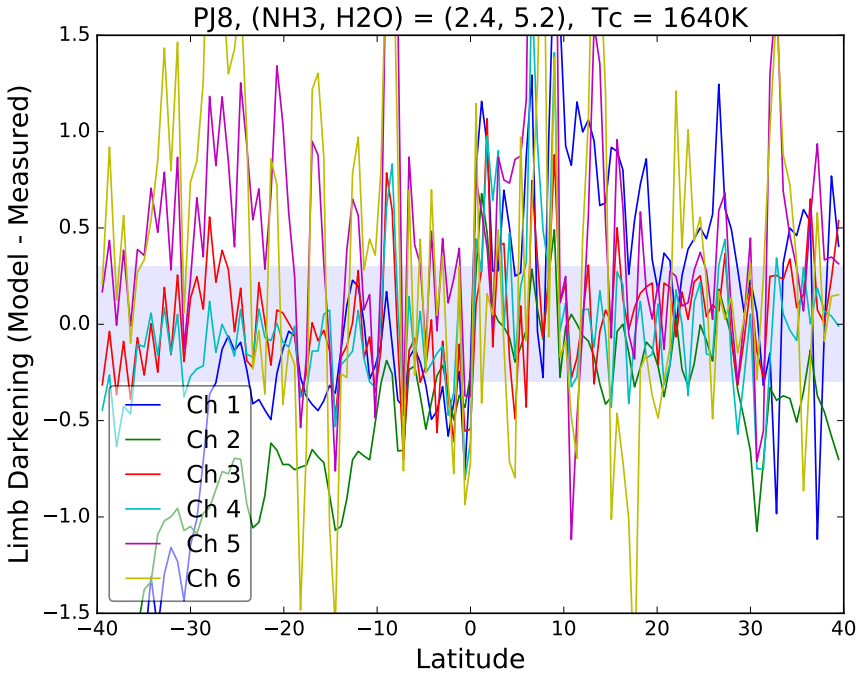

Figure 7.53: Difference between the measured and modeled 45° limb darkening as a function of frequency for each perijove. The shaded region is the 0.3% error box.

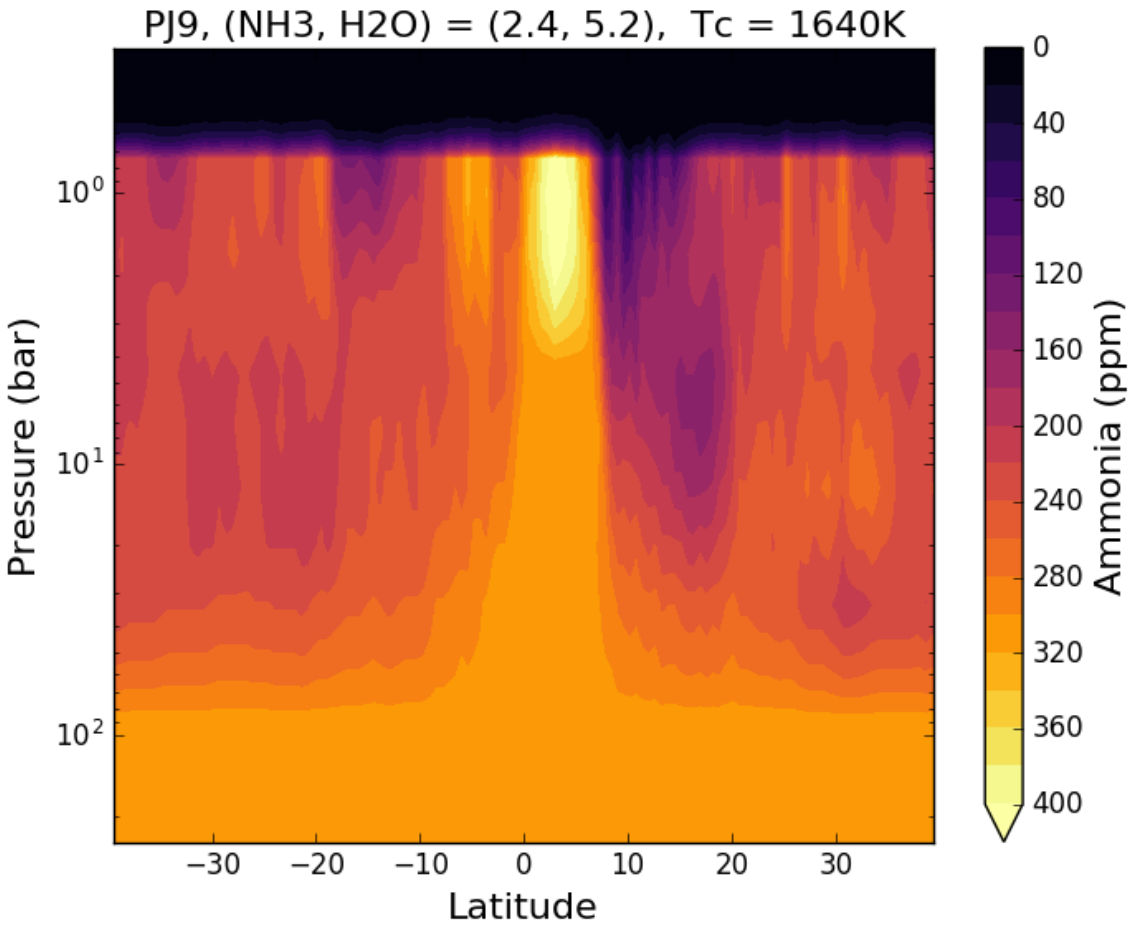

Figure 7.54: Colored contours show the ammonia concentration in parts per million retrieved from nadir brightness temperatures and limb darkening during PJ9 flyby. The assumed deep ammonia abundance is 2.4x solar, the assumed deep water vapor abundance is 5.2x solar, and the assumed alkali metal cutoff temperature is 1640K.

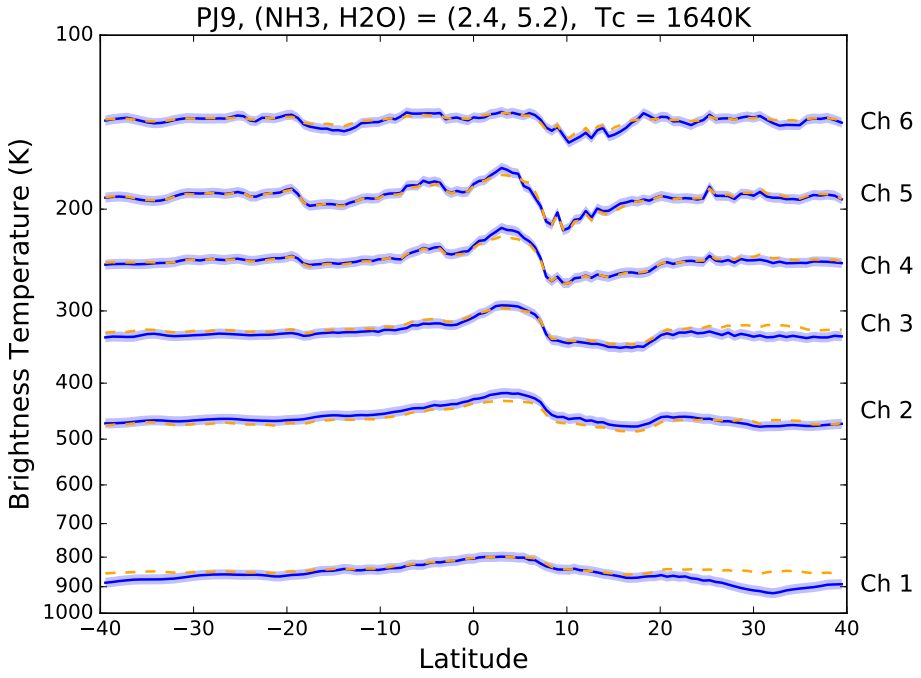

Figure 7.55: Nadir brightness temperature as a function of latitude for PJ9. The solid blue line represents the measured nadir brightness temperature and the dashed orange line is the modeled nadir brightness temperature using the retrieved values. The shaded region represents the 2% measurement error.

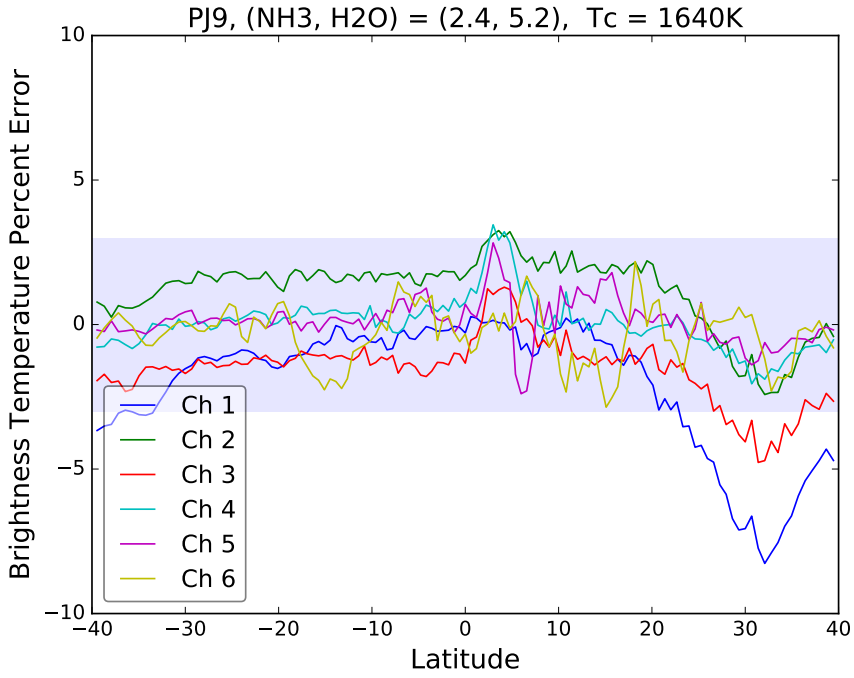

Figure 7.56: Percent difference between the measured and the modeled nadir brightness temperature for each channel. The shaded region represents the 3% error box.

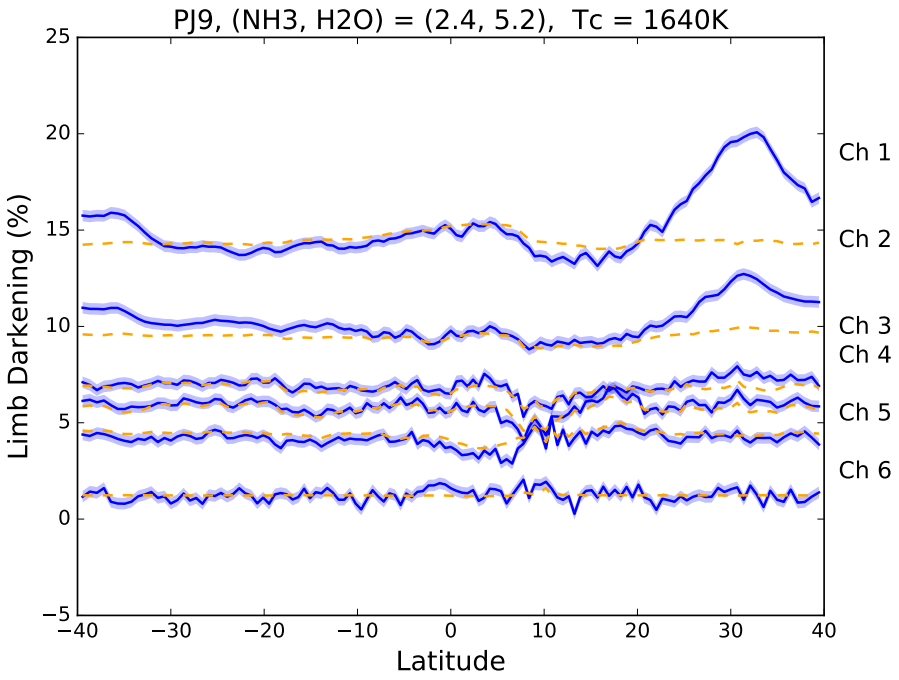

Figure 7.57: 45° Limb Darkening as a function of frequency for each perijove. The solid line represents the measured limb darkening and the dashed line is the modeled limb darkening using the retrieved values. The shaded region represents the 0.3% measurement error.

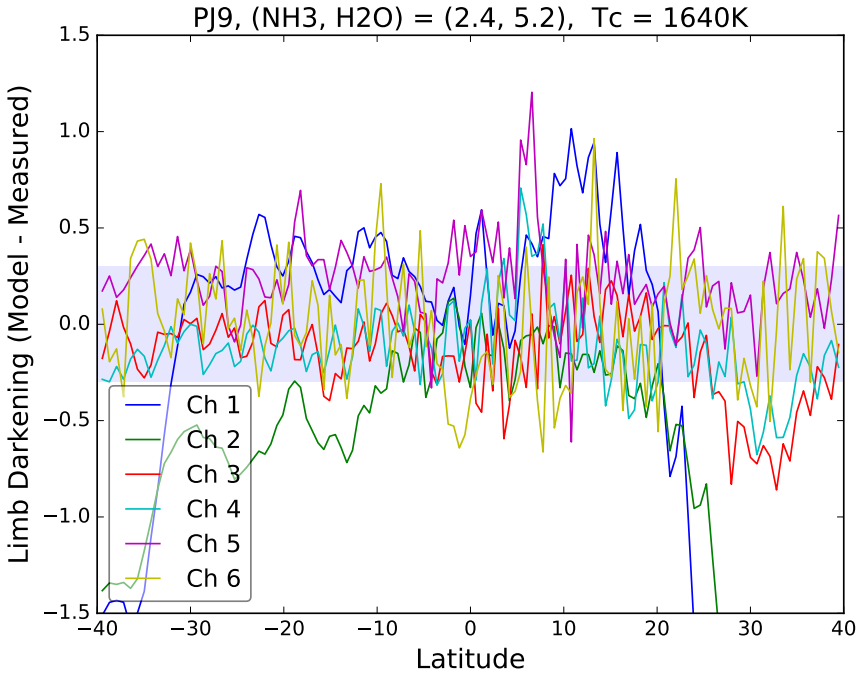

Figure 7.58: Difference between the measured and modeled 45° limb darkening as a function of frequency for each perijove. The shaded region is the 0.3% error box.

7.3 Characterization of Uncertainties in Retrieval Method

The uncertainties associated with the retrieved atmospheric parameters can be split into two types: (i) uncertainty of the measurements (σ_{meas}) and (ii) uncertainty of the atmospheric model (σ_{model}).

The first reflects how instrument uncertainty affects the retrieved atmospheric parameters. That is, assuming a perfect atmospheric parameterization, how much does measurement uncertainty affect the retrieved parameters. The uncertainty in the measurements is characterized in Janssen et al. (2017a) and is described in equations 7.7 and 7.8.

The second reflects how well the atmospheric model parameterization matches the observations, assuming noiseless measurements. The uncertainty in the atmospheric model can be characterized by the average error in modeled brightness temperature and limb darkening when compared with the measured brightness temperature and limb darkening. The modeled brightness temperature and limb darkening are calculated by JAMRT using the retrieved atmospheric parameters. The uncertainties due to measurement noise (σ_{meas}), uncertainties of the retrieval method (σ_{model}), and the total uncertainties (σ_{total}) for both subdomains is shown in Table 7.11.

The total error is calculated by adding both types of errors and is used in the following error propagation.

$$\sigma_{total} = \sigma_{meas} + \sigma_{model} \tag{7.10}$$

The remainder of this section describes an effort to quantify the stochastic uncertainties in the retrieved atmospheric profile parameters (state vector $\mathbf{x}$) derived from the deconvolved Juno MWR measurements using a method adapted from Jenkins et al. (2002). Usually these uncertainties could have been determined from the linearized inverse problem using standard error propagation. However, given the nonlinear nature of the radiative transfer process, a Monte Carlo approach is used. This approach consists of generating synthetic data using JAMRT, adding simulated measurement noise consistent with actual

Table 7.11: Table showing the uncertainties due to measurement noise (σ_{meas}), uncertainties of the retrieval method (σ_{model}) and the total uncertainties (σ_{total}) for brightness temperature (in units of percent of measured value) and limb darkening (in units of percent limb darkening) for each subdomain.

				w/Alkali Metals		w/o Alkali Metals	
		Ch	σ_{meas}	σ_{model}	σ_{total}	σ_{model}	σ_{total}
T_b	Nadir	1	2.0	1.62	3.62	1.84	3.84
		2	2.0	1.94	3.94	1.43	3.43
		3	2.0	1.66	3.66	1.44	3.44
		4	2.0	0.68	2.68	1.37	3.37
		5	2.0	0.63	2.63	1.22	3.22
		6	2.0	0.91	2.91	1.24	3.24
Limb Darkening	20°	1	0.3	0.20	0.50	0.31	0.61
		2	0.3	0.14	0.44	0.16	0.46
		3	0.3	0.05	0.35	0.05	0.35
		4	0.3	0.05	0.35	0.05	0.35
		5	0.3	0.12	0.42	0.13	0.43
		6	0.3	0.13	0.43	0.09	0.39
	30°	1	0.3	0.39	0.69	0.61	0.91
		2	0.3	0.29	0.59	0.34	0.64
		3	0.3	0.10	0.40	0.13	0.43
		4	0.3	0.10	0.40	0.10	0.40
		5	0.3	0.23	0.53	0.26	0.56
		6	0.3	0.26	0.56	0.17	0.47
	45°	1	0.3	0.62	0.92	0.99	1.29
		2	0.3	0.51	0.81	0.63	0.93
		3	0.3	0.19	0.49	0.37	0.67
		4	0.3	0.22	0.52	0.25	0.55
		5	0.3	0.39	0.69	0.48	0.78
		6	0.3	0.48	0.78	0.30	0.60

observations (σ_{total}), and attempting to recover the atmospheric profile parameters used to generated the noise-corrupted measurements.

The target atmospheric profile parameters, $\mathbf{x}$, are modified randomly for each run. In this case, the deep atmospheric abundances of ammonia (NH_3) and water vapor (H_2O) were drawn from a uniform distribution between 1.8–2.7x solar and 1.0–11.0x solar, respectively. Each target ammonia abundance profile ($\mathbf{s}$) was constructed by drawing a scaling factor at each pressure point from a uniform distribution between 10–100%. Finally, the cutoff temperature (T_c), when used in the given subdomain, is drawn from a uniform distribution between 1300–2000K.

For each atmosphere constructed, a set of synthetic measurements was generated using JAMRT. Gaussian noise with a zero mean and a sigma of σ_{total} was added to these synthetic measurement. The algorithm described in Section 7.1 was used to determine the solution profiles for each set of synthetic measurements. The difference between the retrieved atmospheric profile parameters and the target atmospheric profile parameters established the stochastic uncertainties in the retrieval.

For each subdomain, 100 different atmospheres were randomly generated. For each atmosphere, 100 different realizations of instrument noise was used to estimate the stochastic uncertainties in the retrieval. This gives us a total of 10,000 noisy simulated spectra to estimate the uncertainty. Table 7.12 shows the uncertainty in the retrieval parameters for each subdomain. Table 7.13 shows the retrieval results for latitudes near 2.4°N with the estimated uncertainties. Figure 7.59 shows the retrieved ammonia abundance near 4 latitudes for PJ9 assuming a deep layer of ionized alkali metals with the estimated uncertainties. The prior knowledge used in the retrieval forcing the ammonia concentration equal or less to that in an ideal adiabatic atmosphere can also be applied to the estimated uncertainties. If the retrieved ammonia concentration is equal to an ideal adiabatic deep in Jupiter's atmosphere, the uncertainty in the retrieved ammonia concentration would then be equal to the uncertainty in the deep abundance. Figure 7.59 best shows this at 2.39°N and 5.98°N.

Table 7.12: Table showing the uncertainty of the retrieval method due to measurement noise and uncertainty of the atmospheric model for each subdomain and atmospheric parameter

	NH_3	H_2O	Scaling amount at Pressure (bar)											T_c
			92.0	33.1	20.1	12.2	7.39	4.48	2.72	1.65	1.0	0.61	0.3	
w/o alkali	0.23	2.45	0.00	0.25	0.26	0.25	0.24	0.31	0.28	0.28	0.27	0.28	0.32	N\A
w/ alkali	0.26	2.27	0.00	0.26	0.29	0.28	0.26	0.30	0.24	0.27	0.25	0.28	0.31	120

Table 7.13: Table showing retrieved deep abundance of ammonia and water vapor, cutoff temperature and the associated uncertainties at 2.4°N using all perijoves.

State Vector	Value		Unit
	w/o alkali	w/ alkali	
NH_3	2.35 ± 0.23	2.40 ± 0.26	solar
H_2O	8.70 ± 2.45	5.20 ± 2.27	solar
T_c	N/A	1640 ± 120	K

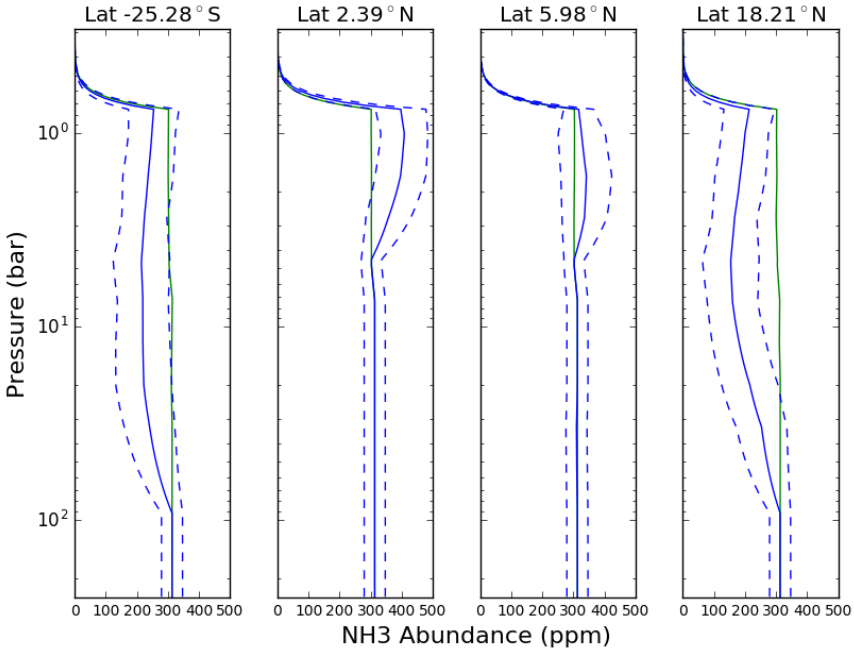

Figure 7.59: Retrieved ammonia abundance near 4 latitudes for PJ9 assuming a deep layer of ionized alkali metals. The green line represented a well mixed profile with an ammonia deep abundance of 2.4x solar. The solid blue line is the retrieved ammonia abundance and the dashed blue lines are the estimated uncertainties (as shown in Table 7.12). Note that uncertainties in the laboratory-derived attenuation coefficients could add up to 2% additional uncertainty in the stated abundance.

CHAPTER 8
CONCLUSIONS

The objective of this doctoral research has been to advance the understanding of Jupiter's atmosphere using measurements taken by the Juno Microwave Radiometer (MWR). As part of this research, high temperature laboratory measurements of the microwave absorption properties of gaseous ammonia and water vapor were taken. The ammonia measurements and pre-existing laboratory measurements (Hanley et al., 2009; Devaraj et al., 2011; Devaraj et al., 2014) were utilized to develop a physically accurate consistent model for the opacity of ammonia, pressure broadened by hydrogen and helium, in both the centimeter and millimeter wavelength range. Additionally, the high temperature measurements of the microwave absorption of water vapor were used to modify the absorption model presented in Karpowicz and Steffes (2011a) so as to more accurately represent the microwave opacity of water vapor under the high temperatures characteristic of the deep jovian atmosphere. Following the laboratory measurements, multiple atmospheric phenomena were modeled using the Jupiter Atmospheric Microwave Radiative Transfer (JAMRT) model. These phenomena included potential virga in the jovian atmosphere, possible deep atmospheric effects such as a radiative zone or the presence of ionized alkali metals, and auroral effects on the jovian microwave emission.

These models were then used to perform retrievals of atmospheric parameters using data from the Juno MWR. The retrieval utilizes a neural network as a surrogate to JAMRT. Once the neural network surrogate is trained, it is able to quickly and accurately predict results from the radiative transfer model. This paired with the L-BFGS-B minimization algorithm allowed for rapid retrievals of the Juno MWR data under multiple subdomains and constraints. This resulted in a two part retrieval: (1) retrieving the deep abundance of ammonia and water vapor at a place most resembling an ideal adiabat, and (2) using the

retrieved values to produce an ammonia distribution map.

8.1 Contributions

The objective of this doctoral research work has been to better understand the jovian atmosphere. During the course of this work, several unique contributions were made to the fields of microwave spectroscopy and planetary science.

8.1.1 Laboratory Measurements and Model

As part of the laboratory measurements campaign, high temperature measurements of the centimeter-wavelength properties of ammonia and water vapor under simulated jovian conditions were made. The ammonia absorption measurements were used in conjunction with previous laboratory measurements to develop an absorption model for ammonia that adheres to strict physical properties. While previous ammonia absorption models (Hanley et al., 2009; Devaraj et al., 2014) fit the available laboratory measurements, anomalous behavior in these models showed that an examination from a physical viewpoint was needed. Seven distinct weaknesses (three in Hanley et al. (2009) and four in Devaraj et al. (2014)) were identified and addressed in the new model.

Additionally, the water vapor absorption expression presented by Karpowicz and Steffes (2011a) contained an additional term (compared with more traditional models) which exhibited non-physical behavior. The additional term was removed and the model was revised. High temperature measurements of water vapor's microwave absorption were then used to verify this revision.

Both of these models were implemented in JAMRT and are now used in the retrieval of atmospheric parameters from measurements taken by the Juno MWR.

8.1.2 Modeling Jovian Atmospheric Phenomena

Accurate retrievals of atmospheric parameters in Jupiter's atmosphere require accurate models. Four models of the microwave properties of different atmospheric phenomena have been developed and implemented as part of this doctoral research.

The first model reflects the effect of virga on the microwave emission spectrum. This model is a time-dependent microphysical model which studies the evolution of water clouds in Jupiter's atmosphere, and simulates how precipitation and its evaporation affect the microwave emission spectrum. The model consists of three parts: calculation of raindrop size and effect on the mole fraction of water vapor, calculation of the complex dielectric constant of aqueous ammonia, and determination of the Rayleigh scattering due to the raindrops present.

The second model determines the effect of a possible radiative zone at temperatures around 1300K. The radiative zone is an area where heat is transferred through radiation instead of convection, and is driven by the infrared opacity. This model calculates where such a zone would occur and its effect on the temperature profile, which reflects itself in the radiated microwave spectrum.

The third model determines the effect of ionized alkali metals in the deep jovian atmosphere. The model uses the Saha ionization equation to determine the degree of ionization due to the thermal collisions of atoms in the plasma. It then uses the Appleton-Hartree equation to calculate the complex refractive index of this cold-magnetized plasma. Finally the complex refractive index is used to calculate the microwave opacity of the plasma.

The fourth model reflects effects of the aurora on the microwave opacity reflected in measurements of the Juno MWR. The model calculates the complex refractive index of the aurora and uses it to calculate the microwave opacity of the aurora. While direct measurements of many of the jovian auroral structural properties are minimal, coarse estimates can be used to better understand these effects.

These models have been presented at multiple conferences and to the Juno Science

Team. Ongoing work is being done using these models by the Juno MWR team to better understand what the Juno MWR is measuring.

8.1.3 Atmospheric Parameter Retrievals

The majority of the work done in this doctoral research involves the retrieval of atmospheric parameters from measurements taken by the Juno MWR. At the core of the retrieval method developed is a neural network used as a surrogate for JAMRT. While surrogate models have a history of use in oceanography and meteorology, this is the first time a surrogate has been used for retrievals in planetary science. By using a neural network surrogate, retrievals were able to be performed in a much quicker way, allowing for better understanding of atmospheric affects on the Juno MWR measurements.

The surrogate neural network was trained using artificial data generated using JAMRT. Once the neural network surrogate was trained, it was able to quickly and accurately predict results from the radiative transfer model. A surrogate neural network for two subdomains was used, one with ionized alkali metals and one without.

The surrogate neural network was then paired with the L-BFGS-B minimization algorithm. The L-BFGS-B minimization algorithm further accelerated the retrieval by fast estimation of the Hessian Matrix of the minimization function. By exploring multiple subdomains using the algorithm's constraints, a two part retrieval was developed. The first part retrieved the deep abundance of ammonia and water vapor, and the cutoff temperature of the deep ionized layer at a place most resembling an ideal adiabat. The second part uses the retrieved deep abundances and cutoff temperatures along with the 6-wavelength MWR data to produce an ammonia distribution map.

8.2 Recommendations for Future Work

While this work is extensive it is by no means complete. The knowledge that will be obtained by the Juno mission will be unprecedented. The fundamental understanding of

Jupiter's atmosphere presented in this work can be applied to three main topics.

The first is future study of the sensitivity of retrievals to atmospheric structure (i.e localized lapse rate variations). The retrieval presented in this work assumes that the deep ammonia and water vapor abundance near 2.4°N latitude is representative of the whole planet. This assumption is based upon the idea that this latitude best represents an idea adiabat. Better understanding of the dynamics occurring in Jupiter's atmosphere will result in more accurate models of the lapse rate. Further work should examine the sensitivity of this and other retrieval methods to localized lapse rate variations.

The second is the study of Jupiter's atmosphere in the polar regions. As Juno's orbits precess, the perijoves will move father north and begin to better map the polar regions. The retrievals presented in this work only span from 40°N to 40°S, however the Juno MWR measures all latitudes during a single orbit. Future work will have to process the data in such a way to identify and remove possible contamination due to synchrotron radiation. Studying these polar regions will help to better understand the dynamics occurring over the entire planet.

The third is the study of Jupiter's aurora and its potential affects on the Juno MWR. The understanding of the auroras will require working with other Juno instrument teams. Using maps from the Ultraviolet spectrometer and the IR camera can help understand what the Juno MWR is measuring. A radiative transfer model of the aurora should be written and applied to measurements taken by the Juno MWR. The deconvolution of the measured auroral antenna temperature to brightness temperature require a potentially different deconvolution method than the one described in this work.

8.3 List of Publications

8.3.1 Refereed Journal Articles (in chronological order)

Bellotti, Amadeo and Paul G Steffes. 2015. “The Millimeter-Wavelength Sulfur Dioxide Absorption Spectra Measured Under Simulated Venus Conditions”. *Icarus* 254, pp. 24–33.

Steffes, Paul G., Patrick Shahan, G. Christopher Barisich, and Amadeo Bellotti. 2015. “Laboratory measurements of the 3.7–20 cm wavelength opacity of sulfur dioxide and carbon dioxide under simulated conditions for the deep atmosphere of Venus ”. *Icarus* 245, pp. 153–161.

Bellotti, Amadeo, Paul G. Steffes, and Garrett Chinsomboom. 2016. “Laboratory Measurements of the 5-20 cm Wavelength Opacity of Ammonia, Water Vapor, and Methane Under Simulated Conditions for the Deep Jovian Atmosphere”. *Icarus* 280, pp. 255–267.

Bellotti, Amadeo, Paul G Steffes, and Garrett Chinsomboon. 2017. “Corrigendum to” Laboratory measurements of the 5-20 cm wavelength opacity of ammonia, water vapor, and methane under simulated conditions for the deep jovian atmosphere”[Icarus 280 (2016) 255-267]”. *Icarus* 284, pp. 491–492.

Ingersoll, Andrew P., Virgil Adumitroaie, Michael D. Allison, Sushil Atreya, Amadeo A. Bellotti, Scott J. Bolton, Shannon T. Brown, Samuel Gulkis, Michael A. Janssen, Steven M. Levin, Cheng Li, Liming Li, Jonathan I. Lunine, Glenn S. Orton, Fabiano A. Oyafuso, and Paul G. Steffes. 2017. “Implications of the ammonia distribution on Jupiter from 1 to 100 bars as measured by the Juno microwave radiometer”. *Geophysical Research Letters* 45.1, pp. 317–325.

Li, Cheng, Andrew Ingersoll, Michael Janssen, Steven Levin, Scott Bolton, Virgil Adumitroaie, Michael Allison, John Arballo, Amadeo Bellotti, Shannon Brown, et al.

2017. “The distribution of ammonia on Jupiter from a preliminary inversion of Juno Microwave Radiometer data”. *Geophysical Research Letters* 44.11, pp. 5317–5325.

Steffes, Paul G., Thomas R. Hanley, Bryan M. Karpowicz, Kiruthika Devaraj, Sahand Noorizadeh, Danny Duong, Garrett Chinsomboon, Amadeo Bellotti, Michael A. Janssen, and Scott J. Bolton. 2017. “High-Precision Laboratory Measurements Supporting Retrieval of Water Vapor, Gaseous Ammonia, and Aqueous Ammonia Clouds with the Juno Microwave Radiometer (MWR)”. *Space Science Reviews* 213.1–4, pp. 187–204.

8.3.2 Conference Presentations (in chronological order)

Bellotti, Amadeo and P.G. Steffes. 2014. “Laboratory Measurements of the Millimeter-Wavelength Sulfur Dioxide Absorption Spectrum under Simulated Venus Conditions”. *Bulletin of the American Astronomical Society*. Vol. 46. Presented at the 46th Annual Meeting of the Division for Planetary Sciences of the American Astronomical Society. Tucson, AZ, p. 113.

Bellotti, Amadeo and Paul G. Steffes. 2015. “Laboratory Measurements in Support of Millimeter-wavelength Observations of the Venus Atmosphere”. *Abstracts of the 13th VEXAG Meeting and International Science Workshop*. Presented at the 13th VEXAG Meeting and International Workshop. Washington, DC, p. 37.

Bellotti, Amadeo and P.G. Steffes. 2015. “Laboratory Measurements of the 5-20 cm Wavelength Opacity of Ammonia and Water Vapor under High-Temperature Conditions characteristic of the Deep Jovian Atmosphere”. *Bulletin of the American Astronomical Society*. Vol. 47. Presented at the 47th Annual Meeting of the Division for Planetary Sciences of the American Astronomical Society. Washington, DC, p. 118.

Bellotti, A and PG Steffes. 2016. “Quicklook Constituent Abundance and Stretch Parameter Retrieval for the Juno Microwave Radiometer using Neural Networks”. *Program of the American Geophysical Union Fall Meeting 2016*. Presented at the 2016 Fall Meeting of the American Geophysical Union (AGU). San Francisco, CA, P33C–2171.

Bellotti, Amadeo and P.G. Steffes. 2016. “Modeling the Potential Effects of Virga on the Microwave Emission from the Jovian Atmosphere in Support of the Juno Microwave Radiometer (MWR)”. *Bulletin of the American Astronomical Society*. Vol. 48. Presented at the 48th Annual Meeting of the Division for Planetary Sciences of the American Astronomical Society. Pasadena, CA.

Janssen, MA, ST Brown, S Gulkis, S Levin, SJ Bolton, JEP Connerney, MD Allison, SK Atreya, AP Ingersoll, JI Lunine, et al. 2016. “First Results at Jupiter from the Microwave Radiometer Investigation”. *Program of the American Geophysical Union Fall Meeting 2016*. Presented at the 2016 Fall Meeting of the American Geophysical Union (AGU). San Francisco, CA, U22A–07.

Oyafuso, FA, S Gulkis, V Adumitroaie, MA Janssen, SK Atreya, ST Brown, A Bellotti, C Li, AP Ingersoll, D Santos-Costa, et al. 2016. “Simulation of Antenna Brightness Temperatures for the Juno Microwave Radiometer”. Presented at the 2016 Fall Meeting of the American Geophysical Union (AGU). San Francisco, CA, P33C–2170.

Bellotti, A. and P. G. Steffes. 2017. “Utilizing Neural Networks in the Retrieval of Jovian Constituent Profiles Using Data from the Juno MWR”. *Bulletin of the American Astronomical Society*. Vol. 49. Presented at the 49th Annual Meeting of the Division for Planetary Sciences of the American Astronomical Society. Provo, UT, p. 118.03.

Bellotti, Amadeo, Paul G. Steffes, Michael A. Janssen, Steven M. Levin, and Samuel Gulkis. 2017. “Use of the Juno Microwave Radiometer (MWR) in the Study of Jovian Atmospheric Composition, Structure, and Dynamics”. *International Union of Radio Science Programs and Abstracts: 2017 National Radio Science Meeting*. Presented at the 2017 URSI National Radio Science Meeting. Boulder, CO, J7–2.

Bellotti, Amadeo, Paul Steffes, Michael Janssen, Steven Levin, and Fabiano Oyafuso. 2017. “Methods of Retrieving the Ammonia Abundance Profile from Data Taken with the Juno Microwave Radiometer”. *Geophysical Research Abstracts*. Vol. 19. Presented

at the 2017 EGU (European Geosciences Union) General Assembly. Vienna, Austria, EGU2017-5531-1.

Bellotti, Amadeo, Paul Steffes, Mike Janssen, Steve Levin, and Fabiano A Oyafuso. 2017. "Studying and Understanding the Jovian Aurora Based on Measurements from the Juno MWR Taken during Perijove 5". *Program of the American Geophysical Union Fall Meeting 2017*. Presented at the 2017 Fall Meeting of the American Geophysical Union (AGU). New Orleans, LA, P31C–2835.

Janssen, Michael A., Scott J. Bolton, Steve M. Levin, Virgil Adumitroaie, Michael D. Allison, John K. Arballo, Sushil K. Atreya, Amadeo Bellotti, Shannon T. Brown, Samuel Gulkis, Andrew P. Ingersoll, Laura A. Jewell, Cheng Li, Liming Li, Jonathan Lunine, Sidharth Misra, Glenn S. Orton, Tobias C. Owen, Fabiano A. Oyafuso, Maarten Roos, Daniel Santos-Costa, Edwin Sarkissian, Paul G. Steffes, and Ross Williamson. 2017. "Early Observations of Jupiter with Juno's Microwave Radiometer (MWR) (invited)". *International Union of Radio Science Programs and Abstracts: 2017 National Radio Science Meeting*. Presented (by Steffes) at the 2017 URSI National Radio Science Meeting. Boulder, CO, J7–1.

Janssen, Michael A, Scott J Bolton, Steven Levin, Virgil Adumitroaie, Michael D Allison, John K. Arballo, Sushil K Atreya, Amadeo Bellotti, Shannon Thomas Brown, Sam Gulkis, Andrew P. Ingersoll, Cheng Li, Liming Li, Jonathan I Lunine, Sidharth Misra, Glenn S Orton, Fabiano A Oyafuso, Daniel Santos-Costa, Edwin Sarkissian, Paul G Steffes, and Zhimeng Zhang. 2017. "Results on Jupiter's Atmosphere from the Juno Microwave Radiometer". *Program of the American Geophysical Union Fall Meeting 2017*. Presented at the 2017 Fall Meeting of the American Geophysical Union (AGU). New Orleans, LA, U21A–05.

Janssen, Michael A, Scott J Bolton, Steve M Levin, Virgil Adumitroaie, Michael D Allison, John K Arballo, Sushil K Atreya, Amadeo Bellotti, Shannon T Brown, Samuel Gulkis,

et al. 2017. “Latest Results on Jupiter’s Atmosphere and Radiation Belts from the Juno Microwave Radiometer”. *European Planetary Science Congress*. Vol. 11.

Janssen, Michael, Scott Bolton, Steven Levin, Michael Allison, Sushil Atreya, Amadeo Bellotti, Shannon Brown, Andrew Ingersoll, Cheng Li, Virgil Adumitroaie, John Arballo, Laura Jewell, Liming Li, Samuel Gulkis, Siddarth Misra, Glenn Orton, Tobias Owen, Fabiano Oyafuso, Daniel Santos-Costa, Edwin Sarkissian, Paul Steffes, Ross Williamson, and Jonathan Lunine. 2017. “Preliminary Results on Jupiter’s Atmosphere Using the Juno Microwave Radiometer”. *Program of the 14th Annual Meeting of the Asia-Oceania Geosciences Society*. Vol. PS08-D5-AM1-331-003, PS08-101. Singapore, p. 358.

Santos-Costa, Daniel, Amadeo Bellotti, Mike Janssen, Samuel Gulkis, Andrew P Ingersoll, Steve Levin, Paul G Steffes, Shannon Thomas Brown, Virgil Adumitroaie, Fabiano A Oyafuso, et al. 2017. “Systematic capture of MeV electron beams by MWR”. *Program of the American Geophysical Union Fall Meeting 2017*. Presented at the 2017 Fall Meeting of the American Geophysical Union (AGU). New Orleans, LA.

Appendices

APPENDIX A
JAMRT TECHNICAL DOCUMENT

A.1 JAMRT Input File

This section provides a description of the JAMRT input file and the key inputs used in this work. At the bottom of the file is a commented block that describes the grammar governing the syntax of the file. The syntax of this file is in the form `key = value`, where `value` is one of the following type (based on keyword):

- a scaler
- an array of scalers
- a boolean value of true or false
- a list of strings
- a list of values

While the order of the keys is not important, some keys may be repeated, in which case the final value of the key is a list of values ordered in the same way they appear. Unknown keys are simply ignored. A list of the keys used in this work is:

- `planet`: Two possible values "Jupiter" and "Saturn". This overrides the value of gravity with a more complicated shape model.
- `g`: The local value of gravity. Overridden by the `planet` key.
- `lat`: Latitude in degrees for the shape model.
- `X_*`: Specifies deep atmosphere abundances and consists of two values. The first is the solar abundance relative to H_2, and the second is the default enrichment for the

planet. The allowed gases consist of CH_4, H_2O, NH_3, H_2S, Ar, PH_3, and Ne. The enrichment factor for NH_3 and H_2O are overridden by the state vector values passed through command line arguments.

- `dsl_*`: Provides a mechanism for artificially specifying a depletion region for NH_3 or H_2O. The first value is the pressure (in bars) where the depletion begins. The depletion is assumed to have the functional form $X = e^{-\alpha z}$, where the extinction coefficient α is the second value. The third value equals the ratio of the mixing ratio at the top of the depletion layer relative to the mixing ratio at the bottom.

- `Tref, Pref`: Provide a reference pressure and temperature, in bars and K, respectively.

- `use_ideal_gas`: Must be true or false. If true, JAMRT must be compiled with compressibility enabled (see JAMRT documentation).

- `dz`: Mesh spacing in meters.

- `Pmax`: Defines the pressure at the bottom of the atmosphere, in bars.

- `freqs`: The set of frequencies (in GHz) over which the code will compute absorption

- `absorption`: A list of absorption models JAMRT will use. Valid gases include `H2_CIA, NH3, PH3, H2S, H2O`. The default H_2O model is the modified Karpowicz model (Bellotti et al., 2016), but may be specified instead to `H2O_Goodman, H2O_Waters, H2O_deBoer`. The cloud absorbers (`H2O_NH3_soln, H2O_ice, NH3_ice, NH4SH_ice`) may be optionally specified with the following format: `<cloud type> = factor` where `factor` is a multiplicative scaling factor applied to the computed cloud opacity. Finally `free-free` includes a rough order-of-magnitude estimate of absorption due to ionization of hydrogen. Any absorption model not specified is not computed and can reduce the computational cost.

- `do_refraction`: Must be true or false. This parameter enables or disables the ray tracing described previously.

- `angles`: Specifies the list of emission angles over which the radiative transfer will be performed.

- `h5_output`: List of quantities to save in the output HDF5 file. Valid values are `obs` (brightness temperatures), `atm` (atmospheric profiles of pressure, temperature, mixing ratios, and cloud densities), `absco` (opacities), and `weight` (weighting functions).

A.2 Implementation of Pencilbeam Forward Model

This section describes the implementation of the pencilbeam forward model. Because this section should be treated as a technical document, it cannot be guaranteed that this section is accurate for versions of JAMRT after August 10, 2016. The goal of this section is not to fully describe the JAMRT code, but to give the reader the ability to examine, understand, and modify the software. The mathematical equations used in JAMRT and an in-depth description of them are found in Karpowicz and Steffes (2013).

The pencilbeam forward model starts in the `main` function found in `driver_juno.C`. It begins by reading the enrichment of ammonia and water vapor, known as the state vector, passed through command line arguments. Following this, the input file is parsed and saved in a class called `AtmParam` (`AtmParam.C`).

The software then evaluates each passed state vector and creates an appropriate atmosphere. This is done in `PencilBeam_FM.C` in the `eval` function. The atmosphere created is contained in a class aptly named `Atmosphere` and computed in the class's `compute` function. The code for this is contained in two files: `Atmosphere_cloud.C`, and `Atmosphere_rad.C`. The `Atmosphere` class contains arrays for all the necessary atmospheric variables (altitude, pressure, temperature, mixing ratio, and cloud density),

where each element in the array is the atmospheric variable's value at that atmospheric altitude.

The `compute` function guesses a possible temperature at the specified maximum pressure. It then iterates this until the specified reference temperature and pressure are met or until the iteration count is too high. There are three helper classes used in the computation of the atmosphere. The first of these is the `Constituents` class, which contains the mixing ratio of all constituents found in the atmosphere at a given atmospheric level and their calculated thermal properties. The second, the `Clouds` class, calculates the vapor pressure profiles of the condensable species. The final class is the `AqueousAmmonia` class, which helps calculate the concentration of ammonia found in the liquid water cloud.

The code, which creates an atmosphere given a bottom pressure and temperature, is found in the `construct_from_Tbot` function in `Atmosphere_cloud.C`. The function sets the mixing ratio at the bottom of the atmosphere to the deep abundance inputs, and iterates up through each layer of the atmosphere while calculating the atmospheric parameters. The first of these parameters is the lapse rate (dT/dz), either wet or dry adiabat. Next, the temperature in the layer is calculated by, $T_i = T_{i-1} + \frac{dT}{dz}dz$. After the temperature is known, the pressure of the layer is calculated. The mixing ratio is then set to that of the previous level. The function than looks for condensation in the atmosphere. The condensates this function considers are: aqueous ammonia, NH_3 ice, H_2O ice, H_2S, and NH_4SH. If condensation is occurring, the function depletes the mixing ratio for the calculated vapor pressure profiles and modifies the temperature and pressure accordingly. Once the top of the atmosphere is reached, the code returns the generated atmosphere to the `compute` function that compares the temperature and pressure at the top of the atmosphere to the reference values. If the computed temperature and pressure match the reference temperature and pressure, the compute function returns the generated atmosphere. If not, the `compute` function modifies the bottom temperature and reruns the `construct_from_Tbot` function.

After the atmosphere is created the code calculates the absorption profile. This is done in the `Atmosphere` class in the `compute_all_absorption_coefficients` function found in `Atmosphere_rad.C`. This function iterates through all specified frequencies and layers, and calculates the total absorption coefficient at each layer. The functions for computing the absorption coefficients are found in `Absorbers.C`. Following this, the ray tracing is done in the `slant_path_of_level` function and the brightness temperature is finally calculated in the `brightnessTemperature` function. Again, both of these are found in `Atmosphere_rad.c`.

REFERENCES

Ackerman, Andrew S and Mark S Marley. 2001. "Precipitating condensation clouds in substellar atmospheres". *The Astrophysical Journal* 556.2, p. 872.

Acton, Charles H. 1996. "Ancillary data services of NASA's navigation and ancillary information facility". *Planetary and Space Science* 44.1, pp. 65–70.

Acton, Charles, Nathaniel Bachman, Boris Semenov, and Edward Wright. 2017. "A look towards the future in the handling of space science mission geometry". *Planetary and Space Science*.

Ajello, Joseph, Donald Shemansky, Wayne Pryor, Kent Tobiska, Charles Hord, Stuart Stephens, Ian Stewart, John Clarke, Karen Simmons, William McClintock, et al. 1998. "Galileo orbiter ultraviolet observations of Jupiter aurora". *Journal of Geophysical Research: Planets* 103.E9, pp. 20125–20148.

Atreya, SK, PR Mahaffy, HB Niemann, MH Wong, and TC Owen. 2003. "Composition and origin of the atmosphere of Jupiter—an update, and implications for the extrasolar giant planets". *Planetary and Space Science* 51.2, pp. 105–112.

Atreya, SK and PN Romani. 1985. "Photochemistry and clouds of Jupiter, Saturn and Uranus". *Recent advances in planetary meteorology* 17, p. 68.

Atreya, SK, MH Wong, TC Owen, PR Mahaffy, HB Niemann, I dePater, P Drossart, and Th Encrenaz. 1999. "A comparison of the atmospheres of Jupiter and Saturn: deep atmospheric composition, cloud structure, vertical mixing, and origin". *Planetary and space science* 47.10, pp. 1243–1262.

Atreya, Sushil K. 2013. *Atmospheres and Ionospheres of the Outer Planets and their Satellites*. Vol. 15. Springer Science & Business Media.

Atreya, Sushil K, A. Crida, T. Guillot, J.I. Lunine, N. Madhusudhan, and M. Mousis. 2017. *Saturn in the 21st Century*. Cambridge Univ. Press.

Bandler, John W, Qingsha S Cheng, Sameh A Dakroury, Ahmed S Mohamed, Mohamed H Bakr, Kaj Madsen, and Jacob Sondergaard. 2004. "Space mapping: the state of the art". *IEEE Transactions on Microwave theory and techniques* 52.1, pp. 337–361.

Barth, Erika L and Owen B Toon. 2003. "Microphysical modeling of ethane ice clouds in Titan's atmosphere". *Icarus* 162.1, pp. 94–113.

Bellotti, Amadeo, Paul G. Steffes, and Garrett Chinsomboom. 2016. "Laboratory Measurements of the 5-20 cm Wavelength Opacity of Ammonia, Water Vapor, and Methane Under Simulated Conditions for the Deep Jovian Atmosphere". *Icarus* 280, pp. 255–267.

Ben-Reuven, A. 1966. "Impact broadening of microwave spectra". *Phys. Rev.* 145, pp. 7–22.

Berge, GL and S Gulkis. 1976. *Earth-based observations of Jupiter: millimeter to meter wavelengths*. Tech. rep. Owens Valley Radio Observatory, Pasadena, Calif.(USA).

Best, AC. 1950. "The size distribution of raindrops". *Quarterly Journal of the Royal Meteorological Society* 76.327, pp. 16–36.

Bjoraker, GL, MH Wong, I de Pater, and M Ádámkovics. 2015. "Jupiter's deep cloud structure revealed using Keck observations of spectrally resolved line shapes". *The Astrophysical Journal* 810.2, p. 122.

Blackwell, William and Frederick Chen. 2009. *Neural networks in atmospheric remote sensing*. Boston London: Artech House. ISBN: 978-1-59693-372-9.

Blanc, M., R. Kallenbach, and N. V. Erkaev. 2005. "Solar System Magnetospheres". *Space Science Reviews* 116.1, pp. 227–298.

Bolton, SJ, Alberto Adriani, V Adumitroaie, M Allison, J Anderson, S Atreya, J Bloxham, S Brown, JEP Connerney, E DeJong, et al. 2017. "Jupiter's interior and deep atmosphere: The initial pole-to-pole passes with the Juno spacecraft". *Science* 356.6340, pp. 821–825.

Brodley, Carla E and Mark A Friedl. 1999. "Identifying mislabeled training data". *Journal of artificial intelligence research* 11, pp. 131–167.

Byrd, Richard H, Peihuang Lu, Jorge Nocedal, and Ciyou Zhu. 1995. "A limited memory algorithm for bound constrained optimization". *SIAM Journal on Scientific Computing* 16.5, pp. 1190–1208.

Chamberlain, J. W. and D. M. Hunten. 1987. *Theory of planetary atmospheres. An introduction to their physics andchemistry.*

Chinsomboon, Garrett. 2012. "New model for the 5-20 cm wavelength opacity of ammonia pressure-broadened by methane under jovian conditions based on laboratory measurements". PhD thesis. Georgia Institute of Technology.

Chu, TS and DC Hogg. 1968. "Effects of precipitation on propagation at 0.63, 3.5, and 10.6 microns". *Bell System Technical Journal* 47.5, pp. 723–759.

Clarke, John T, John Trauger, and J Hunter Waite. 1989. "Doppler shifted H Ly α emission from Jupiter's aurora". *Geophysical research letters* 16.6, pp. 587–590.

Clarke, JT, J Ajello, G Ballester, L Ben Jaffel, J Connerney, J-C Gérard, GR Gladstone, Denis Grodent, W Pryor, J Trauger, et al. 2002. "Ultraviolet emissions from the magnetic footprints of Io, Ganymede and Europa on Jupiter". *Nature* 415.6875, pp. 997–1000.

de Pater, Imke, David DeBoer, Mark Marley, Richard Freedman, and Richard Young. 2005. "Retrieval of water in Jupiter's deep atmosphere using microwave spectra of its brightness temperature". *Icarus* 173.2, pp. 425–438.

de Pater, Imke, David Dunn, Paul Romani, and Kevin Zahnle. 2001. "Reconciling Galileo probe data and ground-based radio observations of ammonia on Jupiter". *Icarus* 149.1, pp. 66–78.

de Pater, Imke and Jack J Lissauer. 2001. *Planetary sciences.* Cambridge University Press.

de Pater, Imke and Steven T Massie. 1985. "Models of the millimeter-centimeter spectra of the giant planets". *Icarus* 62.1, pp. 143–171.

de Pater, Imke and David L Mitchell. 1993. "Radio observations of the planets: The importance of laboratory measurements". *Journal of Geophysical Research: Planets* 98.E3, pp. 5471–5490.

de Pater, Imke, RJ Sault, Bryan Butler, David DeBoer, and Michael H Wong. 2016. "Peering through Jupiter's clouds with radio spectral imaging". *Science* 352.6290, pp. 1198–1201.

de Pater, Imke, BJ Butler, DA Green, R Strom, R Millan, MJ Klein, MK Bird, O Funke, J Neidhöfer, R Maddalena, et al. 2003. "Jupiter's radio spectrum from 74 MHz up to 8 GHz". *Icarus* 163.2, pp. 434–448.

DeBoer, David R. and Paul G. Steffes. 1994. "Laboratory Measurements of the Microwave Properties of H2S under Simulated Jovian Conditions with an Application to Neptune". *Icarus* 109.2, pp. 352–366.

Debye, P. J. W. 1929. *Polar Molecules*. New York: The Chemical Catalog Company Inc.

Devaraj, Kiruthika, Paul G. Steffes, and Danny Duong. 2014. "The centimeter-wavelength opacity of ammonia under deep jovian conditions". *Icarus* 241, pp. 165–179.

Devaraj, Kiruthika, Paul G. Steffes, and Bryan M. Karpowicz. 2011. "Reconciling the centimeter- and millimeter-wavelength ammonia absorption spectra under jovian conditions: Extensive millimeter-wavelength measurements and a consistent model". *Icarus* 212.1, pp. 224–235.

Duong, Danny, Paul G Steffes, and Sahand Noorizadeh. 2014. "The microwave properties of the jovian clouds: A new model for the complex dielectric constant of aqueous ammonia". *Icarus* 229, pp. 121–130.

Elsner, R.F., B.D. Ramsey, J.H. Waite, P. Rehak, R.E. Johnson, J.F. Cooper, and D.A. Swartz. 2005. "X-ray probes of magnetospheric interactions with Jupiter's auroral zones, the Galilean satellites, and the Io plasma torus". *Icarus* 178.2. Jovian Magnetospheric Environment Science, pp. 417–428.

Fegley, Bruce and Katharina Lodders. 1994. "Chemical models of the deep atmospheres of Jupiter and Saturn". *Icarus* 110.1, pp. 117–154.

Fletcher, Leigh N, TK Greathouse, GS Orton, JA Sinclair, RS Giles, PGJ Irwin, and T Encrenaz. 2016. "Mid-infrared mapping of Jupiter's temperatures, aerosol opacity and chemical distributions with IRTF/TEXES". *Icarus* 278, pp. 128–161.

Graves, SDB, CP McKay, CA Griffith, F Ferri, and M Fulchignoni. 2008. "Rain and hail can reach the surface of Titan". *Planetary and Space Science* 56.3, pp. 346–357.

Gross, E. P. 1955. "Shape of Collision-Broadened Spectral Lines". *Phys. Rev.* 97 (2), pp. 395–403.

Guillot, T., G. Chabrier, P. Morel, and D. Gautier. 1994a. "Nonadiabatic Models of Jupiter and Saturn". *Icarus* 112.2, pp. 354–367.

Guillot, T., D. Gautier, G. Chabrier, and B. Mosser. 1994b. "Are the Giant Planets Fully Convective?" *Icarus* 112.2, pp. 337–353.

Guillot, Tristan, David J Stevenson, William B Hubbard, and Didier Saumon. 2004. "The interior of Jupiter". *Jupiter: The Planet, Satellites and Magnetosphere*, pp. 35–57.

Hanley, Thomas. 2008. "The Microwave Opacity Effects of Ammonia and Water Vapor Application to Remote Sensing of the Atmosphere of Jupiter". PhD thesis. Georgia Institute of Technology.

Hanley, Thomas R. and Paul G. Steffes. 2007. "A high-sensitivity laboratory system for measuring the microwave properties of gases under simulated conditions for planetary atmospheres". *Radio Science* 42.6.

Hanley, Thomas R., Paul G. Steffes, and Bryan M. Karpowicz. 2009. "A new model of the hydrogen and helium-broadened microwave opacity of ammonia based on extensive laboratory measurements". *Icarus* 202.1, pp. 316–335.

Hansen, C Frederick. 1979. "Viscosity and thermal conductivity of model Jupiter atmospheres".

Haykin, Simon S, Simon S Haykin, Simon S Haykin, and Simon S Haykin. 2009. *Neural networks and learning machines*. Vol. 3. Pearson Upper Saddle River, NJ, USA:

Hebb, Donald O. 1949. "The Organization of Behavior: A Neuropsychological Theory".

Helliwell, Robert A. 2014. *Whistlers and Related Ionospheric Phenomena (Dover Books on Electrical Engineering)*. Dover Publications.

Hoffman, James Patrick. 2001. "Microwave Opacity of Phosphine: Application to Remote Sensing of the Atmospheres of the Outer Planets". PhD thesis. Georgia Institute of Technology.

Hubbard, William B. 1968. "Thermal structure of Jupiter". *The Astrophysical Journal* 152, pp. 745–754.

James, Gareth M. 2003. "Variance and Bias for General Loss Functions". *Machine Learning* 51.2, pp. 115–135.

Janssen, MA, MD Hofstadter, S Gulkis, AP Ingersoll, M Allison, SJ Bolton, SM Levin, and LW Kamp. 2005. "Microwave remote sensing of Jupiter's atmosphere from an orbiting spacecraft". *Icarus* 173.2, pp. 447–453.

Janssen, MA, AP Ingersoll, MD Allison, S Gulkis, AL Laraia, KH Baines, SG Edgington, YZ Anderson, K Kelleher, and FA Oyafuso. 2013. "Saturn's thermal emission at 2.2-cm wavelength as imaged by the Cassini RADAR radiometer". *Icarus* 226.1, pp. 522–535.

Janssen, MA, JE Oswald, ST Brown, S Gulkis, SM Levin, SJ Bolton, MD Allison, SK Atreya, D Gautier, AP Ingersoll, et al. 2017a. "MWR: Microwave radiometer for the Juno mission to Jupiter". *Space Science Reviews*, pp. 1–47.

Janssen, Michael A. 1993. *Atmospheric Remote Sensing By Microwave Radiometry.* Vol. 1.

Janssen, Michael A, Scott J Bolton, Steve M Levin, Virgil Adumitroaie, Michael D Allison, John K Arballo, Sushil K Atreya, Amadeo Bellotti, Shannon T Brown, Samuel Gulkis, et al. 2017b. "Latest Results on Jupiter's Atmosphere and Radiation Belts from the Juno Microwave Radiometer". *European Planetary Science Congress*. Vol. 11.

Jenkins, Jon M., Marc A. Kolodner, Bryan J. Butler, Shady H. Suleiman, and Paul G. Steffes. 2002. "Microwave Remote Sensing of the Temperature and Distribution of Sulfur Compounds in the Lower Atmosphere of Venus". *Icarus* 158.2, pp. 312–328.

Joiner, Joanna and Paul G Steffes. 1991. "Modeling of Jupiter's millimeter wave emission utilizing laboratory measurements of ammonia (NH3) opacity". *Journal of Geophysical Research: Planets* 96.E2, pp. 17463–17470.

Karpowicz, Bryan M. and Paul G. Steffes. 2011a. “In search of water vapor on Jupiter: Laboratory measurements of the microwave properties of water vapor under simulated jovian conditions”. *Icarus* 212.1, pp. 210–223.

— 2011b. “Corrigendum to “In search of water vapor on Jupiter: Laboratory measurements of the microwave properties of water vapor under simulated jovian conditions” [Icarus 212 (2011) 210–223]”. *Icarus* 214.2, p. 783.

Karpowicz, Bryan M and Paul G Steffes. 2013. “Investigating the H_2–He–H_2O–CH_4 equation of state in the deep troposphere of Jupiter”. *Icarus* 223.1, pp. 277–297.

Karpowicz, Bryan Mills. 2010. “In search of water vapor on Jupiter: laboratory measurements of the microwave properties of water vapor and simulations of Jupiter’s microwave emission in support of the Juno mission”. PhD thesis. Karpowicz.

Kippenhahn, Rudolf, Alfred Weigert, and Achim Weiss. 2012. *Stellar Structure and Evolution (Astronomy and Astrophysics Library)*. Springer.

Kochanov, R.V., I.E. Gordon, L.S. Rothman, P. Wcisło, C. Hill, and J.S. Wilzewski. 2016. “{HITRAN} Application Programming Interface (HAPI): A comprehensive approach to working with spectroscopic data”. *Journal of Quantitative Spectroscopy and Radiative Transfer* 177. {XVIIIth} Symposium on High Resolution Molecular Spectroscopy (HighRus-2015), Tomsk, Russia, pp. 15–30.

Laws, J Otis and Donald A Parsons. 1943. “The relation of raindrop-size to intensity”. *Eos, Transactions American Geophysical Union* 24.2, pp. 452–460.

Lewis, John S. 1969. “The clouds of Jupiter and the NH3—H2O and NH3—H2S systems”. *Icarus* 10.3, pp. 365–378.

Li, Cheng, Andrew Ingersoll, Michael Janssen, Steven Levin, Scott Bolton, Virgil Adumitroaie, Michael Allison, John Arballo, Amadeo Bellotti, Shannon Brown, et al. 2017. “The distribution of ammonia on Jupiter from a preliminary inversion of Juno Microwave Radiometer data”. *Geophysical Research Letters* 44.11, pp. 5317–5325.

Lindal, Gunnar F, GE Wood, GS Levy, JD Anderson, DN Sweetnam, HB Hotz, BJ Buckles, DP Holmes, PE Doms, VR Eshleman, et al. 1981. “The atmosphere of Jupiter: An analysis of the Voyager radio occultation measurements”. *Journal of Geophysical Research: Space Physics* 86.A10, pp. 8721–8727.

Liou, K.N. 2002. *An Introduction to Atmospheric Radiation*. San Diego, California: Academic Press.

Lorentz, H.A. 1906. “The width of spectral lines.” *Proc. Neth. Acad. Arts Sci.* 18, pp. 134–150.

Lunine, Jonathan I and Donald M Hunten. 1987. “Moist convection and the abundance of water in the troposphere of Jupiter”. *Icarus* 69.3, pp. 566–570.

Marshall, John S and W Mc K Palmer. 1948. “The distribution of raindrops with size”. *Journal of meteorology* 5.4, pp. 165–166.

Matousek, S. 2005. *The Juno New Frontiers Mission. Tech. Rep. IAC-05-A3.2.A.04*. Tech. rep. California Institute of Technology.

Mattaei, G. L. and E. Jones. 1980. *Microwave filters, impedance matching networks and coupling structures*. New York: McGraw-Hill.

Merwe, Rudolph van der, Todd K Leen, Zhengdong Lu, Sergey Frolov, and Antonio M Baptista. 2007. “Fast neural network surrogates for very high dimensional physics-based models in computational oceanography”. *Neural Networks* 20.4, pp. 462–478.

Nielsen, Michael A. 2015. *Neural networks and deep learning*. Determination Press USA.

Orton, Glenn S, Candice Hansen, Michael Caplinger, Michael Ravine, Sushil Atreya, Andrew P Ingersoll, Elsa Jensen, Thomas Momary, Leslie Lipkaman, Daniel Krysak, et al. 2017. “The first close-up images of Jupiter’s polar regions: Results from the Juno mission JunoCam instrument”. *Geophysical Research Letters*.

Oyafuso, Fabiano A, Li Cheng, Andrew P Ingersoll, Steve Levin, Mike Janssen, and Virgil Adumitroaie. 2017. “Positional and Angular Dependence of Jupiter’s Thermal Emission from the Juno Microwave Radiometer”. Presented at the 2017 Fall Meeting of the American Geophysical Union (AGU). New Orleans, LA, P31C–2817.

Pallier, Laurent and Renée Prangé. 2001. “More about the structure of the high latitude Jovian aurorae”. *Planetary and Space Science* 49.10. Magnetosphere of the Outer Planets Part II, pp. 1159–1173.

Pickett, H.M., R.L. Poynter, E.A. Cohen, M.L. Delitsky, J.C. Pearson, and H.S.P. Muller. 1998. “Submillimeter, Millimeter, and Microwave Spectral Line Catalog”. *Journal of Quantitative Spectroscopy and Radiative Transfer* 60.5, pp. 883–890.

Pingree, P, M Janssen, J Oswald, S Brown, J Chen, K Hurst, A Kitiyakara, F Maiwald, and S Smith. 2008. “Microwave radiometers from 0.6 to 22 GHz for Juno, a polar orbiter around Jupiter”. *Aerospace Conference, 2008 IEEE*. IEEE, pp. 1–15.

Poynter, R. L. and R. K. Kakar. 1975. “The microwave frequencies, line parameters, and spectral constants for NH3-14”. *ApJS* 29, p. 87.

Ragent, Boris, David S Colburn, Kathy A Rages, Tony CD Knight, Philip Avrin, Glenn S Orton, Padmavati A Yanamandra-Fisher, and Gerald W Grams. 1998. “The clouds of

Jupiter: Results of the Galileo Jupiter mission probe nephelometer experiment". *Journal of Geophysical Research: Planets* 103.E10, pp. 22891–22909.

Rego, D, R Prangé, and L Ben Jaffel. 1999. "Auroral Lyman α and H2 bands from the giant planets: 3. Lyman α spectral profile including charge exchange and radiative transfer effects and H2 color ratios". *Journal of Geophysical Research: Planets* 104.E3, pp. 5939–5954.

Rodgers, Clive D. 2000. *Inverse Methods for Atmospheric Sounding: Theory and Practice (Series on Atmospheric Oceanic and Planetary Physics)*. World Scientific Publishing. ISBN: 981022740X.

Rogers, John H. 1995. *The Giant Planet Jupiter (Practical Astronomy Handbooks)*. Cambridge University Press. ISBN: 0521410088.

Rosenkranz, Philip W. 1998. "Water vapor microwave continuum absorption: A comparison of measurements and models". *Radio Science* 33.4, pp. 919–928.

Rossow, William B. 1978. "Cloud microphysics: analysis of the clouds of Earth, Venus, Mars and Jupiter". *Icarus* 36.1, pp. 1–50.

Rothman, L.S., I.E. Gordon, Y. Babikov, A. Barbe, D. Chris Benner, P.F. Bernath, M. Birk, L. Bizzocchi, V. Boudon, L.R. Brown, A. Campargue, K. Chance, E.A. Cohen, L.H. Coudert, V.M. Devi, B.J. Drouin, A. Fayt, J.-M. Flaud, R.R. Gamache, J.J. Harrison, J.-M. Hartmann, C. Hill, J.T. Hodges, D. Jacquemart, A. Jolly, J. Lamouroux, R.J. Le Roy, G. Li, D.A. Long, O.M. Lyulin, C.J. Mackie, S.T. Massie, S. Mikhailenko, H.S.P. Müller, O.V. Naumenko, A.V. Nikitin, J. Orphal, V. Perevalov, A. Perrin, E.R. Polovtseva, C. Richard, M.A.H. Smith, E. Starikova, K. Sung, S. Tashkun, J. Tennyson, G.C. Toon, Vl.G. Tyuterev, and G. Wagner. 2013. "The {HITRAN2012} molecular spectroscopic database". *Journal of Quantitative Spectroscopy and Radiative Transfer* 130. {HITRAN2012} special issue, pp. 4–50.

Rumelhart, David E., James L. McClelland, and PDP Research Group. 1986. *Parallel Distributed Processing: Explorations in the Microstructure of Cognition: Foundations (Volume 1)*. A Bradford Book. ISBN: 0262181207.

Russell, Stuart and Peter Norvig. 2002. *Artificial Intelligence: A Modern Approach (2nd Edition)*. Prentice Hall. ISBN: 0137903952.

Saha, Meghnad. 1920. "LIII. Ionization in the solar chromosphere". *Philosophical Magazine* 40.238, pp. 472–488.

Samuel, Arthur L. 2000. "Some studies in machine learning using the game of checkers". *IBM Journal of research and development* 44.1.2, pp. 206–226.

Seidelmann, P. Kenneth, B. A. Archinal, M. F. A'hearn, A. Conrad, G. J. Consolmagno, D. Hestroffer, J. L. Hilton, G. A. Krasinsky, G. Neumann, J. Oberst, P. Stooke, E. F. Tedesco, D. J. Tholen, P. C. Thomas, and I. P. Williams. 2007. "Report of the IAU/IAG Working Group on cartographic coordinates and rotational elements: 2006". *Celestial Mechanics and Dynamical Astronomy* 98.3, pp. 155–180.

Seiff, Alvin, Donn B Kirk, Tony CD Knight, Richard E Young, John D Mihalov, Leslie A Young, Frank S Milos, Gerald Schubert, Robert C Blanchard, and David Atkinson. 1998. "Thermal structure of Jupiter's atmosphere near the edge of a 5-micron hot spot in the north equatorial belt". *Journal of Geophysical Research* 103, p. 22.

Student. 1908. "The Probable Error of a mean". *Biometrika* 6.1, pp. 1–25. eprint: `http://biomet.oxfordjournals.org/content/6/1/1.full.pdf+html`.

Toon, Owen B, Christopher P McKay, Régis Courtin, and Thomas P Ackerman. 1988. "Methane rain on Titan". *Icarus* 75.2, pp. 255–284.

Townes, Charles H. and Arthur L. Schawlow. 1975. *Microwave spectroscopy*. Dover Publications.

Vapnik, Vladimir. 2013. *The Nature of Statistical Learning Theory (Information Science and Statistics)*. Springer. ISBN: 9781475732641.

Vleck, J. H.Van and V. F. Weisskopf. 1945. "On the shape of collision-broadened lines." *Rev. Mod. Phys* 17, pp. 227–236.

Waite, John H, JT Clarke, TE Cravens, and CM Hammond. 1988. "The Jovian aurora: electron or ion precipitation?" *Journal of Geophysical Research: Space Physics* 93.A7, pp. 7244–7250.

Waters, J.W. 1976. "2.3. Absorption and Emission by Atmospheric Gases". *Astrophysics Radio Telescopes*. Ed. by M.L. Meeks. Vol. 12, Part B. Methods in Experimental Physics. Academic Press, pp. 142–176.

Weidenschilling, SJ and JS Lewis. 1973. "Atmospheric and cloud structures of the Jovian planets". *Icarus* 20.4, pp. 465–476.

Wexler, Raymond. 1948. "Rain intensities by radar". *Journal of Meteorology* 5.4, pp. 171–173.

Wong, Michael H, Sushil K Atreya, William R Kuhn, Paul N Romani, and Kristen M Mihalka. 2015. "Fresh clouds: A parameterized updraft method for calculating cloud densities in one-dimensional models". *Icarus* 245, pp. 273–281.

Yu, S., B.J. Drouin, and J.C. Pearson. 2010a. *Species tag: 17002 Version 5.*

Yu, S., B.J. Drouin, and J.C. Pearson. 2010b. *Species tag: 17004 Version 5.*

Yu, Shanshan, John C Pearson, Brian J Drouin, Keeyoon Sung, Olivier Pirali, Michel Vervloet, Marie-Aline Martin-Drumel, Christian P Endres, Tetsuro Shiraishi, Kaori Kobayashi, et al. 2010c. "Submillimeter-wave and far-infrared spectroscopy of high-J transitions of the ground and v2= 1 states of ammonia". *The Journal of chemical physics* 133.17, p. 174317.

VITA

Amadeo A. Bellotti was born in November of 1990 in Orlando Florida. He was raised in Orlando, FL until the age of 14 when he moved to Charlotte. There he attended Charlotte Catholic High School and was active in Rugby and Science Olympiad. He graduated from the University of South Carolina in May 2013 with a Bachelor's Degree in Electrical Engineering. While enrolled at South Carolina he was in charge of the GamecockFIRSTers. This high school FIRST robotics team was a joint effort between the university and inner-city schools to introduce STEM. His team made it to the international championship during all of his four years. In August of 2013 he enrolled at the Georgia Institute of Technology and earned a Master's Degree in Electrical and Computer Engineering in May 2015, followed by a doctorate in May 2018.

As a Ph.D student of Dr. Paul Steffes, he originally studied the microwave properties of various gases. His dissertation ranged many topics from the microwave properties of ammonia and water vapor at high temperatures to modeling atmospheric phenomena. The main focus of his dissertation was on using data from the Juno Microwave Radiometer to retrieve jovian atmospheric properties. During this time he also worked with NLA Diagnostics, a start-up company developing non-destructive testing methods for advanced composite materials. While with the company, three SBIR grants were acquired totalling $1.8 million. His work with the company resulted in four product lines and a patent.

Following the completion of his doctorate, he will be joining the Missile Fire and Control group at Lockheed Martin in Dallas, TX.